Representation of visual information within the dendritic tree of pyramidal cells in primary visual cortex

Chiara Baragli

University College London

September 2016

Thesis submitted to UCL for the degree of Doctor of Philosophy

I, Chiara Baragli, confirm that the work presented in this thesis is my own. Where information has been derived from other sources, I confirm that this has been indicated in the thesis.

Abstract

A fundamental aim in system neuroscience is to understand how sensory information is represented in the brain. While a wealth of studies investigated how visual stimuli are encoded in populations of neurons, little is known about how visual information is represented in a single cell at the level of the dendritic tree. This is due in part to difficulties in measuring dendritic activity within dendritic arbours, which are typically fine three dimensional structures. To overcome this, we have used a custom 3D two-photon acousto-optic lens microscope to measure visually-evoked dendritic activity in pyramidal cells in mouse primary visual cortex.

Pyramidal neurons were sparsely co-labelled with the genetically-encoded calcium indicator GCaMP6f and with the red fluorophore TdTomato. Dendritic activity was monitored with GCaMP6f, and simultaneous recording of the activity-independent red TdTomato fluorescence was used to detect movement of the tissue. Random access point measurements were made at 80-120 Hz from multiple locations distributed in three dimensions, and this enabled me to monitor neuronal activity in a substantial fraction of the dendritic tree and in the soma near-simultaneously. Patterns of dendritic activity were characterized in layer 2/3 neurons and in the tuft of layer 5 pyramidal neurons during presentation of gratings in awake animals.

In the tuft of layer 5 neurons, calcium transients tended to be either localized to 1-2 dendritic branches, or to occur in the full-dendritic tuft and in the soma. In contrast, in layer 2/3 neurons calcium transients were mainly local, and somatic calcium transients were rarely accompanied by global events. Visually-evoked dendritic activity was evident in layer 2/3 neurons, and I observed that dendrites tend to have similar orientation tuning curves as the soma. But several dendrites with different preferred orientations were present in all the cells imaged. Dendritic activity in layer 2/3 neurons was little affected by anaesthesia and locomotion. In contrast, apical dendrites of layer 5 neurons showed little response to visual stimuli, but they were strongly modulated by the state of the animal. Indeed, anaesthesia suppressed dendritic activity in these cells, while locomotion enhanced it compared to the resting state.

These data suggest that dendrites in layer 5 and in layer 2/3 pyramidal neurons have different integration mechanisms *in vivo*, and that they process different types of synaptic inputs. While layer 2/3 neurons receive mainly feedforward (bottom-up) visual inputs, apical dendrites in layer 5 cells are driven primarily by top-down inputs (animal state).

Acknowledgments

First and foremost I would like to thank my supervisor, Angus Silver, for his support and guidance. Even in the busiest periods, he always found the time to discuss with me and advise me, and I learnt a lot from his critical thinking, scientific rigour and intellectual honesty. I also wish to thank Thomas Mrsic-Flogel for co-supervising me at the beginning of my PhD, for transmitting to me his enthusiasm about visual neuroscience and for his remarkable patience in explaining to me the basic principles of the visual system.

I am greatly indebted to all past and current members of the Silver lab for technical help and for stimulating discussions, but also for listening to my complaints when experiments did not work, and for being ready to go to the pub to forget those experiments. In particular, Maria Florencia Iacaruso generously taught me everything that I needed to start my project. The microscopy development group, Geoffrey Evans, Victoria Griffiths, Paul Kirkby, Theo Koimtzis, George Konstantinou and Srinivas Nadella, made this project possible, provided continuous support, and always had the patience to explain the basic concepts of optics and system engineering to a biologist. Sadra Sadeh helped me with data analysis, Tommy Younts carried out complementary *in vitro* experiments, Hana Ros helped me to start the experiments in awake animals, and Diccon Coyle was always available to take care of my mice. I also wish to thank Antoine Valera, Alex Cayco Gajic, Boris Marin, and Tomas Fernandez-Alfonso for precious advice and scientific discussions.

I also would like to thank my examiners Ian Thompson and Alasdair Gibb, for taking the time to read and scrutinize my thesis.

Finally, my deepest gratitude goes to my parents and to Pierrick, for putting up with me even in the most difficult times, and for their unwavering support and love.

This work was funded by the Wellcome Trust and ERC.

Table of contents

List of figures

List of tables

1. General introduction

1.1 The mouse visual system

The visual system in the mouse shares many of the same features with higher mammals. In the main visual pathway, neurons project from the retina to the dorsal lateral geniculate nucleus (dLGN) in the thalamus and to the superior colliculus (SC). From the dLGN, sensory information is then relayed to the primary visual cortex (V1) and again to the superior colliculus, in the midbrain. The superior colliculus also projects to V1, and from V1 the sensory information is then transmitted to several cortical higher visual areas (**figure 1.1**).

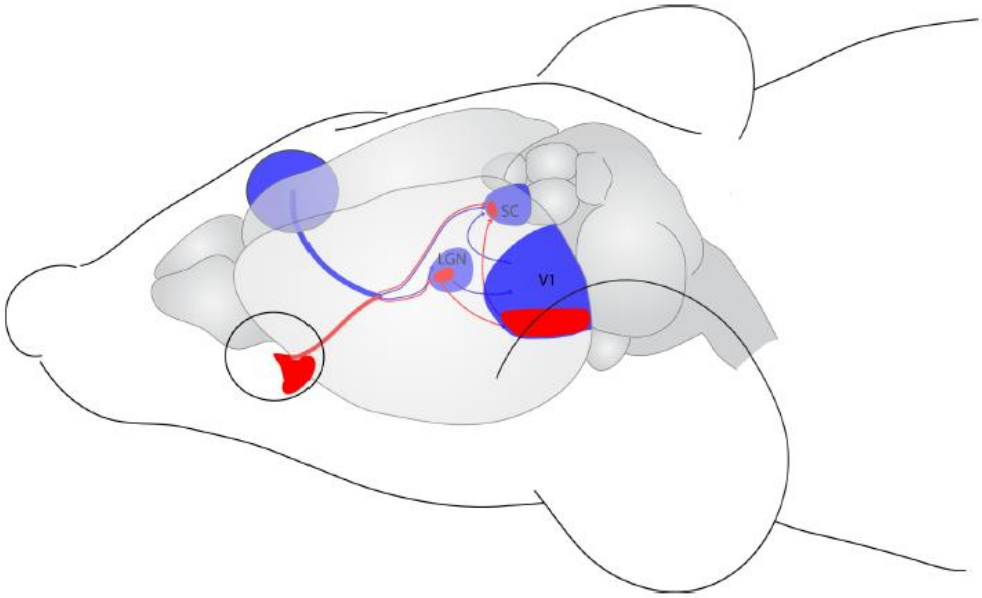

Figure 1.1 Schematic diagram of the mouse visual pathways, reproduced from (Wilks et al., 2013) and showing direct retinal projections to the dorsal lateral geniculate nucleus (LGN) and to the superior colliculus (SC) as well as geniculo-cortical pathways from the LGN to primary visual cortex (V1). In the LGN, the red regions correspond to the termination zones of the ipsilateral-projecting retinal ganglion cells axons, while the blue regions correspond to the termination zones of the contralateral projections of retinal ganglion cells. Analogously in V1 and in SC, the monocular field is shown in blue, while the binocular area is shown in red.

1.1.1 The retina

The retina is a structure with several layers of neurons interconnected by synapses (**figure 1.2**). At the back of the retina, photoreceptors are excited by light, which then transmit the sensory information to bipolar cells, which in turn are connected to ganglion cells. In the main visual pathway, axons of retinal ganglion cells form the optic nerve that projects to the dLGN (see above). In the retina, inhibition is provided by horizontal and amacrine cells: horizontal cells link photoreceptors and bipolar cells by relatively long connections that run parallel to the retinal layers; similarly, amacrine cells link bipolar cells and retinal ganglion cells (Masland, 2001). The major retinal cell types and the circuitry are shared in primates and mice.

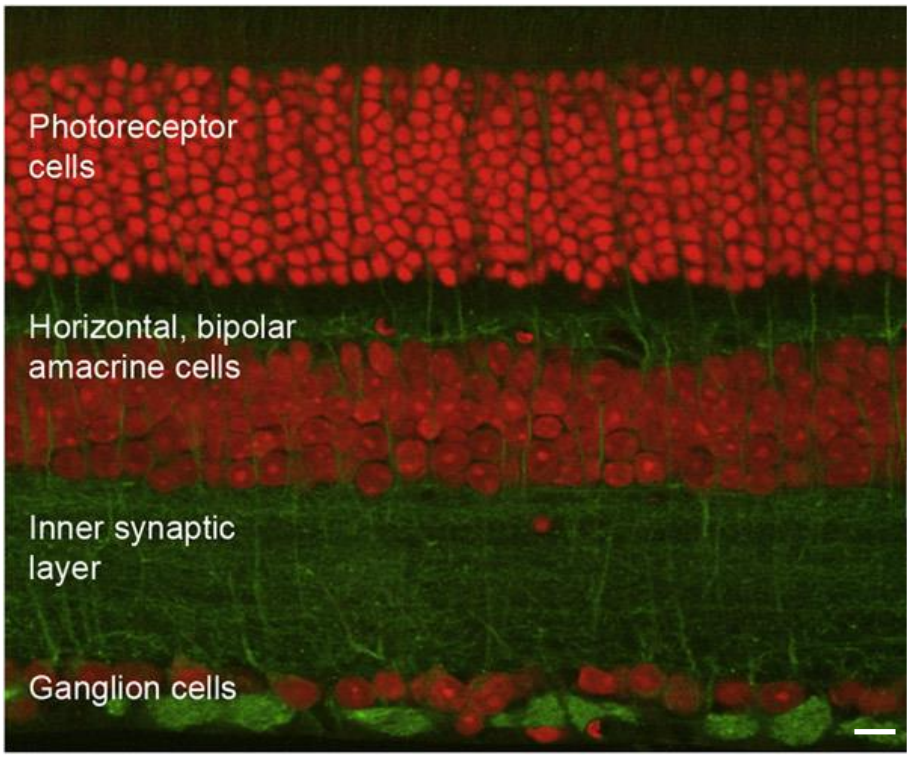

Figure 1.2 The layers of the mouse retina, reproduced from (Masland, 2012; Wässle et al., 2009). Light travels across all the different layers of neurons and then reaches the photoreceptors. Photoreceptor cells connect to bipolar cells, while horizontal and amacrine cells inhibit bipolar and ganglion cells. Bipolar cells and amacrine cells form synapses with ganglion cells dendrites in the inner synaptic layer. The white bar on the bottom right corresponds to 10 μm.

The retinal photoreceptors generate neural signals that represent the image projected onto the eye. There are two types of light receptors at the back of the

retina: rods and cones. Rods are responsible for vision in dim light. Cones are responsible for fine detail and colour. In the mouse, only two types of cones are present: S cones, which respond to short-wavelength light, and M cones, which respond to medium-wavelength light. The L cones, which respond to long-wavelength light in primates, are absent in mice. Because of its rod predominance, as only 3% of mouse photoreceptors are cones (Calderone and Jacobs, 1995), the mouse retina is specialized for vision under low light conditions (Jeon et al., 1998), consistently with the nocturnal behaviour of this animal. Indeed, mice do not have a fovea, and the mouse eye spatial vision seems to be governed by rods (Schmucker et al., 2005). For these reasons, mouse visual acuity is 0.5-0.6 cycles/degree (Gianfranceschi et al., 1999; Prusky and Douglas, 2003), 100 times worse than in humans. But it has been shown that mice use vision to make behavioural choices, for example to choose how to respond to an overhead threat (De Franceschi et al., 2016; Yilmaz and Meister, 2013). Indeed, freely moving rats use eye movements to maintain a continuous overhead binocular field to detect predators coming from above (Wallace et al., 2013).

Photoreceptors signal the absorption of photons via a decrease in the release of the neurotransmitter glutamate, and, depending on the sign of the synapses between photoreceptors and bipolar cells, bipolar and ganglion cells can be depolarized and respond to a spot of light (ON-centre), or hyperpolarized, making them responsive to a dark spot (OFF-centre). Mouse retinal ganglion cells are highly diverse, encompassing at least 22 anatomically distinct subtypes (Volgyi et al., 2009), but the majority of ganglion cells exhibit similar receptive fields (RFs), i.e. the region of visual space in which the presence of a stimulus will alter the firing of that neuron. Most retinal ganglion cells have circular and symmetric RFs, and lateral inhibition from horizontal and amacrine cells establishes centre-surround antagonist RFs (Vaney et al., 2012). The size of the RFs of mouse retinal ganglion cells is approximately 7-10° in diameter (Balkema and Pinto, 1982).

Distinct classes of retinal ganglion cells have different morphologies and computational properties (Sanes and Masland, 2015): ganglion cells can detect edges, motion and direction of motion, spatial and temporal frequencies, and ganglion cells also adapt to contrast and repeated visual patterns (Gollisch and Meister, 2010; Masland, 2012; Nassi and Callaway, 2009). In carnivores and primates, the main subclasses of retinal ganglion cells are 'midget' (X, in carnivores), ‘parasol’ (Y, in carnivores) and bistratified cells (W, in carnivores). Midget cells convey red-green colour opponent signal to the LGN, they receive inputs from only a limited number of photoreceptors and have greater spatial resolution than parasol cells (Dacey, 2000). Parasol cells convey an achromatic signal, they have larger

dendritic trees, so they receive inputs from many photoreceptors and hence they have larger RFs. Parasol cells show higher sensitivity to low contrast stimuli than midget cells (Wassle, 2004). Bistratified ganglion cells convey blue-yellow colour-opponent signal (Dacey and Lee, 1994).

In primates, these subtypes of retinal ganglion cells give rise to anatomically segregated pathways in the dLGN and in higher visual areas (Merigan and Maunsell, 1993; Nassi and Callaway, 2009), while in the mouse these cell types are less distinct (Qu and Myhr, 2011) and the mouse dLGN is not a clear laminated structure. Each class of retinal ganglion cells is organized in a mosaic structure to span all the visual field, so retinal ganglion cells then send parallel representations of an image to the brain, and each representation is obtained by processing different features of the image (Gollisch and Meister, 2010; Masland, 2012; Vaney et al., 2012).

Mammalian retinal ganglion cells project to the dLGN as mentioned above, but also to more than 20 other subcortical targets (Ling et al., 1998), and they mediate behaviours ranging from reflexive eye movements to pupil dilation (Dacey, 2004). The ON directionally selective cell of the rabbit, for example, projects to the accessory optic system and drives optokinetic responses (Buhl and Peichl, 1986). Another example are the photosensitive ganglion cells, that project to the suprachiasmatic nucleus in the hypothalamus and that entrain the circadian pacemaker in the hypothalamus (Berson, 2014; Berson et al., 2002). A full account of the anatomy and physiology of the retina is beyond the scope of this introduction but can be found in (Wassle, 2004; Gollisch and Meister, 2010; Masland, 2012).

1.1.2 The lateral geniculate nucleus

Traditionally, the dorsal lateral geniculate nucleus (dLGN) was considered mainly as a relay of information from the retina to the cortex, but only 10% of the synapses in the dLGN are formed by retinal ganglion cells, while most of the synapses originate from brain stem nuclei. Several studies in primates suggest that the dLGN actively filters the information to transmit to the cortex (Rathbun et al., 2010; Usrey et al., 2000), and that attention can modulate the efficiency of the filtering (Briggs et al., 2013) and alter visual responses (Ling et al., 2015) .

In the dLGN, most neurons sum spatial inputs linearly, and RFs still display classical on and off centre-surround characteristics. In addition, significant differences between ON- and OFF-centre neurons were observed: ON-centre cells are more spontaneously active, and more sensitive to stimulus contrast than OFF-centre cells.

The mouse dLGN neurons have large RFs, approximately 11° diameter (Grubb and Thompson, 2003). Neurons in the mouse dLGN also have both burst and tonic modes of firing (Grubb and Thompson, 2005; Niell and Stryker, 2010).

However, more recently, it has been shown that some dLGN cells in mouse have more complex RFs: orientation selective cells constitute at least 10% of the population of neurons in the mouse dLGN (Marshel et al., 2012; Piscopo et al., 2013; Scholl et al., 2013; Zhao et al., 2013). Also, some neurons in the dLGN show direction selectivity (Cruz-Martín et al., 2014; Piscopo et al., 2013) and spatial frequency tuning (Piscopo et al., 2013), and there is a substantial population of cells that signal the absence of contrast in a visual scene (Piscopo et al., 2013).

Recently, it has also been shown that the dLGN provides orientation-selective inputs to V1: half of the axonal boutons of neurons that project from dLGN to layer 4 in V1 are orientation tuned, and orientation- and direction- tuned thalamic inputs are present in layers 1 to 5 of V1 (Sun et al., 2015). However, a similar study showed instead that most of the axonal boutons from dLGN neurons to layer 4 are not tuned, while axonal boutons from dLGN neurons in more superficial layers of V1 are orientation selective (Kondo and Ohki, 2015). This discrepancy could be caused by the different system used to image the activity of axonal boutons: Kondo and Ohki used a standard 2-photon microscope, and in this system optical aberrations can deteriorate the quality of the recordings for small and deep structures such as layer 4 boutons, while Sun et al. used adaptive optics to correct for these aberrations.

Therefore, orientation and direction selectivity are already computed to some extent in the retina and in the dLGN, but neurons in all cortical layers in V1 still exhibit sharper tuning and a greater diversity of preferred orientations than thalamic boutons (Sun et al., 2015).

1.1.3 The primary visual cortex: structure and cell types

The primary visual cortex (V1) in mice occupies an area of 2-3 mm^2 in the posterior part of the occipital lobe, and it bears many similarities to the visual cortex of higher mammals, with a typical six-layered structure, and a variety of excitatory and inhibitory neuronal subtypes.

V1 receives direct thalamic input from the dLGN and feedback projections from higher-order cortical areas. The primary thalamorecipient layer is layer 4, although the mouse dLGN projects directly also to layer 3,5 and 6 (Constantinople and Bruno,

2013; Cruz-Martín et al., 2014). Rodent V1 exhibits similar circuitry and structure as carnivores and primates (Burkhalter and Bernardo, 1989; Olivas et al., 2012). In the main pathway, layer 4 provides inputs to layer 2/3, which in turn provides inputs to layer 5, the major output layer of V1. Layer 6 neurons receive inputs from all layers and project, among other areas, to the dLGN (Briggs, 2010). Effects of L6 corticogeniculate neurons can be both excitatory and inhibitory on the dLGN (Denman and Contreras, 2015), and the functional role of this feedback connection is still under investigation (Briggs and Usrey, 2008).

However, the functional architecture and synaptic structure of mouse V1 is different. V1 neurons in carnivores and most primates are arranged in vertical columns according to preferred stimulus orientation (Hubel et al., 1976), while in mouse neurons with the same preferred orientation are organized in a “salt and pepper” fashion (Mrsic-Flogel et al., 2007; Ohki et al., 2005; Smith and Häusser, 2010). The mouse also lacks the much wider ocular dominance columns, where neurons favour one eye or the other. Despite this random organization, connections between V1 neurons are specific at the level of single cells: higher connection rates and stronger connections are present between neurons driven by similar visual features (Cossell et al., 2015; Denman and Contreras, 2014; Ko et al., 2011) and with similar spatial RF structure (Cossell et al., 2015). Indeed, layer 2/3 neurons that are connected to each other form subnetworks that share common inputs from layer 2/3, from layer 4 and from the dLGN (Morgenstern et al., 2016; Yoshimura et al., 2005). In addition, the network formed by all the presynaptic neurons of an individual cell arranges in layer-specific modules, where neurons in the same layer share the same preferred stimulus direction (Wertz et al., 2015).

The principal excitatory cells in V1 are pyramidal neurons (Ramon y Cajal, 1909), and they have been divided into three subtypes in layer 5 (Kim et al., 2015), and into two subtypes in layer 6 (Velez-Fort et al., 2014), depending on whether these neurons project mainly to cortical areas or to subcortical areas. In layer 5, cortico-subcortical neurons are more direction-selective, prefer faster stimuli and receive inputs from areas involved in top-down modulation (retrosplenial and cingulate cortex among others), raising the possibility that they might be involved in motion detection and movement-related tasks. In contrast, cortico-cortical neurons receive inputs mainly from higher visual areas and are less selective for stimulus direction. A third type was also identified, a class of L5 pyramidal neurons that project to cortical areas and not to the striatum (Kim et al., 2015). These three subclasses also differ in intrinsic firing properties and in morphology; for example, cortico-cortical neurons are smaller than cortico-subcortical neurons (Harris and Mrsic-Flogel, 2013; Kim et al., 2015). In layer 6, pyramidal cells were also divided into cortico-cortical

and cortico-thalamic neurons; cortico-cortical neurons are more broadly tuned to stimulus orientation and are predominantly innervated by deep layer V1 neurons, while cortico-thalamic neurons are more selective and receive inputs from higher cortical areas (Velez-Fort et al., 2014).

In mouse neocortex, approximately 80% of the neurons are excitatory, and the remaining 20% are GABAergic inhibitory neurons. These inhibitory neurons are morphologically, electrophysiologically and chemically diverse (Markram et al., 2004). In mouse V1, parvalbumin (PV), somatostatin (SOM) and vasoactive intestinal peptide (VIP) are expressed in 36%, 30% and 17% of GABAergic neurons, respectively (Pfeffer et al., 2013). Thus, the three chemically specified subtypes together can account for a majority of total inhibitory neurons.

PV neurons are fast-spiking interneurons and target mainly the perisomatic region, proximal areas of basal dendrites and the axon initial segment. They receive local, dense and diverse excitatory inputs (Hofer et al., 2011), and they have been suggested to perform gain control and stabilize the activity of cortical networks (Atallah et al., 2012).

SOM neurons consist largely of Martinotti cells, and they target tuft dendrites of excitatory neurons and inhibit other interneurons (Pfeffer et al., 2013; Silberberg and Markram, 2007). In layers 2/3 of mouse visual cortex, SOM interneurons are tuned to the orientation of visual stimuli and exert selective and delayed inhibition (Ma et al., 2010). In layer 5, bursts of activity in pyramidal neurons can activate Martinotti cells, which disynaptically inhibit the dendritic tree of the same or neighbouring pyramidal cells (Murayama et al., 2009). This circuit could control the sensitivity or the dynamic range of layer 5 pyramidal neurons (Murayama et al., 2009).

VIP neurons target SOM neurons, thus disinhibiting pyramidal neurons (Fu et al., 2014; Pfeffer et al., 2013). This circuit has been shown to play a role in top-down modulation (Zhang et al., 2014), and it might also increase the network activity during locomotion (Fu et al., 2014).

Other types of interneurons are present in mouse V1, for example neurogliaform interneurons that target predominantly the apical dendrites of layer 5 cells (Tamas et al., 2003). Interestingly, it has also been shown that inhibition from layer 1 interneurons increases the trial-to-trial reliability of sensory-evoked responses of pyramidal neurons in rat barrel cortex (Egger et al., 2015).

1.1.4 The primary visual cortex: responses to visual stimuli

V1 forms a continuous representation of visual space (**figure 1.3**). In this retinotopic map the lower contralateral visual field (dorsal retina) is represented rostrally, while the upper contralateral visual field (ventral retina) is represented caudally (**figure 1.3**) (Wagor et al., 1980).

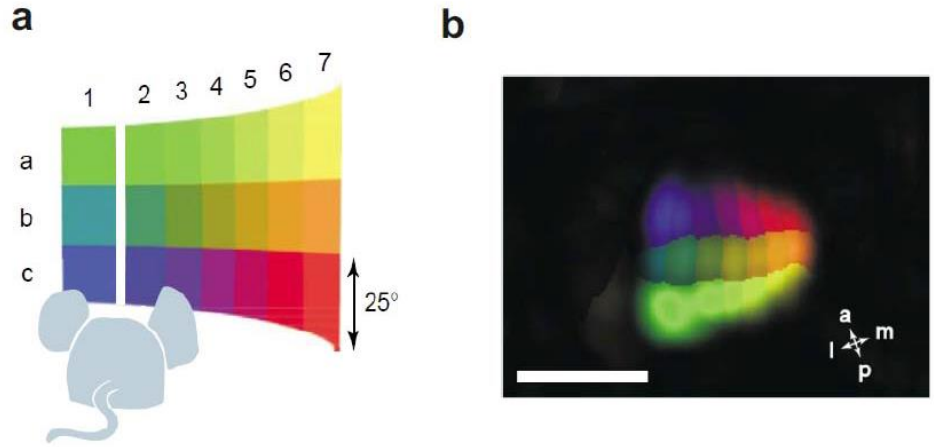

Figure 1.3 Schematic representation of the retinotopic organisation of mouse visual cortex, reproduced from (Hübener, 2003). a: Retinotopic stimulation at adjacent positions within the visual field. b: Colour-coded map of the retinotopic organisation of left V1. The colour of each pixel corresponds to the stimulus position that triggered the strongest response at this pixel. Abbreviations: a, anterior; p, posterior; m, medial; l, lateral. Scale bar: 2 mm.

About 90% of retinal inputs project to the controlateral hemisphere, but the visual field still contains a binocular region that receives inputs from both eyes (Dräger, 1975; Wagor et al., 1980). Cortical inputs from the contralateral dLGN are distributed across the entire V1, whereas inputs from the ipsilateral side terminate in the lateral half of V1, which corresponds to the binocular region (**figure 1.1**).

Most neurons in the retina and in the visual thalamus respond best to small and circular stimuli of high contrast, while most neurons in V1 integrate this information and detect more accurately orientation, direction and spatial and temporal frequency of the stimuli. Indeed, although a significant fraction of inputs from the dLGN are

orientation- and direction- selective (Kondo and Ohki, 2015; Sun et al., 2015), neurons in all cortical layers in V1 exhibit sharper tuning and a greater diversity of preferred orientations compared to their thalamic inputs (Kondo and Ohki, 2015; Sun et al., 2015).

Similarly to cats and monkeys, in mouse V1 simple cells have a clearly delineated RF with two or three antagonistic 'ON' and 'OFF' alternated subfields (**figure 1.4**) (Hubel and Wiesel, 1962; Niell and Stryker, 2008). The spatial organization of the RFs of the most common simple cells of mouse V1 appears to be identical to simple cells in cats and monkeys, except for a difference in spatial scale and maximum discharge frequency. Many RFs have both ON and OFF subregions (55%), 18% of units have only one subregion, while often cells have three subregions (27%) (**figure 1.4**) (Niell and Stryker, 2008). Although the spatial scale of mouse RFs is 5-7° (Niell and Stryker, 2008), up to one or two orders of magnitude larger than cats and monkeys, neurons show selectivity for stimulus parameters, such as orientation and spatial frequency, that is similar to that found in other species. Furthermore, typical response properties, such as linear versus nonlinear spatial summation (i.e., simple and complex cells) and contrast-invariant tuning, are also present in mouse V1 and correlate with laminar position and cell type (Niell and Stryker, 2008).

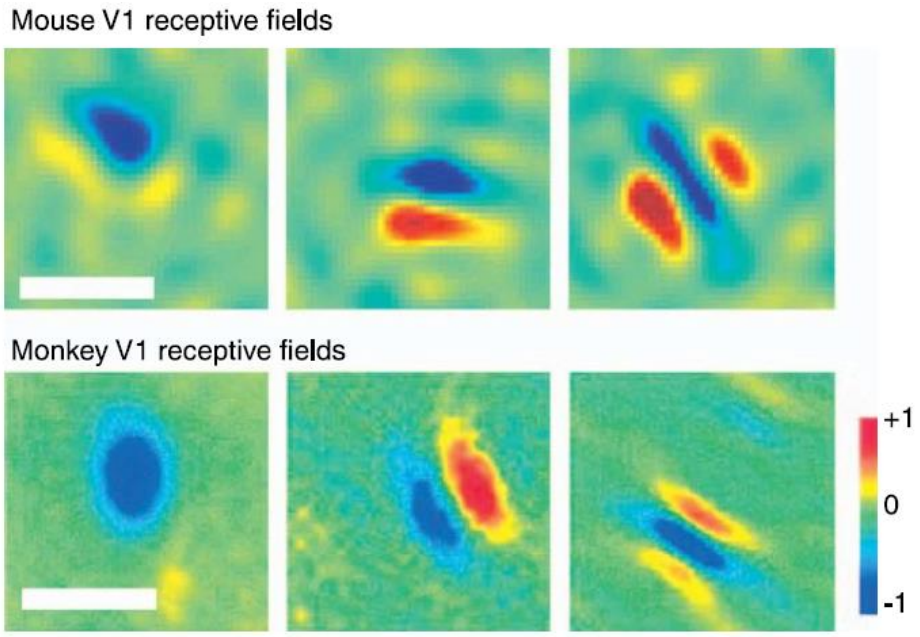

Figure 1.4 Similarity of receptive fields (RFs) in mouse and monkey V1, reproduced from (Huberman and Niell, 2011). Mouse data was from (Niell and Stryker, 2008), and monkey data was from (Ringach, 2002). The panels show three examples of simple cell RFs. The RFs in

mouse V1 were mapped presenting noise movies, and averaging the frames that preceded a spike for each neuron (Niell and Stryker, 2008). In monkey V1, RFs were mapped presenting gratings at different orientations, frequencies and phases, and then correlating the response of the neurons with the luminance values at each pixel. This provided the coefficients with which each pixel should be summed to generate a RF estimate (Ringach, 2002). The scale bar for mouse is 20 degrees, while that for the monkey is approximately 1 degree. Red and blue correspond to ON and OFF subregions, respectively.

The area of maximal sensitivity is called classical receptive field (RF) (Hubel and Wiesel, 1962), but neurons in V1 also display non-classical receptive fields (nRF), areas outside the RF where a visual stimulus can still modulate the neuronal firing rate (Allman et al., 1985). In V1, the response of neurons to stimuli within their RF can be facilitated or suppressed by contextual stimuli in the RF surround in complex ways (Blakemore and Tobin, 1972; Gilbert and Wiesel, 1990; Nelson and Frost, 1978). A typical V1 cell increases its response with increasing grating diameter, up to a peak, and then it is suppressed for further increases in stimulus diameter (Vaiceliunaite et al., 2013). Surround suppression is already present in the retina and in the dLGN, but in V1 additional factors could contribute to generate nRFs: feedforward connections to V1 from the dLGN, long-range V1 lateral connections, and feedback connections to V1 from extrastriate cortex (Angelucci and Bressloff, 2006). Surround suppression in mouse V1 is also mediated by SOM inhibitory neurons, which respond preferentially to the RF surround and inhibit pyramidal cells (Adesnik et al., 2012; Nienborg et al., 2013; Zhang et al., 2014).

1.1.5 Effects of anaesthesia in primary visual cortex

Traditionally, most of the experiments which study vision were performed on anaesthetized animals, but recently it has been shown that different anaesthetics, such as isoflurane and urethane, can affect the properties of neuronal networks in mice and rats (Adesnik et al., 2012; Ayaz et al., 2013; Greenberg et al., 2008; Haider et al., 2013; Keller et al., 2012; Murayama and Larkum, 2009; Niell and Stryker, 2010; Pisauro et al., 2013; Vaiceliunaite et al., 2013).

In awake animals spike rates and spike bursting are higher, both during spontaneous activity and during visually-evoked activity (Greenberg et al., 2008; Niell and Stryker, 2010). Neurovascular coupling is also different under anaesthesia and in awake

animals: the hemodynamic responses that follow neural activity are larger and faster in awake animals (Pisauro et al., 2013).

Orientation selectivity is similar in awake and anaesthetized animals, both in primates (Wurtz, 1969) and in mice (Niell and Stryker, 2010), but visual responses in awake mice are more spatially selective and shorter (Haider et al., 2013; Vaiceliunaite et al., 2013). This difference is caused by enhanced inhibition in awake mice: inhibitory inputs exhibit broad spatial selectivity and then limit neural activity in space and in time (Haider et al., 2013). Also, surround suppression is stronger in superficial cortical layers, and this laminar dependency is abolished under anaesthesia (Vaiceliunaite et al., 2013).

1.1.6 Effects of locomotion in primary visual cortex

Since neuronal activity in visual cortex started to be probed in awake animals, several studies began to investigate the relation between animal behaviour and neuronal activity. In particular, it was observed that locomotion has profound effects on mouse V1, increasing both visually-evoked and spontaneous activity dramatically in the superficial cortical layers (Andermann et al., 2011; Ayaz et al., 2013; Erisken et al., 2014; Keller et al., 2012; Mineault et al., 2016; Niell and Stryker, 2010; Saleem et al., 2013). In contrast, neuronal activity in infragranular layers of V1 seems to be not modulated, or even suppressed, by locomotion (Erisken et al., 2014).

In the absence of visual stimuli, most neurons in layer 2/3 of V1 are modulated by running speed (Saleem et al., 2013). The dependence of the firing rate on the running speed is graded, and half of the neurons modulated by locomotion showed a band-pass tuning, so they responded maximally to a specific running speed (Saleem et al., 2013).

The average firing rate of visually-evoked activity in layer 2/3 in V1 increases by nearly 3-fold during locomotion (Andermann et al., 2011; Erisken et al., 2014; Keller et al., 2012; Niell and Stryker, 2010). This enhancement of visually evoked responses is accompanied by a shift in the local field potential (LFP) from low frequencies to gamma oscillations (Niell and Stryker, 2010) and, in addition, pairwise correlations are reduced during locomotion (Erisken et al., 2014). Locomotion does not affect orientation selectivity (Niell and Stryker, 2010), but it reduces surround suppression, allowing neurons to integrate over larger regions of visual space (Ayaz et al., 2013). Furthermore, locomotion preferentially enhances the gain of neurons

tuned to high-spatial frequencies, thus the population can support better spatial acuity while the animal is running (Mineault et al., 2016).

In a virtual reality environment, nearly half of layer 2/3 V1 neurons are tuned for a weighted sum of running speed and speed of the visual flow (i.e. speed of the virtual reality) (Saleem et al., 2013). However, highest activity in the network is reached in response to a mismatch between the visual flow and the running speed of the animal, suggesting that processing in layer 2/3 of visual cortex may be based on predictive strategies, which use motor-related and visual input to detect mismatches between predicted and actual visual feedback (Keller et al., 2012; Roth et al., 2016).

However, some of the effects on the network attributed to locomotion could be caused by an increase in arousal level. In a recent study (Vinck et al., 2015), the size of the mouse pupil was used as an indicator of the arousal level of the animal (Eldar et al., 2013; Gilzenrat et al., 2012; Reimer et al., 2014), and quiescent states of high and low arousal were compared with running epochs. Arousal suppresses spontaneous firing, increases the power of gamma oscillations, and enhances the visual coding, while the increase in network activity is specific to locomotion (Vinck et al., 2015). In addition, in mice, locomotion often co-occurs with whisking, and the effects of running and whisking has not been fully separated yet (Vervaeke et al, unpublished).

The circuits responsible for the modulation of neuronal activity by locomotion have just begun to be investigated. For instance, optogenetic stimulation of the mesencephalic locomotor region (MLR, located in the midbrain) can induce locomotion and increase the gain of cortical responses (Lee et al., 2014). It has been shown that stimulation of the MLR at subthreshold levels, so that it does not trigger animal movement, changes cortical processing in a similar way (Lee et al., 2014). The MLR projects to the forebrain, and stimulation of the MLR projections to the forebrain also increased the gain of cortical responses (Lee et al., 2014). In addition, cholinergic inputs from the forebrain regulate cortical activity and visual perception in running mice (Fu et al., 2014; Pinto et al., 2013; Polack et al., 2013). It has also been reported that nicotinic inputs from basal forebrain increase the activity of VIP neurons during locomotion, and that VIP neurons inhibit SOM neurons, thus disinhibiting pyramidal neurons (Fu et al., 2014). However, in opposition to the previous study, it has also been shown that both SOM and PV neurons are more depolarized during locomotion (Pakan et al., 2016; Polack et al., 2013), and that this tonic depolarization requires noradrenergic inputs (Polack et al., 2013). Finally, it is not clear if feedforward connectivity contributes to the effects of locomotion observed in V1. While one work showed that locomotion has no effect on neuronal activity in

the dLGN (Niell and Stryker, 2010), a more recent study reported that dLGN neurons are tuned to different running speed in absence of visual stimuli, and that neuronal activity is higher in this brain area when the animal is running (Erisken et al., 2014).

1.1.7 Summary of the functions of mouse primary visual cortex

The mouse primary visual cortex has different roles in processing visual information: it sharpens orientation and direction selectivity, and neurons in V1 show contrast-invariant orientation tuning, and selectivity to spatial and temporal frequencies. nRFs, and in particular surround suppression, allow representation of natural scenes with more efficient sparse codes.

However, the complexity of nRFs makes it difficult to understand how visual information in natural images is encoded in a population of neurons. In addition, freely-viewing animals alternate gaze fixations and saccadic eye movements (Maldonado and Babul, 2007), and the effects of eye movements on visual responses has just begun to be investigated. Also, the circuitry and mechanisms underlying RF formation and the computations performed by a network are not always clear.

In addition, in the recent years it has been shown that activity in mouse V1 is modulated also by a variety of non-visual inputs: motor inputs (Ayaz et al., 2013; Keller et al., 2012; Niell and Stryker, 2010; Saleem et al., 2013), auditory inputs (Ibrahim et al., 2016), somatosensory inputs (unpublished data from Bonin lab), expectation of a reward (Poort et al., 2015; Shuler and Bear, 2006) and animal state (Greenberg et al., 2008; Haider et al., 2013; Niell and Stryker, 2010; Reimer et al., 2014; Vaiceliunaite et al., 2013; Vinck et al., 2015). How all these different types of information are integrated and processed will likely be a prominent question in visual neuroscience in the next years.

Finally, little is known about visual processing at a single-cell level and about the role of subcellular compartments in the integration of visual and non-visual inputs. If we are to understand how V1 processes sensory information, it is fundamental to investigate how a single neuron and its dendrites integrate signals *in vivo*.

1.2 Dendrites

The main excitatory neurons in V1, the pyramidal neurons, exhibit extensive dendritic trees with a characteristic morphology. The vast majority of synaptic inputs of a neuron impinges on the dendrites, and many studies show that dendrites of pyramidal neurons exhibit linear and nonlinear properties, enabling them to integrate synaptic inputs in complex manners and to perform a variety of computations. These computations are likely to be essential for the processing of visual information performed by a neuron and by a network. In this chapter, I will give a brief overview of dendritic structure, properties and computations.

1.2.1 Dendritic structure of pyramidal neurons

Pyramidal neurons are found in most mammalian forebrain structures, such as cerebral cortex, hippocampus and amygdala (Nieuwenhuys, 1994; Spruston, 2008). Pyramidal neurons typically have a single axon that departs from the soma, branches abundantly and makes numerous glutamatergic contacts. The dendritic trees of pyramidal cells can be divided into at least two domains: apical and basal. The thick main apical dendrite ascends from the apex of the soma, branches into oblique dendrites, and then often terminates in a bouquet of dendrites, called the tuft, that is superficial in the cortical layers (**figure 1.5**). The main apical dendrite can extend over hundreds of micrometres, while basal dendrites, which depart from the base of the soma, are usually shorter. Superficial pyramidal neurons, close to the layer 1 boundary, can be more star-shaped and they do not always display an apical trunk (Larkman and Mason, 1990).

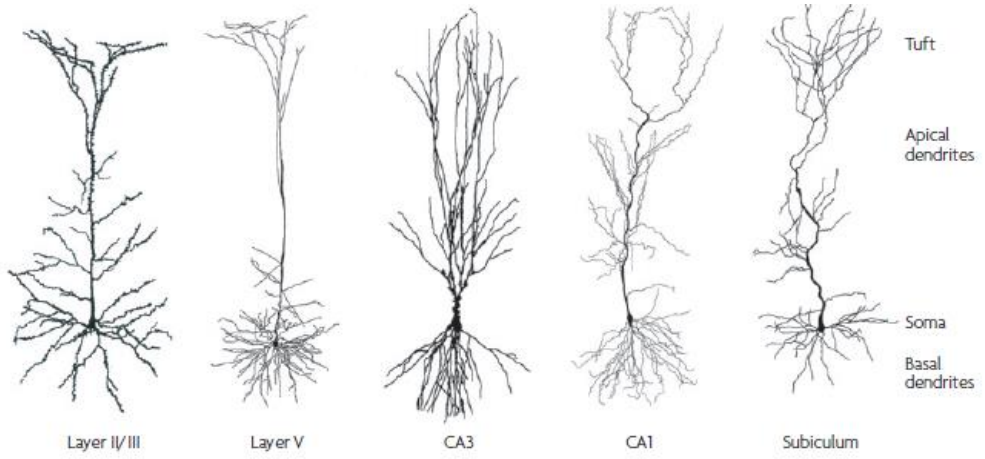

Figure 1.5 Structure of pyramidal neurons in different brain areas, reproduced from (Spruston, 2008). Even if there are differences in morphology across different brain regions, the dendritic tree of all pyramidal neurons can be divided in basal, apical and tuft domains. The full vertical length of each cell is, from left to right: unknown, 1,180 µm, 580 µm, 730 µm, 790 µm.

Different domains in pyramidal neurons receive different types of synaptic inputs: basal dendrites form synapses mainly with adjacent neurons and receive primarily feedforward inputs, while apical dendrites are contacted also by long-range projections and receive modulatory inputs. For example, the basal dendrites and the proximal apical dendrite of layer 2/3 cells in the neocortex receive local inputs from layer 4 and other layer 2/3 cells, while the apical and tuft dendrites receive inputs from other cortical areas, as well as thalamic inputs (Feldmeyer, 2012; Feldmeyer et al., 2002). Similarly, in layer 5, the basal dendrites and proximal apical dendrite receive inputs from layer 4 and layer 5 cells, while the more distal apical dendrites and the tuft receive inputs from layer 2, other cortical areas and from the thalamus (Cauller, 1995; Cauller et al., 1998; Douglas and Martin, 2004; Nieuwenhuys, 1994; Petreanu et al., 2009). The soma and the axon receive only GABAergic inhibitory inputs, while dendrites receive both excitatory and inhibitory inputs. The distinct morphologies and the different types of inputs in basal and apical dendrites suggest that these two domains might integrate synaptic inputs differently.

Both apical and basal dendrites are covered in spines, which are small (< 1 μm^3) membranous protrusions. Dendritic spines are essential for dendritic integration, as they constitute the postsynaptic sites for most excitatory glutamatergic synapses. Spines can vary in size and shape, and they are highly plastic. Most spines contain a single excitatory synapse, but some spines contain multiple synapses (Sorra and Harris, 1993; Yankova et al., 2001). Inhibitory synapses, on the other hand, are found

mainly on the dendritic shaft, but 30% of inhibitory synapses are found on spines (Chen et al., 2012a). Inhibitory synapses on spines are always adjacent to an excitatory synapse in the same spine (Chen et al., 2012a), and they can provide local inhibition within the individual spine (Chiu et al., 2013; Higley, 2014). This inhibition is called “shunting”, because it changes the total conductance of the membrane but it does not change the somatic voltage when active on its own.

Even though all pyramidal neurons share the same basic morphological features, depending on the brain area, pyramidal neurons can exhibit differences in morphology and size. For example, layer 5 cortical neurons have a much longer apical dendrite and fewer oblique dendrites compared to layer 2/3 cortical neurons (**figure 1.5**). In CA3 in hippocampus, the apical dendrite starts branching closer to the soma, and it shows a cluster of dendritic spines in the first 100 µm from the soma, while in the proximal apical dendrite of pyramidal neurons in cerebral cortex spines are less frequent (Spruston, 2008).

1.2.2 Passive properties of dendrites: distance-dependent synaptic integration

To address the question of how dendrites transform and integrate synaptic inputs, it is first useful to consider dendritic passive properties. In this case, dendrites can be treated as electrical cables, i.e. an insulator with a resistance, and dendritic integration is then governed by cable theory (Rall, 1967).

In this framework, the cytoplasm is a low-resistance conductor with an intracellular resistivity R_i, while the plasma membrane has a specific resistivity R_m and capacitance C_m, and the dendritic membrane properties are assumed to be constant in time and space. This model can be used to study how far potentials spread passively (electrotonically) into a cell. High values of R_i and low values of R_m increase the attenuation of synaptic potentials as they propagate passively, while the membrane capacitance C_m filters transient changes in membrane potentials. Therefore, brief PSPs are more attenuated than sustained changes in membrane potential. The membrane time constant, i.e. the product of R_m and C_m, is particularly important PSPs summation: for any change in membrane potential, the voltage decay is determined mainly by the membrane time constant. Thus, the membrane time constant defines the time window over which synaptic potentials can sum. In layer 5 pyramidal neurons, the membrane time constant has been found to be approximately 12 ms in brain slices (Stuart and Spruston, 1998). But it is important to know that this time constant is not a purely passive measure: it is voltage

dependent, it is influenced by voltage-dependent conductances and it varies greatly between different types of neurons (Koch et al., 1996).

EPSPs that propagate in the dendritic tree are filtered by the passive properties of the dendrites: synaptic charge is deposited onto the dendritic capacitance, and it is lost through the membrane resistance. Therefore, a postsynaptic potential decreases its amplitude and slows its time course as current flows from the dendrite to the soma, and inputs far from the soma are then more attenuated and produce a smaller but broader EPSP. On the other hand, synapses located on thin distal dendrites can generate local synaptic potentials with higher amplitudes, due to the higher local input impedance and the smaller local capacitance at this dendritic location, but the amplitudes of these membrane potentials are still greatly reduced as they propagate towards the soma. Synaptic inputs that are far from the soma are then expected to have less influence on generating an action potential than proximal synaptic inputs.

In addition, dendritic branching points are very effective in attenuating voltage, therefore they can create electrical compartments at the level of the dendritic branches (Branco and Häusser, 2010; Vetter et al., 2001). In particular, theoretical considerations predict that voltage propagation at a branching point depends on the ratio of the impedances of the daughter and parent branches, called impedance mismatch (Goldstein and Rall, 1974). If the impedance mismatch is greater than one, i.e. if the combined impedance of the daughter branches is higher than the impedance of the parent branch, voltage propagation is strongly attenuated. Therefore, forward propagation, i.e. from the dendrites to the soma, is facilitated compared to backpropagation, because the diameter of the dendrites increases and the impedance decreases closer to the soma. Interestingly, simulations showed that the efficacy of backpropagation strongly correlated with both the number of branching points and impedance mismatches (Vetter et al., 2001). In conclusion, the geometry of a dendritic tree and the location of a synaptic input in the tree are expected to have a great effect on how that input is integrated.

In a model of CA1 pyramidal neuron with passive dendrites, a synapse proximal to the soma with an excitatory conductance of 0.3 nS can produce an EPSP at the soma of 0.2-0.3 mV, while a synapse with the same conductance in the distal dendrites can produce a somatic EPSP of less than 0.02 mV. Therefore, an EPSP can be attenuated even 10 times, depending on its position in the dendritic tree (Magee and Cook, 2000). Indeed, direct measurements from layer 5 neurons showed that an EPSP is attenuated more than 40 times as it travels from distal

dendrites to the soma (Larkum et al., 2009; Nevian et al., 2007; Williams and Stuart, 2002).

Distal inputs would then appear to have little or no effect on the somatic membrane potential and on the output of the neuron. However, in pyramidal neurons in CA1 in hippocampus, the conductances of synapses are scaled depending on their position in the dendritic tree, so distal synapses have greater conductances to compensate for the loss of charge of an EPSP that propagates to the soma (Magee and Cook, 2000; Nicholson et al., 2006). This mechanism does not seem to be present in cortical pyramidal neurons (Williams and Stuart, 2002), but active conductances in the distal dendrites (see below) and the consequent non-linear summation of synaptic inputs could enhance the impact of distal inputs on the soma (Branco and Hausser, 2011; Larkum et al., 1999a, 2004).

The relative location of two synaptic inputs is also crucial to determine how these inputs are integrated: two EPSPs close to each other sum sublinearly, because the depolarization associated with the first EPSP reduces the driving force for the synaptic current for the second input. Whereas when two EPSPs are electrotonically distant, their summation is maximized (almost linear). In addition, more temporal summation occurs for two EPSPs located in the dendrites than in the soma, because cable filtering of dendritic EPSPs slows their time course, thus increasing temporal summation at the soma.

Finally, since the EPSP rise times change as they spread from different locations in the dendrites to the soma, different sequences of inputs can have different effects on the somatic potential: distal-to-proximal sequences of activation result in a larger depolarization at the soma because the peaks of the EPSPs at the soma coincide (Branco et al., 2010; Rall, 1967). However, it is not yet clear whether this mechanism is used to distinguish patterns of inputs *in vivo*.

1.2.3 Dendritic regenerative events: sodium, calcium and NMDA spikes

The passive properties of dendrites provide sublinear and linear mechanisms for integration of synaptic inputs, but it is now clear that in pyramidal neurons additional computational power and supralinear summation are conferred by a number of voltage-dependent ion channels (reviewed in Major, Larkum, & Schiller, 2013).

Dendritic spikes are non-linear regenerative events, with some properties similar to action potentials: they have a threshold, they can actively propagate and some types

have a refractory period (Larkum and Zhu, 2002). However, dendritic spikes can be very different in shape, spatial spread, rise time and duration. Dendritic spikes create a depolarization that can propagate actively or passively to the soma, so they facilitate, but not assure, action potential firing in the axon. On the other hand, a backpropagating action potential can depolarize the dendrites and lower the threshold for the generation of a dendritic spike (Larkum et al., 1999a). Dendritic events, especially backpropagating action potentials, are also important for synaptic plasticity (Sjostrom et al., 2008). Sodium, calcium and N-methyl D-aspartate (NMDA) voltage-gated channels generate the three major types of dendritic spikes, but dendritic spikes can also have mixed contributions from different ion channels.

Voltage-gated sodium channels are responsible for the generation of action potentials in the axon initial segment, but they are found also at lower density in the dendrites of cortical pyramidal neurons, where they can generate short (<5 ms) dendritic spikes. Voltage-gated sodium channel density is uniform in the soma and in different regions of the dendrites, while it seems to be higher at the axon initial segment (Conti et al., 1976; Kole and Stuart, 2008). Sodium spikes can be initiated both in the dendrites and in the axon, but the axon initial segment has a lower threshold for action potential initiation (Stuart et al., 1997a). In addition, the high density of potassium channels in the dendrites can prevent spike initiation in this region (Golding et al., 2005; Yankova et al., 2001). Therefore, action potentials are generated mainly at the axon initial segment, and then they propagate down the axon and backpropagate in the dendrites supported by the active sodium conductances (Stuart and Sakmann, 1994; Stuart et al., 1997b). Action potential backpropagation is a regenerative process, i.e. an event involving a positive feedback loop, but it is still partially filtered by the dendrites and by the branching points, so the amplitude of action potentials decreases with distance in a frequency-dependent manner, and action potentials also become broader as they backpropagate (Stuart et al., 1997a). Action potential backpropagation is supported also by voltage-gated calcium channels.

Calcium channels are present in dendrites and spines. However, high-threshold L-type and N-type channels are more abundant in the soma and in the proximal dendrites, while the density of low-threshold channels (T-type and R-type) is higher in the more distal dendrites (Ross and Larkum, 2012). Low-threshold calcium channels can be activated by synaptic potentials, so they enhance the spread of EPSPs in spines and dendrites. Calcium regenerative events can be initiated by synchronous activation of spatially co-localized synapses, they can be local (dendrite-restricted) (Schiller et al., 1997), and they mediate long-term potentiation

of synaptic inputs (Golding et al., 2002). These local calcium spikes are usually mixed with NMDA spikes.

Multi-branch calcium spikes are generated at the principal calcium spike initiation zone, located in the trunk of the apical dendrite, near the main apical bifurcation (**figure 1.6**) (Kim and Connors, 1993; Larkum et al., 1999a, 1999b, 2009). Calcium spikes in this region are mediated by L-type calcium channels (Pérez-Garci et al., 2013), and they can be triggered in brain slices by different mechanisms: NMDA spikes in multiple tuft branches (Larkum et al., 2009), a coincident backpropagating action potential and a distal EPSP (Larkum et al., 1999a; Stuart and Häusser, 2001), or high frequency (60-200 Hz) backpropagating action potentials (Larkum et al., 1999b). However, it is not known which of these mechanisms are present *in vivo*, but it has been shown that sensory stimulation, in particular whisker deflection, triggers calcium spikes in the apical dendrite (Helmchen et al., 1999).

Calcium transients in the apical trunk have large amplitudes (~ 50 mV), they can last up to 50 times longer than axonal sodium spikes and they can generate bursts of axonal action potentials. Thus, calcium spikes constitute a mechanism that can couple electrically the distal apical dendrites and the soma: synchronous distal inputs on the tuft can trigger dendritic (calcium and NMDA) spikes in tuft branches, that can initiate a calcium spike in the apical trunk and affect the output of the neuron at the axonal action potential initiation zone (Larkum et al., 2009).

In the thinnest distal dendrites, the dominant depolarization-activated conductance seems to be the NMDA receptor (**figure 1.6**) (Branco and Hausser, 2011; Larkum et al., 2009; Major et al., 2008; Schiller et al., 2000). Indeed, NMDA spikes can be initiated in thin basal, oblique and tuft dendrites (**figure 1.6**).

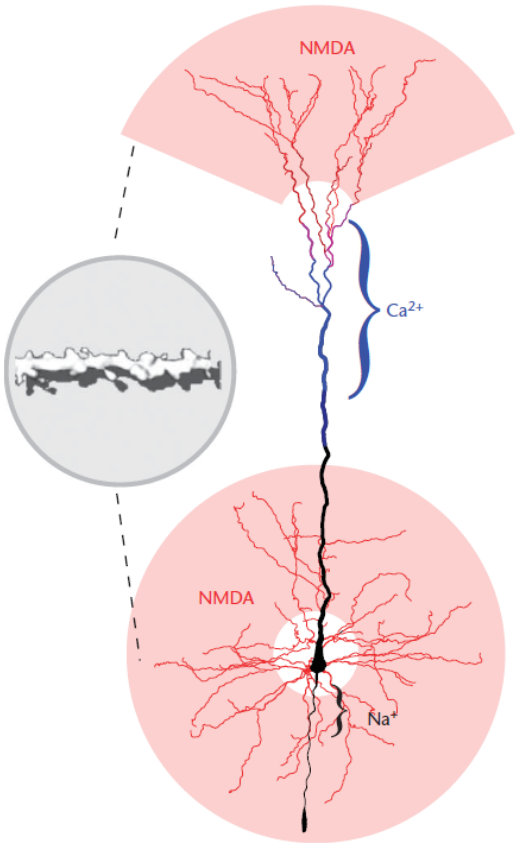

Figure 1.6 Pyramidal neuron showing the principal dendritic spikes generated in each region of the dendritic tree, reproduced from (Larkum et al., 2009). Regions that can initiate mainly sodium spikes are shown in black, dendrites that often generate NMDA spikes are shown in red, while blue shows the principal region for initiation of calcium spikes. The inset shows the high density of spines on a thin dendritic branch.

NMDA receptors are ligand-gated receptor channels, and their activation depends both on the presence of glutamate and on the depolarization of the membrane potential (Edmonds et al., 1995; Gibb and Colquhoun, 1992). In addition, the NMDA response is strongly potentiated by glycine (Johnson and Ascher, 1987). The opening of an NMDA receptor is then gated by binding of two glutamate ions, but the current flow through the channel is voltage dependent, because extracellular magnesium cations can block the open channel. Therefore, strong excitatory inputs onto a dendritic branch can provide glutamate supply and adequate depolarization, causing the NMDA receptors to generate a dendritic spike. Under physiological conditions, excitatory inputs can depolarize the membrane potential through α-amino-3-hydroxy-5-methyl-4-isoxazolepropionic acid (AMPA) receptors and trigger a NMDA spike often mixed with activation of voltage-gated sodium and calcium

channels. As a consequence, the resulting plateau potential is a complex interplay of different conductances: modelling studies suggest that first AMPA receptors generate a fast local sodium spikelet, which elicits a slower-calcium mediated regenerative response, which in turn triggers an NMDA spike (Schiller et al., 2000). However, the majority of basal dendrites do not have enough voltage-gated sodium channels to support a sodium spike, but these branches still generate NMDA spikes; therefore, voltage-gated sodium channels are not necessary to initiate an NMDA spike (Milojkovic et al., 2005).

In vitro and modelling studies suggest that NMDA spikes can be triggered with clustered synaptic excitatory inputs: either with synchronous activation of ~ 10 spatially-clustered single spine inputs, or with synchronous activation of ~ 20 spines randomly distributed on a dendritic branch (Major et al., 2008, 2013; Polsky et al., 2009). A typical terminal dendritic branch bears hundreds of spines, so 5-10 % of these spines need to be active simultaneously in order to initiate a NMDA spike. However, depolarization reduces the NMDA spike threshold (Farinella et al., 2014; Major et al., 2008; Polsky et al., 2009), and depolarization can be provided by another NMDA spike in a nearby location, thus allowing for cooperativity between NMDA spikes (Farinella et al., 2014; Major et al., 2008). Also, high levels of background network activity *in vivo* could reduce the threshold via two mechanisms: first by depolarizing the cell, and secondly by generating sparsely-distributed glutamate-bound NMDA receptors, which would then introduce NMDA receptor conductance (Farinella et al., 2014).

NMDA spikes are characterized by depolarizations with large local amplitude (40-50 mV) (Nevian et al., 2007) and long duration (50-100 ms) (Major et al., 2008; Polsky et al., 2004; Schiller et al., 2000). Large calcium transients that accompany NMDA spikes are usually localized on a dendritic segment of 10-40 µm (Major et al., 2008). Interestingly, NMDA spikes can last up to several hundreds of milliseconds with increased applications of glutamate (Antic et al., 2010; Major et al., 2008). Similarly, *in vivo*-like background activity can introduce a spatially distributed synaptic NMDA conductance and increase the duration of an NMDA spike up to >150 ms (Farinella et al., 2014). In CA3 pyramidal neurons, the decay of the voltage response in a NMDA spike is regulated mainly by G-protein-activated inwardly rectifying potassium channels, and the decay time can change in different dendritic branches of the same cell (Makara and Magee, 2013). Therefore, temporal summation of synaptic inputs can vary over branches, making some dendrites more excitable than others (Makara and Magee, 2013).

In conclusion, a pyramidal neuron can integrate synaptic inputs in sublinear (Longordo et al., 2013), linear (Cash et al., 1998) and supralinear ways (Larkum et al., 2009). The circumstances under which synaptic activation of dendritic voltage-gated channels causes a departure from the passive behaviour of dendrites remains a key question, especially *in vivo*. In addition, dendritic spikes and back-propagating action potentials may have a role in neurotransmitter release, induction of synaptic plasticity and synaptic integration, but their functional role is still under investigation.

1.2.4 Electrotonic coupling of the dendritic tuft and the soma

The dendritic tuft is far from the soma, up to 800 μm in rat layer 5 neurons and 300 μm in layer 3 neurons, so synaptic inputs on distal dendrites can fail to propagate electronically to the soma. However, the active conductances in the dendrites could help to couple electrically the dendritic tuft and the soma. Indeed, investigators proposed that the distal apical dendritic tree in layer 5 cells acts as a separate synaptic integration region, having its own separate spike initiation zone. When the threshold is crossed in this distal compartment, a global dendritic calcium spike is initiated, and a huge dendritic depolarization reaches the somatic region and drives axonal action potentials (Larkum et al., 1999a). In the last two decades several studies addressed the question of whether the tuft and the soma should be considered as two separate electrical compartments.

While subthreshold depolarizations are strongly attenuated along the dendrites, action potential back propagate more efficiently because they are supported by active sodium conductances (Stuart and Sakmann, 1994). However, the voltage of backpropagating action potentials still attenuates with distance, and one action potential is not enough to trigger a regenerative calcium spike in the tuft dendrite (Larkum et al., 1999b; Stuart et al., 1997b; Waters et al., 2003).

Voltage attenuation of backpropagating action potentials is caused by several factors, such as the slower recovery from inactivation of the sodium channels in the dendrites compared to the axon (Colbert et al., 1997; Jung et al., 1997), dendritic morphology, in particular branching points (Vetter et al., 2001), and shunting conductances. Branching points are particularly sensitive regions where action potentials could fail: if the sum of the impedances of the daughter dendrites is higher than the impedance of the parent dendrite, action potentials encounter a step increase in diameter and active propagation can fail. Among shunting conductances, the hyperpolarization-activated current (Ih), a voltage-gated leak conductance

mediated by HCN channels, induces a persistent shunt in apical dendrites because it depolarizes the dendrites at resting membrane potential (Berger et al., 2003; Harnett et al., 2015). In addition, voltage-gated potassium channels are expressed at high density in the apical dendritic tree, and they control calcium electrogenesis and limit the spread of the dendritic spikes from the apical trunk to the tuft dendrites (Harnett et al., 2013).

While a single action potential attenuates strongly along the dendrites and can fail to invade the tuft, a train of action potentials above a critical frequency (60-200 Hz) can trigger a dendritic calcium spike, which invades the tuft dendrites and further depolarizes the soma (Larkum et al., 1999b; Stuart et al., 1997b; Waters et al., 2003). Also, a single action potential can trigger a calcium regenerative event if it is associated with a distal EPSP, and the dendritic calcium spike can then in turn initiate bursts of sodium action potentials in the axon (Larkum et al., 1999a; Stuart and Häusser, 2001; Waters et al., 2003). This sequence of regenerative events is called back-propagation-activated calcium spike firing, or BAC firing (Larkum et al., 1999a). These results were partially confirmed *in vivo* in layer 5 neurons in rat somatosensory cortex, where calcium transients in the tuft dendrites were associated with bursts of action potentials (200-400 Hz), while single or multiple action potentials did not generate dendritic calcium spikes in the tuft (Helmchen et al., 1999).

It is still not clear how the soma and the tuft dendrites are coupled *in vivo*: during tonic firing, the mean firing rate of regular spiking pyramidal neurons *in vivo* is approximately 10-15 Hz, which is well below the critical frequency. Indeed, in slices of rat somatosensory cortex, somatic injections of *in vivo*-like noisy currents resulted in a mean firing rate of approximately 14 Hz, but did not generate any calcium spikes in the distal dendrites (Berger et al., 2003). It seems then unlikely that an action potential could reach the tuft during tonic firing, however bursts of action potentials can occur at the critical frequency or even at higher frequencies (Helmchen et al., 1999). Besides, the critical frequency is strongly modulated by the membrane potential, and it decreases in presence of depolarization in the dendrites (Berger et al., 2003; Larkum et al., 1999a; Stuart and Häusser, 2001). The high levels of activity *in vivo* could then decrease the critical frequency, and they could also increase the probability that distal synaptic inputs generate an action potential (Farinella et al., 2014). On the other hand, inhibitory inputs could also counteract the generation and back propagation of action potentials.

Two recent studies started to address this question *in vivo* in anaesthetized mice, and they observed that basal dendrites of layer 5 neurons were linearly related to spike activity, while calcium transients in the tuft occurred unreliably (Hill et al., 2013;

Palmer et al., 2014). However, a minority of action potentials were coupled to tuft calcium transients (while most tuft calcium transients were coupled to somatic firing), but the average firing frequency during a tuft calcium transient (60 ± 3 Hz, Palmer et al., 2014) was considerably lower than the average critical frequency (98 ± 6 Hz, Larkum et al., 1999b). But it is important to note that it is not clear from these *in vivo* studies whether the tuft calcium transients associated with low firing rates were generated in the tuft, and then caused a train of action potentials, or whether they were backpropagating action potentials.

1.2.5 Role of inhibition in dendritic integration

Dendritic integration and all dendritic spikes are profoundly affected by the spatio-temporal patterns of inhibitory inputs. Dendritic inhibition gates dendritic electrogenesis, so it can control calcium-dependent plasticity and the gain of input-output transformations in pyramidal cells (Farinella et al., 2014; Higley, 2014; Lovett-Barron et al., 2012; Murayama et al., 2009).

Dendritic shafts and spines of pyramidal neurons have both $GABA_A$ and $GABA_B$ receptors. Ionotropic $GABA_A$ inhibition shunts the dendrites and the spines primarily via Cl^- ions, while metabotropic $GABA_B$ receptors are G-protein coupled receptors. $GABA_B$ receptor activation leads to downregulation of cyclic AMP production, activation of inwardly rectifying potassium channels and inhibition of voltage-gated calcium channels (Chalifoux and Carter, 2011). $GABA_B$ receptors have a variety of actions and locations; for example, extrasynaptic $GABA_B$ receptors are involved in tonic inhibition (Semyanov et al., 2004).

Dendritic inhibition is believed to be spatially and temporally very precise (reviewed in Klausberger & Somogyi, 2008). Inhibition of dendritic calcium transients depends on precise spike-timing with a time constant of approximately 5 ms, and it is branch-specific, as inhibitory conductance change is highly local, and potentials attenuate strongly with the distance (Gidon and Segev, 2012; Müllner et al., 2015). In addition, different classes of inhibitory neurons connect selectively to different subcellular domains, and they can even target specifically the origin or the end of an individual branch (Bloss et al., 2016; Megías et al., 2001). Modelling studies suggest that this specific subcellular targeting could enable branch-specific control over initiation of non-linear dendritic events, and over backpropagation of action potentials (Bloss et al., 2016; Gidon and Segev, 2012; Müllner et al., 2015).

Inhibitory inputs are believed to approximately balance excitatory inputs, because in this configuration large excitatory inputs can be nearly completely cancelled by inhibitory inputs, thus generating fluctuations around threshold and resulting in the irregular firing pattern of neurons (van Vreeswijk and Sompolinsky, 1996). Indeed, several experimental studies supported the hypothesis that excitation and inhibition are balanced (Borg-Graham et al., 1998; Gentet et al., 2012; Okun and Lampl, 2008; Shadlen and Newsome, 1994). However, more recently a patch-clamp study in pyramidal neurons showed that in awake animals during sensory-evoked activity inhibitory conductances prevail over excitatory conductances, with a ratio inhibition to excitation of approximately 1.5-3; while in anaesthetized animals the excitation and inhibition are approximately balanced (Haider et al., 2013). It has been proposed that increased inhibition during wakefulness extinguishes spatial and/or temporal spread of feedforward activity elicited by sensory inputs.

1.2.6 Computational role of dendrites

A pyramidal neuron receives between 8,000 - 15,000 excitatory inputs and approximately 500 inhibitory inputs (Bloss et al., 2016; Larkman, 1991), and the majority of the synaptic inputs impinges on dendrites. A single cell has to filter and synthetize all this information into a single output, so it compresses all the inputs into a much smaller amount of information. The computations performed by a neuron are an open field of study (reviewed, among others, in London and Häusser, 2005; Silver, 2010; Sjostrom et al., 2008), and dendritic mechanisms are believed to act as computational building blocks.

When considering the dendrites as passive, multiple neighbouring and synchronous inputs can interact in non-linear ways. When two excitatory inputs are active together at a short distance, each input depolarizes the membrane and reduces the driving force for the other input, so the response to the simultaneous activation is smaller than the sum of the individual responses, resulting in a sub-linear summation (Rall, 1967). Whereas if two excitatory inputs are relatively far from each other, they are summed linearly at the soma. Sub-linear summation of neighbouring inputs could be beneficial to prevent overexcitation of the dendrites.

Excitatory inputs can interact non-linearly also with shunting inhibition. For example, when excitatory and inhibitory inputs are adjacent to each other, inhibition can reduce or even prevent excitation. In this case, the inhibition is local if the inhibitory postsynaptic potential (IPSP) affects local excitation but it does not reach the soma

(Rall, 1967). This mechanism is equivalent to an AND-NOT Boolean logical operator, because excitation and not inhibition need to be active to depolarize the cell (Koch et al., 1983). On the other hand, if inhibition and excitation are separated across dendrites, they sum linearly at the soma, and the inhibition is considered global.

In active dendrites, backpropagation of action potentials creates an internal feedback mechanism inside the neuron. This feedback can then interact with dendritic activity, for example in the BAC firing (Larkum et al., 1999a; Stuart and Häusser, 2001), and it is believed to be important for synaptic plasticity (Magee and Johnston, 1997).

Dendritic spikes are triggered by synchronous excitatory inputs, so they act as coincident detectors of neighbouring inputs. This mechanism is equivalent to the Boolean logical operator AND, and it corresponds to a multiplication of the synaptic inputs. Indeed, it has been shown that in V1 pyramidal neurons clusters of synaptic inputs with similar orientation preference can amplify the dendritic response and increase the selectivity of the cell (Wilson et al., 2016). In this view, BAC firing could be a detector of simultaneous activation (within a time window of ~ 10 ms) of the two main compartments of a neuron, the apical tuft and the basal domain.

In thin dendrites, sodium spikes are activated only by a cluster of synaptic inputs in a narrow time window (3-6 ms), thus constituting a mechanism for very precise coincidence detection (Nevian et al., 2007; Williams and Stuart, 2002). NMDA spikes, on the other hand, keep a memory of prior synaptic activity for 40 ms, the time during which glutamate remains bound to the receptor (Polsky et al., 2004). Then, if a second glutamatergic input arrives within this time window, it can generate an NMDA spike (Polsky et al., 2004). Besides, compared to sodium spikes, NMDA spikes are slower in the rise, longer in duration and they are not inactivated, so NMDA spikes can detect coincident inputs with less temporal precision, and they can even interact with short bursts of input activity.

Regenerative excitation is counteracted by voltage-gated conductances, such as potassium channels and Ih. These currents might be required to balance excitation in dendrites, but they also have a local effect on dendritic spikes. For example A-type potassium channels can be locally inactivated by an EPSP, so the backpropagation of an action potential is facilitated. This mechanism could control and gate plasticity inside a dendritic branch (Hoffman et al., 1997).

Non-linear regenerative events in the dendrites can be localized to one dendritic branch, or they can be global and invade the full dendritic tuft and/or dendritic tree. Local dendritic spikes rely mainly on NMDA conductances, so each branch can be

considered as an independent subunit that performs supralinear summation and can be modelled with a sigmoidal function. In this framework, each dendrite is a small unit with a computational power similar to the element of a neural network, so these dendrites can constitute the first layer of a network model. The output of each subunit is then conveyed through passive propagation to two integration zones, one near the soma and one near the apical tuft. These two integration zones constitute a second layer in the model. A neuron can then be described as a two-layered neuronal network (Mel, 1993; Poirazi et al., 2003; Polsky et al., 2004). This model predicts correctly the mean firing rate and other behaviour of the neuron (Poirazi et al., 2003; Polsky et al., 2004), but it does not take into account the global non-linearities of the dendrites and the temporal properties of spike firing.

Most of the studies mentioned above were carried out in brain slices, but dendrites might behave differently in intact animals. *In vivo* neurons are continuously bombarded by barrages of synaptic inputs that create high levels of stochastic voltage noise. Therefore, the subthreshold membrane potential fluctuates and it can cross the spike threshold and produce a spike even if the mean voltage is below the threshold (Hô and Destexhe, 2000). This mechanism can extend the range of excitatory inputs over which a neuron can signal, thus affecting the gain of the cell (Silver, 2010). In addition, since excitatory background activity depolarizes the dendrites and introduces spatially distributed NMDA conductance, it enables integration of spatially and temporally distributed synaptic inputs, thus extending the spatio-temporal window for dendritic integration in layer 5 pyramidal cells (Farinella et al., 2014).

In conclusion, dendrites can perform a wide array of computations and they can operate in different ways, it is therefore crucial to measure their behaviour in physiological conditions in intact animals.

1.2.7 Dendritic regenerative events *in vivo*

Dendritic activity have been rarely probed *in vivo* because dendrites are small structures and they are difficult to access. Moreover, in intact animals brain tissue is less stable and can displace by several micrometres due to blood circulation, animal breathing and behaviour (Dombeck et al., 2007), so imaging and electrophysiological recordings of fine structures *in vivo* is technically challenging.

However, in brain slices some neuronal processes are cut and the levels of network activity are lower. Therefore, it is difficult to replicate *in vitro* the physiological

spatiotemporal patterns of synaptic inputs, and the nature of the synaptic inputs can drastically change dendritic integration. For example if synaptic inputs are sparse, dendritic summation is linear, but if synaptic inputs are clustered in time and space they can trigger dendritic spikes, and dendritic integration is then non-linear and cooperative (Major et al., 2013).

Modelling studies and 2-photon uncaging experiments showed that ~ 10 neighbouring spines (distributed over 10-20 µm), or ~ 20 spines distributed randomly on a dendritic branch (spread along 100 µm), need to be active simultaneously to generate a NMDA spike (Branco and Hausser, 2011; Major et al., 2008, 2013; Polsky et al., 2009). However, on one hand the high levels of activity *in vivo* could permanently keep the membrane potential above the resting values and reduce the threshold for NMDA spike generation (Farinella et al., 2014), but on the other hand inhibitory inputs seem to predominate excitation in sensory-evoked responses in awake animals (Haider et al., 2013). It is then difficult to predict in which regime dendrites operate in *in vivo*. In the last years several studies started to address this question.

By combining calcium imaging and intracellular recordings in pyramidal neurons in layer 2/3 of anaesthetized rats, Svoboda et al. (Svoboda et al., 1997) reported for the first time dendritic calcium signals *in vivo*. They observed that the amplitude of these calcium transients correlated with somatic action potentials, and that dendritic calcium transients were larger in basal dendrites and smaller in distal dendrites. These results confirmed that action potential backpropagation activates dendritic voltage-gated calcium channels, and that backpropagating action potentials attenuate as they propagate along the dendrites. More recently, other studies also observed that activity at the soma is uncoupled to the activity in the tuft *in vivo* (Hill et al., 2013; Palmer et al., 2014), whereas somatic action potentials correlate with activity in basal dendrites (Chen et al., 2011; Hill et al., 2013).

The first imaging studies on the representation of sensory-evoked activity in dendrites focused on the analysis of subthreshold dendritic calcium signals. In order to accurately map sensory inputs onto dendrites, the cells were hyperpolarized to prevent spiking and to eliminate backpropagating action potentials. Sensory-evoked calcium transients were mapped onto the dendritic trees of layer 2/3 pyramidal neurons in mouse visual cortex (Chen et al., 2013a; Jia et al., 2010), auditory cortex (Chen et al., 2011) and barrel cortex (Chen et al., 2013b). In all these studies, dendritic “hotspots”, i.e. areas subthreshold calcium transients localized within a few microns, were observed. Functionally diverse hotspots appeared to be

heterogeneously distributed across the dendritic tree in all brain areas, thus suggesting that synaptic inputs are not clustered on a dendritic branch.

However, structural imaging of hippocampal neurons revealed non-uniform distribution of spines on the dendritic branches and showed clustered synaptic connectivity patterns (Druckmann et al., 2014). Besides, it was observed that adjacent spines in neocortical pyramidal neurons are frequently synchronized during spontaneous activity (Takahashi et al., 2012), thus supporting the idea that synaptic inputs are clustered in space and time *in vivo*. The reason of this discrepancy is not clear, it could be caused by the different nature of the synaptic inputs (spontaneous compared to sensory evoked), by the different anaesthetic used (urethane in Takahashi et al., isoflurane in the other experiments), or by the fact that in the experiments mentioned in the previous paragraph (Chen et al., 2011, 2013b; Jia et al., 2010) the cells were usually hyperpolarized.

In ferrets, imaging dendritic spines in pyramidal neurons in V1 revealed that synaptic inputs tuned to the same orientation can be clustered, and that differences in orientation selectivity among neurons correlated with the number of clustered spines (Wilson et al., 2016). These data then suggest that dendritic non-linearities are present *in vivo* and play a crucial role to sharpen the selectivity of a neuron. But these experiments were carried out in ferret V1, where there are vertical orientation columns, while in mouse V1 cells tuned to the same orientation have a random salt-and-pepper organization (Ohki et al., 2005).

Therefore, it is still not clear whether synaptic inputs are clustered in physiological conditions in mice. However, NMDA spikes were observed *in vivo* in layer 4 spiny stellate cells in rat barrel cortex in response to whisker deflection (Lavzin et al., 2012), and global calcium signals corresponding to plateau potentials were described in tuft dendrites of layer 5 pyramidal cells in mice performing an object-localization task (Xu et al., 2012). But a more recent study in layer 4 spiny stellate cells in barrel cortex showed that sensory-evoked short-latency EPSPs are integrated linearly and in a non-cooperative way, thus arguing against the presence of dendritic regenerative events (Jia et al., 2014).

Multi-branch NMDA spikes have been observed also in tuft dendrites of layer 2/3 cells and in CA1 hippocampal neurons. In cortical neurons, NMDA spikes in tuft dendrites were generated both during spontaneous and sensory-evoked activity, and they had a large influence on somatic action potentials (Palmer et al., 2014). Similarly, the calcium transients observed in hippocampal neurons were dependent on NMDA receptors and voltage-gated calcium channels, they produced slow spikes

in the somatic membrane potential and they were necessary for generation of complex high-frequency spikes in the soma (Grienberger et al., 2014).

In conclusion, different patterns of dendritic activity have been observed *in vivo* so far (summarized in **figure 1.7**), and their role for sensory processing and behaviour has also begun to be explored in different brain areas.

In barrel cortex (Lavzin et al., 2012) and in visual cortex (Smith et al., 2013) dendritic NMDA spikes have been shown to amplify tuning of neuronal responses to sensory stimuli.

In addition, in barrel cortex, while animals were performing an object-localization task, global dendritic spikes have been observed, and they were activated by both sensory and motor inputs. The amplitude of these calcium events depended on the position of the object, suggesting that these dendritic spikes are related to the animal task and behaviour (Xu et al., 2012). These global dendritic spikes are controlled by voltage-gated potassium channels, both *in vitro* and *in vivo* (Harnett et al., 2013).

Finally, dendritic spikes have also been observed in place cells in the hippocampus, and the prominence of these events correlated with the precision and persistence of the place field (Sheffield and Dombeck, 2015).

However, it is important to note that most of these studies were done in anaesthetized animals (except for Sheffield and Dombeck, 2014; Smith et al., 2013b; Xu et al., 2012), thus precluding the investigation of the role of different dendritic mechanisms in animal behaviour. Besides, anaesthesia has major effects on network (Greenberg et al., 2008; Niell and Stryker, 2010; Pisauro et al., 2013; Vaiceliunaite et al., 2013), dendritic (Murayama and Larkum, 2009; Potez and Larkum, 2008) and synaptic activity (Franks and Lieb, 1994; Haider et al., 2013), so it can also modify dendritic integration.

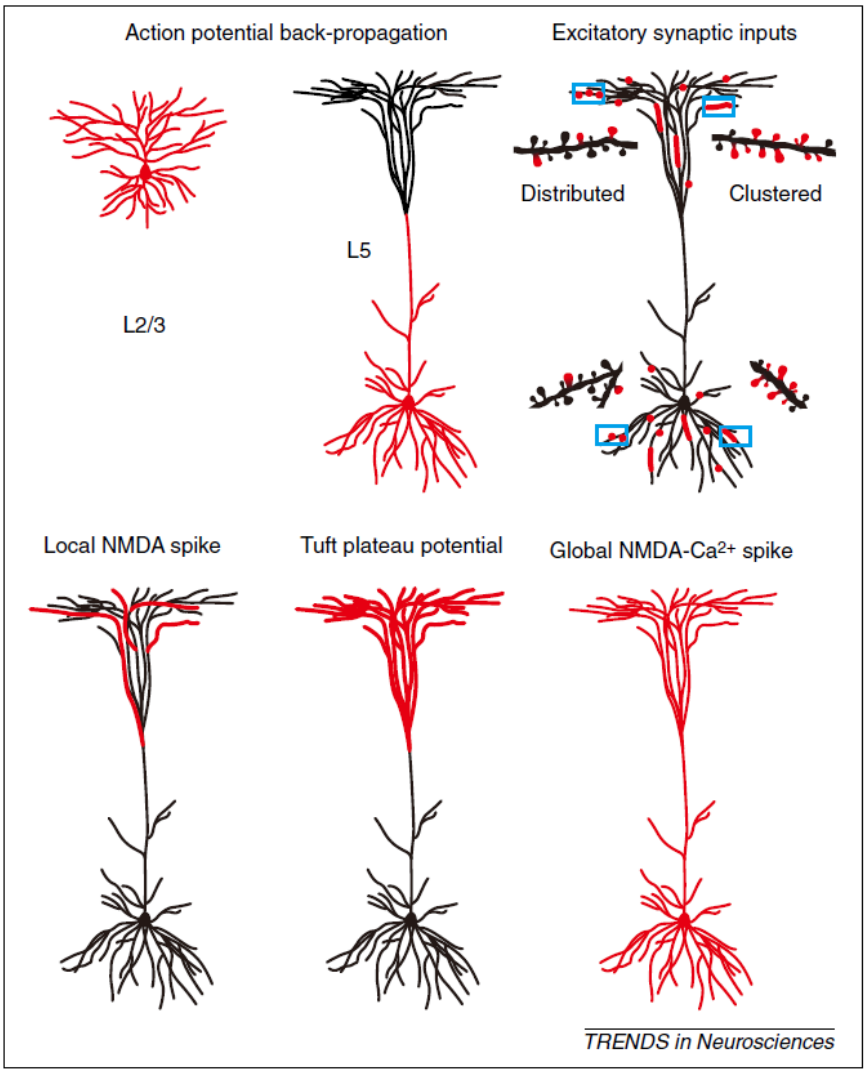

Figure 1.7 Different patterns of dendritic calcium signalling observed *in vivo*, reproduced from (Grienberger et al., 2015). Red indicates regions where simultaneous calcium transients have been observed.

1.2.8 Summary of dendritic properties

In conclusion, dendrites of pyramidal neurons have a complex morphology and express a range of voltage-gated ion channels, thus allowing them to integrate synaptic inputs in a variety of linear and non-linear manners. However, the differences between pyramidal neurons in different brain areas have been less studied so far: these cells have some differences in morphology and functional properties, and it is still an open question whether they operate in a fundamentally different manner, or whether they are just neighbours along a continuum.

Importantly, it is also not clear which mechanisms and computations studied *in vitro* are used to process information *in vivo*. Spatiotemporal patterns of synaptic inputs *in vivo* are crucial to determine whether dendrites will operate in a linear or in a supralinear regime, but so far only excitatory inputs have been mapped in pyramidal neurons in sensory cortices, and exclusively in anaesthetized animals (Chen et al., 2011; Jia et al., 2010). It would therefore be important to investigate both excitatory and inhibitory inputs in awake animals, and how these inputs are distributed across the dendritic tree. In any case, non-linear dendritic events have started to be observed *in vivo*, but their role in information processing, animal behaviour and synaptic plasticity is still unknown.

Characterization of dendritic events *in vivo* is also far from complete, because very few studies probed neuronal activity in different dendritic compartments in awake animals. Besides, in most studies dendritic activity has been probed only in few branches at the time, making it difficult to obtain a full picture of dendritic activity in awake behaving animals.

1.3 Aims and outline of this study

In this study, I investigated dendritic activity in layer 2/3 and in layer 5 pyramidal neurons in V1 in awake mice. I used calcium imaging and a 3D 2-photon acousto-optic lens microscope developed in the Silver lab to probe dendritic activity simultaneously in the vast majority of the dendritic branches. I characterized patterns of dendritic activity in response to visual stimuli, and I compared dendritic activity in different animal states (anaesthetized, awake and stationary, awake and running).

In chapter 3, I discuss the technique used to image dendrites *in vivo*: the protocol to label pyramidal neurons sparsely with the genetically-encoded calcium indicator GCaMP6f (Chen et al., 2013a) and with the red protein TdTomato, and how I used the activity-independent TdTomato to detect movement artefacts. Furthermore, I explain how, after the *in vivo* experiment, I identified the cortical layer of the cells with Nissl staining and imaging the fixed brain.

Chapter 4 shows the characterization of the patterns of dendritic activity in layer 5 and in layer 2/3 neurons. In the apical dendrites of layer 5 neurons, the spatial distribution of dendritic transients follows a bimodal distribution, where local and global events are preferred, and, interestingly, global events are always associated with a somatic calcium transient. In layer 2/3 neurons, somatic calcium transients are often not associated with global dendritic calcium transients, suggesting failures of back-propagating action potentials.

In chapter 5, neuronal responses to sensory stimuli are investigated. In particular, dendritic responses to full-field gratings and orientation tuning are characterized. While layer 5 apical dendrites show little responses to visual stimuli, layer 2/3 dendrites respond to full-field gratings. When considering all calcium transients, most layer 2/3 dendrites have the same preferred orientation as the soma, but few dendrites prefer different orientations. When considering only dendritic events, responses are very sparse.

Chapter 6 shows how the animal state modulates dendritic activity. Locomotion enhances dendritic activity in the apical dendrites of layer 5 cells, while light anaesthesia represses dendritic activity. In contrast, dendrites of layer 2/3 neurons show little or no modulation by the animal state. This data suggest that, while dendrites of layer 2/3 neurons receive primarily bottom-up information (sensory stimuli), apical dendrites of layer 5 cells are driven by top-down inputs (animal state).

Finally, chapter 7 focuses on new technological developments of the acousto-optic lens microscope, and in particular on the new tools that will facilitate imaging dendrites and spines *in vivo*. Dr Srinivas Nadella and Dr Victoria Griffiths in the lab developed random-access scanning in 3D and online movement correction, and we tested these new tools imaging somas, dendrites and spines in awake running animals.

Details about the methods and the tools I used and developed to carry out the present study are given in chapter 2, while chapter 8 contains a general discussion about the interpretation of the data and their significance in the context of the existing research literature.

2. Materials and methods

2.1 Animals

All experimental procedures were carried out in accordance with institutional animal welfare guidelines and licensed by the UK Home Office in accordance with the Animal (Scientific Procedures) Act 1986. Stereotaxic injections were performed between postnatal day 35-65 on C57BL-6 mice and on Cre-reporter TdTomato transgenic mice (Madisen et al., 2010).

Generation and characterization of Ai9 Cre-reporter TdTomato mouse line (B6; 129S6-328Gt(ROSA)26Sortm9(CAG-TdTomato)Hze/J) was as described (Madisen et al., 2010). Briefly, the strong exogenous promoter CAG was inserted in the locus *Rosa26*, followed by a loxP-flanked ('floxed') stop cassette that controlled the gene encoding for the fluorescent protein TdTomato (Shaner et al., 2004). This transgenic line showed intense fluorescent labelling when crossed with different Cre mouse lines.

Head plate and cranial window were implanted from 2 weeks to 4 weeks after the stereotaxic injection, and calcium imaging experiments were performed from 4 weeks up to 3 months after the virus injection. For all experiments, animals of both sexes were used.

2.2 Surgical procedures

All surgical procedures were performed under sterile conditions. Mice were deeply anesthetized with a mixture of Fentanyl (0.05 mg/kg), Midazolam (5.0 mg/kg), and Medetomidin (0.5 mg/kg). A thin layer of cream (Maxitrol eye ointment) was applied to the eyes to prevent dehydration during surgery. During long surgeries, anaesthesia was maintained by injecting one-third of the initial dose approximately every hour. For headplate implant and cranial window, atropine (1-2 µg) and dexamethasone (40 µg) were also injected at the beginning of the surgery. At the end of the surgery, analgesia was administrated via subcutaneous injection of Carprofen (15 mg/kg), and local analgesia (Bupivacaine, 1mg/kg) was administrated to the surgical wound site. The antibiotics Baytril (0.005 mg/kg) was also administrated. A mixture of Naloxone (1.2 mg/kg), Flumazenil anexate (0.5 mg/kg) and Atipamezol (2.5 mg/kg) was used to reverse the aesthetics and wake up the

animals. Mice were monitored for 3-4 days after the surgery, and analgesia (Buprenorphine 0.1 mg/kg, and Caprofen 15 mg/kg) and antibiotics (Baytril 0.005 mg/kg) were administrated daily.

2.2.1 Stereotaxic virus injection

Mice were mounted in a stereotaxic frame (David Kopf Instruments). 5 µl calibrated borosilicate micropipettes were cut to 9-10 µm internal diameter and suction filled with 1 µl of Adeno-associated virus (AAV). GCamp6f (AAV1.Syn.GCaMP6f.WPRE.SV40, Penn Vector Core, titre: $3.58*10^{13}$ Genome Copies GC/ml, diluted 1:2) was injected in primary visual cortex for dense labelling, while for dendritic imaging, sparse labelling was achieved co-injecting GCamp6f-flex (AAV1.Syn.Flex.GCamp6f.WPRE.SV40, Penn Vector Core, titre: $1.52*10^{13}$ GC/ml, diluted 1:2) and Cre recombinase (AAV9.CamKII0.4.Cre.SV40, Penn Vector Core, titre: $4.82*10^{13}$ GC/ml, diluted 1:10,000). For dual sparse labelling with GCaMP6f and TdTomato, GCaMP6f-flex and Cre recombinase were co-injected in Cre-reporter TdTomato transgenic mouse line ((Madisen et al., 2010) and see above). In order to achieve dual sparse labelling, the following viruses were also tested (see table 3.1): AAV1.CAG.Flex.tdTomato.WPRE.bGH, Penn Vector Core, 1.03E12 GC/ml; AAV1.CAG.tdtomato.WPRE.SV40, Penn Vector Core, 7.42E12 GC/ml; AAV1.hSyn1.mRuby2.GSG.P2A.GCaMP6s.WPRE.SV40, AAV1.hSyn1.mRuby2.GSG.P2A.GCaMP6f.WPRE.SV40 and AAV-FLEX-mRuby2-P2A-GCaMP6s 2/1 kindly provided by Dr Tobias Rose and Dr Tobias Bonhoeffer (Rose et al., 2016); AAV8.hSyn.mCherry.Cre, UNC Vector Core. Most of these tests were performed using the Cre virus AAV1.hSyn.Cre.WPRE.hGH, Penn Vector Core, 1.32E13 GC/ml. A small craniotomy was performed above the injection site, which was located 2.7 mm right from lambda and 1.2 mm frontal from the transverse sinus. A total volume of approximately 75 nl of virus for dense labelling, and 20 nl of virus for sparse labelling, was slowly pressure injected at varying depths (from 400 to 100 µm from the pia).

2.2.2 Head plate implant and cranial window

A custom-built metal head plate was fixed to the skull with superglue (PowerFlex Loctite) and dental cement (Paladur, Heraeus Kulzer). To prevent light from the visual stimuli passing through the dental cement during an experiment, some dental cement was mixed with vine black pigment, and a thin layer of black dental cement

was applied around the head plate. A small craniotomy (4 mm diameter) was then carried out above primary visual cortex, 2 – 3.3 mm right from lambda. The exposed cortical surface was washed and kept moist with cortex buffer (125 mM NaCl, 5 mM KCl, 10 mM glucose, 10 mM HEPES, 2 mM MgSO4, and 2 mM CaCl2 [pH 7.4]). The cortex was then sealed with a coverslip and superglue (PowerFlex Loctite) was applied to fix the coverslip to the skull. The size, brightness and position of the fluorescent area were assessed with a Leica MZ10F stereo fluorescence microscope before carrying out an experiment with the 2-photon microscope.

2.3 Acousto-optic lens microscope

2.3.1 Principles

The acousto-optic lens (AOL) is made of four custom acousto-optic deflector (AOD) crystals (TeO_2, Gooch and Housego) arranged in series. In each acousto-optic deflector the laser light interacts with an ultrasonic sound wave (range 25–47 MHz), and the light beam is diffracted at an angle that varies with the frequency of the sound wave:

$$\boldsymbol{\Phi = \frac{\lambda f}{V_{ac}}}$$

where Φ is the angle of diffraction, λ is the optical wavelength, f is the frequency of the sound wave, and V_{ac} is the acoustic velocity (~ 600 m/s). The optical wave front is then deflected and it can be directed to a specific spot in two dimensions. Besides, a curvature in the wave front is caused by a sound wave with linearly increasing frequencies, allowing remote focusing of light. Variations in the slope of the frequency ramp change the focus of the laser beam (Z plane), whereas offsetting the frequency ramp displaces the laser beam in x and y. Two AODs, with counter propagating sound waves, were used to cancel out the movement introduced by the sound propagating across the crystals allowing a stationary focus (Kaplan et al., 2001). The AOL could then address, sequentially, any voxel within the volumetric field of view in 24 µs regardless of the distance between points (Fernández-Alfonso et al., 2014; Kirkby et al., 2010) (**figure 2.1**). Combining this with a dwell time of 4 µs gave a total acquisition time per point of 28 µs or a total serial bandwidth of 36 kHz. If, for example 36 points are imaged, the total time to visit all the points is 36 x 28 µs = 1 ms; then the beam is focused again on the first point and a new cycle starts, resulting in 1 KHz sampling rate per point (**figure 2.1**).

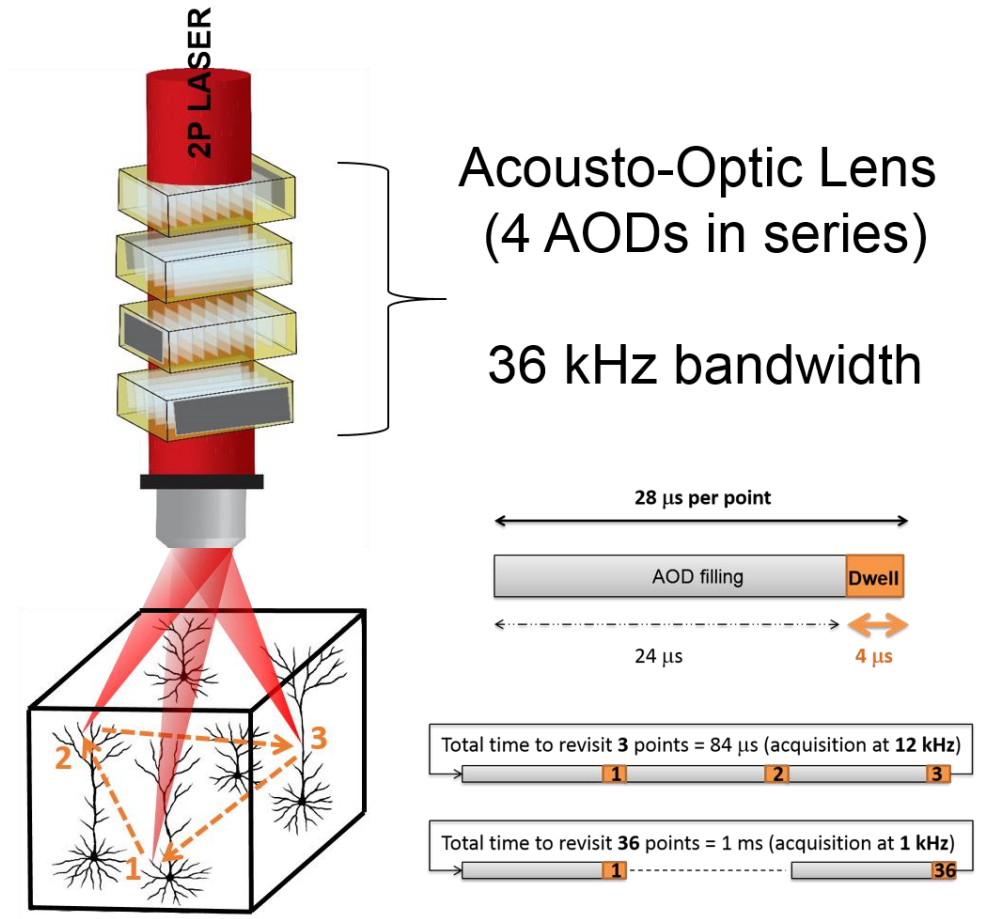

Figure 2.1 Random-access point measurements in the acousto-optic lens (AOL) two-photon microscope, reproduced from (Fernández-Alfonso et al., 2014). Left panel: an AOL consists of 4 acousto-optic deflectors (AODs) in series. The AOL is used to focus and deflect the laser beam, so it is possible to image points sparsely distributed in three dimensions. Right panel: the time to image each point is given by the AOD filling time, 24 µs, plus the dwell time, 4 µs. Each point can then be accessed in 28 µs. Multiple points can be imaged sequentially, thus 3 points can be imaged in 84 µs, and 36 points can be visited in 1 ms.

The movement of the laser beam introduced by the propagation of the sound wave can also be exploited to image points in a line at higher speed. In this case, first the AOL is filled with the sound wave, and then a line of points can be scanned continuously. A line of 200 pixels can then be scanned faster because the AOL needs to be filled only once; in particular, it takes (200 x 4) + 24 = 824 µs for a line scan, instead of 200 x (24 + 4) = 5600 µs with pointing mode. This imaging mode was used to perform raster scanning and acquire full-frame images.

The first generation AOL microscope can perform line scans only at the natural focal plane of the objective, i.e. when the AOL is not used to focus the laser beam on a different plane. When the AOL is used also for remote focussing, the acoustic wave has a frequency ramp and consumes more of the acoustic bandwidth, thus making it impossible to achieve continuous line scanning. The second generation AOL microscope allows shorter dwell times, thus increasing the speed to scan each line and giving access to more bandwidth. Therefore, in the second generation AOL microscope it is possible to perform line scans at any focal plane.

The AOL microscopes were built by the microscopy development group in the Silver lab: Dr Geoffery Evans, Dr Victoria Griffiths, Dr Paul Kirkby, Dr Theo Koimtzis, Dr George Konstantinou and Dr Srinivas Nadella.

2.3.2 First generation acousto-optic lens microscope

A first generation microscope was used to carry out all the experiments presented in this thesis, except for the experiments in section 4.2.2 and in chapter 7.

The first generation of AOL-microscope consisted of a tuneable femtosecond laser source (Ti:sapphire laser, Mai Tai, Spectra-Physics), a customized prechirper (−50,000 fs2 GVD, APE GmbH, Berlin) to compensate for the temporal dispersion introduced by the AOL, a Pockels cell (Model 350-80LA, Conoptics) and a compact AOL (Kirkby et al., 2010), together with the relay optics required to route the beam. AODs were interleaved with quarter wave plates and polarizers to couple the beam into subsequent AODs and also to block the unwanted zero order beam.

Our home built microscope was mounted on top of a SliceScope (Scientifica, UK) with a 25X objective from Nikon with 1.1 NA. The objective was under filled to give an effective NA of 0.6-0.7. The maximum volume where the laser beam can be focused with the AOL is: 220 x 220 x 315 µm and the point spread function size was 0.8 µm in x and y, and 5 µm in z with this objective. Emitted photons, collected through the objective, were separated from excitation photons using a 660 filters nm long-pass dichroic mirror (660dcxr) followed by a 650 nm short-pass filter. Green and Red emitted photons were further isolated using a 575 nm long-pass dichroic (575dcxr) and emission filters (HQ 525/75-2P and HQ 630/100-2P, respectively), and detected using GaAsP (Hamamatsu H7422) and multialkali (Hamamatsu R3896) photomultipliers (PMTs), respectively. PMT signals were amplified with a Scientifica amplifier with 3-4 kHz bandwidth. At each point, a single 4 µs dwell time was used for both raster scanning and 3D RAMP measurements. Excitation light

was shuttered with a Pockels cell except during 4–12 µs spanning the 4 µs dwell time.

Image acquisition, raster scanning and points measurements were controlled by custom software written in LabVIEW (National Instruments) and developed by Dr Srinivas Nadella and Dr Theo Koimtzis.

2.3.3 Second generation acousto-optic lens microscope

A second generation microscope was used to carry out the experiments presented in section 4.2.2 and in chapter 7. The second generation AOL microscope allows imaging at variable dwell times (50, 100, 200, 300 and 500 ns for scanning, 0.05-8 µs for pointing) and line scan at any focal plane. Thus, several new imaging modes are possible with this technology: fast z-stack (**figure 2.2 a**), multi-plane imaging (**figure 2.2 b**), random-access three-dimensional regions (**figure 2.2 c**) and random-access two-dimensional regions (**figure 2.2 d**). Imaging random-access points is also still possible (**figure 2.2 e**).

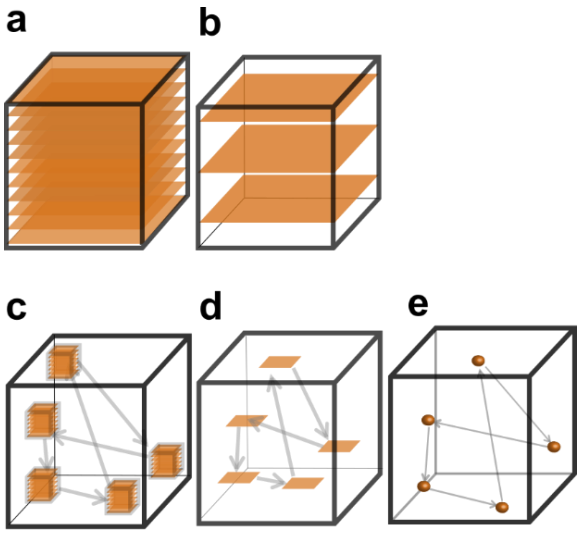

Figure 2.2 Imaging modes in the second generation AOL two-photon microscope, courtesy of Dr Srinivas Nadella. a: fast z-stack, b: multi-plane imaging, c: random-access three-dimensional regions, d: random-access two-dimensional regions, e: random-access points.

The optical layout of the second generation AOL two-photon microscope was the same as in the first generation AOL-microscope, except for the laser (2 W at 920 nm; Chameleon Ultra II, Coherent Inc.), and the objective (Olympus XLUMPlanFLN

20X, NA1.0). With this objective, the maximum volume where the laser beam can be focused with the AOL is: 245 x 245 x 450 µm and the point spread function size was 0.65 µm in x and y, and 3.75 µm in z. The AODs were also slightly bigger, and the fill time went up to 24.5 µs. The two-channel detection system was the same, but both red and green photons were detected with GaAsP PMT (H7422, Hamamatsu, Japan). Output signals from the PMTs were amplified using 200 MHz pre-amplifiers (Series DHPVA 100/200 MHz, FEMTO).

In this microscope, the custom designed FPGA AOL control system consisted of a Xilinx ML506 card and a Texas Instruments DAC card (DAC5672EVM). Commands to control the loading and execution of the frequency records for 3D AOL random-access raster scanning, patch imaging, multi-volume and pointing were generated by the PC and encoded as RAW Ethernet packets, before being passed to the AOL controller via a Gigabit Ethernet interface. The AOL control FPGA used an on-chip, direct digital synthesiser to generate the specified acoustic frequency chirps and these were executed upon receiving a start trigger from the data acquisition system. The synthesized digital waveforms were converted into analogue signals by Digital-to-Analog Converters (Texas Instruments, DAC5672EVM) and amplified by 4 amplifiers before being fed into the AODs. The acquisition system consisted of a high speed ADC add on card (800 MHz, dual channel, NI-5772) together with an FPGA (NI FlexRIO – 7966R) that enabled forty-fold oversampling down to dwell times of 50 ns. The DAQ FPGA acted as the master, synchronising the AOL acoustic frequency ramps and the data acquisition. Signals were down sampled on the DAQ FPGA by integrating over each voxel dwell time before sending frames to the host PC via the National Instruments PXIe interface. Voxel integration was not synchronized to the 80 MHz laser pluses. Peripherals were controlled using a PXI 6733 card. The line scan rate is determined by two factors in our system: the time it takes to scan each line (dwell time x number of pixels) plus the time it takes to refill the crystals to reposition the beam before the next line is acquired (24.5 µs).

The data acquisition software running on the NI FPGA and the user interface running on Windows PC were developed in LabVIEW by Dr Srinivas Nadella, Dr Theo Koimtzis and Dr Victoria Griffiths.

2.3.4 Real time movement correction

Real time movement correction was implemented only on the second generation of AOL microscope, because it needs a FPGA-based control system to operate.

Lateral motion correction was achieved by periodically scanning a small, bright reference feature and adjusting the AOL controller to track the motion with the laser. The size of the reference window was set to be sufficiently large to keep the monitored feature in view between consecutive reference scans. By dynamically tracking the feature, movements of up to tens of micrometres could be tracked with a small reference window. The DAQ FPGA contains a programmable timer that controlled the feedback period for motion control and synchronized the AOL control to correctly interleave reference scans with the main imaging sequence. At the desired time-out the DAQ logic interrupted the AOL controller to load a reference frame and a handshaking protocol was used to resynchronize the acquisition of the reference frame. Following reference frame acquisition, the image was thresholded and passed to the centroid detection logic to calculate the x-y shift in relation to the original reference frame (Δx and Δy).

An on board proportional–integral–derivative (PID) controller was implemented and optimised to feedback the current lateral offset to the AOL controller via a serial link running the Serial Peripheral Interface (SPI) protocol. The AOL control logic converted the pixel offset to the acoustic ramp frequency offsets needed to track the reference. For an AOL system the lateral frequency correction has a dependency on the axial position of the point of interest and is different for each of the four AODs. For each point the axial position was discerned by reading the slope of the acoustic chirp held in its record. The corrected frequency adjustment could then be generated correctly for each of the four AODs. We exploited the speed of the on-chip DSP blocks on the Xilinx Virtex 5 device to perform the calculations by executing fixed point-arithmetical operations in parallel for each AOD. This strategy resulted in the FPGA, which runs at 125MHz, pre-fetching and calculating the four frequency offsets in less than 1µs. Since it takes sound waves 24.5 µs to fill the aperture of the AOL, any new offset sent from the DAQ board could be updated in time to correct the next imaging point dynamically for each point regardless of its axial position.

2.4 Calcium imaging data acquisition

The activity of cortical neurons was monitored by imaging fluorescence changes with a custom-built AOL-based microscope (see above) at 920 nm to image GCaMP6. With the first generation AOL-microscope, a 25X water immersion objective (1.1 NA, Nikon) was used, and the average laser power delivered to the brain was 20 - 30 mW. With the second generation AOL microscope, which was used for the experiments reported in section 4.2.2 and in chapter 7, a 20X objective water

immersion objective was used (1.0 NA, Olympus), and the laser power used for imaging was 20 – 60 mW. Laser intensity was modulated exponentially with depth using the Pockels cell in order to compensate for scattering.

During an experiment, first raster scanning in two dimensions was used to find the area to image, then a Z-stack was acquired to identify the positions of the neurons in different planes, and then only a few points of interest (POIs) in the dendrites and in the soma of each cell were imaged at high sampling rates in three dimensions. In the experiments presented here, typically 300-400 points in a volume of 220 x 220 x 150 µm were imaged at 90-120 Hz. Due to movement of the tissue, every ~ 2 minutes of recording a new stack was acquired, and new POIs were placed.

2.5 Calcium imaging experiments

In experiments on anaesthetized animals, mice were first sedated with Chlorprothixene (0.8 mg/kg). After 30 minutes, the animals were lightly anaesthetized with isoflurane (0.5-1.1%) in a 60:40 mixture of O_2:N_2O, delivered via a small nose cone. Atropine (1-2 µg) was also injected to reduce respiratory tract secretion and to prevent slowing of the heart rate. During experiments on anaesthetized animals, the temperature was maintained at 36.5 - 37° with a heating blanket. Sterile saline (30 ml/kg) was injected subcutaneously during the experiment to avoid dehydration.

In experiments on awake animals, mice were free to run or stand still on a cylindrical Styrofoam wheel (similar to Dombeck et al., 2007). The animals were first familiarised with the setup for 30-60 minutes for one or two days. During the familiarisation sessions and the experiments, animals were offered water and strawberry jelly regularly. Animal speed was measured with an incremental rotatory encoder (RI58, Hengstler, 10,000 pulses per revolution), and the data was acquired with custom software written in LabVIEW (National Instruments).

During the experiments, animals were monitored with two cameras: a webcam to check the behaviour of the animal, and a high-resolution camera (The Imaging Source mono CCD camera, 1280x960 resolution, 3.75x3.75µm pixels, giving 4.80x3.60mm active area, with a sampling rate of 30 hz and with lenses Computar 75.0mm /F2.8-16C 1.5 MP Lens and a Computar 2x Extender, focal length doubler / teleconverter) that was used to track eye movements (see below). Both cameras were sensitive to infrared light, and illumination was provided with two arrays of 48

infrared LEDs. The cameras were controlled with a custom software written in LabVIEW (National Instruments) on a dedicated computer, and the camera data acquisition was synchronized with the calcium imaging data with a hard trigger, and a timestamp for each frame was saved. Video files were saved as binary files and then converted after the experiment into AVI2 files.

2.6 Visual stimulation

Visual stimuli were generated using MATLAB (MathWorks) Psychophysics Toolbox (Brainard, 1997; Kleiner et al., 2007; Pelli, 1997) and displayed on an LED-backlit LCD monitor (27 inches) positioned roughly 20 cm from the left eye, at 45^0 to the long axis of the animal, covering ~ 105 x 85 degrees of visual space.

Dr George Konstantinou synchronized the refresh rate of the monitor with the microscope imaging times to minimize stray light from the monitor that can be collected by the objective. The monitor was on only during the AOD filling time (24 µs, when no data was collected), and it was turned off during the data acquisition, i.e. the dwell time (4 µs) of each point imaged.

Calcium signals were measured in response to sequences of full-field grating. Square-wave gratings (0.035 cycles per degree, 2 cycles/s, 100% contrast, luminance: 30.6 cd/m^2) drifting in eight different directions were interleaved with 4 seconds of grey screen (luminance: 30.2 cd/$m^{2)}$. Each grating was presented for 2 seconds before moving for 2 seconds (10-20 repetitions per grating). For small gratings, square-wave gratings (0.03 cycles per degree, 2 cycles/s, 100% contrast) were presented at 12 neighbouring positions, interleaved by 3 seconds of black screen. In each position, the grating changed orientation every 0.25 seconds, and a total of 8 orientations were presented for 2 seconds in each position (8-20 repetitions per position). Natural images consisted of 3 pictures of mice in a cage; the pictures were converted to grey scale, and adjusted to have the same mean contrast (50%) and luminance (120). Each natural image was presented for 1 second, and images presentations were alternated with 2 seconds of grey screen. Each image was presented 100 – 150 times. Recordings of spontaneous activity were achieved imaging neuronal activity when the monitor was off (luminance: 0 cd/m^2).

2.7 Brain clearing and Nissl staining

Brains were fixed via cardiac perfusion with 4% paraformaldehyde in PBS, then cerebellum, olfactory bulb and frontal cortices were removed and the brains were cleared with the CUBIC protocol (Susaki et al., 2014).

Briefly, brains were immersed in reagent 1 (25% urea, 25% N,N,N',N'-tetrakis(2-hydroxypropyl)ethylenediamine, 15% Triton X-100) for 1 – 1.5 weeks, with gentle agitation at 37 degrees. The brains were then washed with PBS several times at room temperature, and then immersed in 20% sucrose in PBS. After complete exchange, the brains were then immersed in reagent 2 (50% sucrose, 25% urea, 10% 2,2',2'-nitrilotriethanol, 0.1% Triton X-100) for a week with gentle agitation at room temperature. The samples were then put in a custom-built holder and, while immersed in reagent 2, they were imaged through a coverslip with a confocal microscope (Leica SP8Vis) with a 10X and 20X water-immersion objectives (Leica HCX APO L 10X/0.30 U-V-I WD 3.6 mm, Leica HCX APO L 20X/0.50 U-V-I WD 3.5 mm).

Multiple Z-stacks were acquired and tiled together with the software Leica Application Suite X (LASX), so regions of up to 2 x 2 x 1.5 mm were imaged. During this first imaging session, it was possible to see the cells labelled in red (TdTomato) and in green (GCaMP6f), and the dendritic tree of each cell was clearly visible. The cells imaged *in vivo* were identified in the clear brain on the basis of the morphology of the dendritic tree and the positions of the neighbouring cells.

Afterwards, the samples were washed several times in PBS, and immersed in blue Nissl (NeuroTrace 435/455 blue fluorescent Nissl stain, Molecular Probes, 1:50 in PBS with 0.02% sodium azide) for 2-3 weeks at room temperature. The brains were then washed with PBS, immersed in 20% sucrose in PBS, and immersed again in reagent 2 for 3 days. The samples were imaged a second time with horizontal and coronal optical sections to determine the cortical layer of the cells imaged *in vivo*. There was some bleed through from the blue channel into the green channel and into the red channel, so some dendrites were less visible after the Nissl staining. However, comparison between the mosaic images acquired in the clear brain before and after the Nissl staining allowed identification of the cells imaged *in vivo* and their cortical layer in 21 out of 41 cells. In most samples, these cortical layers were distinguishable: layer 1, layer 2/3, layer 4 and layer 5/6.

After imaging, the brains were washed again with PBS, immersed in 20% sucrose in PBS and then stocked in O.C.T. compound at -80 degrees.

2.8 Data analysis

Data analysis was carried out with custom scripts in Matlab (Mathworks), unless specified otherwise. Images were displayed and rendered using ImageJ, Vaa3d (Peng et al., 2010, 2014) or NeuTube (Feng et al., 2015). Multiple Z-stacks were stitched using a stitching plugin available in ImageJ/Fiji (Preibisch et al., 2009).

2.8.1 Datasets

The dataset used to analyse dendritic activity in L5 tuft consisted of 8 cells from 4 mice. When analysing the effects of locomotion on dendritic activity, data from 13 cells from 6 mice was considered.

For L2/3 neurons, given the sparseness of activity in this layer, during experiments mainly active cells were targeted. The dataset for L2/3 neurons consisted of 13 cells from 7 mice, and for 11 of these cells it was possible to distinguish the apical dendrites. Five cells out of 12 were considered responsive to full-field gratings (see below for the criteria used), and three cells out of five were tuned to one orientation, but a fourth cell with >70% of the dendrites selective for orientation was also included in this analysis.

Experiments under light anaesthesia were performed only on a subset of animals, so the datasets consisted of 7 L2/3 neurons from 4 mice and 5 L5 neurons from 4 mice.

Recordings without visual stimulation (i.e. in the darkness) were usually shorter (5-11 minutes), and performed on fewer cells (9 cells from 6 mice for L2/3 neurons, 9 cells from 4 mice for L5 neurons).

Additional experiments were later performed on L5 neurons, and the tuft dendrites and the soma of the cell were imaged simultaneously without visual stimulation. For these experiments, 7 cells from 3 mice were imaged.

2.8.2 Dendrite reconstruction and attribution of imaged points of interest (POIs) to branches

Due to movement of the tissue, a new Z-stack was acquired every 2 minutes of recording and new POIs were placed manually in the dendrites and somas of the imaged cells (see above). Therefore, to pool together all the recordings for the same cell or dendrite, neurons were first traced semi-automatically in each Z-stack using Vaa3d (Peng et al., 2010, 2014) and NeuTube (Feng et al., 2015). In the tracing, dendrites were represented as a series of points, called nodes (**figure 2.3 b** and **c**), and the connectivity of the nodes, spatial coordinates (xyz) and diameter of the dendrites at each node was then saved as a swc file and imported in Matlab using the TREES toolbox (Cuntz et al., 2010). With the TREES toolbox and custom scripts, each dendritic branch was assigned a unique identifying number, which was based on the order of the branch and on the angle of the branch with its parent branch. For first-order branches, the angle between the branch and an imaginary vertical line was used. The angle between two branches was calculated considering two vectors A and B, defined by the first 2 nodes of each branch after the branching point, and using the scalar product and the vector product of A and B:

$$\cos\boldsymbol{\theta} = \frac{\boldsymbol{A_x B_x} + \boldsymbol{A_y B_y}}{\boldsymbol{A_l B_l}}$$

$$\sin\boldsymbol{\theta} = \frac{\boldsymbol{A_x B_y} - \boldsymbol{A_y B_x}}{\boldsymbol{A_l B_l}}$$

where $\boldsymbol{\theta}$ is the angle between vector A and vector B, $\boldsymbol{A_x}$and $\boldsymbol{A_y}$ are the component of A in x and y respectively, and $\boldsymbol{A_l}$ is the length of vector A. The same annotation was used for vector B. Angle $\boldsymbol{\theta}$ was then calculated from sin $\boldsymbol{\theta}$:

If cos $\boldsymbol{\theta}$ > 0, $\boldsymbol{\theta}$ = arcsin(sin $\boldsymbol{\theta}$)

If cos $\boldsymbol{\theta}$ < 0, $\boldsymbol{\theta}$ = π - arcsin(sin $\boldsymbol{\theta}$)

Only positive angles were used, so if the angle $\boldsymbol{\theta}$ was negative, then $\boldsymbol{\theta'}$ = $\boldsymbol{\theta}$+ 2 π was used.

This unique number of each dendritic branch was therefore based on the topology of the neuron and it was not altered by movement of the tissue. Then, the tracing of the neuron was used as a reconstruction of the dendritic tree in space, and using the spatial coordinates of the imaged POIs, it was possible to determine which imaged POI was in which dendritic branch for each Z-stack.

During the tracing, each node in the dendritic tree is assigned a radius based on the intensity of the dendrite in the image. However, the software Vaa3d often underestimated the radius of the dendrite, setting it to 1 pixel, which corresponds to 0.43 µm. Therefore, an offset of 3 pixels was added to all radii of the neurons traced with Vaa3d. In the neurons traced with NeuTube, the radius estimates were more accurate, thus no offset was added. For each node, using the xy coordinates and the radius of the node, a circle was "drawn" centred on the node and with the assigned radius, and all the POIs in the circle were considered in the dendrite (**figure 2.3c** and **d**). In addition, every two nodes, a quadrilateral was "drawn" using the xy coordinates and the radius of each node, and all POIs in the polygon were considered in the branch (**figure 2.3 d**).

To determine if a POI was in the circle around a node, the distance between the POI and the node was calculated in two dimensions and then if the distance was smaller than the radius the POI was considered in the dendrite. A quadrilateral between two nodes with coordinates $\boldsymbol{x_1, y_1}$ and $\boldsymbol{x_2, y_2}$ was obtained first calculating the slope $\boldsymbol{m}$ of the line perpendicular to the line passing through the two nodes:

$$\boldsymbol{m} = -\frac{\boldsymbol{x_2 - x_1}}{\boldsymbol{y_2 - y_1}}$$

Then the vertexes of the quadrilateral were found as points on the line with slope $\boldsymbol{m}$ and passing through node 1, at a distance from the node equal to the radius of the dendrite (**figure 2.3 d**). The following system of two equations expresses these two conditions:

$$\begin{cases} \boldsymbol{y_1 - y_v = m(x_1 - x_v)} \\ \boldsymbol{(x_1 - x_v)^2 + (y_1 - y_v)^2 = R^2} \end{cases}$$

where $\boldsymbol{x_1, y_1}$ are the coordinates of node 1, $\boldsymbol{x_v, y_v}$ are the coordinated of the 2 vertexes of the quadrilateral close to node 1, and $\boldsymbol{R}$ is the radius of the dendrite at node 1.

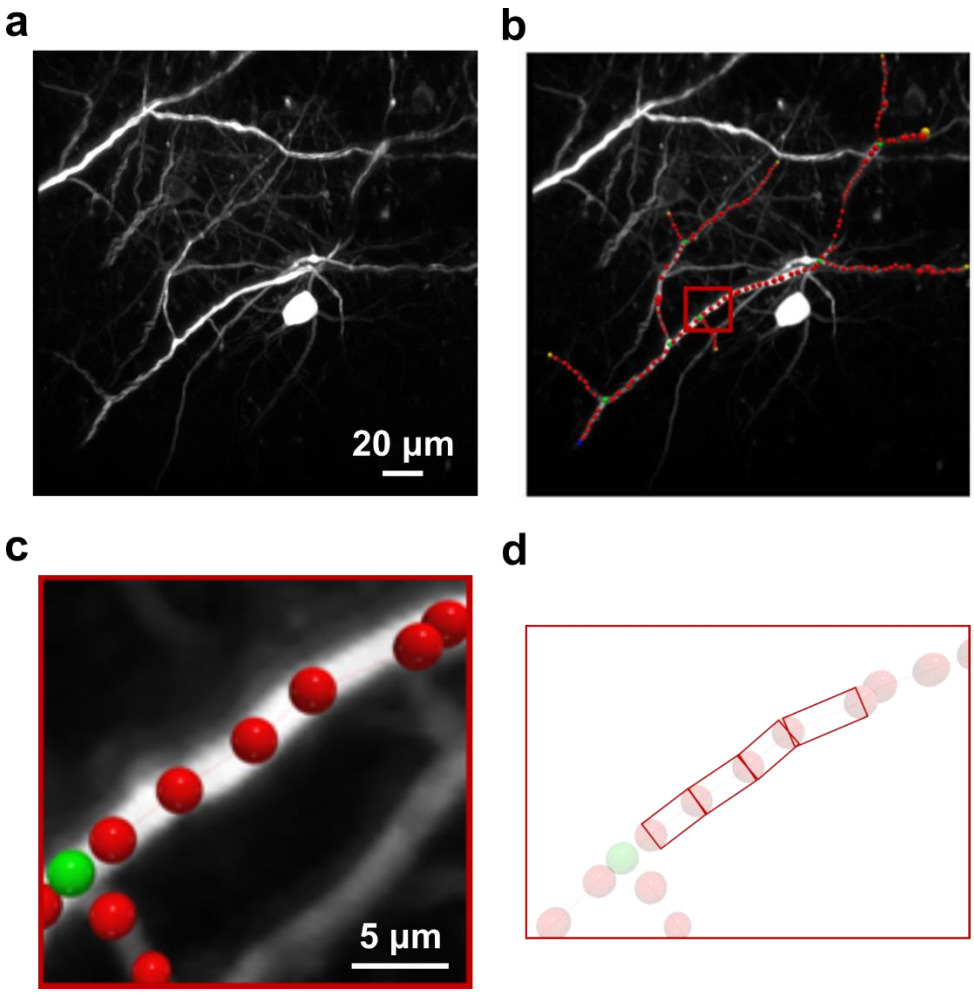

Figure 2.3 Neuron tracing and reconstruction. a: Maximum Z-projection of dendrites labelled with GCaMP6f and imaged with the AOL microscope at 800 nm. b: Semi-automatic tracing of the distal dendritic tree of a L5 neuron. The tracing was done with the software NeuTube (Feng et al., 2015): the dendrites are reconstructed from spheres (nodes) of different colours: blue: root, red: continuation node, green: branching point, yellow: termination node. The area in the red square is expended in c and d. d: The tracing was then imported into Matlab, and to attribute the imaged POIs to a dendritic branch, dendritic branches were reconstructed building a circle around each node, and a quadrilateral between every pair of nodes.

The solution of the system of equations for x_v and y_v is:

$$x_v = x_1 \pm \sqrt{\frac{R^2}{1 + m^2}}$$

$$y_v = -mx_1 + mx_v + y_1$$

These two formulas were applied to the two nodes to find the coordinates of the four vertexes of the quadrilateral. Given the vertexes, it was determined if a POI was in or at the edges of the quadrilateral using a Matlab built-in function.

This calculation was repeated for each node and pair of nodes in each branch, and in each plane in the Z-stack independently, so it was possible to reduce the geometrical problem from three dimensions to two dimensions.

Finally, POIs that were in multiple branches or in multiple cells were discarded to avoid contamination of the signals across cells or dendrites.

2.8.3 Detection of movement artefacts

As mentioned above, approximately every 2 minutes of recordings a new Z-stack was acquired again and new POIs were placed. To detect movement artefacts and the neuronal responses (see below), each 2-minutes recording associated with a Z stack was analysed independently. However, this recording was not continuous but it was divided in trials of 5-10 s length each (depending on the visual stimulation protocol); a small interval of time between trials was necessary to give time to the software to stream and save the data to disk. The time between two trials was 150 - 200 ms, but for the analysis presented below (remove movement artefacts, normalize the data and detect the responses), the trials were concatenated.

Since the animals were awake in most experiments, movement of the brain tissue was significant and it could cause the imaged POIs to move out of the imaged structure. Since the neurons were labelled with the morphological tracer TdTomato, the levels of red fluorescence were used to monitor whether the imaged POI was on the neuron during the recording. If the fluorescent intensity in the red channel dropped below a threshold, it was considered that the POI moved out the dendrite, and the corresponding recording in the green channel was discarded and treated as missing data. This threshold was close to zero, and it was calculated as the average levels of red fluorescence outside a biological structure. The probability that an imaged POI moved from one biological structure to another was also estimated (see **figure 3.6** and section 2.8.4), and it was found to be negligible due to the sparseness of the labelling. A similar approach was also used in another study where populations of neurons were imaged with random-access POIs with an AOL microscope (Cotton et al., 2013).

In case of smaller movements of the tissue, the levels of green and red fluorescence could co-vary and create movement artefacts. Movement artefacts could also consist of an increase in fluorescence, thus they could be erroneously detected as neuronal responses. To reduce these artefacts, I took advantage of the properties of the two fluorophores (TdTomato and GCaMP6): while movement artefacts were visible in both channels, neuronal responses were detected only by GCaMP6. First low-frequency movement artefacts were separated by high-frequency noise in the recordings in the red channel. To do this, the recording in the red channel was smoothed over a temporal window of 1 second with local regression that used a weighted linear least square and a first degree polynomial model. Analogously, the data in the green channel was smoothed with the same method but over a temporal window of only 100 ms. Then, the recording in the red channel was multiplied by a scaling factor that was obtained as the mean of the recording in the green channel divided by the mean of the recording in red channel. Afterwards, the scaled recording in the red channel was subtracted to the recording in the green channel. Finally, to avoid artefacts when computing ΔF/F (see below), the original value of baseline fluorescence in the green channel was set adding the mean of the recording in the green channel, and any negative data points were set to zero.

All POIs in one branch were averaged, and changes in fluorescence of GCaMP6f were expressed relative to its baseline fluorescence (ΔF/F). The recordings were then smoothed with a moving average filter over a time window of 10 time points.

2.8.4 Measurements of distance between dendrites

As mentioned above, the levels of fluorescence in the red channel were used to detect if a POI went out a dendrite, and to compensate for movement artefacts. However, if an imaged POI moved to another biological structure, the data would not be discarded because the levels of red fluorescence would still be high, but the recordings would not be correct. I then estimated the probability of missing an event (false negative), or detecting a calcium event in another dendrite (false positive), because the POI moved to another biological structure. To do this, I first measured the distance between an imaged dendrite and all the other red fluorescent structures.

In each imaged branch, a subset of points was chosen randomly: for each branch the number of points selected was equal to 60% of the number of nodes. In total, more 1200 points were selected in different planes, cells, and animals, and these points were considered representative of the imaged POIs. The other red fluorescent

structures present in the image were identified first by normalizing each image for the mean light level, then filtering the images with a Gaussian filter of 5 microns in size, and finally a threshold was applied. For each point, the red fluorescence of the dendritic branch where the point was placed was removed, because if the POI moved along the same dendrite the recordings would still be valid. The tracing of the neuron was then used to identify the xy coordinates and radius of the dendritic branch where the point was, and the red fluorescence in this branch was set to zero.

The distance between each point and all the points in the red fluorescent structures was then measured in two dimensions. Afterwards, the percentage of space occupied by red fluorescent structures in a radius of 4 or 8 μm (typical size of point displacements) was computed. To estimate the occurrence of false positives and false negatives, these values were then multiplied by the percentage of time during which a dendritic branch is active. The rate of false positives (or false negatives) was found to be < 2%.

2.8.5 Quantification of activity-dependent photons detected in the red channel

In order to use the recordings in the red channel to detect movement artefacts (see section 2.8.3), the levels of red fluorescence must be activity-independent, but some bleed through was measured between the green and the red channel. To investigate whether the fluorescence in the red channel can still be considered activity-independent, I estimated the percentage of GCaMP6f-emitted photons detected by the PMT in the red channel. Since there was bleed through both from the green channel into the red channel, and from the red channel into the green channel, the levels of fluorescence in the red and in the green channel can be expressed as:

$$\begin{cases} RedF = X_R + Bl_{GR} * X_G \\ GreenF = X_G + Bl_{RG} * X_R \end{cases}$$

where $RedF$ and $GreenF$ are the measured levels of red and green fluorescence, respectively. X_R is the number of "red" photons emitted by TdTomato, and X_G is the number of "green" photons emitted by GCaMP6f. Bl_{GR} and Bl_{RG} are measurements of bleed through between the two channels, from the green into the red, and from the red into the green, respectively. These values were obtained measuring the levels of red fluorescence when only GCaMP6f was expressed, and measuring the levels of green fluorescence when only TdTomato was expressed, respectively (**figure 3.3**). Both Bl_{GR} and Bl_{RG} were expressed as percentages.

The solution of the system of equations above is:

$$X_G = \frac{GreenF - RedF * Bl_{RG}}{1 - Bl_{GR} * Bl_{RG}}$$

$$X_R = RedF - Bl_{GR} * X_G$$

Given the recording in a POI, it is then possible to estimate the number of photons emitted by GCaMP6f and the number of photons emitted by TdTomato. The percentage P of activity-dependent photons detected in the red channel is then given by:

$$P = \frac{X_G * Bl_{GR}}{RedF} * 100$$

For a POI, ~2 minutes recordings in the red and in the green channel were averaged over time, and then X_G and P were calculated. This analysis was carried out on two datasets randomly selected dataset for each region in each animal imaged, resulting in a total of >13,000 POIs recordings analysed. The mean value of P was 0.67 %, and the maximum value of P was 1.3 %.

2.8.6 Detection of neuronal responses

Neuronal responses were detected using a template matching algorithm previously published (Clements and Bekkers, 1997). In this algorithm, a template is slid along the trace, fit and scaled to the data. The template function consists of:

$$TEMPLATE(t) = 0 \ \ (t \leq 0)$$

$$TEMPLATE(t) = \left(1 - e^{-t/RISE}\right) * \ e^{-t/DECAY} \ (t > 0)$$

where *t* is the time from onset of the idealised synaptic event, *RISE* is the time constant of the rising phase of the template, and *DECAY* is the time constant of the falling phase of the template. A scaling factor and an offset are then added to the template, and at each point of the trace the scale and offset parameters are calculated to minimize the sum of the square errors between the fitted template and the data region. A detection criterion is then calculated from the ratio between the template scaling factor and the quality of the fit. An event is then detected when it crosses a threshold level, which was set to 2.

Furthermore, a hard threshold was then applied to the events detected with the Clements and Bekkers algorithm. The amplitude of the event had to be higher than three standard deviations of the noise. The noise was measured over a baseline that was at least 3 seconds long, and that was chosen manually as a region with no visible calcium transients. Onsets/ends of the responses were detected as the first/last point higher than three standard deviations of the noise.

For some of the analysis presented here, I calculated the percentage of dendritic branches that were active simultaneously out of all the imaged branches. For this calculation, I considered only cells and datasets where a significant part of the dendritic tree was imaged simultaneously (≥ 5 dendritic branches).

2.8.7 Orientation tuning

Neurons were considered responsive to visual stimuli if the integral of the neuronal activity (ΔF/F) averaged across all branches and soma was significantly different (paired t-test, p- value < 0.05) in the first second of presentation of the stimulus compared to the 1 second of grey screen just before the appearance of the visual stimulus.

Orientation tuning was computed similarly to (Ko et al., 2011). The integral of the activity (ΔF/F) during 2 seconds of drifting grating presentation was taken as the response to each stimulus. Presentations of the 8 gratings were repeated multiple times, and for each repetition, the minimum response was identified, and subtracted to the responses to the other orientations. Afterwards, responses from different repetitions were averaged to obtain the orientation tuning curve. This orientation tuning curve was then interpolated with a third degree polynomial to 360 points, corresponding to 360 degrees, and preferred orientation and preferred direction were defined as the maximum of the curve (D_{best}). The orthogonal directions (D_{ortho}) were obtained adding and subtracting 90 degrees to the preferred direction: these two directions have the same orientation, which corresponds to the null orientation. The direction opposite to the preferred direction, called null direction (D_{null}), was obtained adding 180 degrees to the preferred direction. Preferred, orthogonal and null directions were used to calculate orientation and direction selectivity indexes. Note that orientations were defined only between 0 and 180 degrees, while directions were comprised between 0 and 360 degrees. **Figure 2.4** below illustrates the null and orthogonal directions when the preferred direction is 90 degrees.

The orientation selectivity index (OSI) was calculated as:

$$OSI = \frac{R_{best} - R_{ortho}}{R_{best} + R_{ortho}}$$

where R_{best} is the interpolated response to the preferred orientation and direction D_{best}, and R_{ortho} is the average of the interpolated responses to the two orthogonal directions D_{ortho}.

The direction selectivity index (DSI) was calculated as

$$DSI = 1 - \frac{R_{null}}{R_{best}}$$

where R_{null} is the interpolated response to the null direction D_{null}.

Cells where the soma had OSI > 0.4 were considered tuned for one orientation, and analogously dendrites with OSI > 0.4 were considered selective for one orientation. Somas and dendrites that were selective for one orientation were considered also direction selective if they had DSI > 0.3.

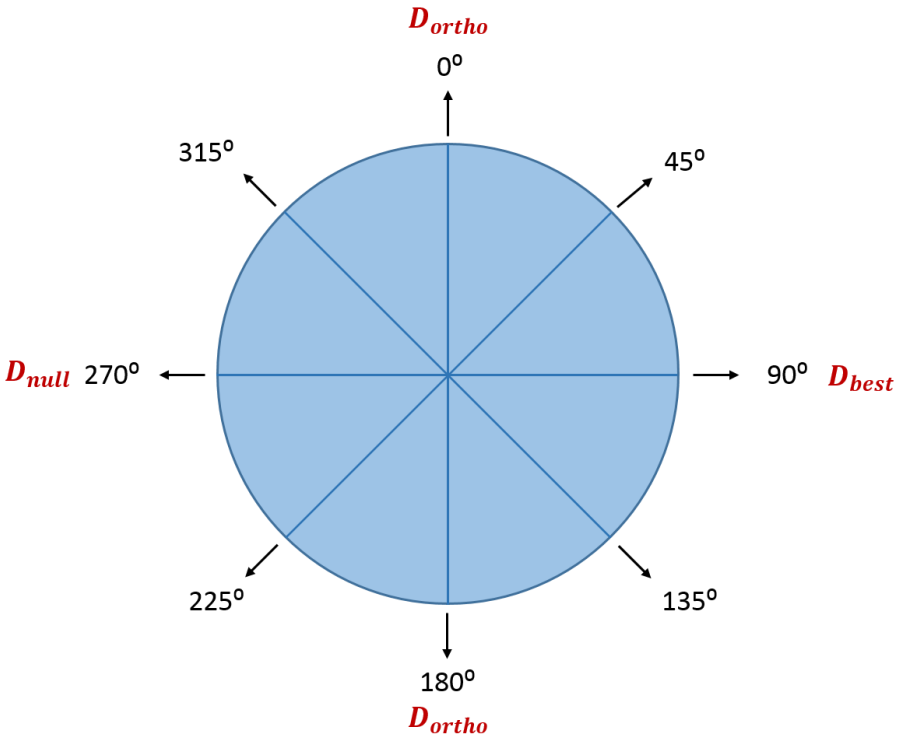

Figure 2.4 Preferred, orthogonal and null directions. Gratings with eight different directions (black arrows) and four different orientations were presented to the animal, and the angle of each grating is written in black. If the preferred direction (D_{best}) is 90 degrees, the orthogonal directions (D_{ortho}) are 0 and 180 degrees, corresponding to the null orientation, which is vertical in this case. While the null direction (D_{null}) is opposite to the preferred direction, so it is 270 degrees in this example.

2.8.8 Tracking eye movements

During an experiment, a camera acquired video files of the mouse eye synchronized with the acquisition of the calcium imaging data, therefore there was one video file associated to each imaging session (~ 2 minutes long). For each video, a region of interest surrounding the pupil and approximately of the size of the eye was selected manually (**figure 2.5 a**). The video file was then cropped to the selected region of interest. Then in each frame the bright reflection of the LEDs was detected, removed and set to grey values, and the luminance of the image was normalized by the average light level (**figure 2.5 b**). Then each frame was smoothed several times with a Gaussian two-dimensional filter, and the pupil was detected applying a threshold to select only the dark pixels in the image (**figure 2.5 b**). Then small objects were removed (**figure 2.5 b**), and the centre of the pupil was found as the centre of mass of the image. An approximate measurement of the area of the pupil was obtained

from the number of pixels with intensity below the threshold. All video files were processed after the experiments to detect movements of the centre of the pupil during recordings.

Frames where the animal blinked or groomed were removed. To detect these frames, the correlations of each frame with the average frame in the video were computed with chi coefficients. Frames with a Pearson coefficient lower than the mean Pearson coefficient minus two standard deviations were removed.

Eye movements during drifting gratings presentation (2 seconds) were then evaluated similarly to (Ayaz et al., 2013). The average position of the centre of the pupil during the grating presentation was computed, and movements of the pupil from the central position were measured with the following formula:

$$\boldsymbol{\theta = arcsin(D/r)}$$

where $\boldsymbol{\theta}$ is the angle of the eye movement, $\boldsymbol{D}$ is the distance of the pupil from the mean pupil position in the trial, and $\boldsymbol{r}$ is the radius of the eye. This formula is valid under the approximation that the eye movements are small compared to the size of the mouse eye. The radius of the mouse eye was considered to be 1.6 mm (Remtulla and Hallett, 1985). Since the size of RF in mouse primary visual cortex is 5-15 degrees (Niell and Stryker, 2008), eye movements were considered significant when larger than 5 degrees. In 9 experiments on 7 mice, the percentage of trials with at least one eye movement larger than 5 degrees during drifting grating presentation was 6.4 ± 2.4 %. Given that eye movements in head-fixed animals are rare, and that they have been reported to have little or none effect on neuronal activity in mouse primary visual cortex (Ayaz et al., 2013; Erisken et al., 2014; Keller et al., 2012; Poort et al., 2015; Saleem et al., 2013), the effect of eye movements on neuronal responses was considered negligible.

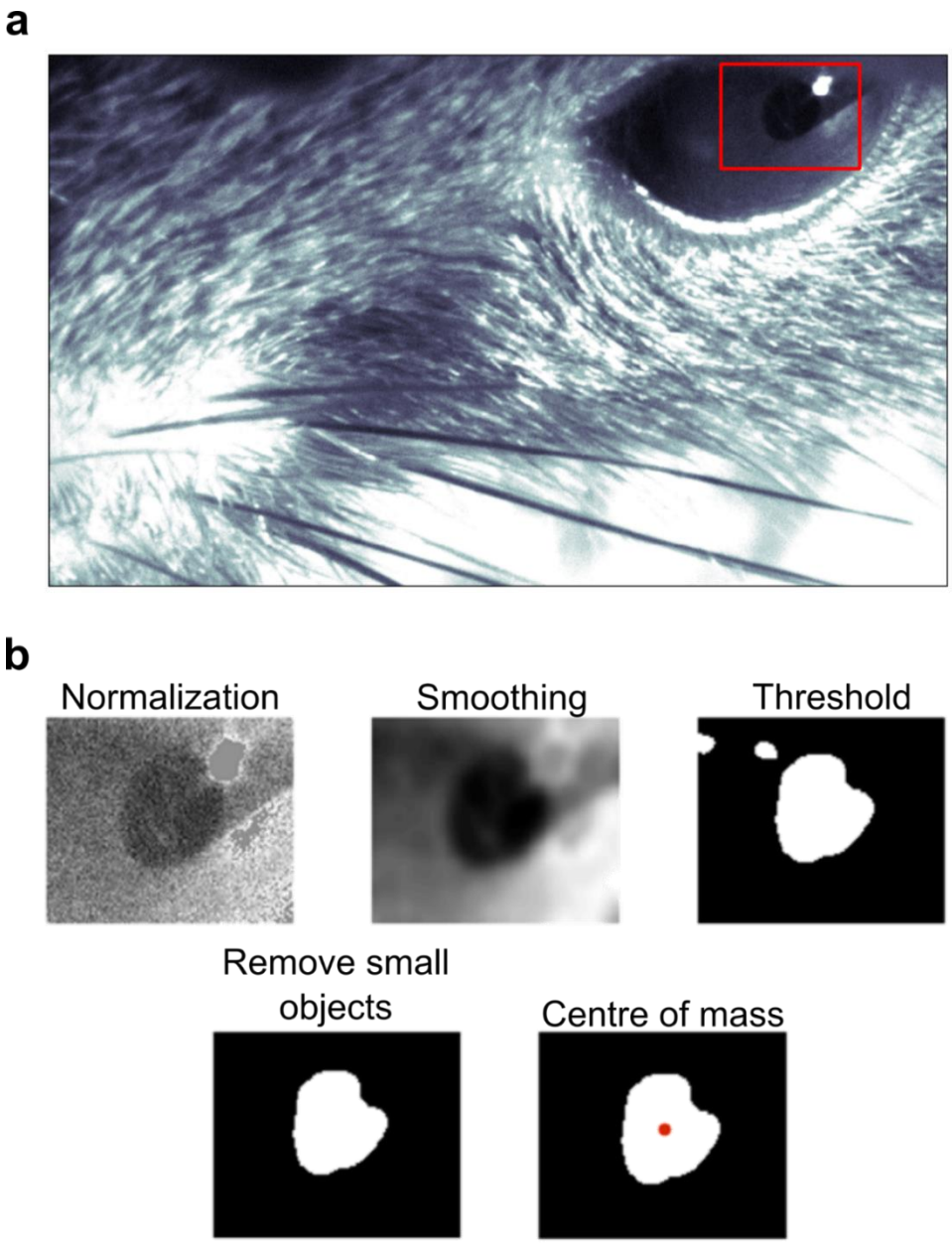

Figure 2.5 Eye tracking. a: Image of the mouse acquired during an experiment. A region of interest centred on the pupil was selected manually for each video (red contour), and each video was approximately 2 minutes long. b: Processing of the region of interest selected to track eye movements. First panel: the reflection of the LEDs light were substituted with grey values and the average luminance of the image was normalized. Second panel: each frame was smoothed with a two-dimensional Gaussian filter. Third panel: the pupil was detected applying a threshold to the image. Forth panel: small objects were removed. Fifth panel: the centre of the pupil was found as the centre of mass of the image.

2.8.9 Modulation of activity by animal state

To compare dendritic activity when the animal was stationary and when the animal was running, neuronal activity recorded during 10-20 repetitions of gratings (10.6 – 21.3 minutes, considering both grey screen and gratings), or while the animal was in the darkness, was considered. The mouse speed data was measured with a rotatory encoder, which acquired data with a time resolution of 2 ms. The speed data was then filtered temporally with a moving average of 20 ms to remove digital steps, and it was interpolated to be at the same temporal scale as the imaging data from the AOL microscope. Given that the resolution of the rotatory encoder was 3 rpm, the animal was considered as running when its speed was above 5 rpm, which corresponded to 0.8 cm/s. For both animal states, the activity was averaged in bins of 100 ms and the mean activity across bins was compared for the two animal states (similar analysis as in Saleem et al., 2013). The size of the bins was varied (50, 200 and 300 ms), but the results did not change significantly. In the figures, the mouse speed data was down sampled by a factor of 10 for the plots.

Analogously, in anaesthetized animals the neuronal activity over 10-20 repetitions of gratings activity was averaged for bins of 100 ms. The size of the bins was also varied (50, 200 and 300 ms), but the results did not change.

2.8.10 Analysis of random-access patches and subvolumes

Imaging data was stored as a time series of images for each patch. Images were corrected for brain motion using the sequential image analysis software suite (SIMA) (Kaifosh et al., 2014). For patch imaging, movement was either corrected patch-by-patch or using a montage of all the patches. The latter approach was particularly effective for imaging regions of interest that were sparsely active and in mice expressing only GCaMP6f. Functional signals were extracted from images by generating masks of cellular structures using a thresholding algorithm. The average of the intensity of voxels across the mask was calculated for each frame and $\Delta f/f$ was calculated. The timing of each data point was calculated at the centre of the region of interest. The data with the mouse running speed was smoothed averaging over a window of 20 ms.

3. Sparse labelling and dual colour expression for imaging dendrites *in vivo*

3.1 Introduction

Dendrites of pyramidal neurons are complex structures and they are difficult to access, especially in intact animals. Dendrites are thin (few micrometres), they are densely packed and distributed in three dimensions. Therefore, in order to visualize the dendritic tree and the morphology of a neuron, only few cells need to be labelled (sparse labelling). Furthermore, *in vivo* the brain tissue can move of several micrometres due to blood circulation, respiration and movements of the animal.

In the work presented here, we decided to probe dendritic activity using an acousto-optic lens (AOL) microscope, which can image random-access points distributed in a three dimensional volume at very high speeds (Fernández-Alfonso et al., 2014; Katona et al., 2012), therefore it is ideal to sample sparse activity from dendrites, which elongate primarily in the third dimension. The main advantage of this approach was that I could record from almost all the dendritic branches in a dendritic tree near-simultaneously. Neuronal activity was measured monitoring the calcium concentration with the genetically-encoded calcium indicator GCaMP6f (Chen et al., 2013a), and movement of the tissue was monitored with the morphological tracer TdTomato (Shaner et al., 2004). Both GCaMP6f and TdTomato were expressed sparsely, so it was possible to identify the dendritic tree of a single pyramidal neuron.

3.2 Results

3.2.1 Sparse labelling of pyramidal neurons with the genetically-encoded calcium indicator GCaMP6

The genetically-encoded calcium indicator GCaMP6f was expressed in the neurons via virus injection in V1 in mice. Sparse labelling can be achieved co-injecting two viruses: a diluted virus with the gene encoding for Cre recombinase, and a concentrated virus with the gene encoding for Cre-dependent GCaMP6f (Chen et al., 2013a; Xu et al., 2012). With this approach, the diluted Cre-expressing virus infects only few cells, while the GCaMP6f -expressing virus infects the neurons densely and with high-number of gene copies, but GCaMP6f is expressed only in the cells infected by both viruses. With this method, it is possible to infect only few

cells with a high number of copies of GCaMP6f gene. The level of sparseness of the labelling can be controlled by the dilution of the Cre-expressing virus (**figure 3.1**). For the experiments presented in this thesis, the Cre virus was diluted by 1:10,000 – 1:12,000. Besides, the gene encoding for Cre recombinase was under the control of the promoter of calcium/calmodulin-dependent protein kinase II (CamKII), which is expressed only in pyramidal neurons. Targeting selectively pyramidal neurons was beneficial for two reasons: it allowed me to image only excitatory neurons, and it increased the sparseness of the labelling. This method to label neurons sparsely with GCaMP6f was developed with the help of Mr. Diccon Coyle.

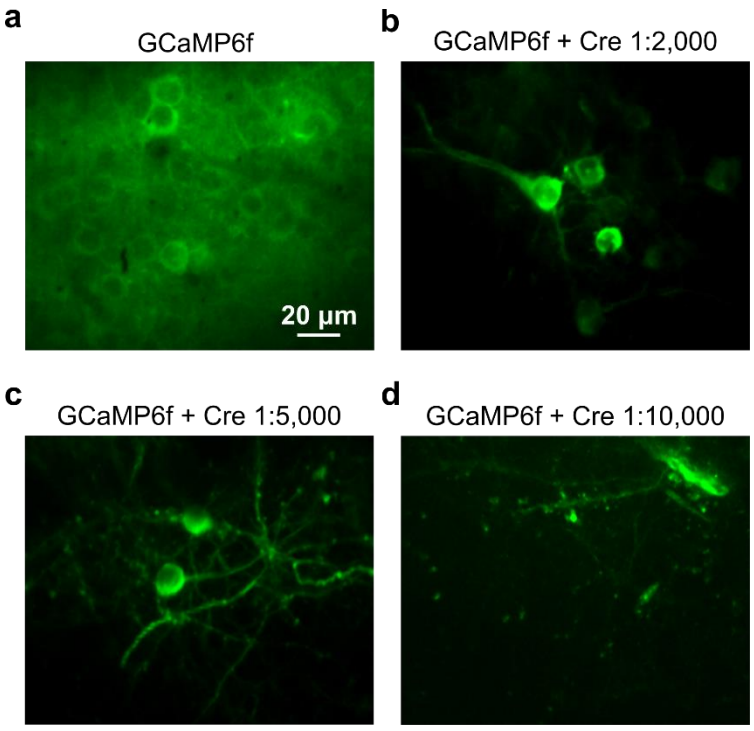

Figure 3.1 Sparse labelling of pyramidal neurons. The dilution of the Cre virus determines the sparseness of the labelling. a-d: Neurons expressing GCaMP6f in *vivo*. a: only GCaMP6f virus was injected. b – d: Cre-dependent GCaMP6f virus was co-injected with Cre virus to label neurons sparsely. The three panels show the labelling from different animals injected with decreasing concentrations of Cre virus.

3.2.2 Dual labelling with the calcium indicator GCaMP6f and the red fluorophore TdTomato

In order to account for movement artefacts, I developed a protocol to co-express sparsely GCaMP6f and a red fluorescent protein.

At first, I co-injected 3 viruses: Cre-recombinase-expressing virus, GCaMP6f-Flex-expressing virus and TdTomato-Flex – expressing virus. I tried several combinations of different concentrations of the three viruses (**table 3.1**), and for each condition I injected 2-4 animals, and the animals were imaged multiple times in a time window of 20-50 days after the virus injection. In some cases, when the cells seemed to be labelled faintly, the animals were imaged even 3 months after virus injection, to allow more time for the fluorescent proteins to be expressed. However, most of these protocols resulted in very dim fluorescent signals, and the labelling with GCaMP6f and with TdTomato often seemed to be mutually exclusive. It is possible that the three viruses are competing for the same cellular machinery for RNA and/or protein synthesis.

Therefore, I then tried a single construct that contained both GCaMP6 and the red fluorescent protein mRuby2 (Kredel et al., 2009), to reduce the number of viruses injected (Rose et al., 2016). Animals injected with a virus expressing this construct also showed very dim fluorescence both in the red and in the green channel (**table 3.1**). I could observe brighter fluorescence signals only 3 months after virus injection, but such a long time of expression is impractical for experiments.

Table 3.1 Combinations of virus constructs and concentrations that were tested in order to label neurons sparsely both with GCaMP6 and with a red fluorescent protein. The first two columns indicate the protocol used, the last two columns provide a short summary of the quality of the labelling at two different times after virus injection. *GCaMP6-mRuby2 construct was designed by Dr Tobias Rose (Rose et al., 2016). **Ai9 transgenic mice are flox-TdTomato transgenic animals (Madisen et al., 2010).

Cre	GCaMP6	TdTomato	20-50 days of expression	> 80 days of expression
-	GCaMP6f 1:2	TdTomato 1:10	red not visible, very dim neuronal responses	
1:2,000	Flex GCaMP6f 1:2	Flex TdTomato 1:4	red not visible, very dim neuronal responses	
1:8,000	Flex GCaMP6f 1:2	Flex TdTomato 1:4	red dim, no green labelling. 1/4 animals see neuronal responses but no red	
1:10,000	Flex GCaMP6f 1:2	Flex TdTomato 1:4	red too dim, very dim neuronal responses	clear neuronal responses, red dim
1:20,000	Flex GCaMP6f 1:2	Flex TdTomato 1:4	labelling too dim	acceptable dual labelling, but red slightly dim
1:5,000	Flex GCaMP6f 1:2	Flex TdTomato 1:16	clear neuronal responses, no red labelling	
-	GCaMP6f-mRuby2*, undiluted		Red labelling visible at 800nm only, not at 920nm Very dim neuronal responses	Red labelling visible at 800nm only, not at 920nm Very dim neuronal responses
-	GCaMP6s-mRuby2*, 1:2		very faint or no labelling Fluorescent residues on the surface	good dual labelling
1:20,000	Flex -GCaMP6s-mRuby2*, 1:2		dim neuronal responses Red labelling visible at 800nm only, not at 920nm	acceptable dual labelling, but both channels dim
mCherry-syn-Cre 1:10,000	Flex GCaMP6f 1:2	-	no labelling	no labelling
1:20,000	Flex GCaMP6f 1:2	Ai9 transgenic mice**	clear neuronal responses and green labelling labelling in the red dim	clear neuronal responses and green labelling labelling in the red dim
1:12,000	Flex GCaMP6f 1:2	Ai9 transgenic mice**	good dual labelling	good dual labelling

Finally, I injected diluted Cre virus and GCaMP6f virus in transgenic animals expressing Cre-dependent TdTomato (Ai9 transgenic mouse line, Madisen et al., 2010) (**table 3.1**). This protocol resulted in bright sparse labelling in both channels (**figure 3.2**), and the fluorescence levels looked stable for several weeks. The time when the cells started to be visible varied from animal to animal, possibly depending on the precise volume of virus injected in each animal. In general, labelling was visible from 4 to 8 weeks after the virus injection, and animals were then imaged for 1 or 2 months.

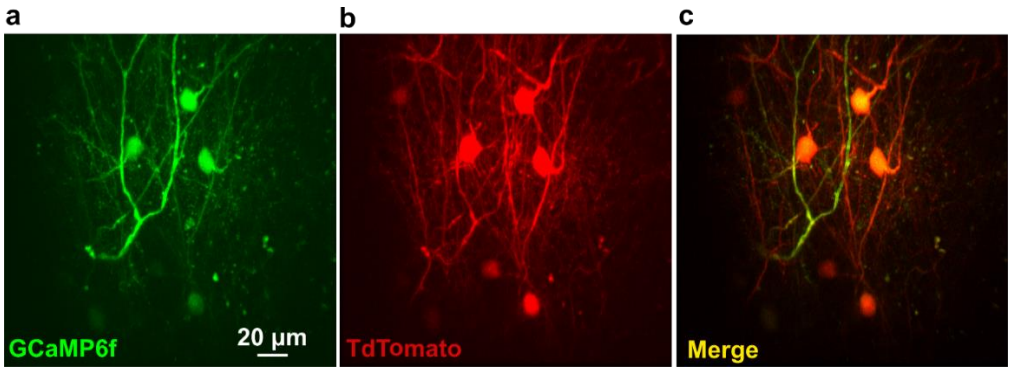

Figure 3.2 Pyramidal neurons labelled sparsely with GCaMP6f (a) and with TdTomato (b) *in vivo*. Panel c shows the images in the two channels merged. All three panels display a maximum intensity Z-projection.

3.2.3 Crosstalk between green and red channel

Due to a small overlap in the emission spectra of GCaMP6f and TdTomato in the region between ~ 550 – 580 nm, some degree of crosstalk between the two channels is possible. I therefore measured the crosstalk between channels in fixed brain slices where neurons were labelled either with GCaMP6f, or with TdTomato (**figure 3.3**).

First, a fixed slice of primary visual cortex labelled only with GCaMP6f was imaged in the same microscope where the *in vivo* experiments were carried out, and I observed almost no fluorescence in the red channel (**figure 3.3 a, b**). Then I imaged a fixed slice of neocortex expressing only TdTomato and I observed fluorescent signals also in the green channel (**figure 3.3 c, d**). Therefore, there is mainly bleed through from the red channel into the green channel, but not vice versa.

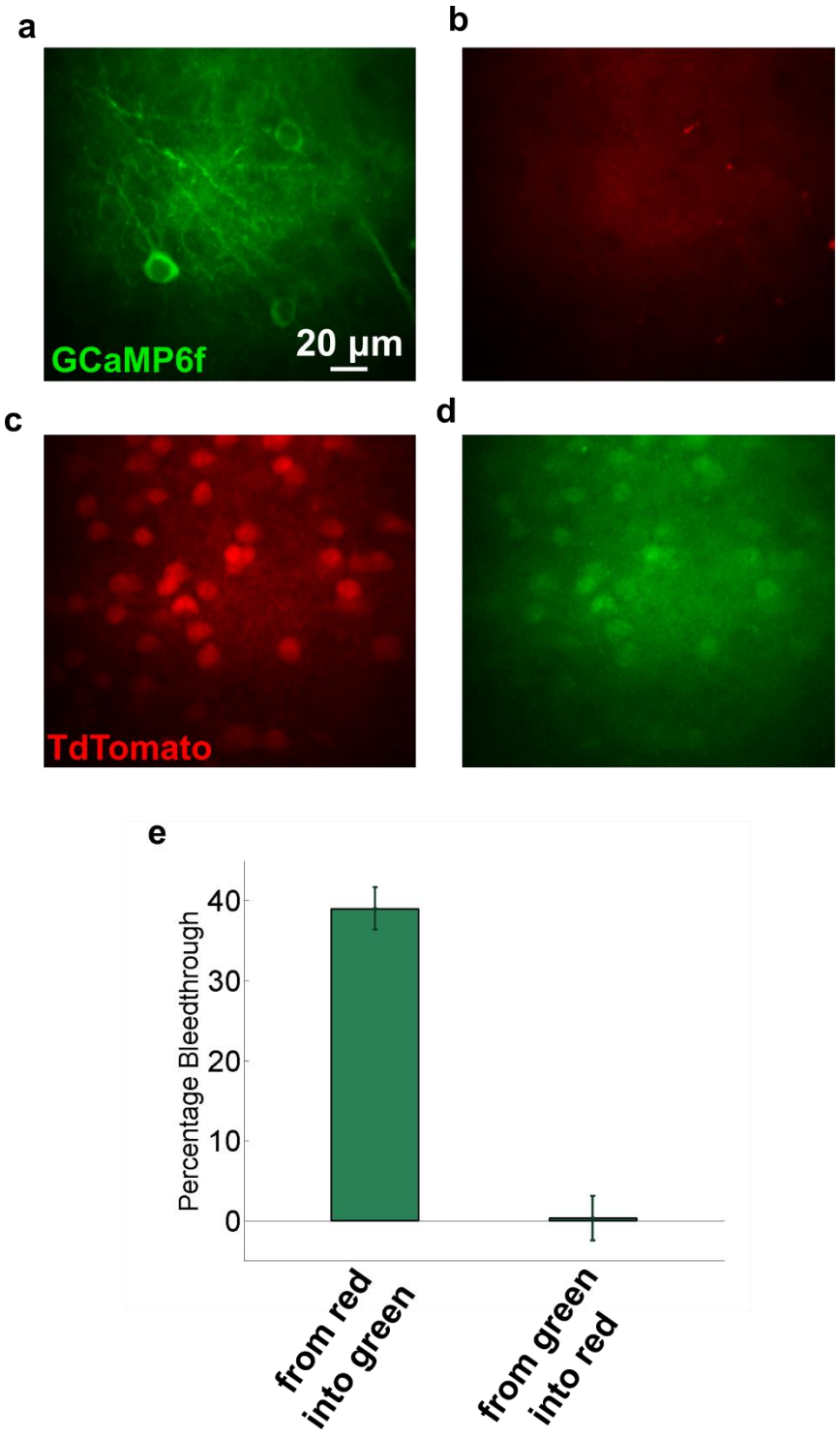

Figure 3.3 Crosstalk between GCaMP6f and TdTomato measured in fixed brain slices. a, b: slice of mouse V1 labelled via virus injection with GCaMP6f, maximum intensity Z-projection of neurons in the green and red channel respectively. c, d: slice of neocortex, where neurons were labelled only with TdTomato. The two panels show maximum intensity Z-projections in the red and green channel respectively. e: quantification of bleed through fluorescence measured for different cells.

In addition, I measured bleed through from the green channel into the red channel also *in vivo* in an awake animal (**figure 3.4**), because the fixation with paraformaldehyde and the different environment in fixed slices could alter the properties of the fluorophores. In an awake animal expressing only GCaMP6f in V1, I observed that 2.4 ± 1.4 % of the green fluorescence was visible in the red channel. This value is similar to the result obtained in fixed brain slices (2 ± 2.7 %).

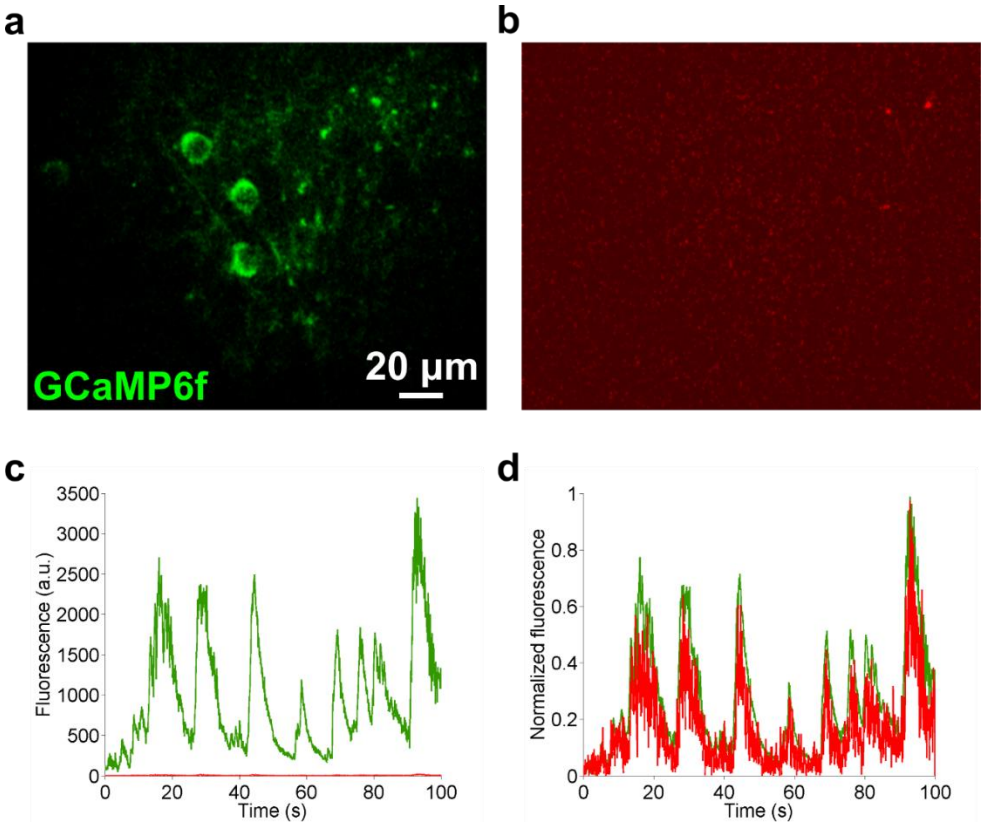

Figure 3.4 Crosstalk between GCaMP6f and TdTomato measured *in vivo*. a, b: Pyramidal neurons in V1 labelled sparsely with GCaMP6f, images acquired in the green and in the red channel, respectively. c: Recording over time of the fluorescence in one point of interest in a soma. The data in the green channel is plotted in green, while the data in the red channel is plotted in red. d: same as c, but the fluorescence levels were normalized for minimum and maximum intensity value in each channel.

To investigate whether the bleed through from the green channel into the red channel was negligible, I estimated the percentage of green photons out of the total number

of photons detected by the PMT in the red channel in animals expressing both TdTomato and GCaMP6f. Given the fluorescence levels in the green channel and in the red channel in animals with dual labelling, and knowing how much bleed through to expect between the two channels (**figure 3.3** and **3.4**), it is possible to estimate the number of photons that are activity-dependent, i.e. emitted by GCaMP6f, and that are detected in the red channel. I carried out this analysis for > 13,000 POIs recordings *in vivo* from different animals, and on average the number of GCaMP6-emitted photons detected in the red channel was 0.67 %, with values varying between 0 and 1.3 %. Therefore, I concluded that bleed through from the green into the red channel should not affect the data significantly.

The bleed through from the red channel into the green channel could mask features of the green labelling with GCaMP6f. Indeed, GCaMP6f is usually not expressed in the cells nuclei, and the somas look hollow. In the experiments presented here though, the neurons in the green channel did not show hollow nuclei because TdTomato was expressed in the whole cell and it filled up the nuclei even in the green channel. This became evident when imaging the neurons at different wavelengths: when imaging at 800 nm, TdTomato was only partially excited, so the image showed almost exclusively GCaMP6 fluorescence and the nuclei of the cells looked hollow (**figure 3.5 a**). While when imaging the same cell at 920 nm, where TdTomato was strongly excited, the soma looked filled (**figure 3.5 b**). Since calcium transients were visible only when imaging GCaMP6f at 920 nm, experiments were carried out imaging at this wavelength.

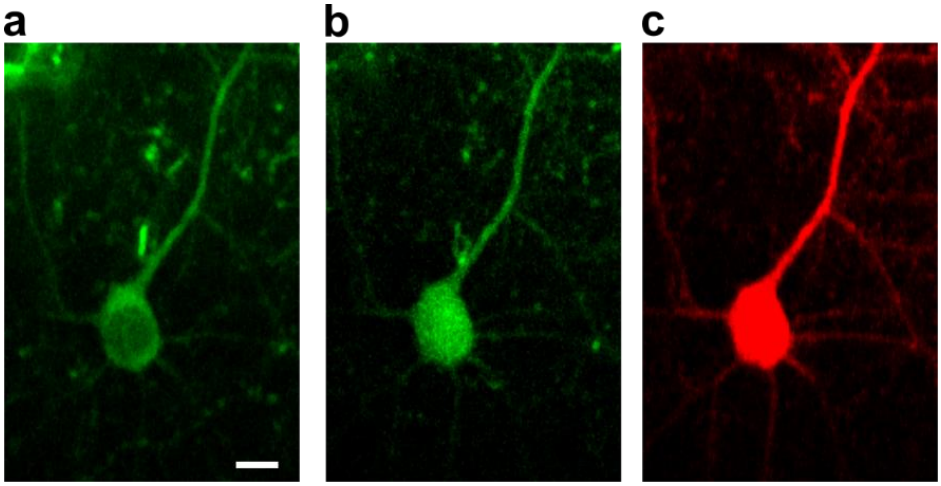

Figure 3.5 Pyramidal neuron labelled with GCaMP6f and TdTomato imaged at different wavelengths *in vivo*. This neuron was located approximately 100 µm below the surface. a:

Image in the green channel acquired at 800 nm. The scale bar corresponds to 10 µm. b: image in the green channel acquired at 920 nm. c: image in the red channel acquired at 920 nm.

The presence of hollow nuclei in GCaMP6 labelling is usually used to control whether the neurons are healthy: indeed, when GCaMP6 is overexpressed, it can accumulate in the nucleus and cause cytomorbidity (Chen et al., 2013a). Unfortunately in the experiments presented here, it was possible to control that GCaMP6f was not expressed in the cells only when imaging at 800 nm, and only when the TdTomato expression levels were low so that the red fluorescence was dim at 800 nm. This control was performed whenever possible, and, in addition, animals were always imaged over the same time window of 4-8 weeks.

In conclusion, I observed bleed through from the red channel into the green channel, while bleed through from the green channel into the red channel was negligible. Unfortunately, red photons read in the green channel can increase the baseline of cells' activity and decrease the signal to noise ratio of the calcium transients. But since there is little bleed through from the green channel into the red channel, the recordings in the red channel can be considered as activity-independent and can then be used to control movement of the tissue.

3.2.4 Recordings in 3D and movement detection

During an experiment *in vivo*, it is possible to image in two modes with an AOL-microscope: slow raster scanning mode, and fast imaging of random-access points. First, raster scanning was used to acquire full-frame images and z-stacks: the sampling rate in this mode is 3.3 Hz for images of 200x200 pixels, and 1 Hz for images of 512x512 pixels. From the full-frame z-stacks, it was possible to select specific points of interest in dendrites and in somas in three dimensions, then these points were imaged sequentially at high speeds.

The time to access each point was determined by the time necessary to fill the AOL with an acoustic wave, i.e. 24 µs in our case, and the dwell time, 4 µs. The total imaging time per point was, therefore, 28 µs; the time necessary to image 5 points was, then, 5x28 µs = 140 µs, resulting in a sampling rate of 7.14 KHz. The temporal resolution, then, decreases with the number of points imaged. But the position of the point does not affect the temporal resolution: all voxels in the volumetric field of view

can be accessed and imaged in 28 µs. During the experiments reported in this thesis, usually 300-500 points were imaged at 70-120 Hz.

The volumetric field of view consisted of 220x220 µm in x and y, and 200 µm in z (with a 25X objective). In the next generation of AOL-microscope, there is a larger field of view: 245x245 µm in x and y, and 400 µm in z (with a 20X objective). It was then possible to image near-simultaneously the majority of the dendritic tree and the soma of neurons in layer 2/3, and the majority of the apical dendrites and the somas of neurons in layer 5 (**figure 3.6**). Basal dendrites of layer 5 neurons were not visible.

In different experiments several points of interest were placed outside any biological structure, in order to measure neuropil activity. Since the labelling was sparse, the recordings in these points showed no calcium transients and no baseline fluorescence (data not shown).

After the experiments, neurons were reconstructed semi-automatically with the software neuTube (Feng et al., 2015) or Vaa3D (Peng et al., 2010, 2014). Each point of interest was attributed automatically to a dendritic branch using the TREES toolbox (Cuntz et al., 2010) and custom codes written in Matlab. The recordings from points in the same branch were averaged and dendritic branches were, then, considered as a single computational unit. I didn't investigate how the calcium signals change along the dendritic branch, because the number of points per branch was not sufficient.

As shown in **figure 3.6 c**, movement artefacts can be observed in the recording in the red channel. To remove these movement artefacts from the recording in the green channel, the trace in the red channel was filtered in the time domain, scaled and then subtracted to the trace in the green channel (trace shown in blue in the figure). This operation removed most of the movement artefacts and affected minimally the amplitudes of the calcium transients. In addition, when the level of fluorescence in the red channel went below a threshold, I assumed that the imaged point of interest went out of the imaged structure, so the data was discarded and considered as missing data. This threshold was computed as the mean red fluorescence in areas without dendrites.

Due to movement of the brain tissue, in each experiment every 1.5-2 minutes of recording a new z-stack was acquired and new points of interest were placed manually in the same structures.

It was possible to image and record calcium transients also in dendritic spines (**figure 3.7**), but spines were not visible in the red channel, probably due to the lower

sensitivity of the PMT in the red channel. Therefore, in my experiments I imaged only dendritic shafts, because it was not possible to control for movement of the tissue when imaging spines.

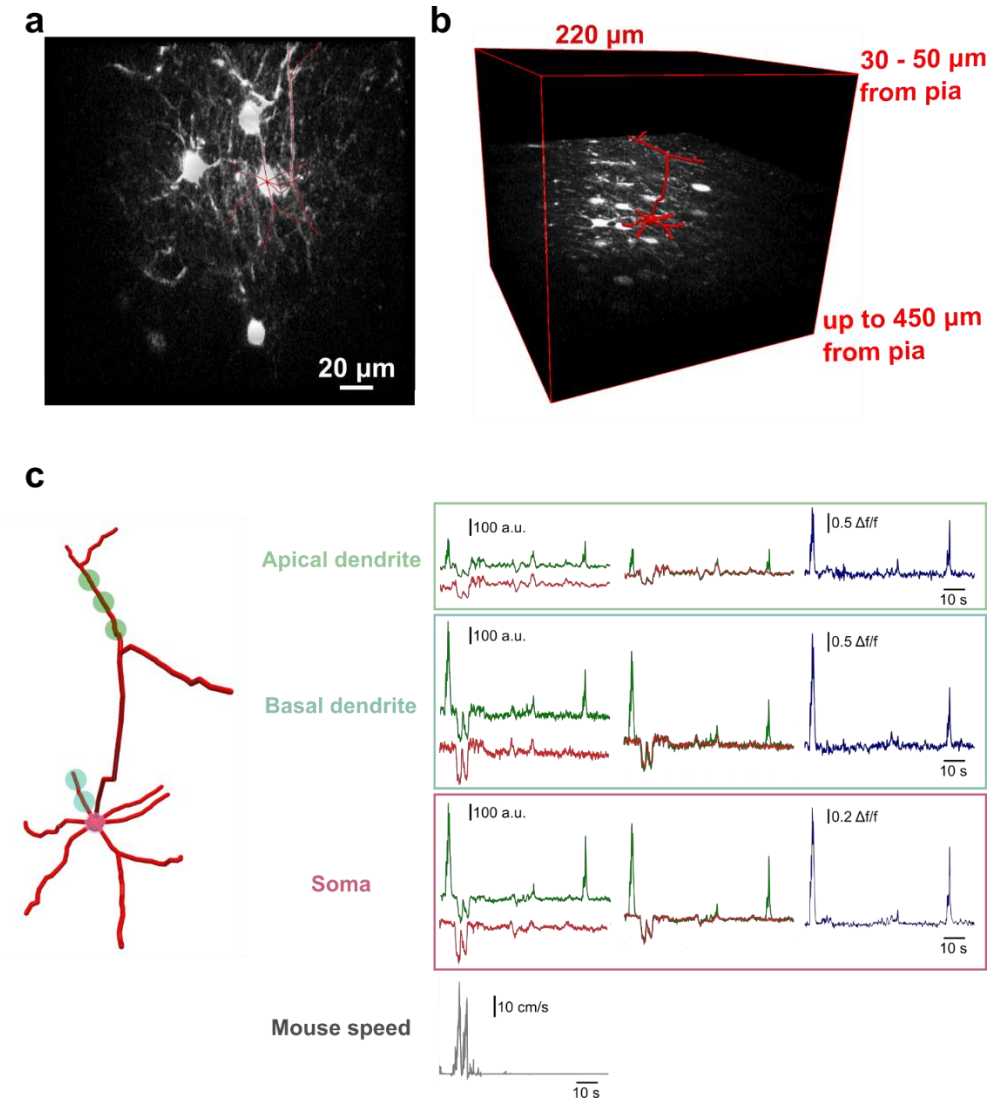

Figure 3.6 Recordings in random-access points of interest in three dimensions in awake mouse. a, b: maximum-intensity projection (a) and 3D rendering (b) of pyramidal neurons labelled with GCaMP6f. The post hoc reconstruction of one neuron, realized and displayed with the software neuTube (Feng et al., 2015), is shown in red. c: Left: Reconstruction of the cell shown in a and b. Examples of points of interest imaged in the apical dendrites, basal dendrites and soma are shown respectively in green, blue and pink. Right: recordings in the points of interest shown on the left. Recordings in the green and in red channel are shown in their respective colour. In blue, the recordings in the green channel corrected for movement artefacts with the trace in the red channel are shown. The mouse running speed on the

cylindrical treadmill is also shown in grey: movement artefacts often coincide with running episodes.

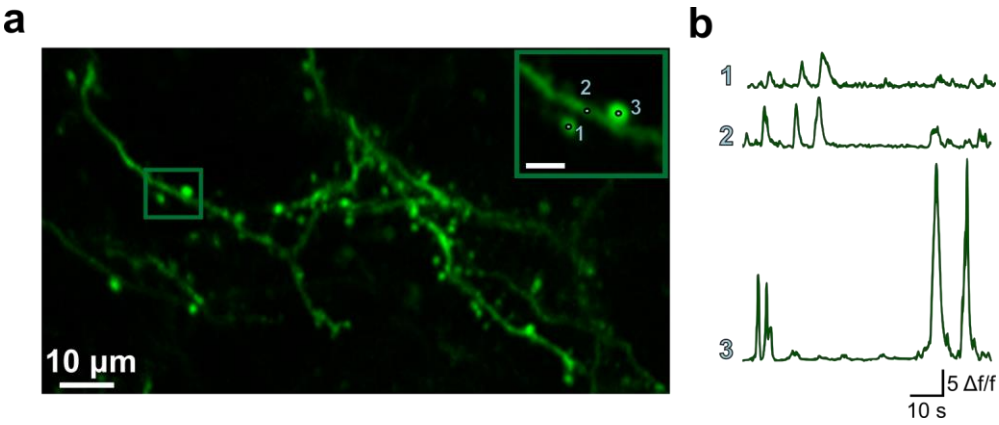

Figure 3.7 Calcium imaging of dendritic spines *in vivo*. a: dendrites and spine of pyramidal neurons labelled with GCaMP6f. This plane was 29 µm below pia. The area in the green square is magnified on the top right corner, where the scale bar corresponds to 2 µm. b: calcium transients recorded in three points of interest on two spines and on the dendritic shaft.

3.2.5 Measurements of sparseness of the labelling

The levels of fluorescence in the red channel were then used to determine if a point of interest fell off the imaged structure. But if many dendrites are labelled with TdTomato, during movement of the tissue a point of interest can by chance move from the intended imaged structure to another dendrite, and in this case the red fluorescence levels would still be high but the recordings would not be valid.

To estimate the probability that a point of interest moves by chance to another biological structure, I calculated the distances between an imaged dendrite and the other red fluorescent structures in the image. For all dendrites imaged, a subset of points in the dendrite was selected randomly, and then for each point I computed the distance from the point to all other red fluorescent structures. A total of >1200 points was considered, and the distribution of distances is shown in **figure 3.8a**.

Typically, in awake animals the tissue movement is 4 µm, with maximal displacements of approximately 8 µm (Dombeck et al., 2007). Dr Victoria Griffiths in the lab also quantified movement of the tissue in the animals used for the work presented here, and she obtained the same values (unpublished data, see chapter 7, **figure 7.4a** for movement characterization). Therefore, for each point in an imaged dendrite, I measured how much space is occupied by the red fluorescence

of another structure in a radius of 4 and 8 μm (**figure 3.8b** and **c**, respectively). For both distributions the median value is zero (with a precision of 10^{-5}), and for 90% of the points the space occupied by another red structure is <7.6% when considering a radius of 4 μm, and <12.1% when considering a radius of 8 μm.

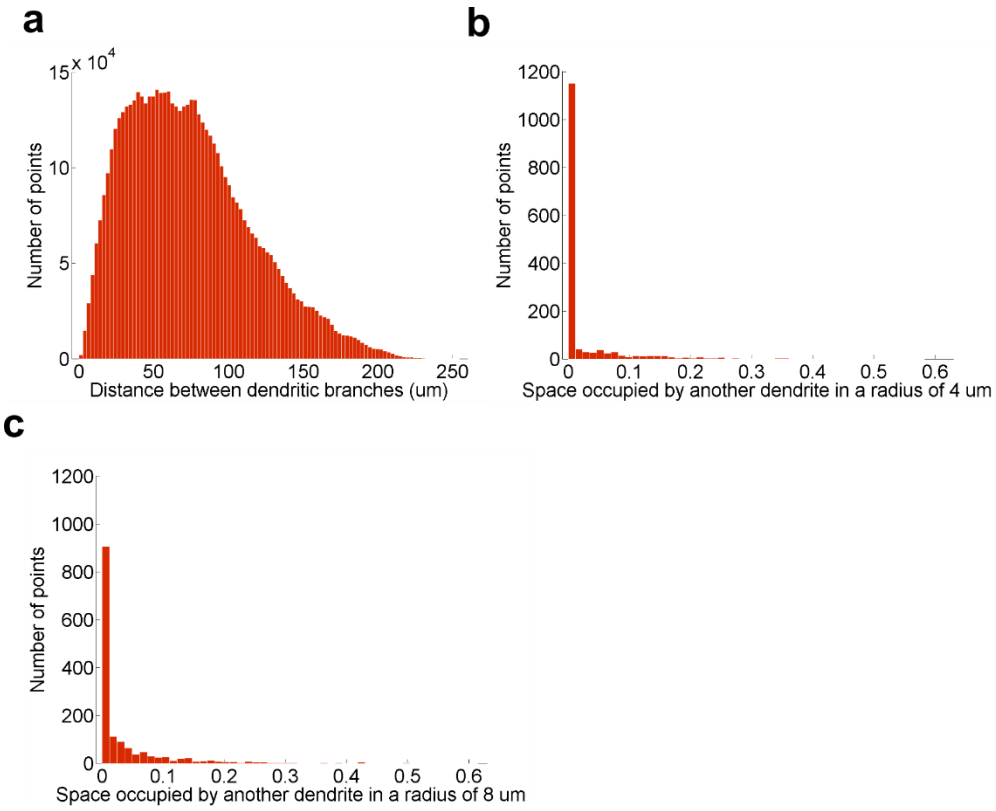

Figure 3.8 Measurements of distance between dendrites. In each imaged dendritic branch, a subset of points was chosen randomly, and the distances between each point and all the other red fluorescent structures in the image were measured. a: distribution of all distances measured for all points considered (>1200). b, c: for each point, the fraction of space occupied by another fluorescent structure in a radius of 4 μm (b) and 8 μm (c) was computed. These measurements were then used to estimate the probability that an imaged point of interest moves by chance to another biological structure, and that in that time the new biological structure fires (false positive), or the originally imaged biological structure fires (false negative).

Finally, I estimated the chance of missing an event (false negatives), or the chance of erroneously detecting an event from another dendrite (false positives), because the point of interest moved to another biological structure. If we assume that movement of the tissue is random, the fraction of space occupied by a red

fluorescent structure is equal to the fraction of time that the imaged point of interest spent on that structure. I then measured the fraction of time during which a dendrite was active, and the median across all imaged dendrites was 11.5%, with a standard deviation of 9%. The multiplication of this value (0.115) by the distributions in **figure 3.8b**, **c** gives the probability of missing an event, or mistakenly detecting an event from another dendrite. In the resulting distributions, for 95% of the points tested the probability of a false positive, or the probability of a false negative, was approximately 1.5% when considering a radius of 5 μm, and 2% when considering a radius of 8 μm. Therefore, I concluded that the probability of recording a false positive or a false negative because the imaged point of interest moved by chance to another biological structure is negligible (<2%).

3.2.6 Characterization of the cortical layer and morphology of the cells in the clear brain

With the AOL-microscope it was possible to image neurons and dendrites spanning over few hundreds micrometres, thus neurons of different cortical layers were imaged. The depth of the soma was indicative of the cortical layer of the cell, and stringent criteria were applied to determine if a cell was in layer 2/3 or in layer 5: somas above 250 μm from the pia were considered to be in layer 2/3, while neurons below 350 μm from the surface were attributed to layer 5.

However, the depth of the layer varies depending on the xy position of the cells in the cortex. In addition, during the implant of the chronic window, a part of the skull was removed and substituted with a glass coverslip, and depending on the precise position of the coverslip, a different amount of pressure can be applied to the brain and can alter the distance of the cortical layers from the surface.

For these reasons, the cortical layer of the imaged cells was confirmed *in vitro* after the experiment *in vivo*. After imaging, the brains were fixed via cardiac perfusion, cleared with the CUBIC protocol (Susaki et al., 2014), stained with Nissl to visualize the cortical layers, and imaged at a confocal microscope (**figure 3.9**). Brain fixation was carried out by Mr Diccon Coyle.

Thanks to the sparseness of the labelling, it was possible to identify in the clear brain the injection site and the cells imaged *in vivo* for 21 out of 41 cells (**figure 3.9 a, b**). Morphology of the dendritic tree, positions of the neighbouring cells and patterns of blood vessels were used to find in the clear brain the neurons imaged *in vivo*.

The CUBIC protocol made the brain transparent, so it allowed imaging of all the cortical layers in the intact brain; indeed, high-quality images were acquired even at a depth of 1.5 mm. Multiple z-stacks were acquired and stitched together, thus it was possible to image areas of 2x2 mm, which comprised the whole labelled area. In addition, blue-Nissl staining labelled all the neurons' somas, so the cortical layers were visible (**figure 3.9 c**). However, layer 5 and layer 6 were not always distinguishable.

All neurons imaged *in vivo* were found to be in layer 2/3 or in layer 5: 13 cells out of 21 were in layer 2/3, and 8 cells were in layer 5. For all cells the cortical layer identified with the Nissl staining was the same as the cortical layer attributed *in vivo*. Therefore, I concluded that the criteria used to determine the layer of a neuron *in vivo* were accurate and robust, so I included in the data also the cells imaged *in vivo* that were not identified in the clear brain.

Imaging the neurons in the clear brain was beneficial also to visualize more clearly the morphology of the neurons: more dendrites were visible in the clear brain, and thanks to a better positioning of the sample and to the larger area imaged, it was possible to distinguish the apical dendrites from the basal dendrites in layer 2/3 neurons, which was not always possible *in vivo*.

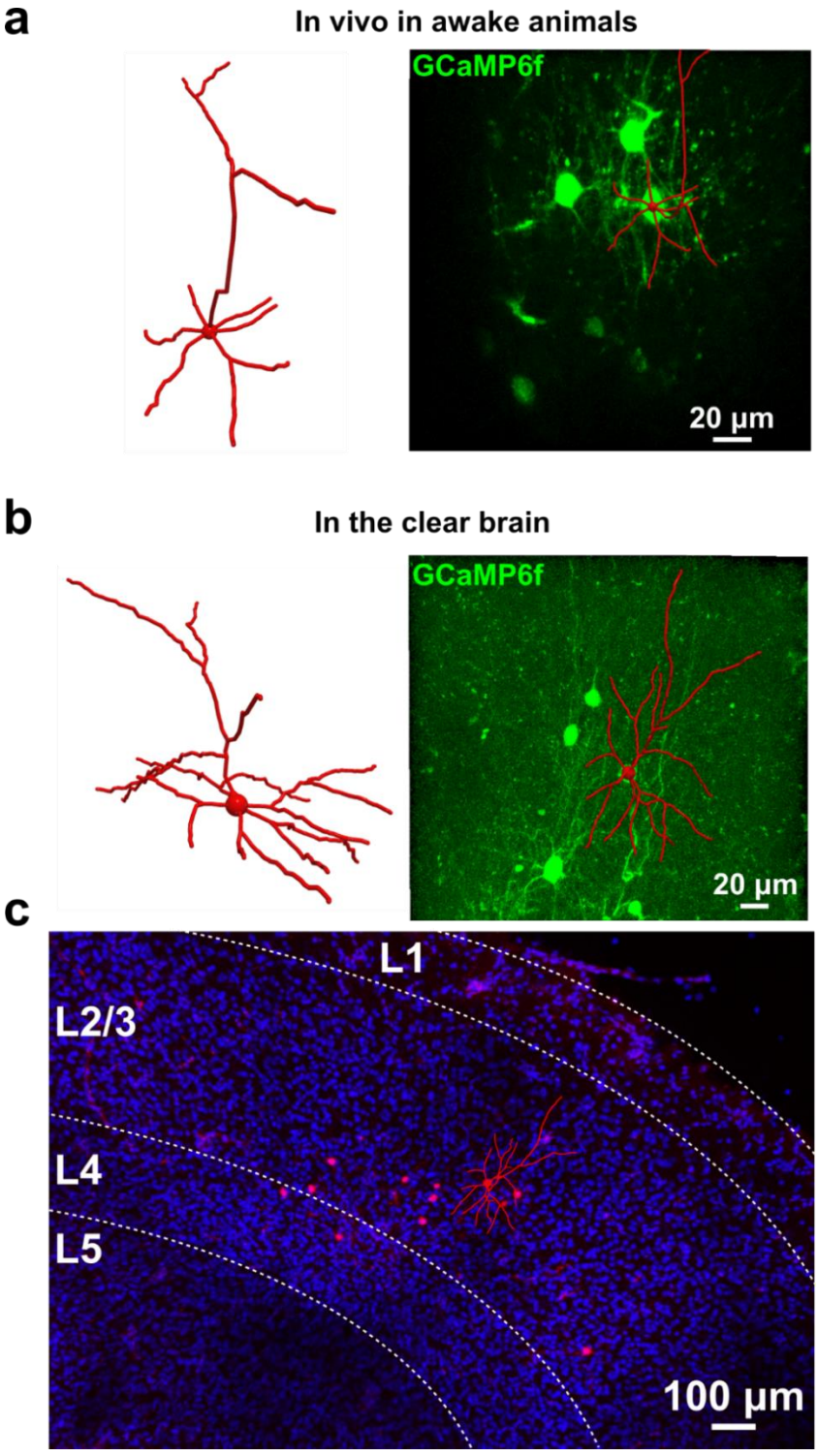

Figure 3.9 Characterization in the clear brain of the cortical layer and morphology of a cell imaged *in vivo*. a: left: reconstruction of the neuron from the images acquired *in vivo*; right: maximum intensity z-projection of the area of the imaged neuron *in vivo*. b: neuron imaged *in vivo* identified in the fixed clear brain. Right and left panels are the same as in a. c: blue-Nissl staining in the clear brain allows visualization of the somas of the neurons and identification of the cortical layers that are here marked in white. The sparse labelling with TdTomato is also shown in red. The red reconstruction of the neuron imaged *in vivo* is superimposed.

3.3 Discussion

In conclusion, in this chapter I described a protocol to label pyramidal neurons sparsely with the genetically-encoded calcium indicator GCaMP6f (Chen et al., 2013a), and with the red fluorescent protein TdTomato (Shaner et al., 2004). Combining the AOL-microscope and the calcium indicator GCaMP6f allowed fast 3D imaging of calcium transients in dendrites and somas with a good signal-to-noise ratio. It was indeed possible to image multiple dendrites simultaneously from neurons in different cortical layers, and movement of the preparation was monitored thanks to labelling with a red activity-independent fluorophore.

Fluorescence levels in the red channel were used to determine if a POI moved out of the dendrite, and in that case the data was discarded. Furthermore, subtraction of the recording in the red channel to the recording in the green channel reduced movement artefacts and flattened the baseline without affecting significantly the amplitude of the calcium transients. With this method it was possible to account for movement even when imaging 3D random-access points. However, this approach had the disadvantage that, when there was too much movement, the data was discarded and could not be recovered, while with 2D imaging, full-frame images can be registered and corrected even in case of larger tissue displacements. But image registration cannot correct for movement in the z-axis, and if neurons move in and out of focus, a movement artefact could be mistakenly considered as a response. While if a morphological tracer is used as a control, it allows to identify most artefacts due to movement and noise. Another limitation of the approach presented here is that every 1-2 minutes of recordings a new Z-stack had to be acquired and new POIs had to be placed on the dendrites, thus less data could be acquired during an experiment compared to continuous 2D imaging. Therefore, an experiment of 3.5 hours resulted in approximately 30 minutes of recordings, and long visual stimulation protocols could not be used.

After the *in vivo* experiments, brains were cleared with the CUBIC protocol (Susaki et al., 2014), and stained with Nissl to visualize the cortical layers. It is important to note that the CUBIC protocol can alter the brain structure and it can cause swelling: therefore, in the clear brain, we used only the Nissl staining to determine the cortical layer of the cells, and not the distance of the soma from the surface.

4. Characterization of patterns of activity in the dendritic tree

4.1 Introduction

A wealth of studies investigated dendritic properties *in vitro*, in cell cultures and in brain slices, and it was found that dendrites of pyramidal neurons can support different types of regenerative events. For example, calcium events can be found predominantly in the apical trunk of layer 5 pyramidal cells (Larkum et al., 1999a), while basal dendrites and thin apical dendrites generate mainly NMDA spikes (Larkum et al., 2009). Back-propagating action potentials reach most dendrites in layer 2/3 cells (Stuart and Sakmann, 1994), whereas they fail to invade the apical tuft of layer 5 neurons if the firing rate is not high enough (Larkum et al., 1999b; Stuart et al., 1997a; Waters et al., 2003).

However, it is not clear if these events are present also in intact animals, and patterns of dendritic activity *in vivo* have just begun to be investigated. One of the first studies that probed dendritic activity *in vivo* imaged tuft dendrites of layer 5 neurons in somatosensory cortex, and they observed only global calcium transients, produced by tuft plateau potentials, during sensory stimulation (Xu et al., 2012). However, two other studies on layer 2/3 pyramidal neurons in somatosensory cortex (Palmer et al., 2014) and on CA1 pyramidal neurons (Grienberger et al., 2014) observed mainly multi-branch calcium transients, and also calcium transients restricted to only one branch.

A thorough characterization of patterns of dendritic activity in pyramidal neurons *in vivo* is indeed missing, partly because only few dendrites were probed at the time. In addition, most studies were carried out in anaesthetized animals, but it is now known that anaesthetics can affect heavily neuronal activity (Haider et al., 2013; Keller et al., 2012; Murayama and Larkum, 2009; Pisauro et al., 2013; Potez and Larkum, 2008; Vaiceliunaite et al., 2013). If we are to understand the input/output relationship of a neuron it is important to measure its activity in the full dendritic tree and in physiological conditions. Therefore, I used the AOL microscope to image neurons in three dimensions, and I could record near-simultaneously from the majority of dendrites and soma of a cell in awake animals. I then investigated and compared the patterns of dendritic activity in layer 5 and in layer 2/3 pyramidal neurons in V1.

4.2 Results

4.2.1 Patterns of dendritic activity in layer 5 pyramidal neurons

I first investigated patterns of dendritic activity in the apical dendrites of layer 5 pyramidal neurons. These experiments were technically easier because neuronal activity was less sparse in layer 5 than in layer 2/3 neurons, and the apical dendrites of layer 5 cells were still easily accessible because they were located in superficial cortical layers. As mentioned above, pyramidal neurons in mouse V1 were sparsely labelled with GCaMP6f and TdTomato. Virus injection and the implant of a headplate and a cranial window were performed on adult mice of both sexes, and after 4-5 weeks of expression the animals were gradually familiarised with the setup. During an experiment, animals were free to stand or run on a wheel. First, a region with only few cells was identified, then a z-stack covering approximately 150-200 µm in layer 1 and 2/3 was acquired. Then, POIs distributed in three dimensions were selected manually on the dendrites in the z-stack, and the microscope imaged only the selected points at high speeds. Typically, 300 – 700 POIs were imaged at 50 – 120 Hz, and almost all tuft dendrites and the main apical dendrite of the same layer 5 cell could be imaged near-simultaneously (**figure 4.1**). After the experiment, dendritic trees were traced and reconstructed with the software Vaa3d (Peng et al., 2014) or neuTube (Feng et al., 2015), POIs were assigned to a dendrite, and recordings from POIs in the same dendritic branch were averaged.

A representative example of the data collected is shown in **figure 4.1**. An image of the dendrites of the neuron and the reconstruction of the dendritic tree are shown in **figure 4.1 a. Figure 4.1 b** shows calcium activity in different dendritic branches. Interestingly, some calcium events were present in all the dendritic branches simultaneously (highlighted with a grey background), while other calcium transients were restricted to only one dendritic branch (for example branch number 2). Recordings in the red channel are also displayed, and they show no variations in the levels of fluorescence, suggesting that no movement artefacts were present in these recordings. These data suggest that different types of calcium events are present in the apical tuft of layer 5 pyramidal neurons: global calcium transients, which occur simultaneously in the vast majority of the dendritic branches imaged, and local calcium transients, which are restricted to only one or two dendritic branches.

Indeed, when I measured how many dendritic branches were active during each calcium transient observed in this cell, the distribution was dominated by events that occurred in 10-20% of the imaged branches (local events), or in 100% of the imaged branches (global events) (**figure 4.2 a**). Note that these percentages were calculated

from the number of dendritic branches active out of the total number of dendritic branches imaged, and it is possible that few dendritic branches were not imaged because they were out of the field of view, or not clearly visible. The same measurements were carried out on multiple cells during presentation of full-field gratings (**figure 4.2 c**), or while the animal was in the dark (**figure 4.2 e**), and this bimodal spatial distribution of the calcium events was observed in both cases. Both these distributions were significantly different from a uniform distribution (one-sample Kolmogorov-Smirnov test, p-values < 0.0001). In addition, I investigated whether calcium transients with greater amplitudes were more likely to occur simultaneously in multiple dendritic branches, but no clear relation between amplitude and spatial distribution of the event was found (**figure 4.2 b**, **d**, and **f).**

The patterns of spontaneous dendritic activity and the patterns of sensory-evoked dendritic activity were compared, but no significant difference was found (two-sample Kolmogorov-Smirnov test, p-value = 0.13), but both distributions were significantly different from a standard normal distribution (one-sample Kolmogorov-Smirnov test, p-values < 0.0001). Similarly, patterns of dendritic activity did not change significantly when the animal was running and when the animal was stationary (two-sample Kolmogorov-Smirnov test, p-value = 0.079, data not shown).

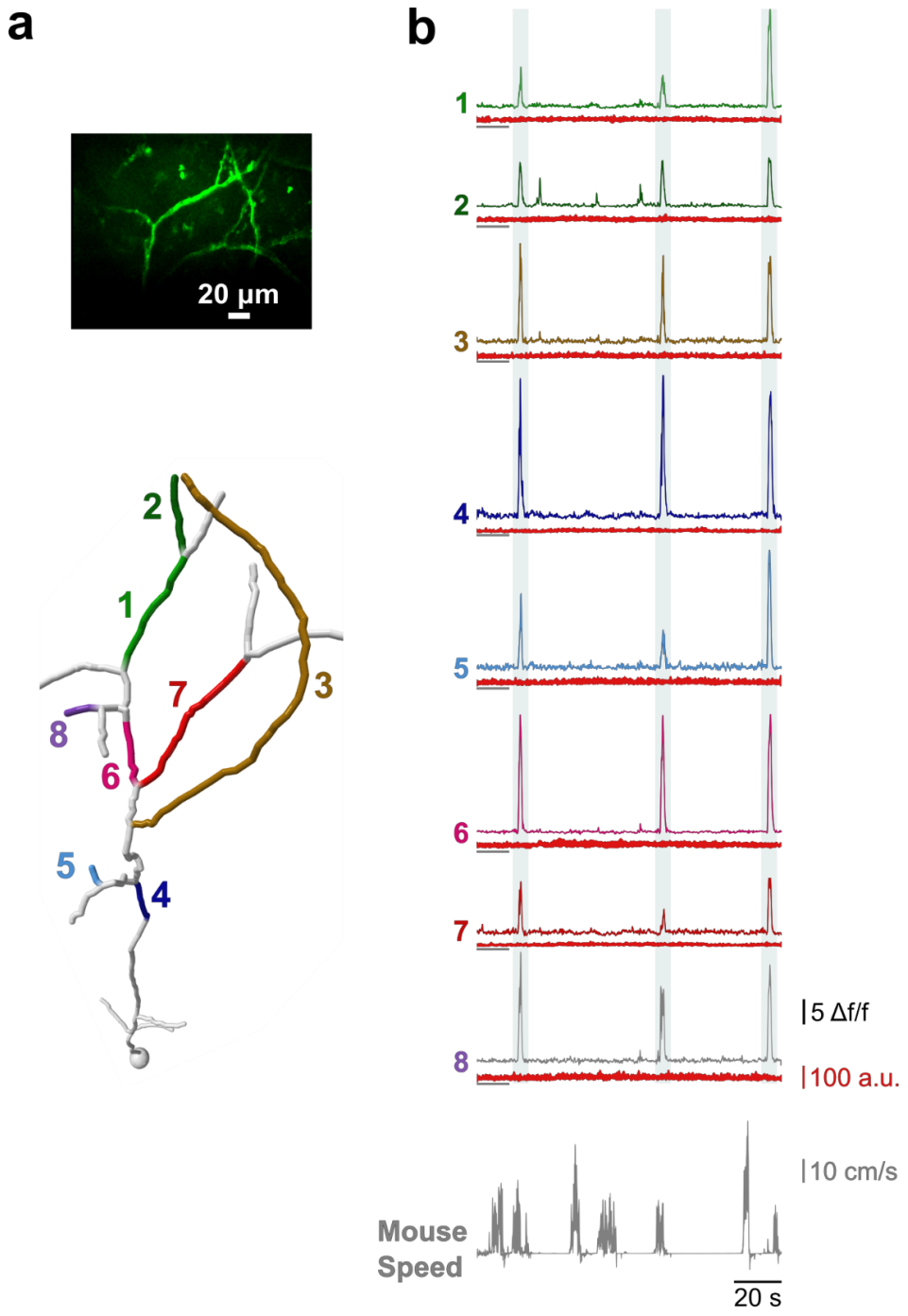

Figure 4.1 Recordings in apical dendrites of a layer 5 neuron in V1 *in vivo*. a: top panel: maximum intensity z-projection in the green channel of few dendrites imaged *in vivo*. Pyramidal neurons were labelled with GCaMP6f and TdTomato. Bottom panel: after the experiment, the cell was traced and reconstructed with the software neuTube (Feng et al., 2015). Different dendrites are assigned a number and a colour, and their respective recordings are shown in b in the same colour. b: recordings in the green channel and in the red channel (plotted in red) are shown for different dendritic branches. The grey horizontal bar shows the zero value for the recording in the red channel. The light grey background highlights the global

calcium transients. The mouse running speed on the cylindrical treadmill is plotted in grey at the bottom.

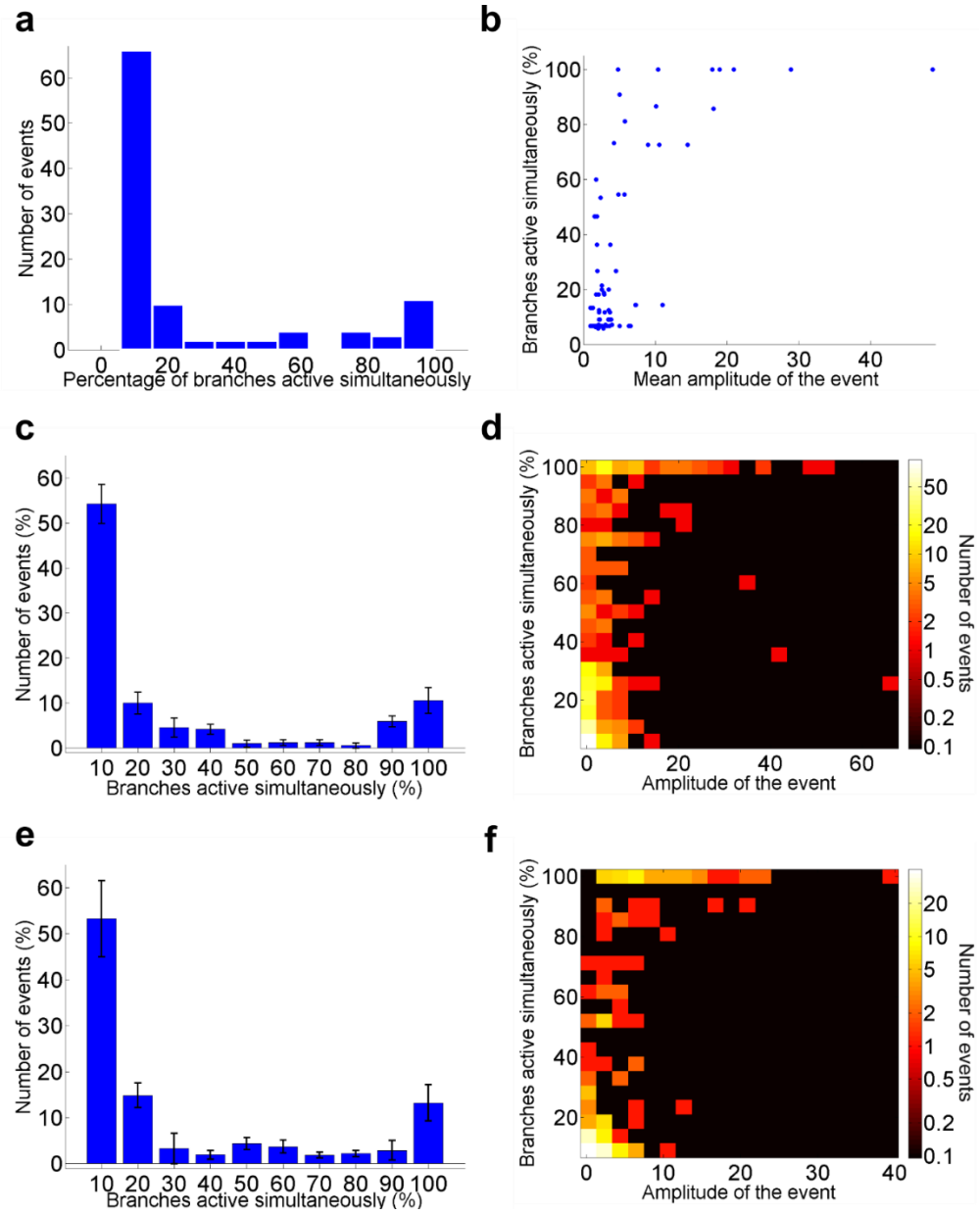

Figure 4.2 Patterns of dendritic activity in layer 5 neurons. a: spatial distribution (number of branches active simultaneously) of the dendritic calcium transients. Both local and global events were observed. b: there is no correlation between the amplitude of a dendritic event (averaged across the dendrites active) and the spatial distribution of the event (number of dendritic branches active). a, b: results for the cell shown in figure 4.1. c, d: same as in a and b, but the analysis was extended to the apical dendrites of 8 layer 5 neurons, and dendritic activity in response to gratings with different orientations was analysed. e, f: same as in a and b, but the animal was in the dark. Dendritic activity from apical dendrites of 5 layer 5 cells was

analysed. Error bars represent standard error of the mean. This analysis was carried out considering both stationary and running periods.

4.2.2 Dendritic activity in layer 5 pyramidal neurons: separating calcium events associated with a somatic calcium transient

To characterize further dendritic activity in layer 5 neurons, I repeated these experiments imaging near-simultaneously (at 100 - 270 Hz) the soma and several (approximately 5-10) tuft dendrites (**figure 4.3**). The second generation of acousto-optic lens microscope (presented in chapter 7) had a different laser with higher power and the crystals in the AOL had higher transmission efficiency, so it was possible to image even 450 - 490 µm deep. Somas and apical trunks of layer 5 neurons could then be visualized and imaged, but the thinner basal or oblique dendrites were not visible (**figure 4.3 a**). In the analysis of these datasets, the main apical dendrite was divided into two compartments of the same size: proximal apical dendrite and distal apical dendrite. These experiments were performed only while the animal was in the dark.

Surprisingly, calcium activity in the soma and in the tuft dendrites was highly correlated, and somatic calcium transients were usually accompanied by calcium transients in one or more distal dendrites (**figure 4.3 b, c**).

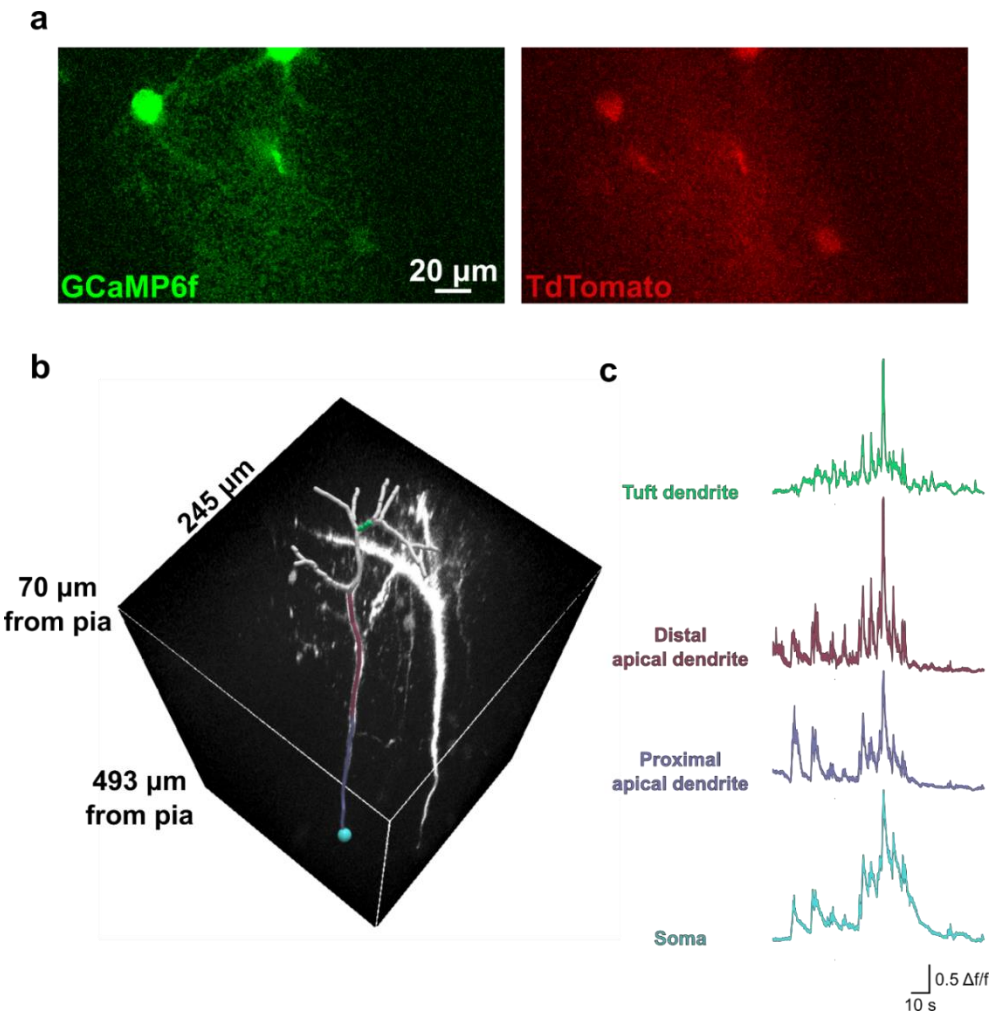

Figure 4.3 Imaging layer 5 apical dendrites and soma near-simultaneously. a: Maximum intensity z-projection of 12 planes between 487 and 493 µm from pia. Pyramidal neurons were labelled with GCaMP6f and TdTomato, and the two panels show the images obtained in the green and in the red channel. b: 3D rendering and reconstruction of layer 5 neurons performed with the software neuTube (Feng et al., 2015). Soma, proximal apical dendrite, distal apical dendrite and one tuft dendrite are shown in the same colour as their respective calcium traces in c.

The calcium transients observed in the dendrites were then divided into two categories: “dendritic events” and “events associated with a somatic transient”, depending on whether the calcium transients in the dendrites occurred simultaneously with a somatic calcium transient (**figure 4.4**). Events associated with somatic calcium transient could be due to backpropagating action potentials, or dendritic non-linear events that triggered somatic activation. Whereas dendritic events that occurred only in the dendrites could be dendritic regenerative events, or subthreshold EPSPs.

Dendritic events were usually restricted to 10-20% of the imaged branches, and they make up the main component of the local events observed in the previous section (**figure 4.4 a**). Interestingly, dendritic events could occur simultaneously in up to 70% of the imaged branches without triggering a detectable somatic calcium transient. On the other side, most somatic events occurred simultaneously with calcium transients in several distal apical dendrites (**figure 4.4 b**). In addition, all events that occurred in the majority of the dendritic tree, i.e. global events, were accompanied by a somatic calcium transient, but not all somatic calcium transients were accompanied by a global event in the tuft. Indeed, in 29.7% of the cases dendritic events associated with somatic transient occurred in half or less of the imaged branches.

When investigating the relation between the amplitude of the event and the number of branches active simultaneously, no clear correlation was visible for dendritic events (**figure 4.4 d**), whereas for events associated with a somatic transient, high amplitudes of the somatic calcium transient corresponded to more branches active simultaneously (**figure 4.4 e**). This behaviour suggests that somatic calcium transients are more efficient at backpropagating in the tuft dendrites when the soma fires at higher frequencies, and/or that dendritic events occurring in multiple branches are more efficient in triggering somatic events.

Finally, I investigated if dendritic branches closer to the soma had higher chances of being active with the soma (**figure 4.4 f**). Analogously, I investigated whether there was a relation between the number of dendritic events in a branch and the distance of the branch from the soma (**figure 4.4 g**). In both cases, only a weak correlation was observed (Pearson's coefficients of -0.5 for events associated with somatic calcium transient, and of 0.5 for dendritic events). Note that in these graphs there are fewer points close to the soma than far from the soma, because close to the soma it was possible to record only from the main apical dendrite, while further from the soma several tuft dendrites were imaged.

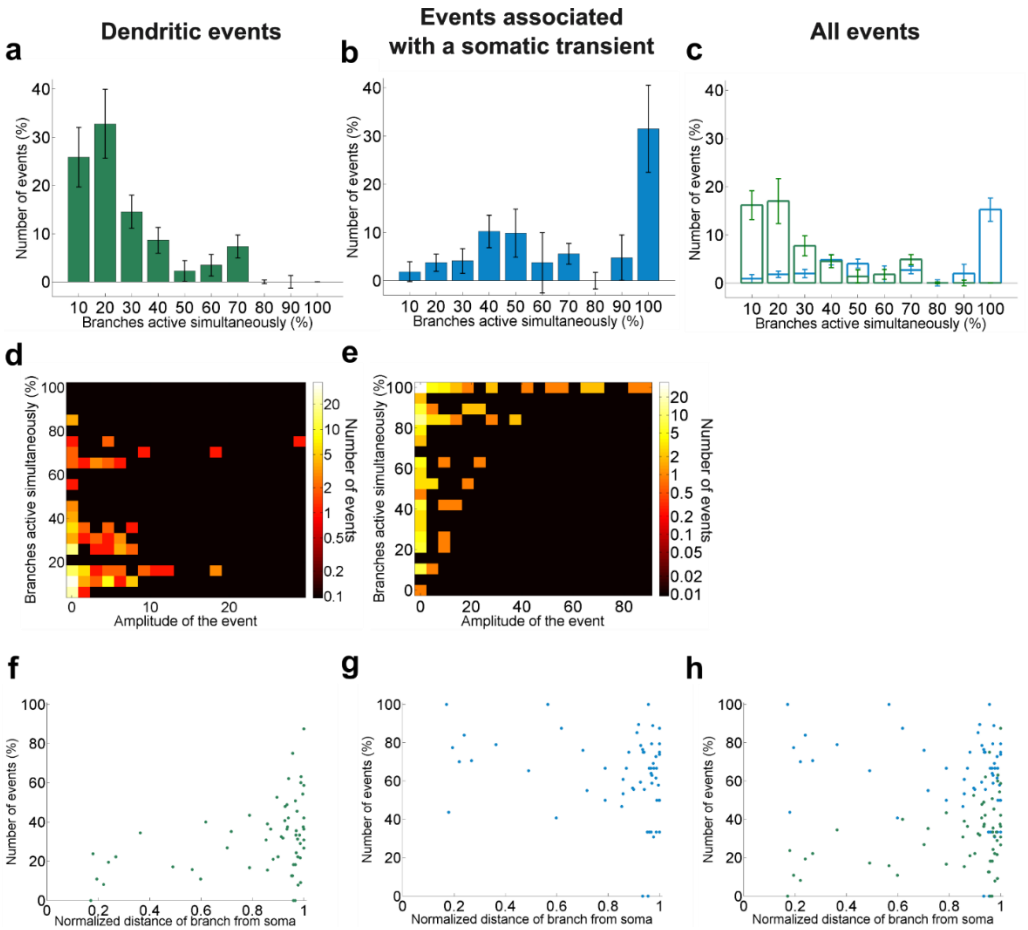

Figure 4.4 Patterns of dendritic activity in layer 5 neurons obtained separating dendritic events associated with somatic calcium transients. Dendritic calcium transients were divided into two categories: dendritic events (a, d, f), and events associated with a somatic transient (b, e, g). a, b, c spatial distribution of dendritic events: not associated with a somatic event, associated with a somatic event, and all dendritic events, respectively. Dendritic events are shown in green, while events associated with a somatic calcium transient are shown in blue. Error bars represent the standard error of the mean, and the sample size was 5 cells from 3 animals. d: density plot of the amplitude of a dendritic event versus the number of branches active simultaneously during the event. The amplitude of the event was obtained averaging the amplitudes of the events in all the branches active. e: as in d, but considering dendritic events associated with a somatic calcium transient, and plotted versus the amplitude of the somatic calcium transients. f, g: for each dendritic branch, the distance of a branch from the soma was plotted against the number of dendritic events and against the number of events associated with somatic calcium transient, respectively. The distance of a branch from the soma was normalized by the maximum and minimum distance of all branches from the soma, because the number of events was also normalized by the total number of calcium events recorded for each cell. h: graph in f and g combined. In f, g and h, dendritic events are plotted in green, while events associated with a somatic calcium transient are plotted in blue.

4.2.3 Patterns of dendritic activity in layer 2/3 pyramidal neurons

Patterns of dendritic activity were characterized also in layer 2/3 pyramidal neurons in V1 in awake animals. Experiments were performed with the first generation AOL microscope, and for each neuron multiple dendrites (up to 20) and the soma were imaged with random-access points measurements at 50-90 Hz. As for the experiments performed on layer 5 neurons, layer 2/3 neurons were reconstructed after the experiments, and recordings from POIs in the same dendritic branch were averaged. **Figure 4.5** shows the data for a representative cell. **Figure 4.5 a** shows the maximum intensity Z-projection of the region imaged, and the neuron reconstructed after the experiment. In **Figure 4.5 b** the recordings in the green and in the red channel from different dendritic branches are shown. Multiple calcium transients were present in most dendritic branches and in the soma, while the levels of fluorescence in the red channel were stable, suggesting that little or no movement of the tissue was present in these recordings. Indeed, the animal was not running in this experiment (grey trace at the bottom in **figure 4.5 b**).

Surprisingly, calcium activity in the dendrites seemed less correlated in layer 2/3 neurons than in layer 5 neurons. In particular, somatic calcium events (in grey background in **figure 4.5 b**) were not always accompanied by a global dendritic calcium transient, because not all dendritic branches were active at the same time as the soma. This data could then suggest failure of backpropagating action potentials even in proximal dendritic branches of layer 2/3 neurons. Alternatively, some dendritic branches might be less excitable (Makara and Magee, 2013) or might lack calcium channels. For example branch 1 in the figure does not show any calcium transients. However, branch 4 in the figure shows high-amplitude calcium transients but no activity correlated with the soma. Branches 5, 7 and 8 show some calcium transients that occur at the same time as somatic events, but there are also other somatic events that do not correlate with activity in these dendritic branches. This data suggests that some dendritic branches in layer 2/3 neurons are capable of generating high amplitude calcium transients, but they do not always exhibit calcium activity correlated to somatic events.

To investigate whether some dendrites do not support calcium transients, I analysed calcium activity in all dendrites in all the cells imaged (n=12). For each dendritic branch, I computed the percentage of somatic calcium transients that occurred simultaneously also in the dendrite, and then I plotted the results for all dendrites (**figure 4.6).** In addition, to control for bleaching and phototoxicity, I divided each day of experiment in two parts, and I compared the activity of the dendrites in the first half (approximately 15 minutes of recording) (blue in **figure 4.6**) and in the second

half of the experiment (purple in **figure 4.6**). Interestingly, in both datasets all dendrites show at least a few calcium transients. These results suggest that GCaMP6f is expressed in all the dendrites, and that all dendrites can generate detectable calcium events. Also, the recordings in the second half of the experiments do not show lower dendritic activity than the data acquired in the first half, indicating that bleaching and phototoxicity are not affecting the data. Indeed, the two distribution are only slightly different (two-sample Kolmogorov-Smirnov test, p-value = 0.029), but in the recordings in the second half of the experiments the mean activity is higher (57% compared to 63% of somatic calcium transients present in the dendrites).

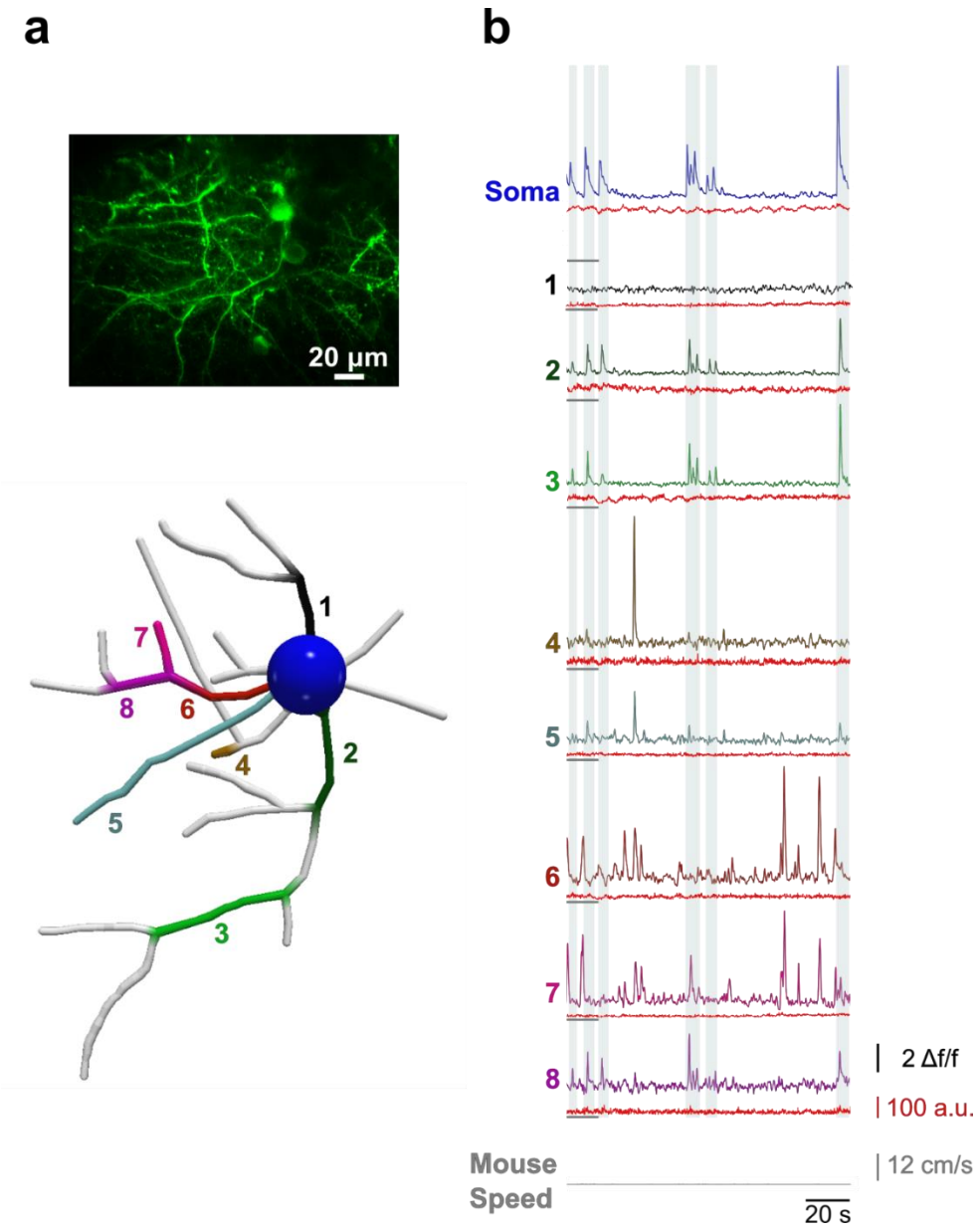

Figure 4.5 Recordings in dendrites and soma of a layer 2/3 neuron in V1 *in vivo*. a: top panel: maximum intensity z-projection in the green channel of the cell imaged *in vivo*. Bottom panel: cell traced and reconstructed after the experiment with the software neuTube (Feng et al., 2015). Different dendrites are assigned a number and a colour, and their respective recordings are shown in the same colour in b. b: recordings in the green channel and in the red channel (plotted in red) are shown for different dendritic branches. The grey horizontal bar shows the zero value for the recording in the red channel. The light grey background highlights the time when somatic calcium transients occurred. The mouse running speed on the cylindrical treadmill is plotted in grey at the bottom.

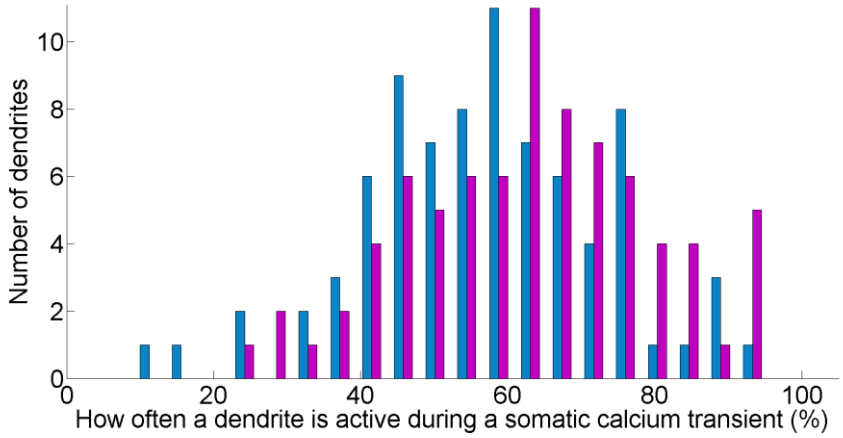

Figure 4.6 Dendritic activity in all imaged dendritic branches, in the first half (blue) and in the second half (purple) of each day of experiment. For each dendrite, it was computed the number of dendritic transients that occurred simultaneously with a somatic calcium transients, out of all the somatic calcium transients. The result, in percentage, for each dendrite was plotted to obtain the distribution above.

The spatial distribution of dendritic calcium transients was then measured (**figure 4.7 a**), and local calcium events were found to be dominant. Similarly to the analysis done for layer 5 neurons, I also investigated whether calcium transients with great amplitudes were more likely to occur simultaneously in multiple dendritic branches, but no correlation between amplitude and spatial distribution of the event was found (**figure 4.7 b)**. This analysis was extended to multiple cells, and both responses to full-field gratings of different orientations (**figure 4.7 c, d**) and spontaneous activity (**figure 4.7 e, f**) were analysed. The spatial distributions of dendritic events for the two conditions (**figure 4.7 c, e**) were significantly different from a uniform distribution (one-sample Kolmogorov-Smirnov test, p-values < 0.0001), and from the distribution of calcium events observed in dendrites of layer 5 neurons (two-sample Kolmogorov-Smirnov test, p-values < 0.0001). Similar patterns of activity were observed on both cases. Analogously, only slight differences in the patterns of activity were found between periods when the animal was running and periods when the animal was stationary (data not shown, two-sample Kolmogorov-Smirnov test, p-value = 0.023). This data suggest that the probability of multi-branch events is lower in layer 2/3 than in layer 5 neurons, and it is consistent with sparser synaptic activation.

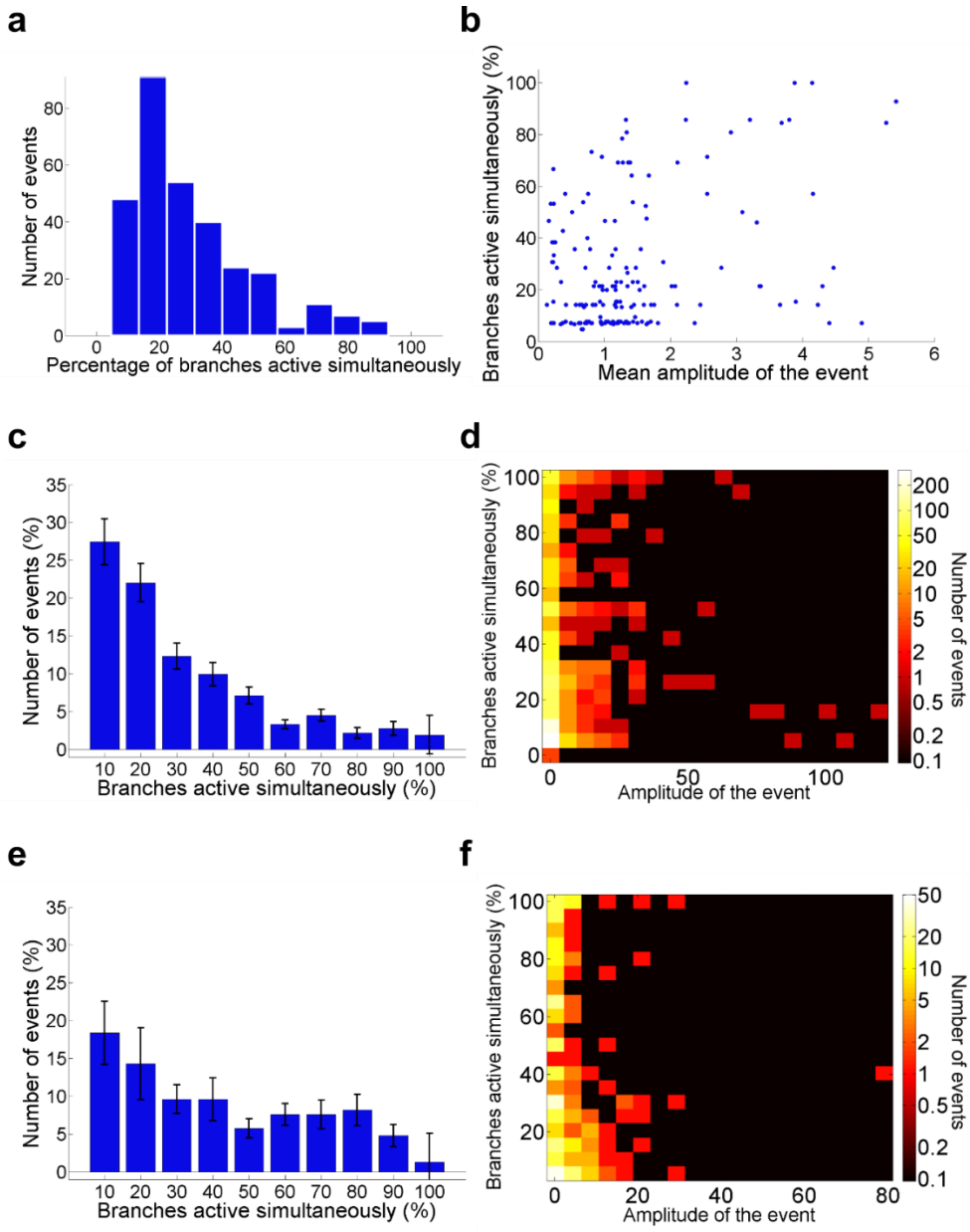

Figure 4.7 Patterns of dendritic activity in layer 2/3 neurons. a: spatial distribution (number of branches active simultaneously) of the dendritic calcium transients. Mainly local events, restricted to 1-4 dendritic branches, were observed. b: there is no correlation between the amplitude of a dendritic event (averaged across the dendrites active) and the spatial distribution of the event (number of dendritic branches active). a, b: results for the cell shown in figure 4.1. c, d: same as in a and b, but the analysis was extended to 12 layer 2/3 neurons, and dendritic activity in response to gratings with different orientations was analysed. e, f: same as in c and d, but the animal was in the dark. Dendritic activity from 7 cells layer 2/3 cells was analysed. Error bars represent standard error of the mean. This analysis was carried out considering both stationary and running periods.

4.2.4 Dendritic activity in layer 2/3 pyramidal neurons: separating calcium events associated with a somatic calcium transient

As for the analysis carried out for layer 5 neurons, I grouped dendritic calcium transients in layer 2/3 neurons into two categories: dendritic events and events associated with a somatic calcium transient. The spatial distributions of these dendritic events, and their relation with the amplitude of the event and with the distance of each branch from the soma are shown in **figure 4.8**. The results of this analysis were similar to the data obtained for layer 5 neurons, but surprisingly layer 2/3 neurons had few global events, suggesting that somatic calcium transients most of the times failed to backpropagate in all the dendrites (**figure 4.8 b**). Interestingly, it appeared that dendritic events tend to have higher amplitudes when they occurred in few branches (**figure 4.8 d**), while the opposite behaviour was visible for the events associated with a somatic calcium transient (**figure 4.8 e**). This data might suggest that when dendritic calcium transients have high amplitudes and occur in many branches simultaneously, they trigger a somatic calcium transient, thus falling in the second category and not appearing in **figure 4.8 d**. On the other side, the data in **figure 4.8 e** could suggest that somatic calcium transients with higher amplitude backpropagate more efficiently in the dendritic branches. The number of events associated with a somatic calcium transients did not depend on the distance of the dendritic branch from the soma (**figure 4.8 g**, Pearson's coefficient = -0.3).

The same analysis was carried out for dendritic activity during presentation of full-field gratings of different orientations (**figure 4.8**) and while the animal was in the dark (**figure 4.9**), and the results were similar. Furthermore, since in layer 5 neurons more global events were observed when recording only from apical dendrites, the spatial distribution of the dendritic calcium transients was analysed only for apical dendrites also in layer 2/3 cells (**figure 4.10**). The apical dendrites of layer 2/3 neurons behaved in a similar way as when all dendrites in layer 2/3 were considered (**figure 4.8**). Unfortunately, the error bars are higher when considering only apical dendrites, because the activity of fewer dendritic branches was analysed, and, in addition, it was not possible to identify clearly apical dendrites in all cells, so two neurons were excluded. In any case, in contrast with apical dendrites in layer 5 neurons (**figure 4.2 c**), apical dendrites of layer 2/3 neurons have few global events (**figure 4.10 c**), thus this difference seems to be due to the different cell type.

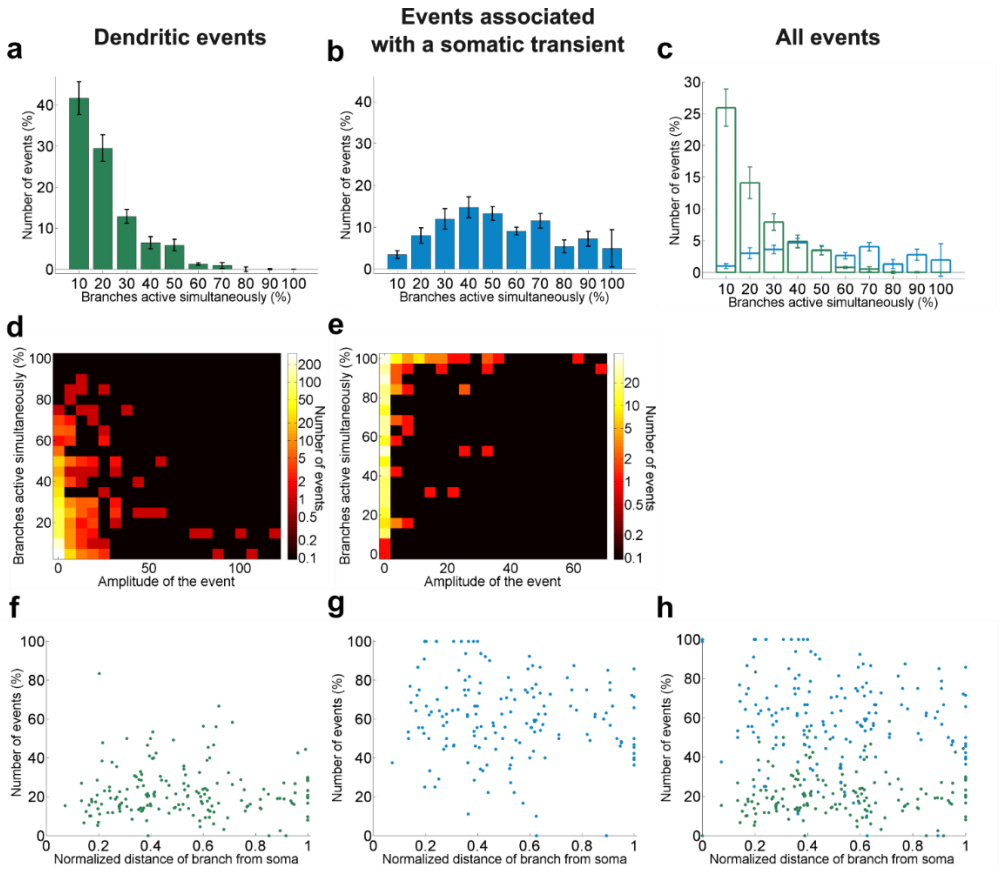

Figure 4.8 Patterns of dendritic activity during gratings presentation in layer 2/3 neurons obtained separating dendritic events associated with somatic calcium transients. a, b, c spatial distribution of dendritic events: not associated with a somatic event, associated with a somatic event, and all dendritic events, respectively. Error bars represent the standard error of the mean, and the sample size was 12 cells from 7 animals. d, e: density plot of the amplitude of a calcium event versus the number of branches active simultaneously during the event, for dendritic events and for events associated with a somatic transient, respectively. f, g: for each dendritic branch, the distance of a branch from the soma was plotted against the number of dendritic events and against the number of events associated with a somatic transient, respectively. h: graph in f and g combined. In f, g and h, dendritic events are plotted in green, while events associated with a somatic transient are plotted in blue.

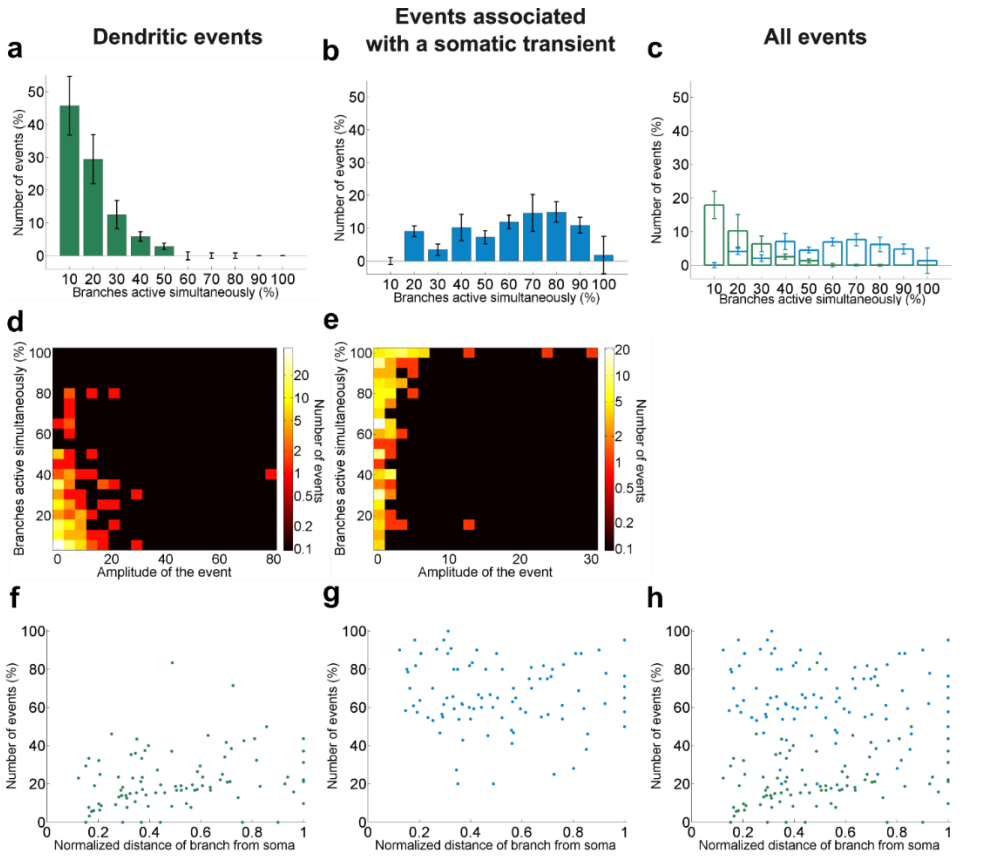

Figure 4.9 Patterns of dendritic activity during darkness in layer 2/3 neurons obtained separating dendritic events associated with somatic calcium transients. Same as figure 4.8, but neuronal activity here was recorded while the animal was in the dark, instead of during presentation of full-field gratings. The sample size for this dataset consisted of 7 neurons from 4 mice.

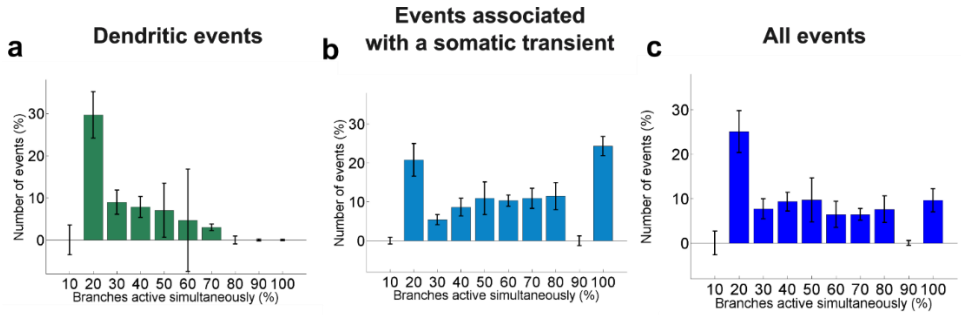

Figure 4.10 Patterns of dendritic activity during gratings presentation in apical dendrites of layer 2/3 neurons. Same as figure 4.8, but only apical dendrites were considered. The sample size in this dataset consisted of 10 cells from 7 mice.

4.3 Discussion

4.3.1 Conclusions

The results presented in this chapter show that I could image near-simultaneously from the majority of dendrites and the soma in layer 2/3 and in the tuft of layer 5 pyramidal neurons in primary visual cortex of awake animals. Apical dendrites in layer 5 neurons show mainly global and local calcium events, and global events are always associated with a somatic calcium transient. Interestingly, somatic calcium transients are almost always (>98% of the times) accompanied by calcium transients in several tuft branches, suggesting that calcium activity in the tuft and in the soma of layer 5 neurons is more coupled than previously thought. On the other side, layer 2/3 dendrites are dominated by local calcium events, and, surprisingly, most somatic calcium transients are not associated with global dendritic events.

4.3.2 Potential origin of local events

In the experiments reported, the local dendritic calcium transients that did not occur simultaneously with a somatic calcium transient could be generated by subthreshold EPSPs and/or by non-linear dendritic events. Subthreshold EPSPs have smaller amplitudes than regenerative events (Major et al., 2008), but the amplitudes of the calcium transients depend also on the calcium indicator and on the microscope used. Furthermore, a calibration of GCaMP6f signals with electrophysiological recordings in dendrites is missing, and GCaMP6f signals can be highly non-linear. It is therefore difficult to determine the nature of the calcium transients observed in the dendrites *in vivo*.

From these data it was also not possible to determine which ion channels are mediating the calcium transients. The calcium entry in the dendrites could be mediated by voltage-gated calcium channels, and/or by NMDA receptors. Voltage-gated calcium channels are driven by voltage, while NMDA receptors are driven by voltage and by glutamate binding. NMDA receptor – mediated events might then be more often restricted to one dendritic branch, because depolarization alone is not enough to open NMDA receptors on a neighbouring branch. It is then possible that the local calcium events were mediated by NMDA receptors, but in order to test this hypothesis it would be necessary to apply NMDA receptor antagonists during the experiments.

4.3.3 Potential origin of global events

Global dendritic events were usually associated with a somatic calcium transient, both in layer 2/3 and in layer 5 neurons. Therefore, these dendritic calcium transients could be due to calcium entry triggered by backpropagating action potentials, and/or global dendritic events triggered somatic calcium transients.

To investigate the nature of the global events, I tried to determine if a calcium transient was generated first in the soma or first in the dendrites. Indeed, two studies in acute brain slices showed that it was possible to "follow" the back propagation of an action potential with an acousto-optic lens microscope (Fernández-Alfonso et al., 2014; Katona et al., 2012). Given that the speed of a backpropagating action potential is between 0.15-0.23 m/s (Fernández-Alfonso et al., 2014; Katona et al., 2012; Stuart and Sakmann, 1994), and that in layer 5 neurons the tuft dendrites are 350-400 µm apart from the soma, a backpropagating action potential would reach the tuft dendrites approximately 1.5 – 2.7 ms after being generated in the soma. Then, in a subset of experiments on layer 5 neurons, only 10 points of interest were placed on tuft dendrites and on the soma, thus it was possible to image at 3.5 KHz. I estimated the onset of the calcium transients using different methods (fitting the calcium transients with a double exponential, and identifying the first time point that was 3 standard deviations above the noise). Unfortunately, precise estimates were difficult because the rise time of GCaMP6f is slow (45-50 ms for a single action potential in the soma, Chen et al., 2013b), and recordings *in vivo* can be noisy. In these data, differences in the onset of a calcium transient in the soma and in the dendrites varied between 10 -15 ms, an order of magnitude higher than the expected difference. Therefore, I concluded that these measurements were not accurate, and that a faster calcium indicator and a better signal to noise ratio are needed to obtain this data *in vivo*.

Back propagation of action potentials has been studied in the lab by Dr Thomas Younts and, surprisingly, he observed that in acute brain slices even single action potentials reached the tuft dendrites of layer 5 neurons (unpublished data). These data are in contrast with previous studies, where it was observed that backpropagating action potentials reach distal dendrites of layer 5 neurons only when the cell fires above a critical frequency (Larkum et al., 1999b). The reason of this discrepancy could be that in our lab the experiments were performed in V1, while published studies focussed on somatosensory cortex, but this hypothesis is still under investigation.

In conclusion, at the moment it is not possible to distinguish back propagating action potentials from dendritic events that triggered a somatic transient *in vivo*. In any case, the data presented here suggest that layer 5 tuft dendrites are more coupled to the soma than previously thought, whereas in layer 2/3 neurons calcium activity in the dendrites and in the soma is less correlated than expected.

4.3.4 Possible mechanisms for failure of action potential backpropagation in layer 2/3 neurons

It is known that backpropagating action potentials can fail to reach distal dendrites, especially in layer 5 neurons, but in the data presented here calcium activity even in proximal dendrites often did not correlate with somatic activity in layer 2/3 neurons. This data might suggest that back propagating action potentials can fail to invade all the dendritic tree *in vivo*. Interestingly, in some cases, different somatic calcium transients just a few seconds apart were absent and then present in a dendritic branch (**figure 4.5**). Furthermore, some calcium events were observed in all imaged branches (**figure 4.6**), suggesting that all the dendrites imaged had calcium channels and were capable of generating detectable calcium transients. The number of dendritic branches active with somatic calcium transients depended on the amplitude of the somatic calcium transient (**figure 4.8 e**), but it did not depend on the distance of the branch from the soma (**figure 4.8 g**). Indeed, the branches imaged in layer 2/3 neurons were on average close to the soma (10 – 120 µm), and therefore back propagating action potentials should not be significantly attenuated by the filtering properties of the dendrites.

It is known that in hippocampus different dendrites can have different intrinsic excitability (Makara and Magee, 2013), but this is unlikely to be the only cause for the phenomenon observed here, because no dendritic branch was found to be consistently less active than others. Inhibitory inputs can reduce the size of back propagating action potentials (Müllner et al., 2015), but it is currently not known if inhibition is capable of blocking completely a back propagating action potential. But it is maybe possible that a combination of inhibition, which is very high in awake animals (Haider et al., 2013), and different levels of excitability in different dendrites can cause failures of back propagating action potentials in a branch-specific manner. Finally, if calcium entry triggered by backpropagating action potentials was mediated primarily by NMDA receptors, it is possible that calcium transients are generated only in those branches where NMDA receptors are bound to glutamate. In this case,

the activation of the dendritic tree due to backpropagating action potentials could be “patchy”, because it would depend on the local supply of glutamate.

It would be very interesting to test these hypothesis with experimental and modelling studies, because this phenomenon could have important consequences for induction of synaptic plasticity in dendrites.

5. Responses to visual stimuli across the dendritic tree

5.1 Introduction

Responses of a neuron to sensory stimuli have been extensively studied in mice, but it is still not clear how these responses are generated in the cell and how dendrites respond to sensory stimuli. A few years ago, a pioneering work from Konnerth lab mapped sensory inputs onto the dendritic tree of layer 2/3 pyramidal neurons in V1 (Jia et al., 2010). Subthreshold local dendritic calcium transients were observed in response to gratings presentation, and, interestingly, it was reported that single dendrites received sensory inputs with different orientation preferences. But a more recent work studied dendritic spikes in layer 2/3 neurons in V1, and it was observed that dendrites had similar orientation tuning as the soma (Smith et al., 2013). It is then not clear how these results relate to the work of Jia et al., where each neuron seemed to receive inputs tuned to many different orientations. Furthermore, Smith et al. monitored dendritic activity only in one dendritic branch at the time, therefore it is not known if different dendritic branches in the same cell share the same orientation selectivity, and it is not fully understood how their orientation tuning relates to the tuning of the soma. To address these questions, I used the AOL microscope to image the majority of the dendritic tree near-simultaneously while presenting gratings with different orientations. I then computed orientation tuning in different dendritic branches and in the soma of the same cells in awake animals, and I compared the results in layer 2/3 and in layer 5 pyramidal neurons.

5.2 Results

5.2.1 Visual responses in dendrites of layer 2/3 neurons

Eight full-screen square-wave gratings drifting in different directions were presented to the animals. The protocol for visual stimulation consisted of: 2 seconds of grey screen, 2 seconds of static gratings, 2 seconds of drifting gratings, and 2 seconds of grey screen. Each grating was presented 10-20 times.

Neurons were considered responsive to visual stimuli if neuronal activity ($\Delta F/F$) averaged across all branches and soma was significantly higher (paired t-test, p-value < 0.05) in the first second of presentation of the stimulus compared to the 1

second of grey screen just before the appearance of the visual stimulus. Twelve active layer 2/3 neurons were imaged, and five cells out of twelve were considered responsive to the gratings. In **figure 5.1**, the responses to three different orientations for a representative cell are shown. Neuronal activity during all trials is displayed for the soma and for a dendrite. Even if there are some differences in the activity of the soma and in the activity of the dendrite, the orientation preference seems similar, as they both respond reliably to the orientation shown in **figure 5.1 b** and to some extend in **d**, but not in **c**.

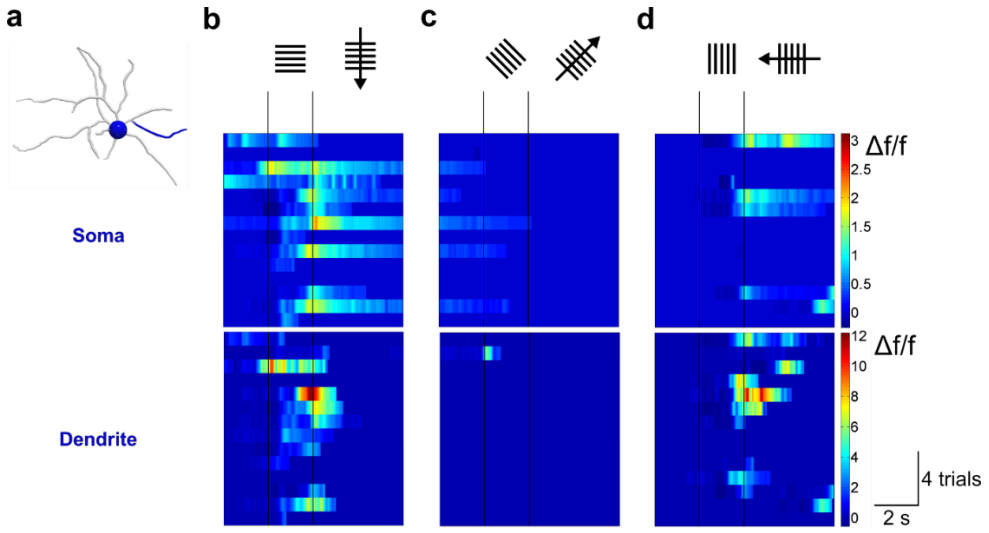

Figure 5.1 Visual responses to gratings in the soma and a dendrite of a layer 2/3 pyramidal neuron in awake mouse. a: the neuron imaged *in vivo* was reconstructed with the software neuTube (Feng et al., 2015). Neuronal activity is shown in b, c and d for the soma and for a dendrite, which are plotted in blue in a. b, c and d: neuronal responses to gratings with three different orientations for the soma and a dendrite. Upper panels show the orientation and drifting direction of the grating. The visual stimulation protocol was: 2 seconds of grey screen, 2 seconds of static gratings, 2 seconds of drifting gratings and 2 seconds of grey screen. For the drifting gratings, an arrow in the direction of the drifting is drawn. Two long vertical lines for each panel show when the static grating, and when the drifting grating appeared, respectively. Medium and lower panels: neuronal responses for all trials for the soma and the dendrite, respectively. The plots are color-coded for the activity (Δf/f).

Dendritic calcium transients that occurred simultaneously also in the soma could have been triggered by backpropagating action potentials, thus these events might not be informative of the orientation tuning of the inputs received by the dendritic branch. Dendritic activity was then divided into calcium events that occurred

simultaneously also in the soma, and calcium events that occurred only in the dendrite (**figure 5.2**). As expected, calcium events that occurred simultaneously in the soma and in the dendrite showed similar orientation preference as the soma, but the dendritic events were sparse.

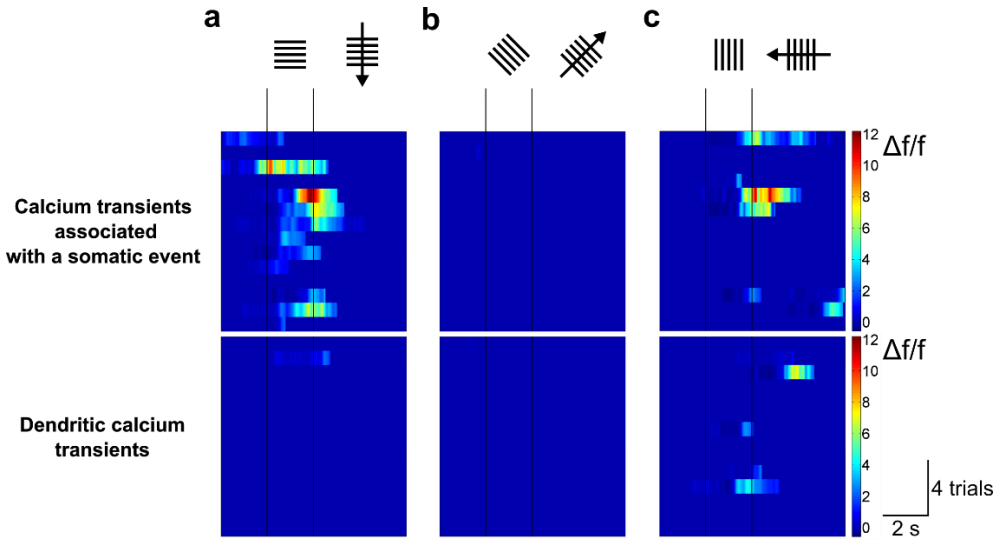

Figure 5.2 Visually-evoked dendritic activity in a layer 2/3 neuron. a, b and c: neuronal responses to three different orientations for the dendrite in figure 5.1 a. Upper panels show the orientation and drifting direction of the grating. For the drifting gratings, an arrow in the direction of the drifting is drawn. Two long vertical lines for each panel show when the static grating, and when the drifting grating appeared, respectively. Medium and lower panels: neuronal responses for all trials for calcium transients that occurred simultaneously in the dendrite and in the soma, and for the calcium events that occurred only in the dendrite, respectively. The plots are color-coded for the activity (Δf/f).

Since these recordings were performed in awake animals, the mice could move their eyes, and that could affect the visual inputs received by the neurons in visual cortex. But it has been reported that eye movements are rare in head-fixed animals, and that they do not affect significantly neuronal activity in visual cortex (Ayaz et al., 2013; Erisken et al., 2014; Keller et al., 2012; Poort et al., 2015; Saleem et al., 2013). In the experiments presented here eye movements were also tracked during some experiments, and it was confirmed that only few saccades occurred: in 9 days of experiments on 7 mice, only 6.4 ± 2.4 % of the trials showed a movement of the pupil larger than 5 degrees during drifting grating presentation. Since eye movements

were rare and seemed to have little effect on neuronal activity in V1, they were considered negligible and were not investigated further.

5.2.2 Orientation tuning in dendrites of layer 2/3 neurons

To compute orientation tuning, the integral of the response to the drifting grating was considered. Each grating was presented multiple times (10-20), and the integrals of the responses were averaged for all repetitions of the same grating. Orientation tuning curves could then be obtained considering the mean response to each grating. Orientation selectivity index (OSI) and direction selectivity index (DSI) were also calculated. OSI is computed from the ratio of the neuronal response to the preferred orientation and the response to the null orientation, which is orthogonal to the preferred orientation. DSI is calculated from the ratio of the response to the preferred direction and the response to the null direction, which is opposite to the preferred direction. Both indexes are equal to one for perfect selectivity, while they are equal to zero for an equal response to all orientations/directions (see Materials and Methods, section 2.8.7 for details). Neurons were considered orientation tuned if they showed statistically significant responses to gratings compared to grey screen presentation (paired t-test, p-value < 0.05), and if the OSI of the soma was higher than 0.4 (Ko et al., 2011). Cells that were selective for one orientation were considered also direction selective if the DSI of the soma was higher than 0.3 (Ko et al., 2011). Out of 12 layer 2/3 neurons imaged, 4 cells were found to be selective both for orientation and direction.

Figure 5.3 shows the orientation tuning curves for the soma and the dendrite of the example cell displayed in **figure 5.1**. In this neuron, the preferred orientation for the soma was 180 degrees, but there was a smaller peak also at 270 degrees (**figure 5.3 a**). When considering all calcium transients in the dendrite, two preferred orientations emerged, at 180 and 270 degrees (**figure 5.3 b**). The tuning curves for the dendrite and for the soma were similar, but the dendrite showed similar responses to a grating at 180° and a grating at 270°, while the soma was more selective for the 180° orientation. The orientation tuning curve of the dendrite did not change significantly when only the calcium transients associated with a somatic event were considered (**figure 5.3 c**). But when dendritic events not associated with a somatic transient were considered, a preference for the 270° orientation could be observed (**figure 5.3 d**). However, for the dendritic events that occurred only in the dendrites, it is important to note that the calcium transients were very sparse (**figure 5.2**), and that it is then difficult to determine whether orientation tuning of these

events was relevant. Therefore, in the next figures, the orientation tuning curves of the calcium events that occurred only in the dendrites will be omitted.

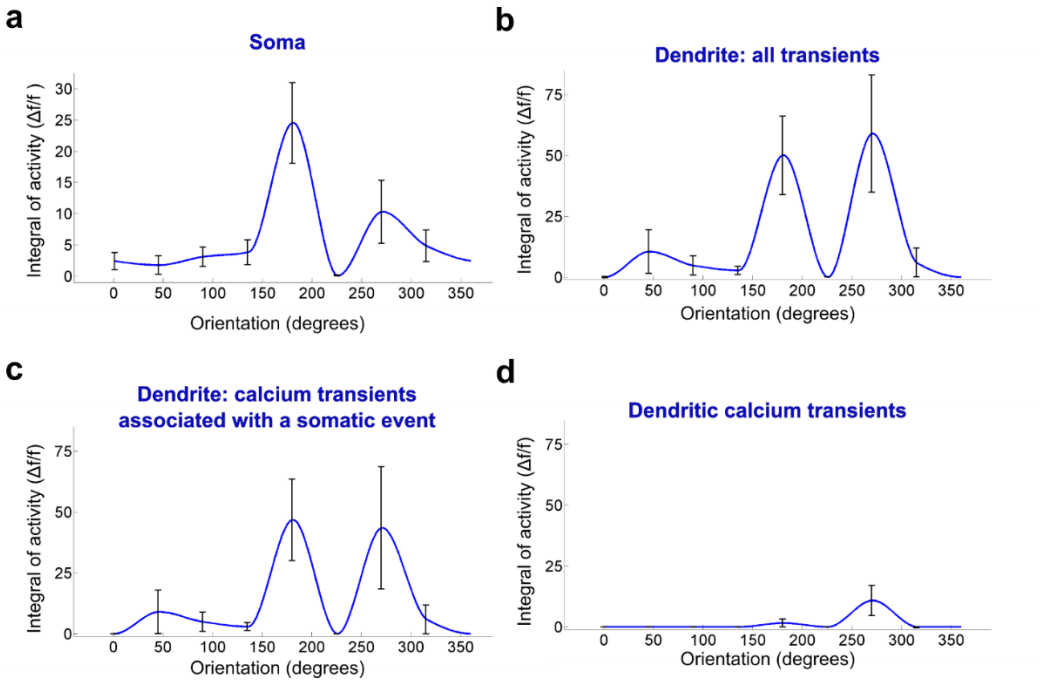

Figure 5.3 Orientation tuning curves in the soma and in a dendrite of a layer 2/3 neuron. a: orientation tuning curve of the soma of the neuron showed in figure 5.1a. b, c and d: orientation tuning curves of the dendrite shown in blue in figure 5.1a, computed considering first all calcium transients (b), then only the calcium transients that occurred simultaneously in the soma and in a dendrite (c), and finally considering only the calcium events that occurred in the dendrite but not in the soma (d). Error bars represent standard error of the mean across repetitions of the same grating.

When considering the orientation tuning curves of all dendrites in the cell, a similar behaviour was observed in all branches. In **figure 5.4 a**, the orientation tuning curves of all dendritic branches in the cell are shown in different colours, while the tuning curve of the soma is plotted with a thicker black line. Dendrites had a similar tuning curve as the soma, but there were some differences mainly in the ratios between the peaks of the preferred orientations. Indeed, when considering the preferred orientation for each dendrite (**figure 5.4 b**), most dendrites had the same preferred orientation as the soma, but few dendrites had a different preferred orientation. When only the calcium transients associated with a somatic calcium transient were considered (**figure 5.4 c** and **d**), the results were similar, but the orientation tuning

of the dendrites was closer to the tuning of the soma. Indeed, co-activation of a dendrite and the soma might be caused by backpropagating action potentials, thus these dendritic calcium events could be biased towards the preferred orientation of the soma. But few dendritic branches still had a different orientation preference than the soma (**figure 5.4 c** and **d**), probably because somatic events were often not accompanied by global calcium events in the full dendritic tree.

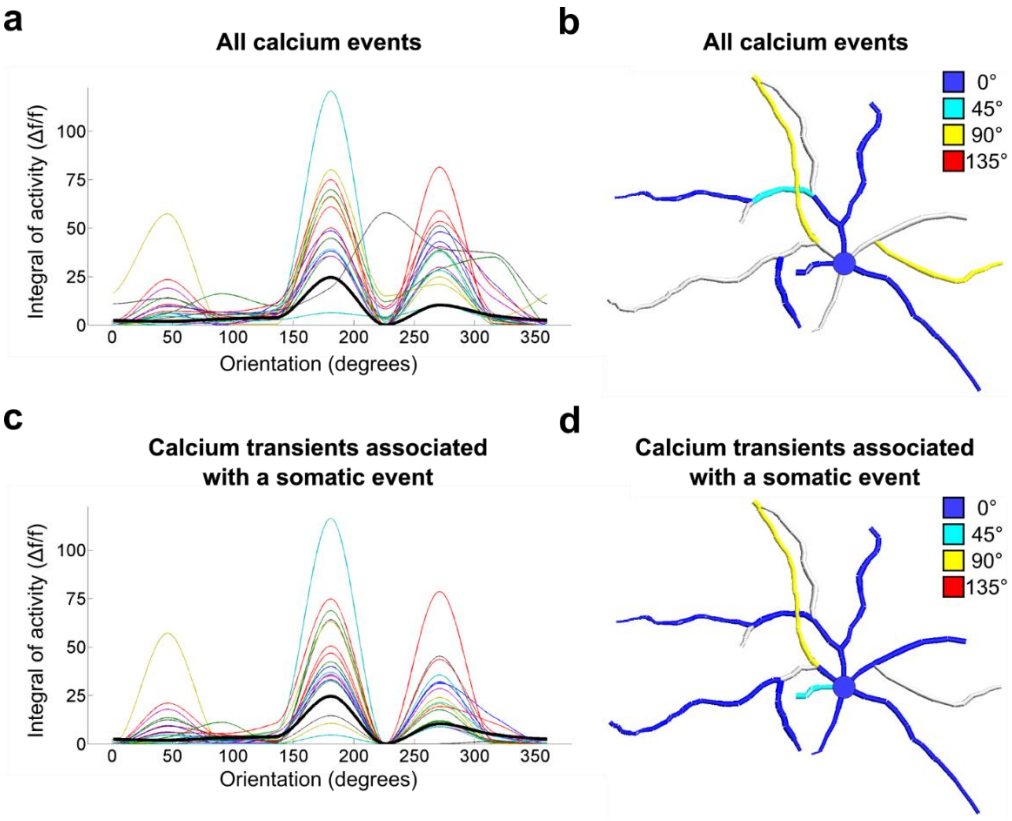

Figure 5.4 Orientation tuning in all the dendrites of a layer 2/3 neuron. Orientation tuning was computed first considering all calcium transients in the dendrites (a, b), and then considering only the calcium transients that occurred simultaneously in the soma and in the dendrites (c, d). a, c: orientation tuning curves of the dendrites are plotted in different colours, while the orientation tuning curve of the soma is drawn in a thicker black line. b, d: reconstruction of the neuron imaged, where each dendrite and the soma are color-coded for their preferred orientation. Dendrites that were not significantly tuned are shown in white.

Analogous results were observed in the other 3 cells imaged that were selective for one orientation (**figure 5.5**). In this figure, in the last cell (**figure 5.5 e** and **f**) the soma was not selective for one orientation (orientation selectivity index < 0.4), but since

more than 70% of its dendrites were selective for one orientation, this cell was included into the dataset.

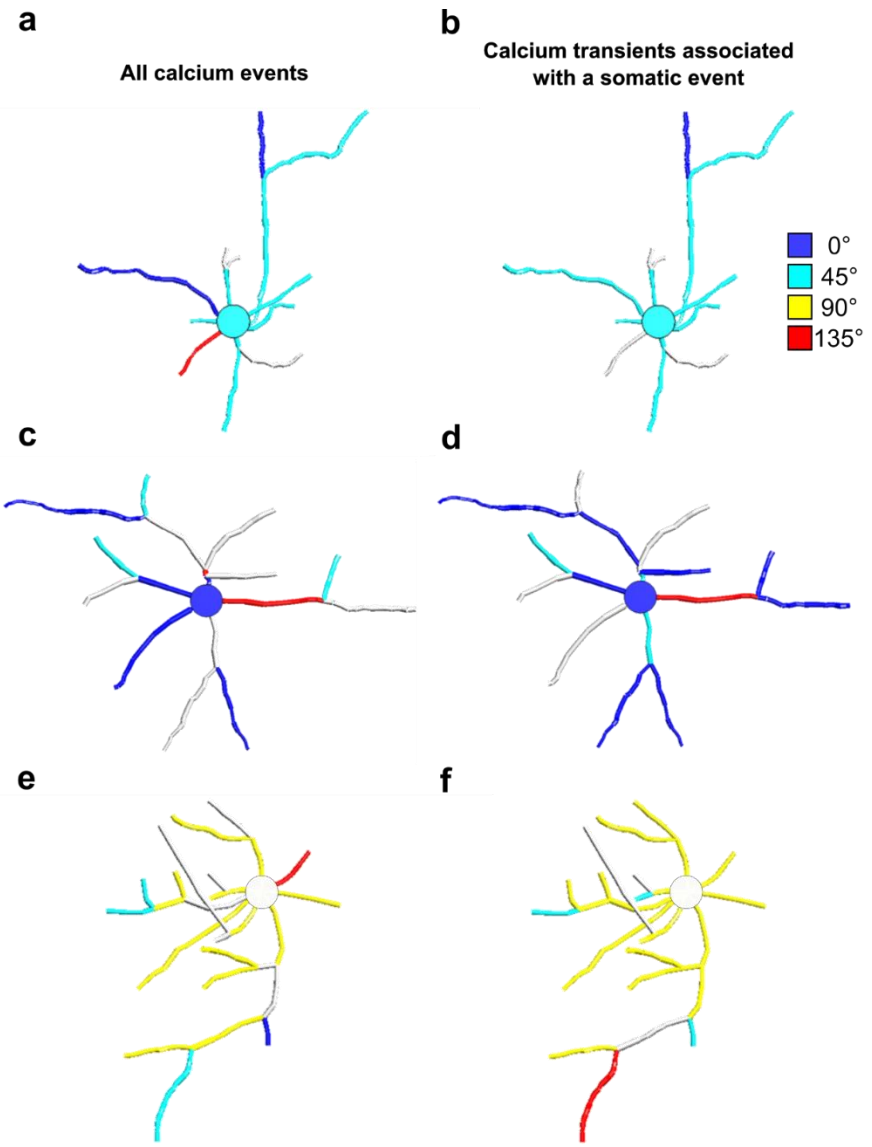

Figure 5.5 Orientation tuning in the dendrites of three layer 2/3 pyramidal neurons. Panels a and b show orientation tuning for one cell, c and d for the second cell, and e and f for the third neuron. Orientation tuning was computed considering all calcium transients in the dendrites (a, c, e), and then considering only the calcium transients that occurred simultaneously in the soma and in the dendrites (b, d, f). All panels show reconstruction of the neurons imaged *in vivo*, each dendrite and the soma are color-coded for their preferred orientation. Dendrites and somas that were not significantly tuned are shown in white.

In conclusion, most dendrites in layer 2/3 cells had the same preferred orientation as the soma, but few dendrites exhibited different orientation selectivity. When considering only dendritic events not associated with a somatic calcium transient, dendritic activity was very sparse, and it was difficult to compute orientation tuning.

Finally, we considered orientation selectivity index (OSI) and direction selectivity index (DSI) for all dendrites imaged in the five layer 2/3 neurons that were responsive to gratings (**figure 5.6**). Both OSI and DSI of dendrites spanned from 0.1 to 1, and on average direction selectivity index was higher than orientation selectivity index. Indeed, the mean value for OSI was 0.53 ± 0.02, while the mean value for DSI was 0.79 ± 0.02. Both distributions were different from the uniform distribution (one-sample Kolmogorov-Smirnov test, for OSI p-value = 0.03, for DSI p-value < 0.001), and from the normal distribution (one-sample Kolmogorov-Smirnov test, both p-values < 0.001). The values of OSI and DSI were not significantly different when considering all calcium transients, or when considering only dendritic events associated with a somatic transient (paired t-test, p-value > 0.5).

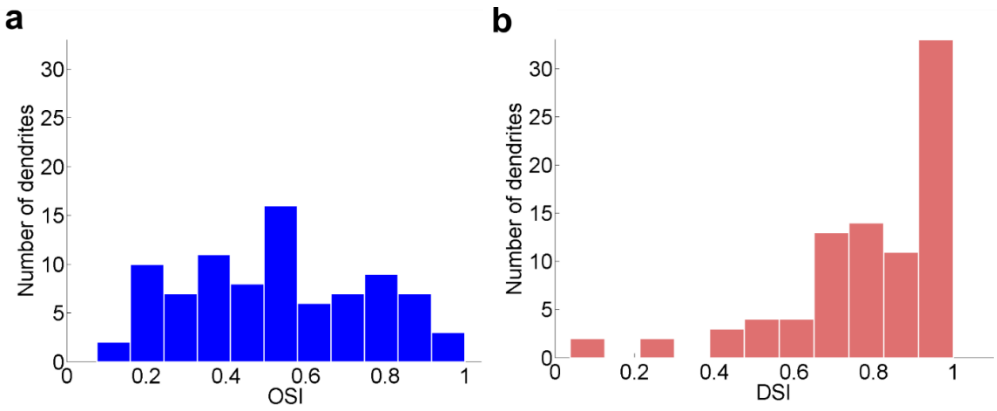

Figure 5.6 Orientation and direction selectivity in dendrites of layer 2/3 pyramidal neurons. Distribution of orientation selectivity indexes (OSI) in a, and direction selectivity indexes (DSI) in b, for 86 dendrites in 5 cells.

5.2.3 Visual responses in tuft dendrites of layer 5 neurons

Responses to static and drifting gratings of different orientations were analysed also in the apical and tuft dendrites of layer 5 neurons. In these dendrites, visual responses appeared sparse and most of the times unreliable. As for layer 2/3 cells, a layer 5 neuron was considered responsive to gratings if calcium activity (ΔF/F)

averaged across all dendritic branches was significantly different (paired t-test, p-value < 0.05) during grating presentation compared to grey screen. Dendritic activity from nine layer 5 neurons was analysed, and only one cell showed significant responses to gratings, while two cells showed significant reduction in activity when the grating appeared. The cell that exhibited significant responses to gratings is shown in **figure 5.7**; in **figure 5.7 a** an image with several tuft dendrites of the cell is displayed, while the full reconstruction of the dendritic tree is shown in **figure 5.7 b**. Dendritic responses to two gratings are shown in **figure 5.7 c**, while the average of all the dendritic responses to all orientations and for all repetitions is shown in **figure 5.7 d**. In these figures, the mean number of dendritic branches active, and not the Δf/f, is represented at each time point in order to show the level of activation of the full dendritic tree. Interestingly, the mean dendritic activity shows a peak just after the grating appeared (at 2 s), and also a smaller peak when the grating started to drift in one direction (at 4 s), suggesting that this neuron responded to the visual stimuli (**figure 5.7 d**). But when the dendritic responses in each trial are considered (**figure 5.7 c**), dendritic activity looks sparse and unreliable. When activity of individual branches was considered, dendritic responses were also sparse (data not shown). One cell that significantly decreased dendritic activity during grating presentation is shown in **figure 5.8**. When considering the mean response of this neuron to grating presentation (**figure 5.8 d**), dendritic activity started to decrease approximately at 2 s, when the static grating appeared, and it increased again just after 6 s, when the grating disappeared and a grey screen was shown to the animal. However, also in this cell, when dendritic responses are observed trial by trial (**figure 5.8 c**), neuronal activity looks unreliable. Dendritic activity was sparse also when responses of individual branches were considered (data not shown).

In conclusion, the tuft dendrites of layer 5 neurons showed little or no response to static and drifting gratings. Dendritic responses of layer 5 apical dendrites to small gratings and to natural images were also analysed, but neuronal activity was sparse and unreliable also with these visual stimuli (data not shown).

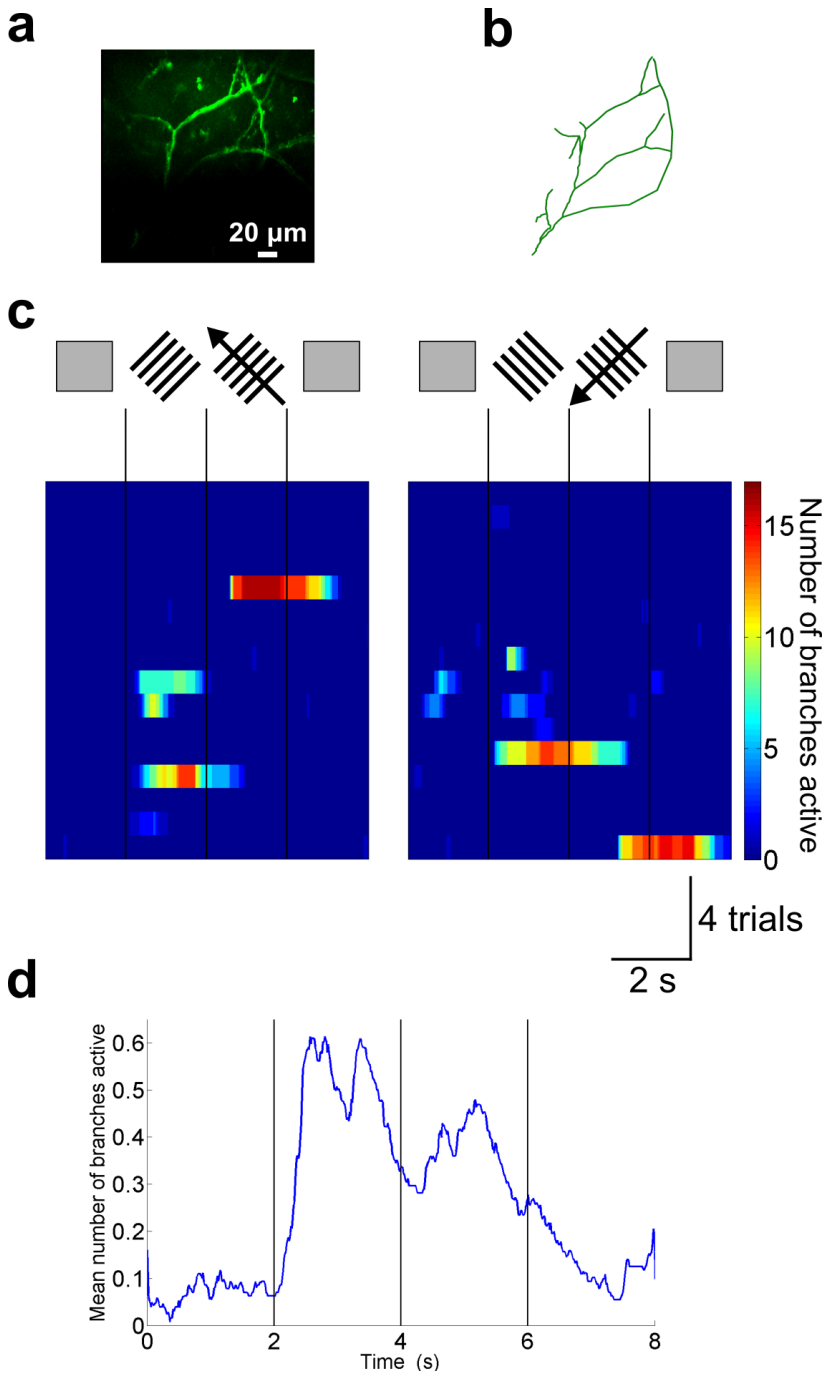

Figure 5.7 Visual responses in apical dendrites of a layer 5 neuron. a: maximum intensity Z-projection of the planes with most of the dendrites imaged in this cell *in vivo*. The neuron was labelled with GCaMP6f and TdTomato. b: Reconstruction of the dendrites imaged *in vivo*. Neurons were traced, reconstructed and visualized with the software NeuTube (Feng et al., 2015). c: visual responses to static and drifting gratings of two different orientations (left and right panel). The visual stimulation protocol was: 2 seconds of grey screen, 2 seconds of static gratings, 2 seconds of drifting gratings and 2 seconds of grey screen. In the drawing of the gratings, the arrows show the direction of drifting. The responses to all repetitions of the gratings are shown in the vertical axes, and the plots are color-coded for the number of

branches active. d: mean number of branches active during a trial, averaged over all trials and all orientations.

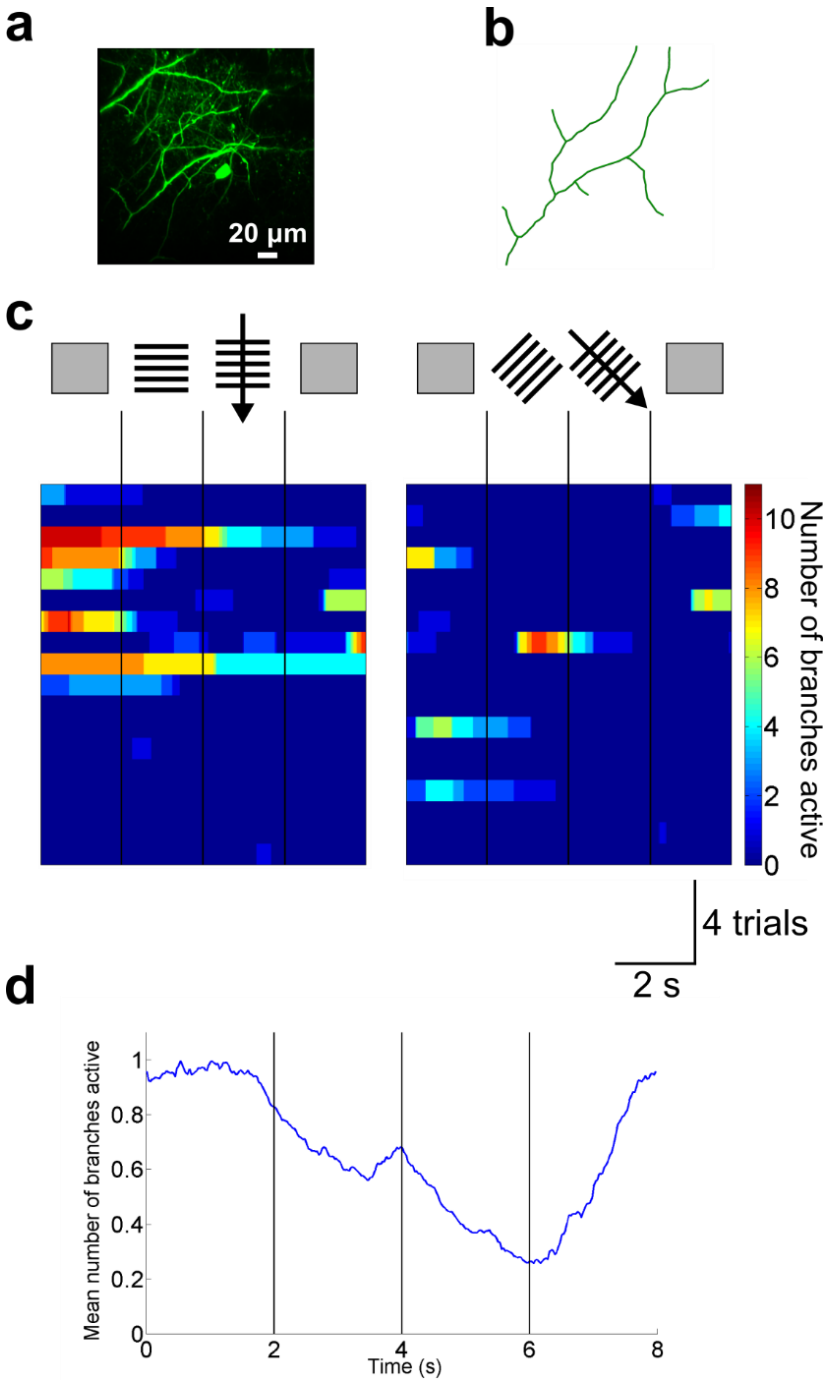

Figure 5.8 Dendritic activity is repressed by gratings presentation in the apical dendrites of some layer 5 neurons. a: maximum intensity Z-projection of the planes with most of the dendrites imaged in this cell *in vivo*. The neuron was labelled with GCaMP6f and TdTomato. b: Reconstruction of the dendrites imaged *in vivo*. c: visual responses to static and drifting

gratings of two different orientations (left and right panel). The responses to all repetitions of the gratings are shown in the vertical axes, and the plots are color-coded for the number of branches active. d: mean number of branches active during a trial, averaged over all trials and all orientations.

5.3 Discussion

5.3.1 Conclusions

In this chapter I showed that calcium transients are evoked in dendrites of layer 2/3 neurons in response to grating presentation, and that dendritic branches can be orientation selective. Dendrites of layer 2/3 neurons are mainly tuned to the same orientation as the soma, but some dendrites have a different preferred orientation than the soma, because not all somatic calcium transients invade all the dendrites, and because some calcium events occur only in the dendrites and not in the soma. When considering only calcium events that occurred in the dendrites and not in the soma, dendritic activity is sparse. On the other side, in layer 5 pyramidal neurons, the vast majority of apical and tuft dendrites imaged does not respond to gratings, and in two cells out of nine dendritic activity was reduced by gratings presentation.

Unfortunately, it is not known how the observed patterns of activity relate to the electrical signalling, and the nature of the calcium transients recorded could not be determined. In addition, some small events, such as EPSPs or single action potentials, might have been missed. But it is known that calcium transients represent dendritic and somatic activity, and indeed calcium imaging has been used successfully in previous studies to measure sensory-evoked activity and orientation tuning in dendrites (Jia et al., 2010; Varga et al., 2011; Xu et al., 2012) and in somas (Mrsic-Flogel et al., 2007; Ohki et al., 2005; Smith and Häusser, 2010).

5.3.2 Orientation tuning in dendrites of layer 2/3 neurons

Orientation tuning was computed considering the integral of the calcium responses over time, and the calcium indicator used was GCaMP6f (Chen et al., 2013a). GCaMP6 signals increase in a highly non-linear way with the calcium concentration, and orientation selectivity could then be amplified by the non-linearities of the calcium probe. However, in two recent papers, orientation tuning of neurons in mouse V1 was measured both with calcium imaging with GCaMP6 and with

electrophysiological recordings, and the results were similar (Sun et al., 2015; Wilson et al., 2016), thus suggesting that the non-linearities of GCaMP6 do not alter significantly the measurements of orientation selectivity.

The results presented here are in agreement with previous reports, which showed that each neuron received inputs from cells selective for different orientations and directions (Jia et al., 2010; Wertz et al., 2015; Wilson et al., 2016), but at the same time many dendritic branches in layer 2/3 pyramidal neurons in V1 had similar orientation selectivity as the soma (Smith et al., 2013). But the data presented here constitutes, to my knowledge, the first characterization of orientation selectivity in the full dendritic tree in awake animals, and it contributes to understanding how visual responses in the dendrites relate to visual responses in the soma. Surprisingly, dendritic events that occurred only in the dendrites and not in the soma were sparse and unreliable, maybe because the majority of the dendritic calcium transients observed were dendritic spikes. Dendritic EPSPs might be less sparse and more reliable, while dendritic non-linear events could be rarer.

Thanks to the AOL-microscope ability to image in three dimensions, visual responses were recorded in almost 90 dendritic branches from different cells. The orientation and direction selectivity index (OSI and DSI, respectively) were measured for all dendrites, and compared with the reported distribution of OSI and DSI for somas in layer 2/3 neurons. In mouse, it has been reported that 74% of the cells had a OSI higher than 0.5 (Niell and Stryker, 2008), while in the data reported here only 56% (48/86) dendrites had a high OSI. For direction selectivity, on the other hand, only 23% of the cells imaged had a DSI higher than 0.5 (Niell and Stryker, 2008), while 91% of dendrites (78/86) had a high DSI in my data. These results seem to suggest that dendrites have low orientation selectivity and high direction selectivity compared to somas. However, in Niell and Stryker 2008, neuronal activity was measured with multi-electrodes recordings, and with this technique the sampling of the neurons can be biased towards more active cells. Indeed, while the mean OSI was approximately 0.9 in Niell and Stryker 2008, and 0.5 for dendrites in my data, another study performed with calcium imaging reported a mean OSI of 0.32 for excitatory neurons in the soma in layer 2/3 (Sohya et al., 2007). These measurements can probably change depending on the technique used, on the visual stimulation protocol and on how the data was analysed. In conclusion, for the next experiments it would be interesting to measure orientation tuning in the somas for a population of layer 2/3 neurons in the same conditions as the experiments performed imaging dendrites, so it would be possible to compare orientation and direction selectivity in somas and dendrites.

5.3.3 Responses to visual stimuli in dendrites of layer 5 neurons

Apical and tuft dendrites of layer 5 neurons showed little or no responses to the visual stimuli tested (full-field gratings, small gratings and natural images). In two cells out of nine, dendritic activity was even repressed by full-field grating presentation. Full-field gratings might suppress dendritic activity via SOM inhibitory neurons, because these interneurons target the dendrites of pyramidal neurons and are responsive to the surround of the receptive field (Adesnik et al., 2012). However, it has also been reported that the somas of layer 5 pyramidal neurons are tuned to orientation and direction (Sun et al., 2015), so it is possible that orientation-selective inputs impinge primarily on basolateral dendrites. Interestingly, unpublished data from Dr LM Palmer and ME Larkum on layer 2/3 neurons in somatosensory cortex showed that dendritic activity can be repressed in distal dendrites during multimodal sensory stimulation (data presented at Society for Neuroscience Conference SFN 2015). Therefore, it is also possible that tuft dendrites of layer 5 neurons are involved in processing different types of sensory inputs, or top-down inputs, and that they do not respond or are repressed by visual inputs.

6. Dendritic activity is modulated by the state of the animal

6.1 Introduction

Most experiments on the visual system were performed on anaesthetized animals, but it is now clear that anaesthesia can affect neuronal activity (Adesnik et al., 2012; Greenberg et al., 2008; Haider et al., 2013; Niell and Stryker, 2010; Pisauro et al., 2013; Vaiceliunaite et al., 2013). In particular, in awake animals, firing rates are higher, pair-wise correlations are lower (Greenberg et al., 2008) and inhibition is enhanced (Haider et al., 2013). In 2007, Dombeck et al. developed a new technique to image the brains of awake animals: mice were head-fixed, but they could run on a spherical treadmill (Dombeck et al., 2007). This new setup allowed to study also the effects of locomotion on brain activity. Interestingly, it was found that locomotion is associated with arousal and pupil dilation (Erisken et al., 2014; Vinck et al., 2015), so it corresponds to a different animal state and it can affect neuronal activity in many ways. In mouse V1, locomotion increases dramatically the mean firing rate of neurons in layer 2/3 (Erisken et al., 2014; Keller et al., 2012; Niell and Stryker, 2010), it increases the gain of visual responses (Niell and Stryker, 2010; Polack et al., 2013) and, in particular, it preferentially enhances the gain of neurons tuned to high-spatial frequencies (Mineault et al., 2016). Therefore, during a state of locomotion and heightened attention, the population can support better spatial acuity. But it is still not clear how the activity of interneurons is affected by locomotion. One study showed that running activated VIP-expressing interneurons via cholinergic inputs from the basal forebrain, and that these neurons inhibited SOM interneurons, thus disinhibiting pyramidal cells (Fu et al., 2014). However, other reports showed that both SOM neurons and PV neurons increased their firing rate during locomotion (Pakan et al., 2016; Polack et al., 2013).

Therefore, in the recent years, several studies began to investigate how the animal state affects neuronal activity in visual cortex, but little is known on the effects of animal state on dendritic activity. In rat somatosensory cortex, one study reported that anaesthesia inhibited activity in the dendrites of layer 5 neurons, while it enhanced activity in the dendrites of layer 2/3 neurons (Murayama and Larkum, 2009), but the effects of anaesthesia on dendritic activity in visual cortex are not known. Furthermore, the effects of locomotion on dendritic activity have not been studied and are difficult to predict: on one hand locomotion increases the firing rate of the network, but on the other hand higher excitation could be compensated by higher inhibition from SOM neurons, which target specifically the dendrites of

pyramidal neurons. Therefore, to investigate the effects of anaesthesia and locomotion on dendritic activity in mouse V1, I imaged dendrites of layer 2/3 and layer 5 pyramidal neurons while the animals were anaesthetized, when they were awake and stationary, and when they were running on a wheel.

6.2 Results

6.2.1 Effects of anaesthesia on dendritic activity

Adult mice were first sedated with chlorprothixene, and then anaesthetized lightly with isoflurane (0.5-1.1%). The animal temperature was kept at 36.5-37° during the whole experiment. Gratings with different orientations were presented to the animal, and calcium activity was recorded in the dendrites of layer 2/3 and layer 5 pyramidal neurons, as previously explained. The mean dendritic activity during recordings of 10-20 minutes was compared when the animal was anaesthetized and when the animal was awake and stationary. Dendritic activity (in Δf/f) was divided into bins of 100 ms, the average activity during each bin was calculated, and then the mean activity across bins was compared for the two animal states (similar analysis as in Saleem et al., 2013). The size of the bins was also varied (50, 200 and 300 ms), but the results did not change significantly.

Figure 6.1 a and **b** show a layer 2/3 neuron with the dendrites colour-coded for the mean activity when the animal was anaesthetized and when the animal was awake and stationary. Interestingly, dendritic activity does not seem to be strongly affected by anaesthesia in this neuron (**figure 6.1 a, b**). Effects of anaesthesia varied slightly across cells, because few neurons seemed unaffected by anaesthesia while others showed a small decrease in activity when the animal was anaesthetized. But when the mean activity was compared for all dendrites in all neurons imaged (7 layer 2/3 cells in 4 animals), no significant difference was found between the anaesthetized and the awake state (paired t-test, p-value > 0.05) (**figure 6.1 c**). Apical dendrites were then analysed separately (**figure 6.1 d**), as they might receive more top-down modulation than basolateral dendrites; but also apical dendrites did not seem to be significantly modulated by anaesthesia. Analogously, activity of somas of layer 2/3 neurons was not significantly modulated by anaesthesia (**figure 6.1 e**), confirming that the anaesthesia was light. In some cases, it was not possible to see the same dendrites across different days of experiments, therefore for a few dendrites the mean activity is known only in one state. Patterns of dendritic activity were also compared when the animal was awake and when the animal was anaesthetized. But

in 3 cells out of 7, anaesthesia reduced the number of dendritic events and there were not enough calcium transients to characterize patterns of dendritic activity. In one cell, the number of global events was significantly increased when the animal was anaesthetized (two-sample Kolmogorov-Smirnov test, p-value < 0.001), but the other 3 neurons imaged showed little or no difference in the patterns of dendritic activity in the two animal states (data not shown). Therefore, it was not possible to draw any conclusion on the effects of anaesthesia on patterns of dendritic activity.

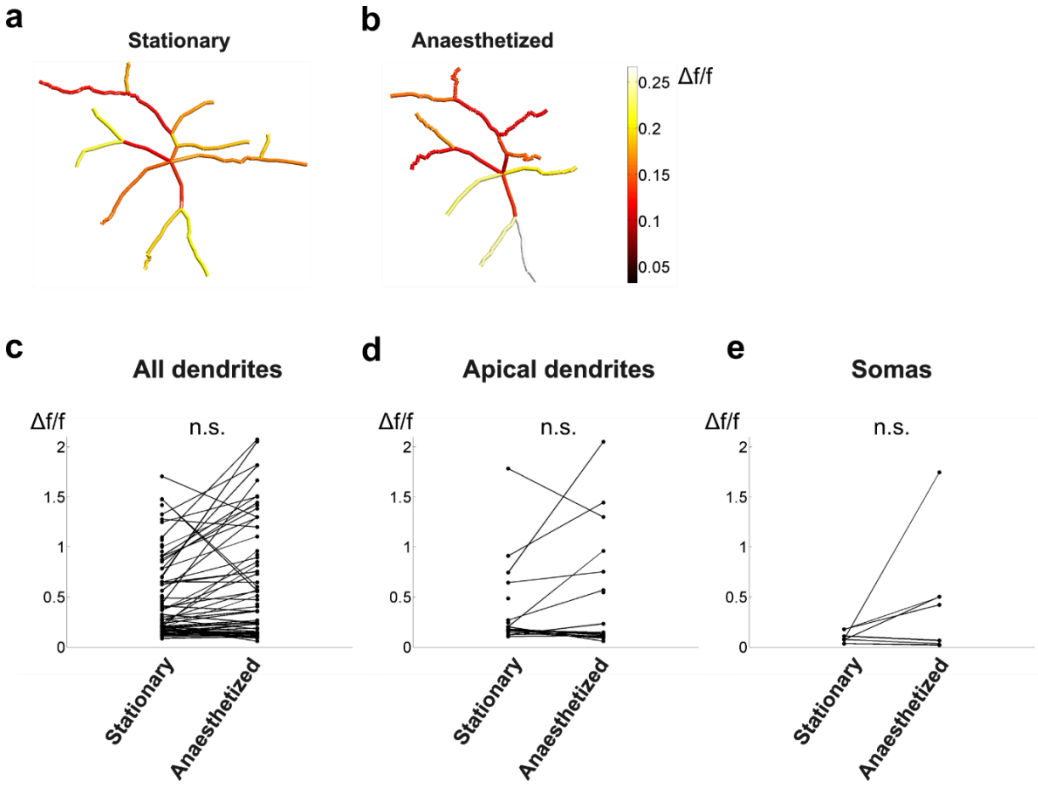

Figure 6.1 Dendritic activity in anaesthetized animals in layer 2/3 neurons. Mice were anaesthetized lightly with isoflurane. a, b: reconstruction of a neuron imaged *in vivo*, where dendrites are color-coded for the mean activity over 10-20 minutes of recording in awake stationary animals, and in anaesthetized animals, respectively. c, d, and e: mean activity in awake stationary and anaesthetized animals for all dendrites, only apical dendrites and for somas, respectively. The sample consisted of 7 cells from 4 mice. n.s. stands for non-significant (p-value > 0.05).

The same measurements were obtained for apical dendrites of layer 5 neurons (**figure 6.2**). In contrast with layer 2/3 neurons, in all the layer 5 cells imaged neuronal activity was strongly suppressed by anaesthesia in the tuft dendrites.

Unfortunately, I did not record neuronal activity in the soma of layer 5 neurons when the animals were anaesthetized, thus it is not possible to compare the effects of anaesthesia on different compartments of layer 5 neurons. Nevertheless, these results show that light anaesthesia has different effects on apical dendrites of layer 2/3 neurons and on tuft dendrites of layer 5 neurons. Activity in distal dendrites of layer 5 pyramidal neurons is strongly modulated by anaesthesia, suggesting that these dendrites receive top-down information about the animal state.

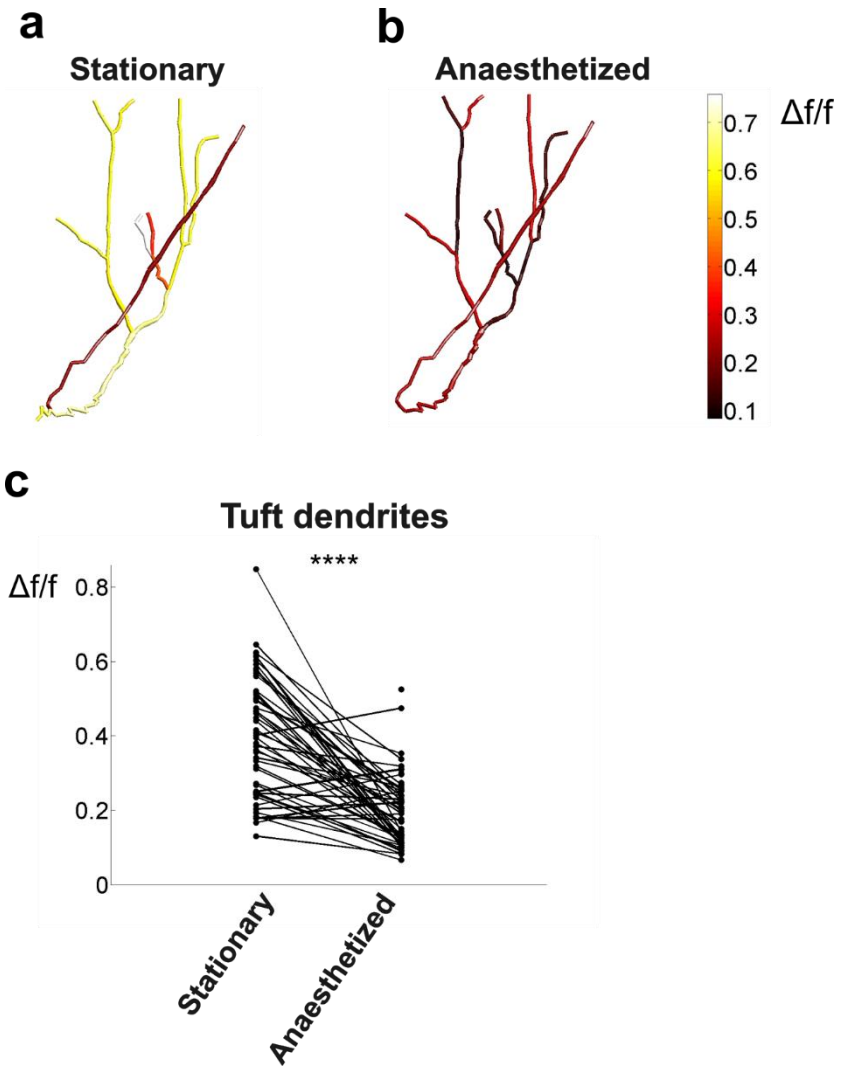

Figure 6.2 Neuronal activity in anaesthetized animals in apical dendrites of layer 5 neurons. Mice were anaesthetized lightly with isoflurane. a, b: reconstruction of dendrites imaged *in vivo*, where dendrites are color-coded for the mean activity over 10-20 minutes of recording in awake stationary animals, and in anaesthetized animals, respectively. c: mean activity in awake stationary and anaesthetized animals for all dendrites imaged. The sample size was 5

cells from 4 mice. Anaesthesia strongly suppresses activity in layer 5 tuft dendrites (p-value = 1.8 x 10-9).

6.2.2 Effects of locomotion on dendritic activity

The effects of locomotion on dendritic activity were also investigated. The mean activity of each dendrite during gratings presentation was compared when the animal was stationary (animal speed < 0.8 cm/s) and when the animal was walking or running (animal speed > 0.8 cm/s), both for layer 2/3 and for layer 5 neurons.

In **figure 6.3 a-d**, two representative layer 2/3 neurons are shown. The cells were reconstructed after the experiment and each dendrite was color-coded for its mean activity, analogously to the analysis done to measure the effect of anaesthesia on dendritic activity (**figure 6.2**). Locomotion did not seem to change significantly the activity in the first cell (**figure 6.3** a and **b**), while for the second cell there was a global increase in dendritic activity when the animal was running (**figure 6.3 c** and **d**). Indeed, the effects of locomotion varied in different layer 2/3 neurons, but when considering all imaged cells (13 neurons) no significant difference was found in dendrites (**figure 6.3 e**), apical dendrites (**figure 6.3 f**) or somas (**figure 6.3 g**) of layer 2/3 neurons (paired t-test, p-value > 0.05).

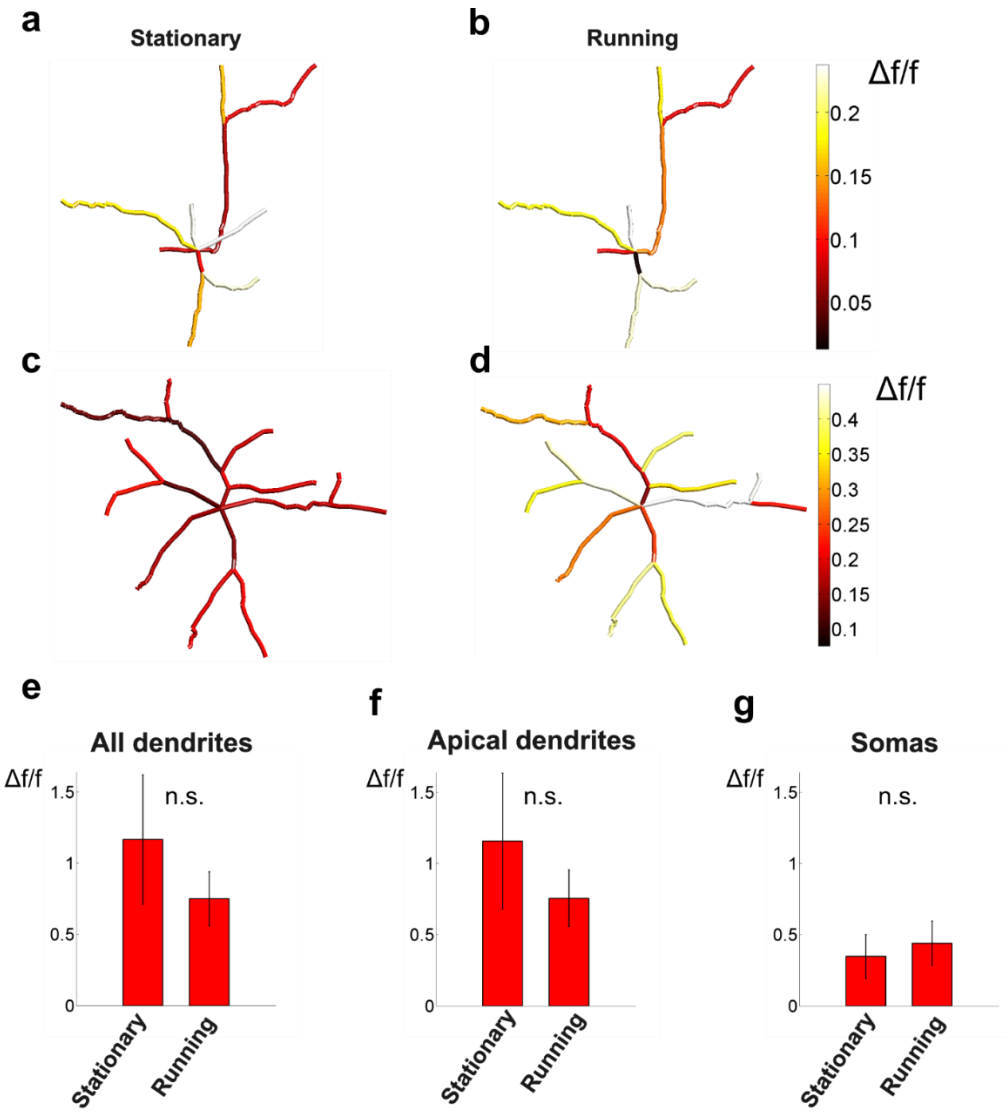

Figure 6.3 Effects of locomotion on dendritic activity of layer 2/3 pyramidal neurons during gratings presentation. a-d: reconstruction of two neurons imaged *in vivo*, where dendrites are color-coded for the mean activity. The first cell is shown in a and b, the second neuron is shown in c and d. Dendritic activity was averaged over stationary periods (a and c), and running periods (b and d). e, f and g: mean activity in awake stationary and running animals for all dendrites, only apical dendrites and for somas, respectively. The sample consisted of 13 cells from 7 mice. n.s. stands for non-significant (p-value > 0.05).

A similar analysis was carried out for the apical dendrites of layer 5 neurons (**figure 6.4**). But, in contrast with layer 2/3 neurons, the activity in apical dendrites of layer 5 neurons was consistently enhanced by locomotion.

The effects of locomotion on the dendritic activity of layer 2/3 and layer 5 neurons were measured also when the animals were in the darkness (**figure 6.5** and **figure**

6.6). Interestingly, in dendrites of layer 2/3 neurons, activity showed a small but significant enhancement when the animal was running (**figure 6.5 a**, **b**). On the other side, the activity of the somas in layer 2/3 neurons was not significantly modulated by running (**figure 6.5 c**). But it is important to note that the sample size was smaller when considering somas than dendrites (77 dendrites and 6 somas were imaged), thus it is possible that the effect of locomotion was similar in both dendrites and soma, but no significant difference was measured in the soma due to the small sample size. To investigate the effects of locomotion on layer 5 neurons while the animal was in the dark, layer 5 neurons were imaged with the second generation AOL microscope, so it was possible to monitor calcium activity both in the tuft dendrites and in the somas of layer 5 cells. Interestingly, it was found that activity in apical dendrites was enhanced by locomotion even when the animal was in the darkness (**figure 6.6 a**), while running had no effect on somatic activity (**figure 6.6 b**).

In conclusion, these data suggest that locomotion enhances neuronal activity preferentially in the apical dendrites of layer 5 neurons.

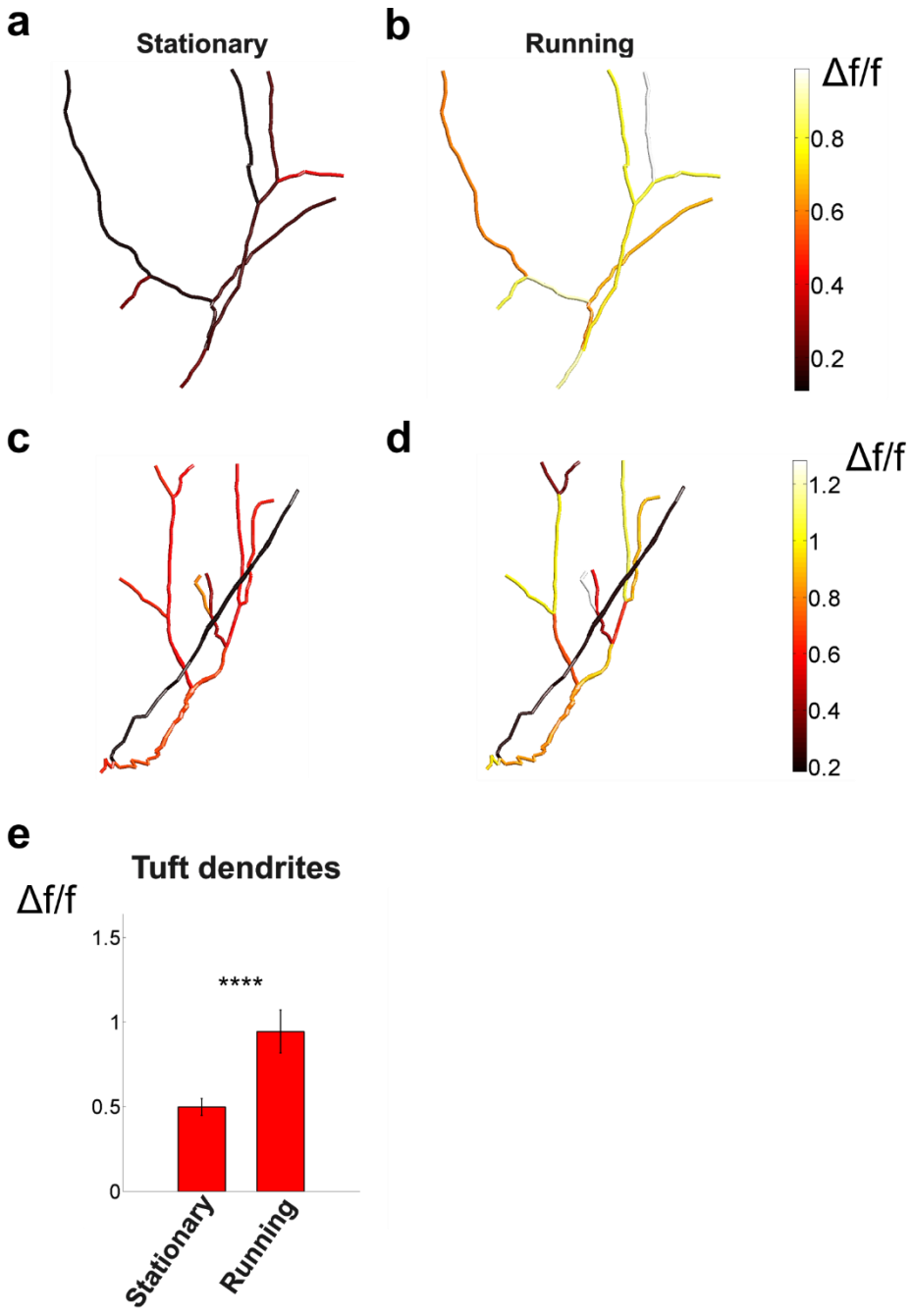

Figure 6.4 Effects of locomotion on dendritic activity in apical dendrites of layer 5 pyramidal neurons during gratings presentation. a-d: reconstruction of two neurons imaged *in vivo*, where dendrites are color-coded for the mean activity. The first cell is shown in a and b, the second neuron is shown in c and d. Dendritic activity was averaged over stationary periods (a and c), and running periods (b and d). e: mean activity in awake stationary and running animals for all dendrites. The sample size consisted of 13 cells from 6 mice. Modulation of dendritic activity by locomotion is significant in the dendrites of layer 5 cells (p-value = 3.4 x 10-5).

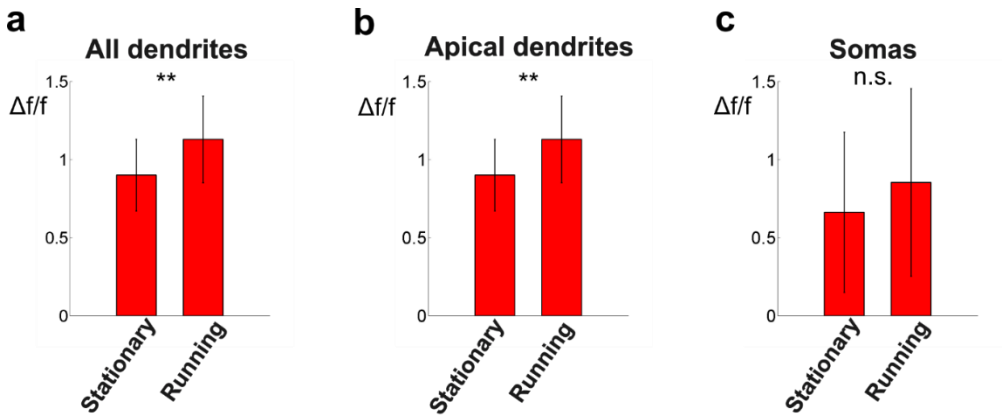

Figure 6.5 Effects of locomotion on neuronal activity in layer 2/3 cells while the animal is in the darkness. a-c: mean activity when the animal was stationary and when the animal was running for all imaged dendrites (a), for apical dendrites (b) and for somas (c). The sample consisted of 6 cells from 4 mice, and the p-values were: 0.0052, 0.0052 and 0.16 respectively.

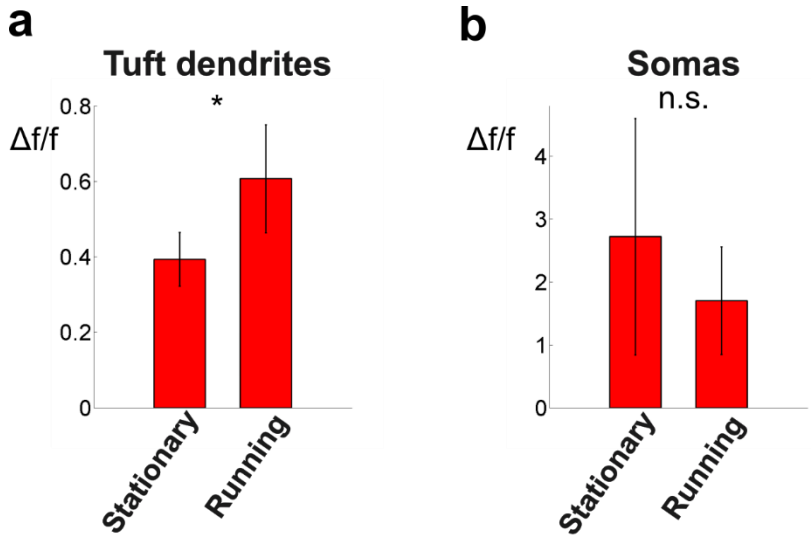

Figure 6.6 Effects of locomotion on neuronal activity in layer 5 cells while the animal is in the darkness. a-b: mean activity when the animal was stationary and when the animal was running for tuft dendrites (a), and for somas (b). The sample consisted of 9 cells from 4 mice for the dendrites, and 7 cells from 3 animals for the somas. The p-values were respectively: 0.019 and 0.38.

6.3 Discussion

My results show that anaesthesia and locomotion have cell-specific and even sub-cellular specific effects on calcium activity in mouse V1. In particular, anaesthesia reduces dendritic activity, while locomotion enhances dendritic activity in the tuft of layer 5 neurons. But locomotion does not seem to affect significantly the somas of layer 5 neurons. In layer 2/3 pyramidal cells, neuronal activity in the soma, basolateral and apical dendrites seems to be only marginally affected by the animal state.

Therefore, the results on the effects of anaesthesia on dendritic activity are similar to those obtained by Murayama et al. in rat somatosensory cortex. In both cases, in animals anaesthetised with isoflurane dendritic activity was found to be strongly reduced in layer 5 neurons (Murayama and Larkum, 2009). But the effect of anaesthesia in dendrites of layer 2/3 neurons was different: in Murayama et al. it was observed that anaesthesia enhanced dendritic activity, while I did not observe any effect. This discrepancy might be due to the different brain region imaged, or the different animal model used.

Even somas of layer 2/3 neurons did not show any modulation by anaesthesia and locomotion, while several studies reported that the activity in these neurons is affected by both (Greenberg et al., 2008; Keller et al., 2012; Niell and Stryker, 2010). But in layer 2/3 cells the effects of animal state were highly variable depending on the cell, and only when averaging across cells the modulation of neuronal activity by animal state was not significant. But this does not exclude the possibility that the modulation by animal state is significant in a subset of layer 2/3 neurons. Furthermore, it should be considered that in these experiments only few somas were imaged (5-13 cells), while when populations of neurons are imaged, the sample sizes are much larger (100 – 1,000 neurons). Finally, the anaesthesia was kept very light during all experiments.

Even if few cells were imaged, many dendrites were imaged and apical dendrites of layer 5 neurons were found to be consistently strongly modulated by animal state. In contrast, activity in apical dendrites of layer 2/3 neurons was not affected by animal state. But dendrites of layer 2/3 neurons were found to receive more visual inputs than apical dendrites of layer 5 cells (see chapter 5). All together, these data support a model where apical and basal dendrites in layer 2/3 neurons are driven mainly by feedforward bottom-up inputs, while apical dendrites of layer 5 neurons receive mostly top-down information. But it has been reported that the somas of layer 5 neurons are responsive to visual stimuli (Sun et al., 2015), thus it is possible that

cells in layer 3 and in layer 4 transmit sensory information onto basolateral dendrites of layer 5 neurons. In this case, layer 5 pyramidal cells could integrate visual and top-down information. Layer 5 neurons could play a more important role in integrating different types of information than layer 2/3 neurons, which seemed to receive mainly visual inputs and little top-down modulation. Layer 5 neurons also form the main output of V1, thus it possible that these cells transmit highly processed information to other brain areas.

7. Technological developments of acousto-optic lens microscope

7.1 Introduction

As shown in the previous chapters, the first generation of acousto-optic lens microscope allows imaging of randomly distributed (random-access) points in a three dimensional volume at high speeds (Fernández-Alfonso et al., 2014; Katona et al., 2012; Kirkby et al., 2010). In this microscope, the time to image each point is given by the time that the acoustic wave takes to fill the acousto-optic lens (AOL), 24 µs, plus the dwell time, 4 µs (see **section 2.3** for more details). However, when imaging in the natural focal plane of the objective, i.e. when the AOL is used only to deflect the laser beam in xy and not to focus it in z, the lens can be used for scanning. In this case, it is possible to use the same acoustic wave to scan all points that are in a line in a single refresh time of the AOL, resulting in an increased duty cycle and in faster scanning. But when the AOL is used also for remote focussing, an acoustic wave with a frequency ramp runs through the AOL, consuming more of the acoustic bandwidth, and making it less available for continuous line scanning. Indeed both scanning and focussing consume acoustic bandwidth, and scanning away from the natural focal plane can require acoustic frequencies that lie outside the optimal frequency band of the AOL. In summary, the first generation of AOL microscope can perform fast raster scanning only in the natural focal plane, and z-stacks are then acquired more slowly because the AOL needs to be filled with a new acoustic wave at every voxel. Therefore, to image at high speeds in three dimensions, only random-access single voxels are imaged instead of full frames.

The prototype microscope that I used for my studies has two main disadvantages: first, z-stack acquisition is slow, as it takes approximately 7 seconds to acquire one 512x512 pixels image, and secondly, imaging random-access points is problematic *in vivo* because the imaged structure moves with respect to the imaged point, which is fixed. In chapter 3 I showed how movement of the tissue can be monitored with co-expression of a calcium indicator and a morphological tracer, but this dual labelling is often technically challenging. Furthermore, this method only enabled me to identify and to discard the data when there was too much movement. On the other hand, post hoc image registration can be used to correct for motion when two dimensional images are acquired, but this cannot be used for random-access point measurements because there is no spatial information, and movement is large compared to the size of the point.

Therefore, the microscopy development group in the Silver lab, which consists of Dr Srinivas Nadella, Dr Victoria Griffiths, Dr Hana Ros, Dr George Konstantinou, Dr Theo Koimtzis, Mr Geoffrey Evans and Dr Paul Kirkby, worked on a second generation AOL microscope. With this new system, it is possible to do continuous line scanning in the full three dimensional volume. This was achieved thanks to two main technical advances: a new design of the crystals with higher transmission efficiency (from ~15% to ~25%), and the development of a custom field programmable gate array (FPGA) board in the acquisition system. An FPGA can operate at high speeds, so it was possible to decrease the dwell time from 4 µs to 50, 100 or 200 ns: with shorter dwell times, the line scan speed is higher, thus reducing the time that the AOL requires to scan and allowing more of the acoustic bandwidth to be used for focussing. With this system, new imaging modes are possible: fast z-stack, multi-plane imaging, random-access two dimensional (2D) and three dimensional (3D) regions of interest. Since the dwell time is shorter and the duty cycle is higher, a 512x512 image can now be acquired at any focal plane in approximately 25 ms, corresponding to a frame rate of 39 Hz. Therefore, fast z-stack and multi-plane imaging can be used to record neuronal activity. In addition, the temporal resolution can be further increased by imaging random-access 2D and 3D regions instead of the full volume. This imaging mode is suited to monitor sparsely distributed neuronal signalling in a three dimensional space, and, compared to point measurements, post hoc movement correction can be used because each imaged region contains spatial information.

Furthermore, Dr Victoria Griffiths, with the help of the other members of the microscopy development group, developed a real time movement correction. The AOL microscope was used here to image periodically a reference object in the brain, and the fast FPGA processing was used to track movement and to adjust in real time the position of the imaged points of interest in order to correct for the movement of the tissue. Compared to post hoc movement correction, online movement correction is more advantageous because it does not require complex post-processing of the data, it can be used also when imaging random-access points, and the imaged structures never fall out of the field of view.

To test these new technological developments for use in *in vivo* experiments, I collaborated with Dr Srinivas Nadella, Dr Victoria Griffiths and Dr Hana Ros, and we imaged neurons in V1 in awake animals. In this chapter my contribution was to perform virus injections and surgery on the animals and to carry out a part of the experiments, while the experiments shown in the figures 7.3, 7.4 and 7.6 were carried out by Dr Ros, and most of the analysis was carried out by Dr Nadella and Dr Griffiths. The same animal preparation as discussed in chapter 3 was used, so

pyramidal neurons were labelled sparsely with GCaMP6f and TdTomato. First we imaged random-access 2D and 3D regions of interest, then we tested real time movement correction. To track movement of the tissue, we used a soma imaged in the red channel as a reference, and we recorded calcium transients in dendritic spines in awake and running mice.

7.2 Results

7.2.1 Imaging of random-access two dimensional regions

First we used the second generation AOL microscope to acquire a z-stack covering a volume of 250x250x250 µm in V1 in awake mice (**figure 7.1 a**). As mentioned above, when a dwell time of 50 ns was used, a plane of 512x512 could be acquired in 25.4 ms. Therefore, a z-stack covering a volume of 250 µm with a plane every 2 µm was acquired in approximately 3 seconds.

After acquiring a full volume z-stack, we selected 2D regions of interest (patches) sparsely distributed in the z-stack, and we imaged only those regions. Compared to the experiments reported in the previous chapters, only mice with denser labelling were selected to test this new imaging mode. Indeed, in this case it was not necessary to trace the full dendritic tree of a cell, and it was preferable to image multiple structures to record neuronal activity in different cells and in different subcellular compartments. Fourteen patches distributed in the volumetric field of view of 220 x 220 x 200 µm were imaged, and somas and dendrites of layer 2/3 neurons were targeted (**figure 7.1**). The dwell time used was 50 ns per voxel, and each patch consisted of 51 x 50 voxels, covering 22 x 21.5 µm. The patch cycle rate, i.e. 1/ (time to scan all patches), was 52.8 Hz. Since each patch contained spatial information, it was possible to perform post hoc movement correction was applied to a montage of all the patches, in particular the open source python software SIMA was used (Kaifosh et al., 2014). Functional signals were extracted from images by identifying cellular structures using a thresholding algorithm, and then the average intensity of voxels in the structure was calculated for each frame. The visual inspection of the calcium transients measured both in somas and dendrites indicated that the recordings had a good signal to noise ratio, and most of the biological structures imaged showed neuronal activity.

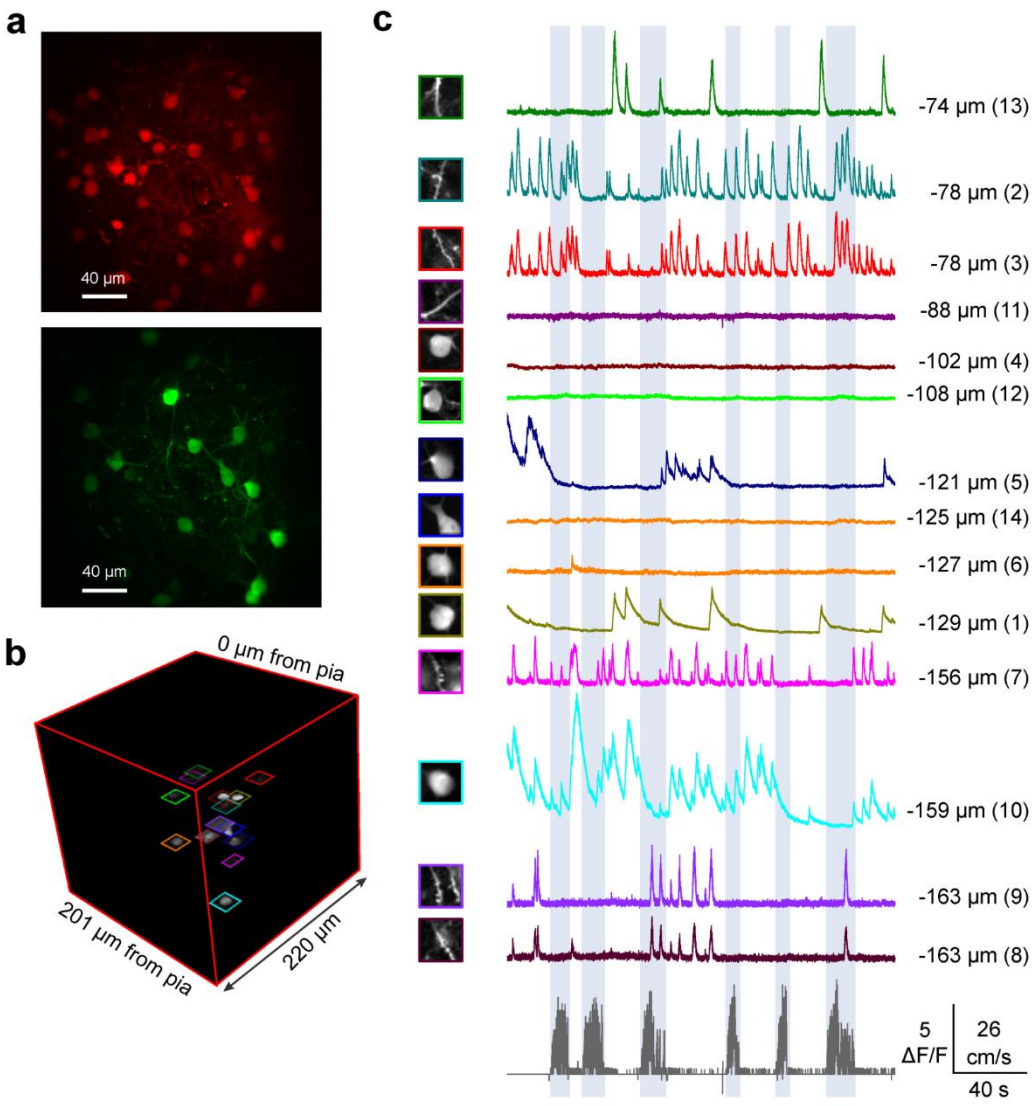

Figure 7.1 Random-access patch imaging of neurons in layer 2/3 of primary visual cortex in an awake behaving mouse. a: Maximum intensity projection of cells in layer 2/3 visual cortex sparsely expressing td-Tomato and GCaMP6f. b: location of 14 X-Y patches within the imaging volume, distributed between 74 µm to 163 µm below the pia. c: Averaged images of cellular structures scanned near-simultaneously at 50 ns/voxel. Traces to the right show Δf/f responses extracted from each patch. Depth and patch number indicated on right. Grey trace at the bottom shows the speed of the animal on the cylindrical treadmill. Blue-grey shading indicates periods of locomotion.

This experiment was performed on a mouse with dual labelling in the red and in the green channel, and, due to the crosstalk between these two channels, the hollow nuclei characteristic of GCaMP6 labelling could not be seen (see **Chapter 3** for more

details). It is possible that these cells showed high calcium signals because they were overexpressing GCaMP6f, which would indicate that the cells were unhealthy.

To exclude this possibility, we repeated the same experiment on a mouse that was expressing only GCaMP6f and where the neurons displayed hollow nuclei (**figure 7.2**). Fourteen patches distributed between 76 µm and 235 µm below the pia were imaged. Each patch consisted of 46 x 40 pixels, and it covered a volume of 22 x 19.4 µm. Two patches were selected on the same soma to check that the same calcium responses could be measured at different times of the imaging cycle. In this experiment, the same patches were imaged with different dwell times: 50, 100, 200 and 300 ns, which gave sampling rates of 67 Hz, 61 Hz, 53 Hz and 47 Hz. Interestingly, recordings with good signal to noise ratio could be obtained for all dwell times, due in part to the fact that multiple voxels were averaged for each biological structure imaged.

These results show that random-access patch imaging is a new imaging method well suited for monitoring neuronal activity in 10 – 200 neurons distributed in 3D during behaviour.

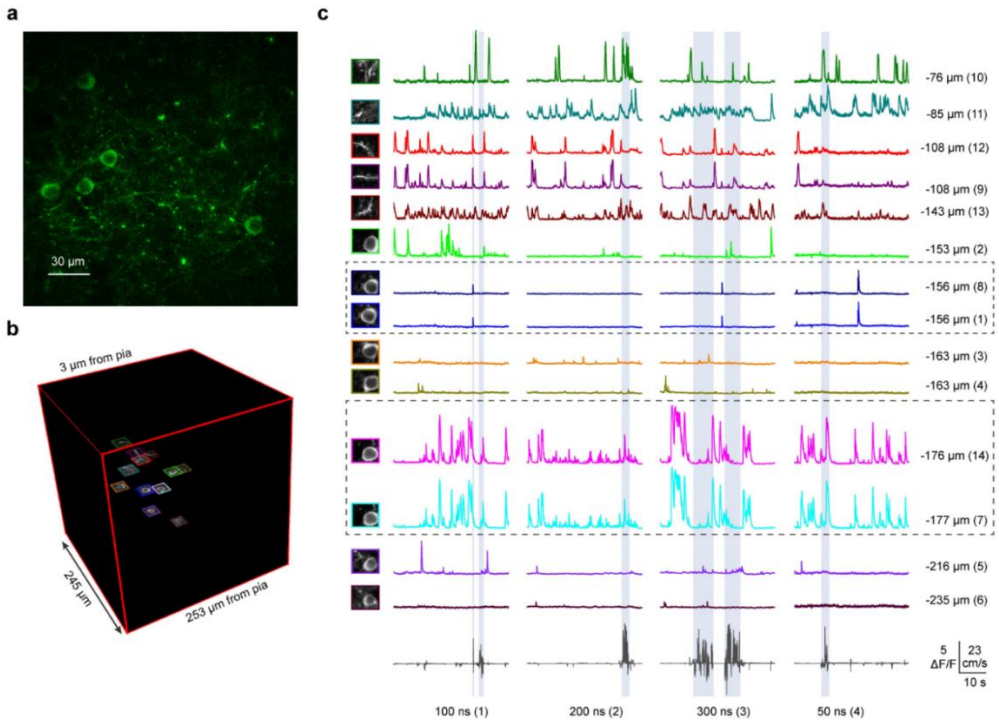

Figure 7.2 Random-access patch imaging of layer 2/3 neurons expressing only GCaMP6f in primary visual cortex of awake behaving mouse using different dwell times and post hoc movement correction. a: image from a Z-stack showing the cells in layer 2/3 visual cortex sparsely expressing GCaMP6f. b: location of 14 selected X-Y patches (46 x 40 voxels, 22 µm x 19.4 µm) within the imaging volume, distributed between 76 µm to 235 µm below the pia. c: averaged movement corrected images of cellular structures scanned near-simultaneously in the 14 patches. Traces to the right show Δf/f responses extracted from each patch when imaged at 50, 100, 200 and 300 ns/voxel dwell time. Numbers within brackets at the bottom indicate measurement sequence. Depth and patch number indicated on right. Dashed boxes indicate instances where two patches monitored the same soma. Grey trace at the bottom shows the speed of locomotion of the animal on the wheel. Grey shading indicates periods of locomotion.

7.2.2 Imaging of random-access three dimensional regions

Dendrites typically occupy only a small fraction of the total imaging volume and often project through many focal planes, therefore two dimensional regions of interest often cover only a small segment of the dendrite. Therefore, we imaged sub-volumes distributed in the volumetric field of view. Compared to imaging the full volume of a z-stack, the time resolution is significantly higher.

Three sub-volumes of interest were imaged, each consisting of 6 planes of 224 x 59 voxels, spaced 4 µm apart, encompassed the soma, a proximal dendrite and a distal

dendrite (**figure 7.3**). Using this approach, all three sub-volumes could be imaged at 27.9 Hz with a dwell time per voxel of 50 ns. A full volume z-stack covering the same volume and with the same distance between planes would take 513 ms to be acquired, resulting in a sampling rate of 1.9 Hz. Therefore, imaging only few regions of interest instead of full-frame images can substantially increase the temporal resolution.

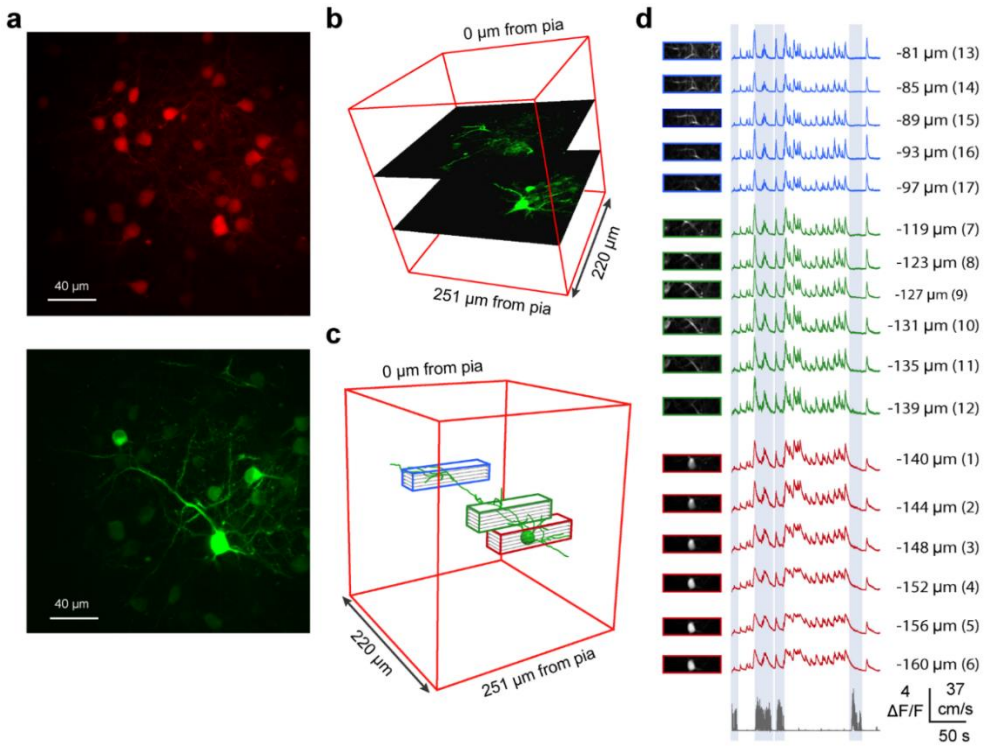

Figure 7.3 Rapid 3D multi-volume scanning of the dendrites and soma of a layer 2/3 pyramidal neuron in the visual cortex during locomotion, courtesy of Dr Hana Ros and Dr Srinivas Nadella. a: maximum intensity projection of cells in layer 2/3 visual cortex sparsely expressing td-Tomato and GCaMP6f. b: Two planes showing the somatic and dendritic sections. c: Location of 3 sub-volumes within the imaging volume together with partial reconstruction of imaged neuron that includes the soma, proximal dendrite and distal dendrite. d: Images of different regions of the pyramidal cell from the planes making up each sub-volume after post hoc movement correction. Traces show Δf/f responses extracted from the cellular component present in each plane, where red, green and blue indicate soma, proximal dendrite and distal dendrite, respectively. Grey trace at the bottom shows the speed of locomotion of the animal. Blue-grey shading indicates periods of locomotion.

7.2.3 Real time movement correction

Movement of the tissue was monitored by tracking a fluorescence reference object, which could be located anywhere in the volumetric field of view. This was achieved by periodically scanning a patch of between 10 x 10 and 20 x 20 pixels. The FPGA on the image acquisition side was configured to calculate the positon of the object within the reference scan with a centroid analysis, and the instantaneous movement 'error' was then computed using the current position and the position in the original reference image. The measured x - y shifts were then sent directly to the FPGA board controlling the AOL, which shifted the laser beam to match the lateral shifts in brain movements.

During an experiment, the functional imaging of the points of interest was interleaved with scanning the reference object to keep correcting in real time for the movements of the tissue. The reference object was typically scanned every 2-4 ms, and the time to scan the patch could vary between 0.25 and 0.57 ms, depending on the size of the patch (from 10 x 10 to 20 x 20 pixels) and the dwell time used (50, 100 or 200 ns). This incurred an overhead in temporal resolution of points' recordings by 11 – 22% when using movement correction. To examine the effectiveness of real time movement correction *in vivo*, we selected a cell body for tracking within the imaging volume, and we used the red activity-independent channel for the reference scans. Real-time tracking of cell bodies revealed that movements of several micrometres in x and y were correlated with bouts of locomotion (**figure 7.4**). When real time movement correction was activated, the AOL dynamically shifted the field of view in x and y, mirroring the brain movement. This reduced the displacement error to less than 0.51 µm (**figure 7.4 a**).

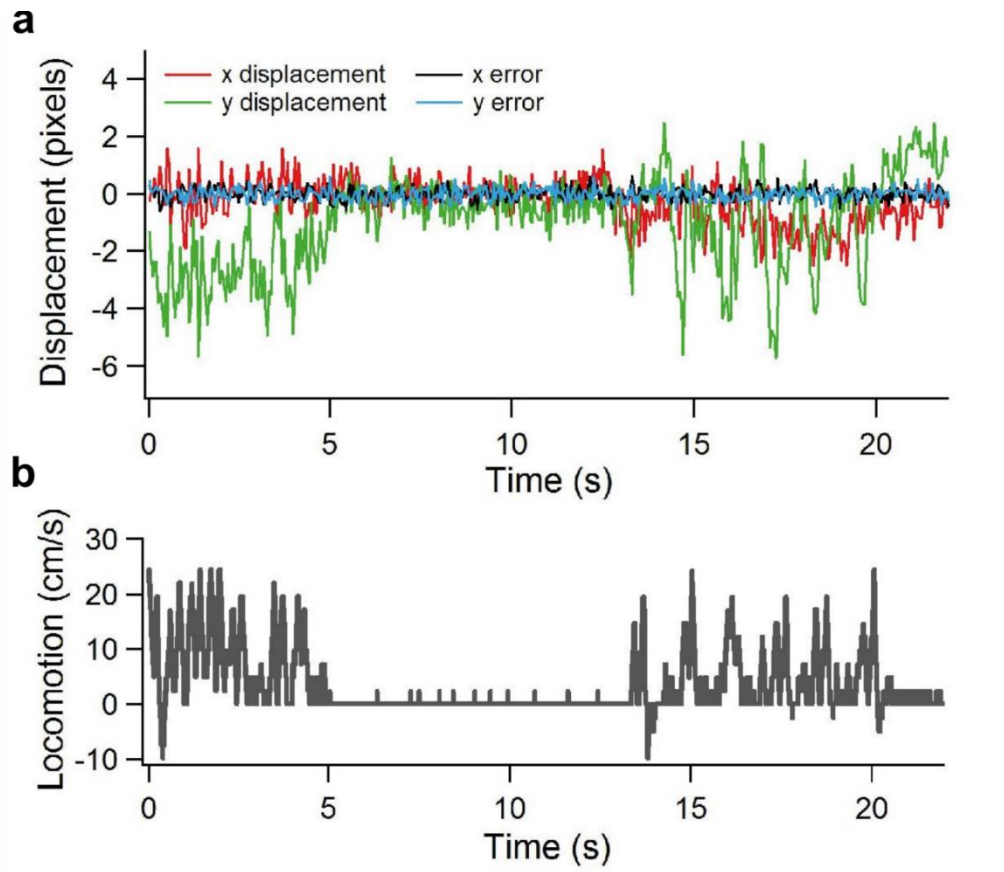

Figure 7.4 Monitoring and compensating for brain movement in an awake and behaving animal, courtesy of Dr Hana Ros and Dr Victoria Griffiths. a: Movement monitored tracking the soma of a layer 2/3 pyramidal neuron labelled with GCaMP6f and TdTomato. Only the images in the red channel were used for tracking movement, because they are activity-independent. Displacements in x and y are shown in red and green, respectively. Each pixel corresponds to 0.88μm. The residual x and y errors with real time movement correction are shown in black and blue, respectively. b: speed of the mouse on the wheel during the recordings shown in a.

To test the capabilities of online movement correction, we imaged dendritic spines, which are considerably smaller than tissue displacements, with random-access point measurements (**figure 7.5**). Points of interest were placed on spines and dendrites on different planes, and a soma was selected as a reference to track movement. We recorded from the same points with (**figure 7.5 b**) and without movement correction (**figure 7.5 c**). The data show that the recordings without movement correction were noisier, and that the calcium transients in these recordings often did not have the typical exponential rise and decay, raising the possibility that some of these transients were movement artefacts.

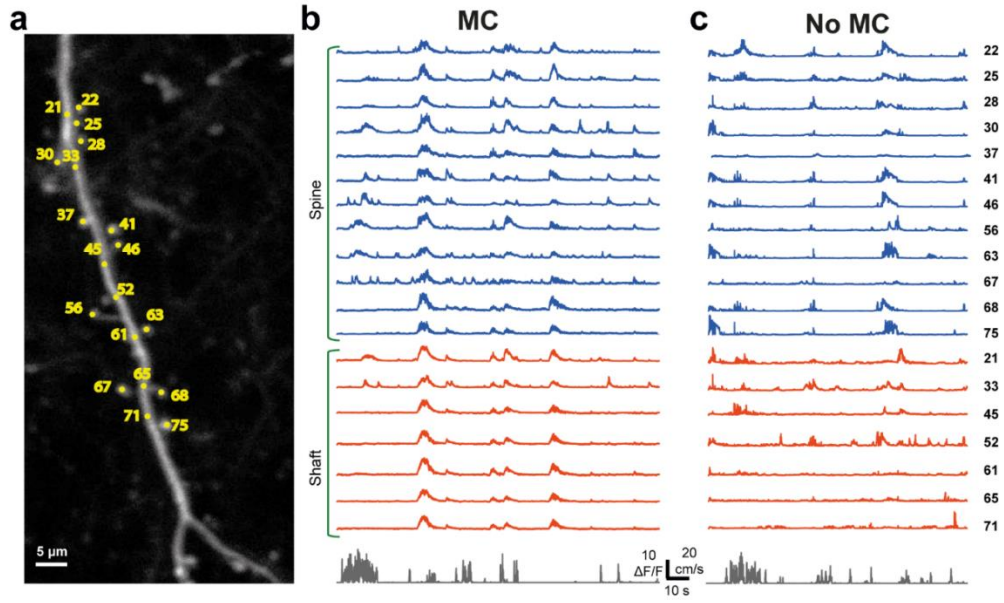

Figure 7.5 Recordings from spines in an awake and behaving animal with and without real time movement correction (MC). a: random access points of interest imaged on the dendritic shaft and on spines of al layer 2/3 pyramidal neuron labelled with GCaMP6f and TdTomato. b and c: random-access point measurements for the points shown in a, with (b) and without movement correction (c). Recordings on the spines are plotted in blue, while recordings on the shaft are displayed in orange. The speed of the mouse is shown in grey at the bottom.

To further test the performance of real time movement correction, we investigated whether we could record from axons, since action potential propagation along an axon is expected to result in highly correlated calcium signals in the presynaptic boutons. **Figure 7.6 a** shows a section of an axon in layer 2/3 of mouse visual cortex with 5 varicosities, together with the locations of the points of interest imaged. Also in this case, we imaged the same points without (**Figure 7.6 b**) and with (**Figure 7.6 c**) movement correction. In the absence of movement correction, a correlated signal was observed while the animal was stationary only in 4 of the 5 varicosities (**Figure 7.6 b**). Moreover, the red channel revealed large low frequency fluctuations in intensity indicating that the points of interest were often not on the axon. In contrast, in the presence of movement correction, the responses were clearer, and numerous calcium transients were observed synchronously in all 5 boutons, both when the animal was stationary and when the animal was running (**Figure 7.6 c**). Moreover, with movement correction the activity-independent red channel was relatively constant with no abrupt changes in intensity.

Therefore, this data suggests that real time movement correction can track and compensate for brain movements with high precision, thus allowing imaging of small biological structures in awake running mice, with just a small decrease in time resolution.

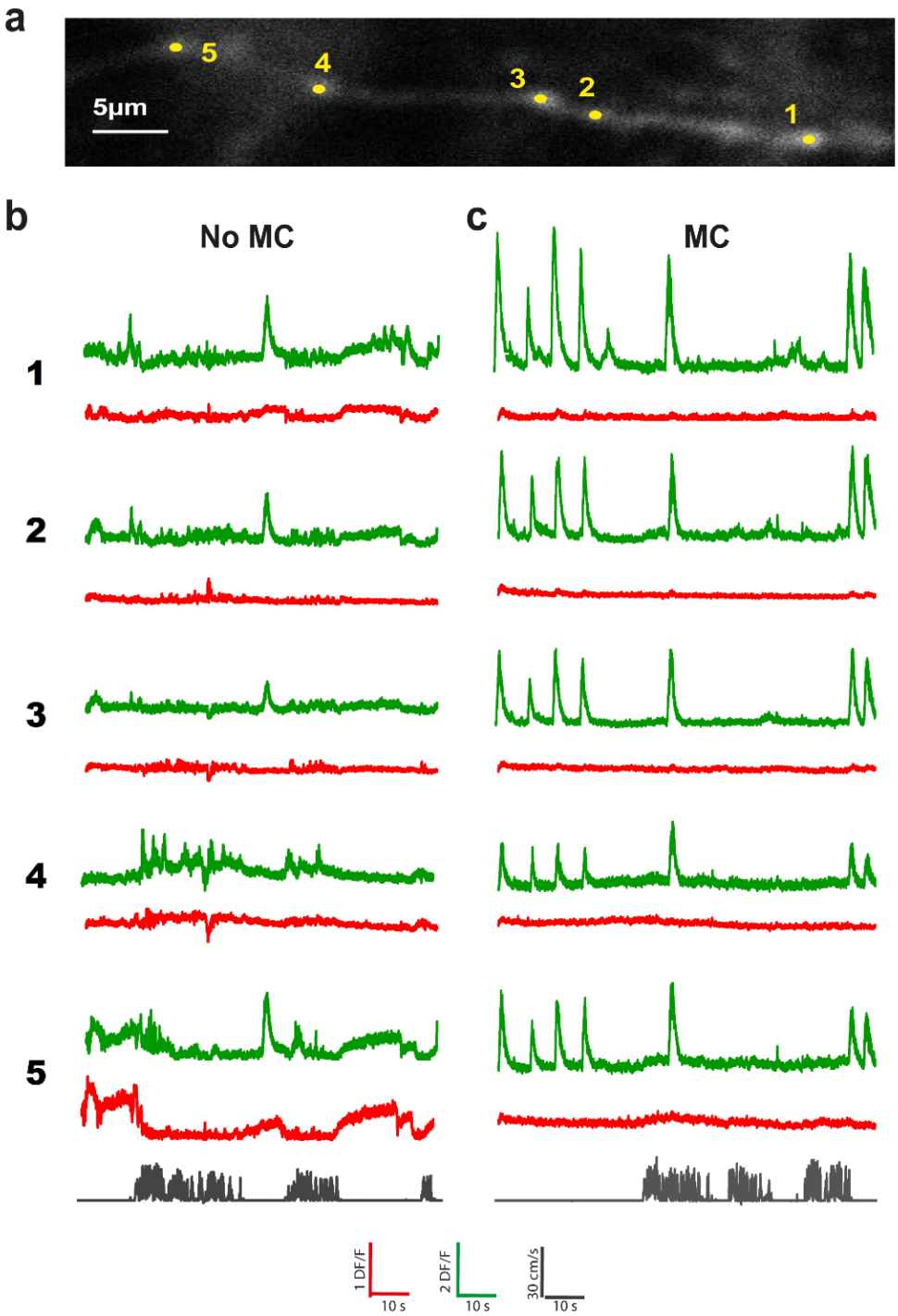

Figure 7.6 Recordings from axonal boutons in an awake and behaving animal with and without real time movement correction (MC), courtesy of Dr Hana Ros and Dr Victoria Griffiths. a: random access points of interest imaged on the varicosities of an axon in layer 2/3. Neurons were labelled with GCaMP6f and TdTomato, the image in a shows the labelling with GCaMP6f. b and c: random-access point measurements for the points shown in a, without (b) and with movement correction (c). Recordings in the green channel are shown in green, while recordings in the red channel are plotted in red. The speed of the mouse is shown in grey at the bottom.

7.3 Discussion

In conclusion, the Silver lab has developed a new generation AOL two-photon microscope that combines rapid focusing in three dimensional space with continuous line scanning in any plane, thereby overcoming a major limitation of previous AOL microscopes. This new functionality enables rapid full-frame, multiplane, random-access patch and sub-volume imaging, as well as conventional point's measurements. Furthermore, combination of AOL-imaging and FPGA-based image processing provides a new way to track and compensate for rapid brain movements with sub-micrometre accuracy.

In order to increase the speed of the line scan the dwell time had to be reduced from 4 µs to 50 – 300 ns. When the dwell time is shorter fewer photons can be collected, and the signal to noise ratio of the recordings can quickly degrade. Therefore, we could expect lower quality recordings with the new imaging modes than with points imaging. However, in patch and sub-volumes imaging, many pixels can be averaged, counteracting the effect on the signal to noise ratio. Indeed, our measurements in patches and sub-volumes still showed calcium transients with good signal to noise ratio. In addition, the post hoc movement correction reduced the noise arising from movement of the tissue. Finally, on average higher laser power was used during these experiments: 20 - 60 mW, while in the previous AOL microscope only up to 30 mW could be used because the laser had lower power. No photo-bleaching and no phototoxicity was observed even after several imaging sessions, suggesting that fast imaging with short dwell times reduces photo-bleaching compared to slow imaging with longer dwell times, as reported also by other groups (Chen et al., 2012b).

Compared to existing microscopy technologies for imaging in three dimensions, such as a combination of piezoelectric to focus and a resonant galvanometer mirror to scan, AOL imaging of patches and sub-volumes adds random-access functionality, fast focussing and uniform velocity scanning, thereby enabling fast and flexible three dimensional two-photon microscopy.

Real time movement correction enables high-quality ultra-fast recordings in random-access points, and it is likely to be used in future experiments to image dendritic spines or axonal boutons in behaving animals. At the moment, movement correction operates only in x and y, but Dr Victoria Griffiths is working to enable also movement correction in the z dimension. Furthermore, real time movement correction could be combined with fast piezoelectric micromanipulators to follow cell movement in real time enabling movement stabilization for *in vivo* whole-cell patch-clamp recordings. Moreover, it is likely to have applications in other biological fields, including cardiac

physiology and bacterial tracking, where movement is an intrinsic property of the system.

8. General discussion

8.1 Summary of main results

Dendrites of pyramidal neurons have been extensively studied *in vitro*, in brain slices and in cell cultures, and it has been shown that they can integrate synaptic inputs with a variety of linear and non-linear mechanisms. But fewer studies investigated dendritic function *in vivo*, because dendrites are difficult to access, as they are fine three dimensional structures.

In this thesis, I characterized patterns of dendritic activity in the dendrites of layer 2/3 and layer 5 pyramidal neurons in mouse V1 *in vivo*, and I investigated how presentation of visual stimuli and animal state affect dendritic activity. To do this, I used an AOL microscope developed in the Silver lab that allowed me to image in three dimensions and to monitor a large fraction of the dendritic tree near-simultaneously. I developed dual sparse labelling with the genetically-encoded calcium indicator GCaMP6f and the red fluorescent protein TdTomato. While GCaMP6f signals were used to monitor neuronal activity in the dendrites and in the soma, the activity-independent TdTomato enabled detection of movement of the tissue. Furthermore, post hoc brain fixation, clearing and staining allowed me to confirm the cortical layer of the neurons imaged.

I recorded calcium activity in the majority of dendrites and in the soma of pyramidal neurons in awake animals. Patterns of dendritic activity were characterized in the apical dendrites of layer 5 neurons and in dendrites of layer 2/3 neurons. In the apical dendrites of layer 5 neurons, the spatial distribution of dendritic calcium transients followed a bimodal distribution: mainly global events and events restricted to 1-2 branches occurred, while events where half of the dendritic tree was active were rare. Interestingly, global events were always associated with a somatic calcium transient, suggesting that either global events caused somatic activation, or they arose from backpropagating action potentials. In contrast, in layer 2/3 neurons, dendritic activity was dominated by local events, both in basal and in apical dendrites. Surprisingly, most of the somatic transients did not occur simultaneously with global events in the full dendritic tree, possibly indicating failure of action potential back propagation.

Dendritic responses to full-field gratings were also investigated. Dendrites in layer 2/3 neurons tend to have similar orientation tuning curves as the soma, but in all cells multiple dendrites with different preferred orientations were observed. In

contrast, apical dendrites of layer 5 neurons showed little or no response to visual stimuli, and in some cells gratings presentation even suppressed dendritic activity.

Dendritic activity was also measured in anaesthetized and in running animals, and it was observed that light anaesthesia suppressed activity in layer 5 apical dendrites, while locomotion enhanced it. On the other side, both apical and basal dendrites in layer 2/3 were affected only marginally by the animal state. Therefore, tuft dendrites in layer 5 neurons seem to be driven mainly by top-down inputs (animal state), while dendrites in layer 2/3 neurons receive mainly feedforward inputs (visual).

Finally, new imaging modes and real-time movement correction for the AOL microscope were developed by the microscopy development group and tested in awake mice. These technological advances are likely to be used in the near future to investigate neuronal activity in dendritic spines and axonal boutons in behaving animals.

8.2 Patterns of dendritic activity

To investigate dendritic activity *in vivo*, I used calcium imaging and measured changes in calcium concentration. Calcium entry could be mediated by voltage-gated calcium channels, calcium-induced calcium release, and/or NMDA receptors. It has been shown that pyramidal neurons in mouse V1 can support NMDA receptor-mediated dendritic events (Smith et al., 2013), but unfortunately I cannot determine the nature of the dendritic events observed because only calcium imaging was used for this study. Analogously, it is not known if the calcium transients that I observed in the dendrites were elicited by subthreshold EPSPs, and/or by regenerative events. Since the calcium indicator used, GCaMP6f, is highly non-linear (Chen et al., 2013a), it is possible that the recordings were biased towards large events, and that only supralinear events were observed.

Even though it was not possible to determine the origin of the calcium events observed, it is known that calcium transients represent dendritic activity, and it was possible to compare patterns of dendritic activity in different animal conditions and in different cells. Both in layer 2/3 and in layer 5 neurons, different types of dendritic calcium events were observed: local events (restricted to 1 branch), multi-branch events and global events. Similarly, previous studies that investigated dendritic activity in pyramidal neurons in anaesthetized animals described also three main types of calcium events: hotspots, multi-branch events and global events

(Grienberger et al., 2014; Hill et al., 2013; Jia et al., 2010; Palmer et al., 2014; Wilson et al., 2016; Xu et al., 2012). Hotspots are localised to a small portion of the dendritic branch (approximately 4 µm) (Grienberger et al., 2014; Jia et al., 2010; Palmer et al., 2014), multi-branch events occur simultaneously in multiple neighbouring branches (Grienberger et al., 2014; Hill et al., 2013; Palmer et al., 2014), while global events spread across all dendrites (Hill et al., 2013; Xu et al., 2012). Unfortunately, in my experiments it was not possible to characterize the spatial extent of calcium events inside a dendritic branch since only few POIs were placed in each dendritic branch in a non-systematic way. Therefore, the local events observed in my experiments could be hotspots restricted to a few micrometres, and/or calcium events occurring in the full dendritic branch.

Even if the types of calcium events that I observed were similar to previous reports, in my data local events were prevalent both in layer 2/3 and in layer 5 neurons, while previous studies found that global or multi-branch events occurred more often than local events (Grienberger et al., 2014; Palmer et al., 2014). These discrepancies could be caused by the different animal state: these studies were performed on anaesthetized animals, while my experiments were carried out in awake animals. Since in awake animals the levels of inhibition are higher (Haider et al., 2013), the number of global and multi-branch events could be reduced. To compare the results presented in this thesis with the papers mentioned above, I also tried to characterize the number of local, multi-branch and global events in anaesthetized animals. But dendrites of layer 5 neurons had too little activity when the animal was anaesthetized, so the number of calcium transients was too low and this analysis could not be carried out. For dendrites of layer 2/3 neurons, some cells also had little activity while the animal was anaesthetized, while the other neurons gave contrasting results (data not shown). Unfortunately, it was then not possible to draw any conclusion about the spatial spread of the calcium events in anaesthetized animals.

But in 2012 Xu et al. imaged tuft dendrites of layer 5 neurons in somatosensory cortex of awake animals, and they observed only global events, while in my experiments more than 50% of the observed events were localized to only one or two dendritic branches. But in the experiments reported by Xu et al., only two-dimensional images were acquired, therefore it is possible that local events were missed due to limited sampling of the dendritic tree. In addition, the animals were performing an object-localization task, and maybe the higher levels of attention and/or the expectation of a reward changed the dendritic activity of these neurons. Alternatively, it is also possible that dendrites in visual cortex and dendrites in barrel cortex behave differently.

Interestingly, in the experiments reported here, the spatial distribution of calcium events in the apical dendrites of layer 5 neurons followed a bimodal distribution. This bimodal distribution resulted from the tendency of calcium events to be either global or localized to only 1-2 branches. This data shows that activity in the tuft is not a gradual response, where different numbers of branches are equally likely to be active. Instead, only few dendritic branches or all branches were activated, resulting in a bimodal distribution instead of a uniform distribution. Indeed, the spatial distribution of calcium events measured was significantly different from a uniform distribution (one-sample Kolmogorov-Smirnov test, p-value < 0.0001). The global events detected were always associated with a calcium transient in the soma, thus these global dendritic events could be backpropagating action potentials, and/or dendritic regenerative events that triggered somatic action potentials. In the second case, the bimodal distribution of the dendritic events might suggest that there is cooperativity between dendritic spikes in different branches (Farinella et al., 2014; Major et al., 2008), and that when a critical number of dendrites is active, the dendritic events depolarize also the other tuft dendrites and activate the full tuft. Alternatively, it has been shown in acute brain slices that a critical number of dendrites active can reach the threshold to activate a global calcium spike, which can then spread into the full tuft (Larkum et al., 2009). In summary, these data suggest that dendritic integration in the tuft comprise two non-linear processes: first a threshold to generate a dendritic spike, such as an NMDA spike, and secondly a threshold to activate the full tuft. In the future, it would be interesting to repeat the experiments applying NMDA receptors blockers or calcium channels antagonists, in order to investigate which channels mediate the global events in the tuft.

In conclusion, the data reported in this thesis shows that dendritic trees of pyramidal neurons exhibit local, multi-branch and global calcium transients, in agreement with previous studies. But in the experiments described here, an AOL microscope was used for the first time to monitor dendritic activity *in vivo*, thus I was able to image in three dimensions and to record from an unprecedented number of dendrites near-simultaneously. I could then characterize the patterns of dendritic activity in layer 2/3 and in layer 5 pyramidal neurons in V1 in awake animals, and I observed that local events are predominant in layer 2/3 neurons, while the spatial distribution of the calcium events in tuft dendrites of layer 5 neurons follows a bimodal distribution. These data indicate that dendritic activation in the tuft of layer 5 neurons is non-linear.

8.3 Coupling of dendrites and soma in layer 2/3 neurons

When characterizing patterns of dendritic activity in layer 2/3 neurons, perhaps the most surprising result was that somatic calcium transients were often not associated with dendritic events in all imaged dendrites, suggesting that action potentials fail regularly to backpropagate in the dendritic branches of layer 2/3 neurons.

Since calcium imaging was used to monitor neuronal activity, small signals might be missed (Grewe et al., 2010; Hofer et al., 2011; Vogelstein et al., 2009), but backpropagating action potentials should generate strong calcium signals, thus these events are usually detected clearly. It is then unlikely that calcium entry triggered by backpropagating action potentials was not detected due to insufficient signal-to-noise ratio. But it is possible that the number of dendritic events not associated with an action potential was overestimated, because somatic calcium transients generated by single action potentials have small amplitudes and could have been missed. It is then possible that only calcium events triggered by more than 2 action potentials were detected. During an experiment, mainly cells that showed high levels of activity were targeted, and, since the firing rates of layer 2/3 neurons in awake animals can vary between 0 and 20 Hz (Crochet et al., 2011), it is likely that mainly cells with a high firing rate were imaged.

Dendritic calcium events could have been missed if the imaged POIs were not on the dendrite during the recording. However, the fluorescence in the red channel was used to monitor movement of the tissue. Furthermore, in some cases, a continuous recording of a few points on the same dendrite showed one transient associated with a somatic calcium transient, and a few seconds later the same points showed no activity during a second somatic transient. Most of these recordings were also inspected visually, and no variations in the red fluorescence were observed. It seems then unlikely that dendritic events triggered by backpropagating action potentials were missed due to an artefact.

However, other studies *in vivo* reported reliable backpropagation of action potentials in layer 2/3 neurons, especially in basal dendrites (Hill et al., 2013; Jia et al., 2010). But in these studies, the experiments were carried out in anaesthetized animals, where inhibition levels are lower (Haider et al., 2013). Indeed, in a more recent study in pyramidal neurons in the hippocampus of awake animals, the authors mentioned that they did not observe reliable activation of dendritic branches when the soma was active (Sheffield and Dombeck, 2015).

Since in my experiments dendritic branches that were closer to the soma did not have higher probability of being active during a somatic calcium transient, failure of backpropagating action potentials was probably not caused by the filtering properties of the dendrites. Indeed, the dendrites imaged were usually only 100 - 150 µm far from the soma. It is then possible that some dendritic branches are less excitable than others (Makara and Magee, 2013), and/or have less calcium transients. The calcium transients observed in my experiments might have been mediated by voltage-gated calcium channels, and it is possible that some dendritic branches did not express these channels and could not support calcium entry. However, all dendritic branches imaged displayed some calcium events during the experiments. Alternatively, if the dendritic events were mainly mediated by NMDA receptors, then backpropagating action potentials would elicit calcium entry in a dendrite only if the local NMDA receptors were bound to glutamate. In this case, backpropagating action potentials would trigger calcium transients in a branch-specific manner, and could lead to a "patchy" activation of the dendritic tree, similarly to what I observed in my experiments. This hypothesis could be tested in acute brain slices, where calcium transients triggered by backpropagating action potentials could be monitored in the presence and in absence of glutamate.

Another possibility is that strong levels of inhibition *in vivo* could reduce or prevent action potential backpropagation in a branch-specific manner. A recent study in acute brain slices indeed showed that inhibition can strongly reduce calcium transients triggered by action potential backpropagation (Müllner et al., 2015), while anatomical and modelling studies suggest that inhibitory synapses are located in strategic positions to have optimal control over dendritic regenerative events and backpropagating action potentials (Bloss et al., 2016). But it remains to be determined whether inhibitory inputs can be strong enough to block calcium transients triggered by backpropagating action potentials. It would then be very interesting to manipulate the levels of inhibition *in vivo* or *in vitro*, either pharmacologically or with optogenetic tools, and to observe the effects on dendritic activity.

Since calcium transients triggered by backpropagating action potentials play a crucial role in mediating synaptic plasticity (Magee and Johnston, 1997), lack of calcium entry in some dendritic branches could limit synaptic potentiation or depression. In this case, synaptic plasticity would not depend only on the timing of the inputs, but also on the position of the synapses in the dendritic tree. It would be very important then to investigate the causes of failures of calcium entry during backpropagating action potentials, because they could be key players in gating synaptic plasticity.

8.4 Coupling of dendrites and soma in layer 5 neurons

In layer 5 neurons, I observed that 84% of the somatic events were associated with calcium transients that occurred in at least half of the dendritic tuft. Surprisingly, somatic calcium transients were associated with global dendritic events more often in the tuft of layer 5 neurons (31.5% of the somatic transients) than in the dendrites of layer 2/3 neurons (4.9% of the somatic transients). In contrast with previous studies in acute brain slices, these data suggest that *in vivo* apical dendrites in layer 5 neurons are more tightly coupled to the soma than dendrites of layer 2/3 neurons.

This difference in soma-dendrite coupling between layer 2/3 and layer 5 neurons might be due to the different firing rates of these two cell types. Layer 5 neurons have higher firing rates and display more bursts of action potentials than layer 2/3 neurons (studies summarized in Barth and Poulet, 2012), and high-frequency action potentials are more likely to backpropagate efficiently across the dendritic tree. In my experiments, mainly layer 2/3 cells with high levels of activity were targeted, but spike extraction algorithms were not used, therefore the firing rates of the neurons imaged are not known. In order to monitor more accurately somatic activity, it would then be useful to repeat these experiments patching the soma and imaging the dendrites in layer 5 neurons, and look at natural patterns of activity in layer 5 cells.

But surprisingly, in a previous report where calcium imaging and whole-cell patch clamp was used, it was found that somatic activity was uncoupled from tuft activity in layer 5 pyramidal cells (Hill et al., 2013). The experimental conditions in this study were slightly different: the experiments were carried out in anaesthetized animals, only few dendritic branches were imaged simultaneously, and the experiments were done on a different brain region (motor cortex). Indeed, I observed that anaesthesia can strongly suppress dendritic activity in layer 5 pyramidal neurons, so it is possible that it affects also the coupling between the tuft and the soma. Furthermore, I observed that in layer 5 pyramidal cells all the somatic calcium transients were associated with a calcium event in at least one tuft dendrite, but most somatic events were not associated with a global dendritic event. It is then possible that, since Hill et al were imaging only 1-2 dendritic branches at the time, they detected almost only global events associated with a somatic transient, therefore the number of dendritic events associated with a somatic transient might have been underestimated. Finally, it is also possible that pyramidal neurons in different brain areas show different patterns of dendritic activity.

Indeed, several studies in acute brain slices of somatosensory and motor cortex reported that only bursts of action potentials reached the tuft of layer 5 neurons

(Larkum et al., 1999b; Stuart and Sakmann, 1994; Stuart et al., 1997b; Waters et al., 2003), while Dr Thomas Younts in the lab clearly observed that even single action potentials reached tuft dendrites in V1 brain slices (unpublished data). Therefore, it is possible that tuft dendrites in layer 5 neurons in V1 are more excitable than in other cortical areas. At the moment, Dr Thomas Younts is addressing this question repeating the experiments on slices from somatosensory cortex, and also trying different slicing solutions, to check whether different protocols for slice preparation could affect the excitability of the cells.

In conclusion, I observed that in layer 5 pyramidal neurons the activity in the tuft dendrites is more coupled to the soma than previously reported, while somatic activity in layer 2/3 neurons is less correlated to dendritic activity than previously thought. It would be important to investigate the mechanisms underlying these phenomena to better understand dendritic integration *in vivo*.

8.5 Responses to visual stimuli in dendrites

Dendritic responses to gratings of different orientations showed that dendrites in layer 2/3 neurons can have different preferred orientations from the soma. This data is consistent with previous experiments performed in mice and ferrets, where it was shown that each dendrite receives different sensory inputs (Jia et al., 2010; Smith et al., 2013; Wilson et al., 2016). Surprisingly, dendritic events that were not associated with somatic calcium transients were sparse. It is puzzling that the somatic transients responded more reliably to visual stimuli than the dendritic events, but it is possible that the application of a threshold to generate action potentials filters noise signals and generates a more reliable output. Alternatively, it is possible that dendritic calcium activity did not entirely reflect voltage, and that only regenerative events were observed with calcium imaging. In this case, subthreshold events might be more reliable but were not detected.

Finally, tuft dendrites of layer 5 neurons were found to be modulated primarily by top-down inputs (animal state), and they showed little responses to visual stimuli. But interestingly, a recent study showed that mice that learnt a behavioural task increased the responsiveness to relevant stimuli in mouse V1 (Poort et al., 2015). It would then be interesting to measure activity in tuft dendrites of layer 5 neurons while mice perform a behavioural task. In this case, the visual stimuli would become more relevant to the animal, and it would be possible to investigate whether “interesting” stimuli elicit more visually-evoked responses in the dendrites of layer 5 neurons. In

addition, depending on the behavioural task, it might also be possible to study whether attention can modulate dendritic activity.

8.6 Modulation of dendritic activity by animal state

Similarly to previous reports, I observed that anaesthesia strongly suppresses neuronal activity in the tuft dendrites of layer 5 neurons (Murayama and Larkum, 2009; Potez and Larkum, 2008), while dendritic activity in layer 2/3 neurons was not significantly affected (Adesnik et al., 2012; Palmer et al., 2014; Smith et al., 2013).

In the experiments presented in this thesis, the anaesthetic used was isoflurane. This drug has multiple effects, and it is also a competitive antagonist of NMDA receptors (Nishikawa and MacIver, 2000). Suppression of dendritic activity might have then been mediated by blockade of NMDA receptors, but since it was selective for layer 5 dendrites, other mechanisms might be involved.

In contrast, locomotion enhanced dendritic activity in tuft dendrites of layer 5 neurons. This data might be surprising, considering that it was reported that locomotion can suppress neuronal activity in infragranular layers of V1 (Erisken et al., 2014). However, this effect was very small and present only in a subset of neurons, while on the other side locomotion is known to increase activity dramatically in the whole network in layer 2/3 (Keller et al., 2012; Niell and Stryker, 2010; Saleem et al., 2013). Therefore dendritic activity could be higher due to increased excitatory inputs. Furthermore, one study reported that locomotion increased the activity of VIP-expressing interneurons, which disinhibit SOM interneurons (Fu et al., 2014); since SOM interneurons target preferentially the dendrites of pyramidal cells, dendritic activity could be increased also due to disinhibition. However, it was also reported that SOM neurons increase their activity during locomotion in visual cortex (Pakan et al., 2016; Polack et al., 2013). Furthermore, in my data dendritic activity in layer 2/3 neurons was only marginally affected by locomotion. It then remains to be investigated which mechanisms could drive increased dendritic activity selectively in the tuft dendrites of layer 5 neurons.

To address this question, in future experiments channelrhodopsin and/or archaerhodopsin could be expressed in different classes of inhibitory neurons, to manipulate the levels of activity of different interneurons and examine the effects on dendritic activity in layer 2/3 and layer 5 pyramidal neurons. These experiments

could help to investigate the effects of inhibition on dendritic activity, and they could shed light on the microcircuit involved in driving dendritic activity during locomotion.

8.7 Conclusions and future directions

In this thesis I showed that the AOL microscope can be used with a fluorescent protein and a genetically-encoded calcium indicator to monitor dendritic activity in three dimensions and at high speeds in awake behaving animals. Imaging random-access points in three dimensions enabled recordings of neuronal activity in most of the dendritic tree and in the soma near-simultaneously in mouse V1. In addition, new imaging modes such as multi-plane imaging, random-access patches and sub-volumes, and real time movement correction have recently been implemented and tested on awake animals.

In my experiments, I characterized patterns of dendritic activity in layer 2/3 and in layer 5 pyramidal neurons in response to visual stimuli in awake and in anaesthetized animals. Interestingly, these data showed that somatic transients are often not accompanied by global dendritic events in layer 2/3 neurons, while the tuft of layer 5 neurons was more tightly coupled to the soma than previously thought. In addition, layer 5 apical dendrites were often activated by global events, while in layer 2/3 neurons dendritic activity was mainly restricted to local calcium events. Finally, dendrites in layer 2/3 neurons responded mainly to visual stimuli (feedforward inputs), while activity in apical dendrites of layer 5 neurons was modulated primarily by the animal state (top-down).

These data suggest that apical dendrites of layer 5 neurons and dendrites of layer 2/3 neurons use different integration mechanisms and process different types of inputs *in vivo*. These differences might be due to the different roles of these neurons in processing sensory information: layer 2/3 neurons could represent and amplify specific features of a visual scene, and they might use sparse synaptic activation and sparse codes because they are more efficient. In contrast, layer 5 neurons might play a key role in combining sensory information with top-down inputs, and activation of the full tuft could be necessary to couple the distal apical dendrites, that receive top-down inputs, with oblique and basolateral dendrites, which receive mainly feedforward inputs (Cauller, 1995; Cauller et al., 1998; Douglas and Martin, 2004; Nieuwenhuys, 1994; Petreanu et al., 2009).

It is important to note that mainly superficial layer 2/3 neurons were targeted (100 - 250 µm from pia), and it is possible that deeper layer 2/3 neurons have a behaviour more similar to layer 5 neurons. It would then be interesting to characterize dendritic activity also in neurons deeper in layer 2/3 and in layer 4, to investigate whether there is a continuum or whether cells in different layers have clearly distinguished patterns of dendritic activity. Furthermore, it would be interesting to compare patterns

of dendritic activity across different cell types, for example dendritic activity in interneurons could be characterized using a very similar approach to the one presented here (using a PV-Cre or SOM-Cre mouse line instead of injecting Cre-virus).

For the next experiments, combination of calcium imaging and patch-clamp techniques would enable us to investigate the nature of the dendritic calcium transients observed. For example, loading the NMDA receptor blocker MK-801 intracellularly via the patching pipette would suppress NMDA spikes, while the compound QX-314 would block sodium spikes (Grienberger et al., 2014; Palmer et al., 2012). These tools would then allow to isolate the contribution of different voltage-gated conductances to the dendritic calcium transients observed.

Furthermore, real-time movement correction and/or random-access patch imaging can be used to image small structures such as dendritic spines in awake animals. For example, it would be possible to study whether synaptic inputs are spatially and temporally clustered on the dendrites, in order to investigate how dendritic spikes are generated *in vivo*. This question has already been addressed in multiple studies (Chen et al., 2011; Jia et al., 2010; Takahashi et al., 2012; Varga et al., 2011), but the results of these studies are conflicting and experiments were always performed on anaesthetized animals. In ferrets, clustering of excitatory inputs seems to have a crucial role in determining the orientation selectivity of the neurons (Wilson et al., 2016), but it is not clear whether the same mechanism is present in mice, where orientation columns are absent. Furthermore, it would be interesting to map different sensory inputs (auditory, visual, somatosensory) on the dendritic tree of pyramidal neurons, and to investigate whether inputs from different sensory modalities are interspersed in the dendritic tree, or whether similar inputs localize preferentially on the same dendrites.

Bibliography

Adesnik, H., Bruns, W., Taniguchi, H., Huang, Z.J., and Scanziani, M. (2012). A neural circuit for spatial summation in visual cortex. Nature *490*, 226–231.

Allman, J., Miezin, F., and McGuinness, E. (1985). Responses from beyond the classical receptive field : Neurophysiological Mechanisms for Local-Global Comparisons in Visual Neurons. Annu. Rev. Neurosci. *8*, 407–430.

Andermann, M.L., Kerlin, A.M., Roumis, D.K., Glickfeld, L.L., and Reid, R.C. (2011). Functional specialization of mouse higher visual cortical areas. Neuron *72*, 1025–1039.

Angelucci, A., and Bressloff, P.C. (2006). Contribution of feedforward, lateral and feedback connections to the classical receptive field center and extra-classical receptive field surround of primate V1 neurons. Prog. Brain Res. *154*, 93–120.

Antic, S.D., Zhou, W.-L., Moore, A.R., Short, S.M., and Ikonomu, K.D. (2010). The decade of the dendritic NMDA spike. J. Neurosci. Res. *88*, 2991–3001.

Atallah, B. V., Bruns, W., Carandini, M., and Scanziani, M. (2012). Parvalbumin-Expressing Interneurons Linearly Transform Cortical Responses to Visual Stimuli. Neuron *73*, 159–170.

Ayaz, A., Saleem, A.B., Schölvinck, M.L., and Carandini, M. (2013). Locomotion Controls Spatial Integration in Mouse Visual Cortex. Curr. Biol. *23*, 890–894.

Balkema, G.W., and Pinto, L.H. (1982). Electrophysiology of retinal ganglion cells in the mouse: a study of a normally pigmented mouse and a congenic hypopigmentation mutant, pearl. J. Neurophysiol. *48*, 968–980.

Barth, A.L., and Poulet, J.F.A. (2012). Experimental evidence for sparse firing in the neocortex. Trends Neurosci. *35*, 345–355.

Berger, T., Senn, W., and Lüscher, H.-R. (2003). Hyperpolarization-activated current Ih disconnects somatic and dendritic spike initiation zones in layer V pyramidal neurons. J. Neurophysiol. *90*, 2428–2437.

Berson, D.M. (2014). Intrinsically Photosensitive Retinal Ganglion Cells. In The New Visual Neurosciences, J.S. Werner, and L.M. Chalupa, eds. (MIT Press), pp. 183–196.

Berson, D.M., Dunn, F. a, and Takao, M. (2002). Phototransduction by retinal ganglion cells that set the circadian clock. Science *295*, 1070–1073.

Blakemore, C., and Tobin, E.A. (1972). Lateral inhibition between orientation detectors in the cat's visual cortex. Exp. Brain Res. *15*, 439–440.

Bloss, E.B., Cembrowski, M.S., Karsh, B., Colonell, J., Fetter, R.D., and Spruston, N. (2016). Structured Dendritic Inhibition Supports Branch-Selective Integration in CA1 Pyramidal Cells. Neuron *89*, 1–15.

Borg-Graham, L.J., Monier, C., and Fregnac, Y. (1998). Visual input evokes transient and strong shunting inhibition in visual cortical neurons. Nature *393*, 369–373.

Brainard, D.H. (1997). The Psychophysics Toolbox. Spat. Vis. *10*, 433–436.

Branco, T., and Hausser, M. (2011). Synaptic Integration Gradients in Single Cortical Pyramidal Cell Dendrites. Neuron *69*, 885–892.

Branco, T., and Häusser, M. (2010). The single dendritic branch as a fundamental functional unit in the nervous system. Curr. Opin. Neurobiol. *20*, 494–502.

Branco, T., Clark, B.A., and Hausser, M. (2010). Dendritic discrimination of temporal input sequences in cortical neurons. Science *329*, 1671–1675.

Briggs, F. (2010). Organizing principles of cortical layer 6. Front. Neural Circuits *4*, 1–3.

Briggs, F., and Usrey, W.M. (2008). Emerging views of corticothalamic function. Curr. Opin. Neurobiol. *18*, 403–407.

Briggs, F., Mangun, G.R., and Usrey, W.M. (2013). Attention enhances synaptic efficacy and the signal-to-noise ratio in neural circuits. Nature *499*, 476–480.

Buhl, E.H., and Peichl, L. (1986). Morphology of rabbit retinal ganglion cells projecting to the medial terminal nucleus of the accessory optic system. J. Comp. Neurol. *253*, 163–174.

Burkhalter, A., and Bernardo, K.L. (1989). Organization of corticocortical connections in human visual cortex. Proc. Natl. Acad. Sci. U. S. A. *86*, 1071–1075.

Calderone, J.B., and Jacobs, G.H. (1995). Regional variations in the relative sensitivity to UV light in the mouse retina. Vis. Neurosci. *12*, 463–468.

Cash, S., Yuste, R., b, C.S.., and R.a, Y. (1998). Input summation by cultured pyramidal neurons is linear and position- independent. J. Neurosci. *18*, 10–15.

Cauller, L. (1995). Layer I of primary sensory neocortex: where top-down converges upon bottom-up. Behav. Brain Res. *71*, 163–170.

Cauller, L.J., Clancy, B., and Connors, B.W. (1998). Backward Cortical Projections to Primary Somatosensory Cortex in Rats Extend Long Horizontal Axons in Layer I. J. Comp. Neurol. *390*, 297–310.

Chalifoux, J.R., and Carter, A.G. (2011). GABAB Receptor Modulation of Voltage-Sensitive Calcium Channels in Spines and Dendrites. J. Neurosci. *31*, 4221–4232.

Chen, J.L., Villa, K.L., Cha, J.W., So, P.T.C., Kubota, Y., and Nedivi, E. (2012a). Clustered Dynamics of Inhibitory Synapses and Dendritic Spines in the Adult Neocortex. Neuron *74*, 361–373.

Chen, T.-W., Wardill, T.J., Sun, Y., Pulver, S.R., Renninger, S.L., Baohan, A., Schreiter, E.R., Kerr, R.A., Orger, M.B., Jayaraman, V., et al. (2013a). Ultrasensitive fluorescent proteins for imaging neuronal activity. Nature *499*, 295–300.

Chen, X., Leischner, U., Rochefort, N.L., Nelken, I., and Konnerth, A. (2011). Functional mapping of single spines in cortical neurons in vivo. Nature *475*, 501–505.

Chen, X., Leischner, U., Varga, Z., Jia, H., Deca, D., Rochefort, N.L., and Konnerth, A. (2012b). LOTOS-based two-photon calcium imaging of dendritic spines in vivo. Nat. Protoc. *7*, 1818–1829.

Chen, X., Rochefort, N.L., Sakmann, B., and Konnerth, A. (2013b). Reactivation of the same synapses during spontaneous up states and sensory stimuli. Cell Rep. *4*, 31–39.

Chiu, C.Q., Lur, G., Morse, T.M., Carnevale, N.T., Ellies-Davies, G.C.R., and Higley, M.J. (2013). Compartmentalization of GABAergic inhibition by dendritic spines. Science *340*, 759–762.

Clements, J.D., and Bekkers, J.M. (1997). Detection of spontaneous synaptic events with an optimally scaled template. Biophys. J. *73*, 220–229.

Colbert, C.M., Magee, J.C., Hoffman, D. a, and Johnston, D. (1997). Slow recovery

from inactivation of Na+ channels underlies the activity-dependent attenuation of dendritic action potentials in hippocampal CA1 pyramidal neurons. J. Neurosci. *17*, 6512–6521.

Constantinople, C.M., and Bruno, R.M. (2013). Deep cortical layers are activated directly by thalamus. Science *340*, 1591–1594.

Conti, F., Hille, B., Neumcke, B., Nonner, W., and Stampfli, R. (1976). Measurement of the Conductance of the sodium channel from current fluctuation. J Physiol. *262*, 699–727.

Cossell, L., Iacaruso, M.F., Muir, D.R., Houlton, R., Sader, E.N., Ko, H., Hofer, S.B., and Mrsic-flogel, T.D. (2015). Functional organization of excitatory synaptic strength in primary visual cortex. Nature *518*, 399–403.

Cotton, R.J., Froudarakis, E., Storer, P., Saggau, P., and Tolias, A.S. (2013). Three-dimensional mapping of microcircuit correlation structure. Front. Neural Circuits *7*, 151.

Crochet, S., Poulet, J.F. a, Kremer, Y., and Petersen, C.C.H. (2011). Synaptic mechanisms underlying sparse coding of active touch. Neuron *69*, 1160–1175.

Cruz-Martín, A., El-Danaf, R.N., Osakada, F., Sriram, B., Dhande, O.S., Nguyen, P.L., Callaway, E.M., Ghosh, A., and Huberman, A.D. (2014). A dedicated circuit links direction-selective retinal ganglion cells to the primary visual cortex. Nature *507*, 358–361.

Cuntz, H., Forstner, F., Borst, A., and Häusser, M. (2010). One rule to grow them all: A general theory of neuronal branching and its practical application. PLoS Comput. Biol. *6*, e1000877.

Dacey, D. (2004). Origins of perception: retinal ganglion cell diversity and the creation of parallel visual pathways. In The Cognitive Neurosciences III, M.S. Gazzaniga, ed. (MIT Press), pp. 281–301.

Dacey, D.M. (2000). Parallel Pathways for Spectral Coding in Primate Retina. Annu. Rev. Neurosci. *23*, 743–775.

Dacey, D.M., and Lee, B.B. (1994). The “blue-on” opponent pathway in primate retina originates from a distinct bistratified ganglion cell type. Nature *367*, 731–735.

De Franceschi, G., Vivattanasarn, T., Saleem, A.B., and Solomon, S.G. (2016). Vision Guides Selection of Freeze or Flight Defense Strategies in Mice. Curr. Biol. *26*, 2150–2154.

Denman, D.J., and Contreras, D. (2014). The structure of pairwise correlation in mouse primary visual cortex reveals functional organization in the absence of an orientation map. Cereb. Cortex *24*, 2707–2720.

Denman, D.J., and Contreras, D. (2015). Complex Effects on In Vivo Visual Responses by Specific Projections from Mouse Cortical Layer 6 to Dorsal Lateral Geniculate Nucleus. J. Neurosci. *35*, 9265–9280.

Dombeck, D. a, Khabbaz, A.N., Collman, F., Adelman, T.L., and Tank, D.W. (2007). Imaging large-scale neural activity with cellular resolution in awake, mobile mice. Neuron *56*, 43–57.

Douglas, R.J., and Martin, K.A.C. (2004). Neuronal Circuits of the Neocortex. Annu. Rev. Neurosci. *27*, 419–451.

Dräger, U.C. (1975). Receptive fields of single cells and topography in mouse visual cortex. J. Comp. Neurol. *160*, 269–290.

Druckmann, S., Feng, L., Lee, B., Yook, C., Zhao, T., Magee, J.C., and Kim, J. (2014). Structured Synaptic Connectivity between Hippocampal Regions. Neuron *81*, 629–640.

Edmonds, B., Gibb, A.J., and Colquhoun, D. (1995). Mechanisms of activation of glutamate receptors and the time course of excitatory synaptic currents. Annu. Rev. Physiol. *57*, 495–519.

Egger, R., Schmitt, A.C., Wallace, D.J., Sakmann, B., Oberlaender, M., and Kerr, J.N.D. (2015). Robustness of sensory-evoked excitation is increased by inhibitory inputs to distal apical tuft dendrites. Proc. Natl. Acad. Sci. U. S. A. *112*, 14072–14077.

Eldar, E., Cohen, J.D., and Niv, Y. (2013). The effects of neural gain on attention and learning. Nat. Neurosci. *16*, 1146–1153.

Erisken, S., Vaiceliunaite, A., Jurjut, O., Fiorini, M., Katzner, S., and Busse, L. (2014). Effects of locomotion extend throughout the mouse early visual system. Curr. Biol. *24*, 2899–2907.

Farinella, M., Ruedt, D.T., Gleeson, P., Lanore, F., and Silver, R.A. (2014). Glutamate-Bound NMDARs Arising from In Vivo-like Network Activity Extend Spatio-temporal Integration in a L5 Cortical Pyramidal Cell Model. PLoS Comput. Biol. *10*, e1003590.

Feldmeyer, D. (2012). Excitatory neuronal connectivity in the barrel cortex. Front. Neuroanat. *6*, 1–22.

Feldmeyer, D., Lübke, J., Silver, R.A., and Sakmann, B. (2002). Synaptic connections between layer 4 spiny neurone-layer 2/3 pyramidal cell pairs in juvenile rat barrel cortex: physiology and anatomy of interlaminar signalling within a cortical column. J. Physiol. *538*, 803–822.

Feng, L., Zhao, T., and Kim, J. (2015). neuTube 1.0: A New Design for Efficient Neuron Reconstruction Software Based on the SWC Format. eNeuro *2*, ENEURO.0049–14.2014.

Fernández-Alfonso, T., Nadella, K.M.N.S., Iacaruso, M.F., Pichler, B., Roš, H., Kirkby, P. a, and Silver, R.A. (2014). Monitoring synaptic and neuronal activity in 3D with synthetic and genetic indicators using a compact acousto-optic lens two-photon microscope. J. Neurosci. Methods *222*, 69–81.

Franks, N.P., and Lieb, W.R. (1994). Molecular and cellular mechanisms of general anaesthesia. Nature *367*, 607–614.

Fu, Y., Tucciarone, J.M., Espinosa, J.S., Sheng, N., Darcy, D.P., Nicoll, R.A., Huang, Z.J., and Stryker, M.P. (2014). A cortical circuit for gain control by behavioral state. Cell *156*, 1139–1152.

Gentet, L.J., Kremer, Y., Taniguchi, H., Huang, Z.J., Staiger, J.F., and Petersen, C.C.H. (2012). Unique functional properties of somatostatin-expressing GABAergic neurons in mouse barrel cortex. Nat. Neurosci. *15*, 607–612.

Gianfranceschi, L., Fiorentini, A., and Maffei, L. (1999). Behavioural visual acuity of wild type and bcl 2 transgenic mouse. Vision Res. *39*, 569–574.

Gibb, A.J., and Colquhoun, D. (1992). ACTIVATION OF N-METHYL-D-ASPARTATE RECEPTORS BY L-GLUTAMATE IN CELLS DISSOCIATED FROM ADULT RAT HIPPOCAMPUS. J. Physiol. *456*, 143–179.

Gidon, A., and Segev, I. (2012). Principles Governing the Operation of Synaptic

Inhibition in Dendrites. Neuron *75*, 330–341.

Gilbert, C.D., and Wiesel, T.N. (1990). The influence of contextual stimuli on the orientation selectivity of cells in primary visual cortex of the cat. Vision Res. *30*, 1689–1701.

Gilzenrat, M.S., Nieuwenhuis, S., and Cohen, J.D. (2012). Pupil diameter tracks changes in control state predicted by the adaptive gain theory of locus coeruleus function. Cogn Affect Behav Neurosci *10*, 252–269.

Golding, N.L., Staff, N.P., and Spruston, N. (2002). Dendritic spikes as a mechanism for cooperative long-term potentiation. Nature *418*, 326–331.

Golding, N.L., Mickus, T.J., Katz, Y., Kath, W.L., and Spruston, N. (2005). Factors mediating powerful voltage attenuation along CA1 pyramidal neuron dendrites. J. Physiol. *568*, 69–82.

Goldstein, S.S., and Rall, W. (1974). Changes of Action Potential Shape and Velocity for Changing Core Conductor Geometry. Biophys. J. *14*, 731–757.

Gollisch, T., and Meister, M. (2010). Eye smarter than scientists believed: neural computations in circuits of the retina. Neuron *65*, 150–164.

Greenberg, D.S., Houweling, A.R., and Kerr, J.N.D. (2008). Population imaging of ongoing neuronal activity in the visual cortex of awake rats. Nat. Neurosci. *11*, 749–751.

Grewe, B.F., Langer, D., Kasper, H., Kampa, B.M., and Helmchen, F. (2010). High-speed in vivo calcium imaging reveals neuronal network activity with near-millisecond precision. Nat. Methods *7*, 399–405.

Grienberger, C., Chen, X., and Konnerth, A. (2014). NMDA receptor-dependent multidendrite Ca(2+) spikes required for hippocampal burst firing in vivo. Neuron *81*, 1274–1281.

Grienberger, C., Chen, X., and Konnerth, A. (2015). Dendritic function in vivo. Trends Neurosci. *38*, 45–54.

Grubb, M.S., and Thompson, I.D. (2003). Quantitative characterization of visual response properties in the mouse dorsal lateral geniculate nucleus. J. Neurophysiol. *90*, 3594–3607.

Grubb, M.S., and Thompson, I.D. (2005). Visual Response Properties of Burst and Tonic Firing in the Mouse Dorsal Lateral Geniculate Nucleus. J. Neurophysiol. *93*, 3224–3247.

Haider, B., Häusser, M., and Carandini, M. (2013). Inhibition dominates sensory responses in the awake cortex. Nature *493*, 97–100.

Harnett, M.T., Xu, N.-L., Magee, J.C., and Williams, S.R. (2013). Potassium channels control the interaction between active dendritic integration compartments in layer 5 cortical pyramidal neurons. Neuron *79*, 516–529.

Harnett, M.T., Magee, J.C., and Williams, S.R. (2015). Distribution and Function of HCN Channels in the Apical Dendritic Tuft of Neocortical Pyramidal Neurons. J. Neurosci. *35*, 1024–1037.

Harris, K.D., and Mrsic-Flogel, T.D. (2013). Cortical connectivity and sensory coding. Nature *503*, 51–58.

Helmchen, F., Svoboda, K., Denk, W., and Tank, D.W. (1999). In vivo dendritic calcium dynamics in deep-layer neocortical pyramidal neurons. Nature *2*, 989–996.

Higley, M.J. (2014). Localized GABAergic inhibition of dendritic Ca(2+) signalling. Nat. Rev. Neurosci. *15*, 567–572.

Hill, D.N., Varga, Z., Jia, H., Sakmann, B., and Konnerth, A. (2013). Multibranch activity in basal and tuft dendrites during firing of layer 5 cortical neurons in vivo. Proc. Natl. Acad. Sci. U. S. A. *110*, 13618–13623.

Hô, N., and Destexhe, a (2000). Synaptic background activity enhances the responsiveness of neocortical pyramidal neurons. J. Neurophysiol. *84*, 1488–1496.

Hofer, S.B., Ko, H., Pichler, B., Vogelstein, J., Ros, H., Zeng, H., Lein, E., Lesica, N. a, and Mrsic-Flogel, T.D. (2011). Differential connectivity and response dynamics of excitatory and inhibitory neurons in visual cortex. Nat. Neurosci. *14*, 1045–1052.

Hoffman, D. a, Magee, J.C., Colbert, C.M., and Johnston, D. (1997). K+ channel regulation of signal propagation in dendrites of hippocampal pyramidal neurons. Nature *387*, 869–875.

Hubel, B.Y.D.H., and Wiesel, A.D.T.N. (1962). RECEPTIVE FIELDS, BINOCULAR INTERACTION AND FUNCTIONAL ARCHITECTURE IN THE CAT ' S VISUAL

CORTEX. J. Physiol. *160*, 106–154.

Hübener, M. (2003). Mouse visual cortex. Curr. Opin. Neurobiol. *13*, 413–420.

Huberman, A.D., and Niell, C.M. (2011). What can mice tell us about how vision works? Trends Neurosci. *34*, 464–473.

Ibrahim, L.A., Mesik, L., Ji, X., Zingg, B., Zhang, L.I., Ibrahim, L.A., Mesik, L., Ji, X., Fang, Q., Li, H., et al. (2016). Cross-Modality Sharpening of Visual Cortical Processing through Layer-1-Mediated Inhibition and Article Cross-Modality Sharpening of Visual Cortical Processing through Layer-1-Mediated Inhibition and Disinhibition. Neuron *89*, 1–15.

Jeon, C.J., Strettoi, E., and Masland, R.H. (1998). The major cell populations of the mouse retina. J. Neurosci. *18*, 8936–8946.

Jia, H., Rochefort, N.L., Chen, X., and Konnerth, A. (2010). Dendritic organization of sensory input to cortical neurons in vivo. Nature *464*, 1307–1312.

Jia, H., Varga, Z., Sakmann, B., and Konnerth, A. (2014). Linear integration of spine Ca2+ signals in layer 4 cortical neurons in vivo. Proc. Natl. Acad. Sci. U. S. A. *111*, 9277–9282.

Johnson, J.W., and Ascher, P. (1987). Glycine potentiates the NMDA response in cultured mouse brain neurons. Nature *325*, 529–531.

Jung, H.Y., Mickus, T., and Spruston, N. (1997). Prolonged sodium channel inactivation contributes to dendritic action potential attenuation in hippocampal pyramidal neurons. J. Neurosci. *17*, 6639–6646.

Kaifosh, P., Zaremba, J., and Danielson, N. (2014). SIMA: Python software for analysis for calcium imaging data. Front. Neuroinformatics, Prep. *8*, 1–10.

Kaplan, a, Friedman, N., and Davidson, N. (2001). Acousto-optic lens with very fast focus scanning. Opt. Lett. *26*, 1078–1080.

Katona, G., Szalay, G., Maák, P., Kaszás, A., Veress, M., Hillier, D., Chiovini, B., Vizi, E.S., Roska, B., and Rózsa, B. (2012). Fast two-photon in vivo imaging with three-dimensional random-access scanning in large tissue volumes. Nat. Methods *9*, 201–208.

Keller, G.B., Bonhoeffer, T., and Hübener, M. (2012). Sensorimotor mismatch

signals in primary visual cortex of the behaving mouse. Neuron *74*, 809–815.

Kim, H.G., and Connors, B.W. (1993). Apical dendrites of the neocortex: correlation between sodium- and calcium-dependent spiking and pyramidal cell morphology. J. Neurosci. *13*, 5301–5311.

Kim, E.J., Juavinett, A.L., Kyubwa, E.M., Jacobs, M.W., and Callaway, E.M. (2015). Three Types of Cortical Layer 5 Neurons That Differ in Brain-wide Connectivity and Function. Neuron *88*, 1253–1267.

Kirkby, P.A., Srinivas Nadella, K.M.N., and Silver, R.A. (2010). A compact Acousto-Optic Lens for 2D and 3D femtosecond based 2-photon microscopy. Opt. Express *18*, 13721–13745.

Klausberger, T., and Somogyi, P. (2008). Neuronal diversity and temporal dynamics: the unity of hippocampal circuit operations. Science *321*, 53–57.

Kleiner, M., Brainard, D., and Pelli, D. (2007). What ' s new in Psychtoolbox-3 ? Eur. Conf. Vis. Percept.

Ko, H., Hofer, S.B., Pichler, B., Buchanan, K. a, Sjöström, P.J., and Mrsic-Flogel, T.D. (2011). Functional specificity of local synaptic connections in neocortical networks. Nature *473*, 87–91.

Koch, C., Poggio, T., and Torre, V. (1983). Nonlinear interactions in a dendritic tree: localization, timing, and role in information processing. Proc. Natl. Acad. Sci. U. S. A. *80*, 2799–2802.

Koch, C., Rapp, M., and Segev, I. (1996). A brief history of time (constants). Cereb. Cortex *6*, 93–101.

Kole, M.H.P., and Stuart, G.J. (2008). Is action potential threshold lowest in the axon? Nat. Neurosci. *11*, 1253–1255.

Kondo, S., and Ohki, K. (2015). Laminar differences in the orientation selectivity of geniculate afferents in mouse primary visual cortex. Nat. Neurosci. *19*, 1–6.

Kredel, S., Oswald, F., Nienhaus, K., Deuschle, K., Röcker, C., Wolff, M., Heilker, R., Nienhaus, G.U., and Wiedenmann, J. (2009). mRuby, a bright monomeric red fluorescent protein for labeling of subcellular structures. PLoS One *4*, e4391.

Larkman, A.U. (1991). Dendritic Morphology of Pyramidal Neurones of the Visual

Cortex of the Rat: III. Spine Distributions. J. Comp. Neurol. *306*, 332–343.

Larkman, A., and Mason, A. (1990). Correlations between morphology and electrophysiology of pyramidal neurons in slices of rat visual cortex. I. Establishment of cell classes. J. Neurosci. *10*, 1407–1414.

Larkum, M.E., and Zhu, J.J. (2002). Signaling of layer 1 and whisker-evoked Ca2+ and Na+ action potentials in distal and terminal dendrites of rat neocortical pyramidal neurons in vitro and in vivo. J. Neurosci. *22*, 6991–7005.

Larkum, M.E., Zhu, J.J., and Sakmann, B. (1999a). A new cellular mechanism for coupling inputs arriving at different cortical layers. Nature *398*, 338–341.

Larkum, M.E., Kaiser, K.M., and Sakmann, B. (1999b). Calcium electrogenesis in distal apical dendrites of layer 5 pyramidal cells at a critical frequency of back-propagating action potentials. Proc. Natl. Acad. Sci. U. S. A. *96*, 14600–14604.

Larkum, M.E., Senn, W., and Lüscher, H.-R. (2004). Top-down dendritic input increases the gain of layer 5 pyramidal neurons. Cereb. Cortex *14*, 1059–1070.

Larkum, M.E., Nevian, T., Sandler, M., Polsky, A., and Schiller, J. (2009). Synaptic Integration in Tuft Dendrites of Layer 5 Pyramidal Neurons: a New Unifiying Principle. Science *325*, 756–760.

Lavzin, M., Rapoport, S., Polsky, A., Garion, L., and Schiller, J. (2012). Nonlinear dendritic processing determines angular tuning of barrel cortex neurons in vivo. Nature *490*, 397–401.

Lee, A.M., Hoy, J.L., Bonci, A., Wilbrecht, L., Stryker, M.P., and Niell, C.M. (2014). Identification of a brainstem circuit regulating visual cortical state in parallel with locomotion. Neuron *83*, 455–466.

Ling, C., Schneider, G.E., and Jhaveri, S. (1998). Target-specific morphology of retinal axon arbors in the adult hamster. Vis. Neurosci. *15*, 559–579.

Ling, S., Pratte, M.S., and Tong, F. (2015). Attention alters orientation processing in the human lateral geniculate nucleus. Nat. Neurosci. *18*, 496–498.

London, M., and Häusser, M. (2005). Dendritic computation. Annu. Rev. Neurosci. *28*, 503–532.

Longordo, F., To, M.-S., Ikeda, K., and Stuart, G.J. (2013). Sublinear integration

underlies binocular processing in primary visual cortex. Nat. Neurosci. *16*, 714–723.

Lovett-Barron, M., Turi, G.F., Kaifosh, P., Lee, P.H., Bolze, F., Sun, X.-H., Nicoud, J.-F., Zemelman, B. V, Sternson, S.M., and Losonczy, A. (2012). Regulation of neuronal input transformations by tunable dendritic inhibition. Nat. Neurosci. *15*, 423–430.

Ma, W., Liu, B., Li, Y., Huang, Z.J., Zhang, L.I., and Tao, H.W. (2010). Visual representations by cortical somatostatin inhibitory neurons--selective but with weak and delayed responses. J. Neurosci. *30*, 14371–14379.

Madisen, L., Zwingman, T. a, Sunkin, S.M., Oh, S.W., Zariwala, H. a, Gu, H., Ng, L.L., Palmiter, R.D., Hawrylycz, M.J., Jones, A.R., et al. (2010). A robust and high-throughput Cre reporting and characterization system for the whole mouse brain. Nat. Neurosci. *13*, 133–140.

Magee, J.C., and Cook, E.P. (2000). Somatic EPSP amplitude is independent of synapse location in hippocampal pyramidal neurons. Nat. Neurosci. *3*, 895–903.

Magee, J.C., and Johnston, D. (1997). A synaptically controlled, associative signal for Hebbian plasticity in hippocampal neurons. Science *275*, 209–213.

Major, G., Polsky, A., Denk, W., Schiller, J., and Tank, D.W. (2008). Spatiotemporally Graded NMDA Spike / Plateau Potentials in Basal Dendrites of Neocortical Pyramidal Neurons. J. Neurophysiol. *99*, 2584–2601.

Major, G., Larkum, M.E., and Schiller, J. (2013). Active properties of neocortical pyramidal neuron dendrites. Annu. Rev. Neurosci. *36*, 1–24.

Makara, J.K., and Magee, J.C. (2013). Variable Dendritic Integration in Hippocampal CA3 Pyramidal Neurons. Neuron *80*, 1438–1450.

Maldonado, P.E., and Babul, C.M. (2007). Neuronal activity in the primary visual cortex of the cat freely viewing natural images. Neuroscience *144*, 1536–1543.

Markram, H., Toledo-Rodriguez, M., Wang, Y., Gupta, A., Silberberg, G., and Wu, C. (2004). Interneurons of the neocortical inhibitory system. Nat. Rev. Neurosci. *5*, 793–807.

Marshel, J.H., Kaye, A.P., Nauhaus, I., and Callaway, E.M. (2012). Anterior-posterior direction opponency in the superficial mouse lateral geniculate nucleus. Neuron *76*,

713–720.

Masland, R.H. (2001). The fundamental plan of the retina. Nat. Neurosci. *4*, 877–886.

Masland, R.H. (2012). The neuronal organization of the retina. Neuron *76*, 266–280.

Megías, M., Emri, Z., Freund, T.F., and Gulyás, a I. (2001). Total number and distribution of inhibitory and excitatory synapses on hippocampal CA1 pyramidal cells. Neuroscience *102*, 527–540.

Mel, B.W. (1993). Synaptic integration in an excitable dendritic tree. J. Neurophysiol. *70*, 1086–1101.

Merigan, W.H., and Maunsell, J.H.R. (1993). How parallel are the primate visual pathways? Annu. Rev. Neurosci. *16*, 369–402.

Milojkovic, B.A., Wuskell, J.P., Loew, L.M., and Antic, S.D. (2005). Initiation of sodium spikelets in basal dendrites of neocortical pyramidal neurons. J. Membr. Biol. *208*, 155–169.

Mineault, P.J., Tring, E., Trachtenberg, J.T., and Ringach, D.L. (2016). Enhanced Spatial Resolution During Locomotion and Heightened Attention in Mouse Primary Visual Cortex. J. Neurosci. *36*, 6382–6392.

Morgenstern, N.A., Bourg, J., and Petreanu, L. (2016). Multilaminar networks of cortical neurons integrate common inputs from sensory thalamus. Nat. Neurosci. *19*, 1034–1040.

Mrsic-Flogel, T.D., Hofer, S.B., Ohki, K., Reid, R.C., Bonhoeffer, T., and Hübener, M. (2007). Homeostatic regulation of eye-specific responses in visual cortex during ocular dominance plasticity. Neuron *54*, 961–972.

Müllner, F.E., Wierenga, C.J., and Bonhoeffer, T. (2015). Precision of Inhibition: Dendritic Inhibition by Individual GABAergic Synapses on Hippocampal Pyramidal Cells Is Confined in Space and Time. Neuron *87*, 576–589.

Murayama, M., and Larkum, M.E. (2009). Enhanced dendritic activity in awake rats. Proc. Natl. Acad. Sci. U. S. A. *106*, 20482–20486.

Murayama, M., Pérez-Garci, E., Nevian, T., Bock, T., Senn, W., and Larkum, M.E. (2009). Dendritic encoding of sensory stimuli controlled by deep cortical

interneurons. Nature *457*, 1137–1141.

Nassi, J.J., and Callaway, E.M. (2009). Parallel processing strategies of the primate visual system. Nat. Rev. Neurosci. *10*, 360–372.

Nelson, J.I., and Frost, B.J. (1978). Orientation-selective inhibition from beyond the classic visual receptive field. Brain Res. *139*, 359–365.

Nevian, T., Larkum, M.E., Polsky, A., and Schiller, J. (2007). Properties of basal dendrites of layer 5 pyramidal neurons: a direct patch-clamp recording study. Nat. Neurosci. *10*, 206–214.

Nicholson, D.A., Trana, R., Katz, Y., Kath, W.L., Spruston, N., and Geinisman, Y. (2006). Distance-Dependent Differences in Synapse Number and AMPA Receptor Expression in Hippocampal CA1 Pyramidal Neurons. Neuron *50*, 431–442.

Niell, C.M., and Stryker, M.P. (2008). Highly selective receptive fields in mouse visual cortex. J. Neurosci. *28*, 7520–7536.

Niell, C.M., and Stryker, M.P. (2010). Modulation of visual responses by behavioral state in mouse visual cortex. Neuron *65*, 472–479.

Nienborg, H., Hasenstaub, A., Nauhaus, I., Taniguchi, H., Huang, Z.J., and Callaway, E.M. (2013). Contrast dependence and differential contributions from somatostatin- and parvalbumin-expressing neurons to spatial integration in mouse V1. J. Neurosci. *33*, 11145–11154.

Nieuwenhuys, R. (1994). The neocortex. Anat. Embryol. (Berl). *190*, 307–337.

Nishikawa, K., and MacIver, M.B. (2000). Excitatory synaptic transmission mediated by NMDA receptors is more sensitive to isoflurane than are non-NMDA receptor-mediated responses. Anesthesiology *92*, 228–236.

Ohki, K., Chung, S., Ch'ng, Y.H., Kara, P., and Reid, R.C. (2005). Functional imaging with cellular resolution reveals precise micro-architecture in visual cortex. Nature *433*, 597–603.

Okun, M., and Lampl, I. (2008). Instantaneous correlation of excitation and inhibition during ongoing and sensory-evoked activities. Nat. Neurosci. *11*, 535–537.

Olivas, N.D., Quintanar-Zilinskas, V., Nenadic, Z., and Xu, X. (2012). Laminar circuit organization and response modulation in mouse visual cortex. Front. Neural Circuits

6, 1–21.

Pakan, J.M.P., Lowe, S.C., Dylda, E., Keemink, S.W., Currie, S.P., Coutts, C.A., and Rochefort, N.L. (2016). Behavioral-state modulation of inhibition is context-dependent and cell type specific in mouse visual cortex. Elife *5*, e14985.

Palmer, L.M., Schulz, J.M., Murphy, S.C., Ledergerber, D., Murayama, M., and Larkum, M.E. (2012). The Cellular Basis of GABAb mediated interhemispheric inhibition. Science *335*, 989–993.

Palmer, L.M., Shai, A.S., Reeve, J.E., Anderson, H.L., Paulsen, O., and Larkum, M.E. (2014). NMDA spikes enhance action potential generation during sensory input. Nat. Neurosci. *17*, 383–390.

Pelli, D.G. (1997). The VideoToolbox software for visual psychophysics: transforming numbers into movies. Spat. Vis. *10*, 437–442.

Peng, H., Ruan, Z., Long, F., Simpson, J.H., and Myers, E.W. (2010). V3D enables real-time 3D visualization and quantitative analysis of large-scale biological image data sets. Nat. Biotechnol. *28*, 348–353.

Peng, H., Bria, A., Zhou, Z., Iannello, G., and Long, F. (2014). Extensible visualization and analysis for multidimensional images using Vaa3D. Nat. Protoc. *9*, 193–208.

Pérez-Garci, E., Larkum, M.E., and Nevian, T. (2013). Inhibition of dendritic Ca2+ spikes by GABAB receptors in cortical pyramidal neurons is mediated by a direct Gi/o-β-subunit interaction with Cav1 channels. J. Physiol. *591*, 1599–1612.

Petreanu, L., Mao, T., Sternson, S.M., and Svoboda, K. (2009). The subcellular organization of neocortical excitatory connections. Nature *457*, 1142–1145.

Pfeffer, C.K., Xue, M., He, M., Huang, Z.J., and Scanziani, M. (2013). Inhibition of inhibition in visual cortex: the logic of connections between molecularly distinct interneurons. Nat. Neurosci. *16*, 1068–1076.

Pinto, L., Goard, M.J., Estandian, D., Xu, M., Kwan, A.C., Lee, S.-H., Harrison, T.C., Feng, G., and Dan, Y. (2013). Fast modulation of visual perception by basal forebrain cholinergic neurons. Nat. Neurosci. *16*, 1857–1863.

Pisauro, M. a., Dhruv, N.T., Carandini, M., and Benucci, a. (2013). Fast

Hemodynamic Responses in the Visual Cortex of the Awake Mouse. J. Neurosci. *33*, 18343–18351.

Piscopo, D.M., El-Danaf, R.N., Huberman, a. D., and Niell, C.M. (2013). Diverse Visual Features Encoded in Mouse Lateral Geniculate Nucleus. J. Neurosci. *33*, 4642–4656.

Poirazi, P., Brannon, T., and Mel, B.W. (2003). Pyramidal Neuron as Two-Layered Neural Network. Neuron *37*, 989–999.

Polack, P.-O., Friedman, J., and Golshani, P. (2013). Cellular mechanisms of brain state-dependent gain modulation in visual cortex. Nat. Neurosci. *16*, 1331–1339.

Polsky, A., Mel, B.W., and Schiller, J. (2004). Computational subunits in thin dendrites of pyramidal cells. Nat. Neurosci. *7*, 621–627.

Polsky, A., Mel, B., and Schiller, J. (2009). Encoding and decoding bursts by NMDA spikes in basal dendrites of layer 5 pyramidal neurons. J. Neurosci. *29*, 11891–11903.

Poort, J., Khan, A.G., Pachitariu, M., Nemri, A., Orsolic, I., Krupic, J., Bauza, M., Sahani, M., Keller, G.B., Mrsic-Flogel, T.D., et al. (2015). Learning Enhances Sensory and Multiple Non-sensory Representations in Primary Visual Cortex. Neuron *86*, 1478–1490.

Potez, S., and Larkum, M.E. (2008). Effect of Common Anesthetics on Dendritic Properties in Layer 5 Neocortical Pyramidal Neurons. J. Neurophysiol. *99*, 1394–1407.

Preibisch, S., Saalfeld, S., and Tomancak, P. (2009). Globally optimal stitching of tiled 3D microscopic image acquisitions. Bioinformatics *25*, 1463–1465.

Prusky, G.T., and Douglas, R.M. (2003). Developmental plasticity of mouse visual acuity. Eur. J. Neurosci. *17*, 167–173.

Qu, J., and Myhr, K.L. (2011). The morphology and intrinsic excitability of developing mouse retinal ganglion cells. PLoS One *6*, e21777.

Rall, W. (1967). Distinguishing theoretical synaptic potentials computed for different soma-dendritic distributions of synaptic input. J. Neurophysiol. *30*, 1138–1168.

Ramon y Cajal, S. (1909). Histologie du Systeme Nerveux de l'Homme et des

Vertebres. (Paris: A. Maloine Editeur).

Rathbun, D.L., Warland, D.K., and Usrey, W.M. (2010). Spike timing and information transmission at retinogeniculate synapses. J. Neurosci. *30*, 13558–13566.

Reimer, J., Froudarakis, E., Cadwell, C.R., Yatsenko, D., Denfield, G.H., and Tolias, A.S. (2014). Pupil Fluctuations Track Fast Switching of Cortical States during Quiet Wakefulness. Neuron *84*, 355–362.

Remtulla, S., and Hallett, P.E. (1985). A schematic eye for the mouse, and comparisons with the rat. Vision Res. *25*, 21–31.

Ringach, D.L. (2002). Spatial Structure and Symmetry of Simple-Cell Receptive Fields in Macaque Primary Visual Cortex. J. Neurophysiol. *88*, 455–463.

Rose, T., Jaepel, J., Hübener, M., and Bonhoeffer, T. (2016). Cell-specific restoration of stimulus preference after monocular deprovation in visual cortex. Science *352*, 1319–1322.

Ross, W.N., and Larkum, M. (2012). Dendrites. In eLS, (Chichester: John Wiley & Sons, Ltd), pp. 1–7.

Roth, M.M., Dahmen, J.C., Muir, D.R., Imhof, F., Martini, F.J., and Hofer, S.B. (2016). Thalamic nuclei convey diverse contextual information to layer 1 of visual cortex. Nat. Neurosci. *19*, 148.

Saleem, A.B., Ayaz, A., Jeffery, K.J., Harris, K.D., and Carandini, M. (2013). Integration of visual motion and locomotion in mouse visual cortex. Nat. Neurosci. *16*, 1864–1869.

Sanes, J.R., and Masland, R.H. (2015). The Types of Retinal Ganglion Cells: Current Status and Implications for Neuronal Classification. Annu. Rev. Neurosci. *38*, 221–246.

Schiller, J., Schiller, Y., Stuart, G., and Sakmann, B. (1997). Calcium action-potentials restricted to distal apical dendrites of rat neocortical pyramidal neurons. J. Physiol. *505*, 605–616.

Schiller, J., Major, G., Koester, H.J., and Schiller, Y. (2000). NMDA spikes in basal dendrites of cortical pyramidal neurons. Nature *404*, 285–289.

Schmucker, C., Seeliger, M., Humphries, P., Biel, M., and Schaeffel, F. (2005).

Grating acuity at different luminances in wild-type mice and in mice lacking rod or cone function. Investig. Ophthalmol. Vis. Sci. *46*, 398–407.

Scholl, B., Tan, A.Y.Y., Corey, J., and Priebe, N.J. (2013). Emergence of orientation selectivity in the Mammalian visual pathway. J. Neurosci. *33*, 10616–10624.

Semyanov, A., Walker, M.C., Kullmann, D.M., and Silver, R.A. (2004). Tonically active GABAA receptors: Modulating gain and maintaining the tone. Trends Neurosci. *27*, 262–269.

Shadlen, M.N., and Newsome, W.T. (1994). Noise, neural codes and cortical organization. Curr. Opin. Neurobiol. *4*, 569–579.

Shaner, N.C., Campbell, R.E., Steinbach, P.A., Giepmans, B.N.G., Palmer, A.E., and Tsien, R.Y. (2004). Improved monomeric red, orange and yellow fluorescent proteins derived from Discosoma sp. red fluorescent protein. Nat. Biotechnol. *22*, 1567–1572.

Sheffield, M.E.J., and Dombeck, D.A. (2015). Calcium transient prevalence across the dendritic arbour predicts place field properties. Nature *517*, 200–204.

Shuler, M.G., and Bear, M.F. (2006). Reward Timing in the Primary Visual Cortex. Science *311*, 1606–1609.

Silberberg, G., and Markram, H. (2007). Disynaptic Inhibition between Neocortical Pyramidal Cells Mediated by Martinotti Cells. Neuron *53*, 735–746.

Silver, R.A. (2010). Neuronal arithmetic. Nat. Rev. Neurosci. *11*, 474–489.

Sjostrom, P.J., Rancz, E.A., Roth, A., and Hausser, M. (2008). Dendritic Excitability and Synaptic Plasticity. Physiol Rev *88*, 769–840.

Smith, S.L., and Häusser, M. (2010). Parallel processing of visual space by neighboring neurons in mouse visual cortex. Nat. Neurosci. *13*, 1144–1149.

Smith, S.L., Smith, I.T., Branco, T., and Häusser, M. (2013). Dendritic spikes enhance stimulus selectivity in cortical neurons in vivo. Nature *503*, 115–120.

Sohya, K., Kameyama, K., Yanagawa, Y., Obata, K., and Tsumoto, T. (2007). GABAergic neurons are less selective to stimulus orientation than excitatory neurons in layer II/III of visual cortex, as revealed by in vivo functional Ca2+ imaging in transgenic mice. J. Neurosci. *27*, 2145–2149.

Sorra, K., and Harris, K.M. (1993). Occurrence and three-dimensional structure of multiple synapses between individual radiatum axons and their target pyramidal cells in hippocampal area CA1. J. Neurosci. *13*, 3736–3748.

Spruston, N. (2008). Pyramidal neurons: dendritic structure and synaptic integration. Nat. Rev. Neurosci. *9*, 206–221.

Stuart, G., and Spruston, N. (1998). Determinants of voltage attenuation in neocortical pyramidal neuron dendrites. J. Neurosci. *18*, 3501–3510.

Stuart, G.J., and Häusser, M. (2001). Dendritic coincidence detection of EPSPs and action potentials. Nat. Neurosci. *4*, 63–71.

Stuart, G.J., and Sakmann, B. (1994). Active propagation of somatic action potentials into neocortical pyramidal cell dendrites. Nature *367*, 69–72.

Stuart, G., Spruston, N., Sakmann, B., and Hausser, M. (1997a). Action potential initiation and back propagation in neurons of the mammalian central nervous system. Trends Neurosci. *20*, 125–131.

Stuart, G., Schiller, J., and Sakmann, B. (1997b). Action potential initiation and propagation in rat neocortical pyramidal neurons. J. Physiol. *503*, 617–632.

Sun, W., Tan, Z., Mensh, B.D., and Ji, N. (2015). Thalamus provides layer 4 of primary visual cortex with orientation- and direction-tuned inputs. Nat. Neurosci. *19*, 308–315.

Susaki, E. a., Tainaka, K., Perrin, D., Kishino, F., Tawara, T., Watanabe, T.M., Yokoyama, C., Onoe, H., Eguchi, M., Yamaguchi, S., et al. (2014). Whole-brain imaging with single-cell resolution using chemical cocktails and computational analysis. Cell *157*, 726–739.

Svoboda, K., Denk, W., Kleinfeld, T., and Tank, D.W. (1997). In vivo dendritic calcium dynamics in neocortical pyramidal neurons. Nature *385*, 161–165.

Takahashi, N., Kitamura, K., Matsuo, N., Mayford, M., Kano, M., Matsuki, N., and Ikegaya, Y. (2012). Locally Synchronized Synaptic Inputs. Science *335*, 353–356.

Tamas, G., Lorincz, A., Simon, A., and Szabadics, J. (2003). Identified Sources and Targets of Slow Inhibition in the Neocortex. Science (80-.). *299*, 1902–1905.

Usrey, W.M., Alonso, J.M., and Reid, R.C. (2000). Synaptic interactions between

thalamic inputs to simple cells in cat visual cortex. J. Neurosci. *20*, 5461–5467.

Vaiceliunaite, A., Erisken, S., Franzen, F., Katzner, S., and Busse, L. (2013). Spatial integration in mouse primary visual cortex. J. Neurophysiol. *110*, 964–972.

Vaney, D.I., Sivyer, B., and Taylor, W.R. (2012). Direction selectivity in the retina: symmetry and asymmetry in structure and function. Nat. Rev. Neurosci. *13*, 194–208.

Varga, Z., Jia, H., Sakmann, B., and Konnerth, A. (2011). Dendritic coding of multiple sensory inputs in single cortical neurons in vivo. Proc. Natl. Acad. Sci. U. S. A. *108*, 15420–15425.

Velez-Fort, M., Rousseau, C. V, Niedworok, C.J., Wickersham, I.R., Rancz, E. a, Brown, A.P.Y., Strom, M., and Margrie, T.W. (2014). The Stimulus Selectivity and Connectivity of Layer Six Principal Cells Reveals Cortical Microcircuits Underlying Visual Processing. Neuron *83*, 1431–1443.

Vetter, P., Roth, a, and Häusser, M. (2001). Propagation of action potentials in dendrites depends on dendritic morphology. J. Neurophysiol. *85*, 926–937.

Vinck, M., Batista-Brito, R., Knoblich, U., and Cardin, J.A. (2015). Arousal and Locomotion Make Distinct Contributions to Cortical Activity Patterns and Visual Encoding. Neuron *86*, 740–754.

Vogelstein, J.T., Watson, B.O., Packer, A.M., Yuste, R., Jedynak, B., and Paninski, L. (2009). Spike inference from calcium imaging using sequential Monte Carlo methods. Biophys. J. *97*, 636–655.

Volgyi, B., Chheda, S., and Bloomfield, S.A. (2009). Tracer coupling patterns of the ganglion cell subtypes in the mouse retina. J. Comp. Neurol. *512*, 664–687.

van Vreeswijk, C., and Sompolinsky, H. (1996). Chaos in neuronal networks with balanced excitatory and inhibitory activity. Science *274*, 1724–1726.

Wagor, E., Mangini, N.J., and Pearlman, A.L. (1980). Retinotopic organization of striate and extrastriate visual cortex in the golden hamster (Mesocricetus auratus). *193*, 187–202.

Wallace, D.J., Greenberg, D.S., Sawinski, J., Rulla, S., Notaro, G., and Kerr, J.N.D. (2013). Rats maintain an overhead binocular field at the expense of constant fusion.

Nature *498*, 65–69.

Wassle, H. (2004). Parallel processing in the mammalian retina. Nat Rev Neurosci *5*, 747–757.

Wässle, H., Heinze, L., Ivanova, E., Majumdar, S., Weiss, J., Harvey, R.J., and Haverkamp, S. (2009). Glycinergic transmission in the Mammalian retina. Front. Mol. Neurosci. *2*, 1–12.

Waters, J., Larkum, M., Sakmann, B., and Helmchen, F. (2003). Supralinear Ca2+ influx into dendritic tufts of layer 2/3 neocortical pyramidal neurons in vitro and in vivo. J. Neurosci. *23*, 8558–8567.

Wertz, A., Trenholm, S., Yonehara, K., Hillier, D., Raics, Z., Leinweber, M., Szalay, G., Ghanem, A., Keller, G., Rózsa, B., et al. (2015). Single-cell-initiated monosynaptic tracing revelas layer-specific cortical network modules. Science *349*, 70–74.

Wilks, T. a, Harvey, A.R., and Rodger, J. (2013). Seeing with Two Eyes: Integration of Binocular Retinal Projections in the Brain. In Functional Brain Mapping and the Endeavor to Understand the Working Brain, F. Signorelli, and D. Chirchiglia, eds. (InTech), pp. 227–250.

Williams, S.R., and Stuart, G.J. (2002). Dependence of EPSP efficacy on synapse location in neocortical pyramidal neurons. Science *295*, 1907–1910.

Wilson, A.D.E., Whitney, D.E., Scholl, B., and Fitzpatrick, D. (2016). Orientation selectivity and the functional clustering of synaptic inputs in primary visual cortex. Nat. Neurosci. *19*, 1003–1009.

Wurtz, R.H. (1969). Visual receptive fields of striate cortex neurons in awake monkeys. J. Neurophysiol. *32*, 727–742.

Xu, N., Harnett, M.T., Williams, S.R., Huber, D., O'Connor, D.H., Svoboda, K., and Magee, J.C. (2012). Nonlinear dendritic integration of sensory and motor input during an active sensing task. Nature *492*, 247–251.

Yankova, M., Hart, S. a, and Woolley, C.S. (2001). Estrogen increases synaptic connectivity between single presynaptic inputs and multiple postsynaptic CA1 pyramidal cells: a serial electron-microscopic study. Proc. Natl. Acad. Sci. U. S. A. *98*, 3525–3530.

Yilmaz, M., and Meister, M. (2013). Rapid innate defensive responses of mice to looming visual stimuli. Curr. Biol. *23*, 2011–2015.

Yoshimura, Y., Dantzker, J., and Callaway, E. (2005). Excitatory cortical neurons form fine-scale functional networks. Nature *433*, 868–873.

Zhang, S., Xu, M., Kamigaki, T., Phong Hoang Do, J., Chang, W.-C., Jenvay, S., Miyamichi, K., Luo, L., and Dan, Y. (2014). Long-range and local circuits for top-down modulation of visual cortex processing. Science *345*, 660–665.

Zhao, X., Chen, H., Liu, X., and Cang, J. (2013). Orientation-selective responses in the mouse lateral geniculate nucleus. J. Neurosci. *33*, 12751–12763.